

UCLA

UCLA Electronic Theses and Dissertations

Title

Seismic Risk Assessment of Spatially Distributed Levee System in the Sacramento-San Joaquin Delta

Permalink

<https://escholarship.org/uc/item/25r3275x>

Author

Liu, Zehan

Publication Date

2024

Peer reviewed|Thesis/dissertation

UNIVERSITY OF CALIFORNIA

Los Angeles

Seismic Risk Assessment of Spatially Distributed Levee System in the Sacramento-San Joaquin

Delta

A dissertation submitted in partial satisfaction

of the requirements for the degree

Doctor of Philosophy in Civil Engineering

by

Zehan Liu

2024

© Copyright by

Zehan Liu

2024

## ABSTRACT OF THE DISSERTATION

Seismic Risk Assessment of Spatially Distributed Levee System in the Sacramento-San Joaquin  
Delta

by

Zehan Liu

Doctor of Philosophy in Civil Engineering

University of California, Los Angeles, 2024

Professor Scott Joseph Brandenburg, Chair

The approximately 1,100 miles of levees in the Sacramento-San Joaquin Delta is critical to aquatic and terrestrial habitat, agriculture, California's water supply and distribution system, and other infrastructure investments, and the levee system protects them from flooding and salt water intrusion. However, the levee system is threatened by a variety of hazards. Land due to oxidation of the rich Delta peat soils, and due to sea level risk act together to effectively increase the levee hydraulic loading. Consolidation of peat soils beneath levees can lead to their continued settlement over time. Delta levees are also threatened by potential sudden shocks from floods events and earthquakes. Numerous advances with greater proliferation and more sophisticated methods of risk

assessments have been made since the most recent risk study of the Delta was completed. Therefore, assessing multi-hazard risks of the Delta levee system by leveraging newly available data and knowledge is of great importance for decision makers to implement improvements in response to those long-term and short-term stressors.

This study primarily focuses on seismic risk assessment of Bacon Island in the central Delta. The seismic capacity, demand, spatial correlations of levee systems, and system reliability analysis are four essential components throughout the seismic risk assessment.

Newly available LiDAR, bathymetry data, geotechnical site investigation results, and measurements from advanced geophysical tests significantly facilitate determining geometry, soil stratigraphy/layering, and soil property of levees. Consequently, the levee fragility functions which reflect the system seismic capacity are developed from a large number of time-series nonlinear finite element simulations using OpenSees. An overview of updated probabilistic seismic hazard analysis results for the Delta region is discussed. Moreover, an algorithm for selecting a subset of events for hazard-consistent analysis of spatially distributed infrastructures is introduced, and performed to analyze the regional probabilistic seismic hazard analysis of the Bacon Island levee system, which quantifies seismic demand of the levees. The correlation functions of capacity are derived based on field geophysical measurements and geo-statistics analysis. Furthermore, the system reliability analysis using level crossing statistics method is implemented to assess seismic risk for Bacon Island levees based on the developed levee fragility, correlation lengths, and selected event subset.

The dissertation of Zehan Liu is approved.

Jonathan Paul Stewart

Henry V. Burton

Paolo Zimmaro

Timu Gallien

Scott Joseph Brandenburg, Committee Chair

University of California, Los Angeles

2024

*For my parents, who support me in every endeavor.*

# TABLE OF CONTENTS

ABSTRACT OF THE DISSERTATION .....	ii
TABLE OF CONTENTS .....	vi
LIST OF FIGURES .....	x
LIST OF TABLES .....	xxii
ACKNOWLEDGEMENTS.....	xxiv
CURRICULUM VITA.....	xxvi
CHAPTER 1: Introduction .....	1
1.1 Motivation of Research.....	1
1.2 Research Objectives and Scope .....	3
1.3 Organization.....	5
CHAPTER 2: Regional Probabilistic Seismic Hazard Analysis .....	8
2.1 Seismic Hazard Analysis at a Point .....	8
2.1.1 Probabilistic Seismic Hazard Analysis Calculations .....	11
2.2 Regional Probabilistic Seismic Hazard Analysis Framework .....	21
2.3 Updated Site and Path Models for the Delta Region .....	27
2.3.1 Site Models for the Delta Region.....	28
2.3.2 Path Models for the Delta Region.....	32
2.3.3 Site and Path Model Implementation.....	34
CHAPTER 3: Fragility Functions of Bacon Island Levee System.....	43



3.1 Characterization of Bacon Island Levees .....	43
3.1.1 Levee Geometry.....	44
3.1.2 Geotechnical Site Investigation Data.....	49
3.1.3 Geophysical Data.....	62
3.1.4 Soil Properties.....	67
3.2 Ground Motion Selection.....	82
3.3 Nonlinear Finite Element Modeling .....	95
3.3.1 Pre-processing.....	95
3.3.2 Finite element analysis.....	113
3.3.3 Post-processing .....	123
3.4 Seismic Fragility Function Development .....	129
3.4.1 Literature Review.....	129
3.4.2 Ground Motion Selection for Levee Crest Settlement.....	132
3.4.2 Model for levee settlement vs. <i>PGV</i> .....	138
3.4.3 Construct Levee Seismic Fragility Functions.....	149
CHAPTER 4: Event Selection Algorithm for Delta Region Levee Risk Assessment.....	155
4.1 LASSO Regression-Based Event Selection Methodology .....	155
4.1.1 LASSO Regression .....	158
4.1.2 Tensor Rank Reduction Transformation .....	159
4.1.3 Event Selection .....	161

4.1.4 Including Magnitude and/or Source-to-Site Distance.....	163
4.1.5 Comparison of LASSO and Mixed Integer Linear Optimization.....	167
4.2 Selecting Event Subset for the Delta Region.....	168
4.2.1 Event Subset for <i>PGV</i> Hazard Matching.....	172
4.2.2 Event Subset for <i>PGA</i> Hazard Matching.....	179
4.2.3 Event Subset for <i>PGA</i> and M Hazard Matching.....	189
4.2.4 Summary.....	201
CHAPTER 5: System Reliability Analysis.....	203
5.1 System Reliability Analysis Framework.....	203
5.2 Reach Length and Spatial Correlation of Demand.....	207
5.2.1 Reach Length.....	208
5.2.2 Spatial Correlation of Demand.....	209
5.3 Spatial Correlation of Capacity.....	210
5.4 Spatial Correlation of Limit State Function.....	217
5.5 Levee System Reliability Analysis Case Studies.....	218
5.5.1 1980 Livermore Earthquake.....	218
5.5.2 2014 South Napa Earthquake.....	221
5.6 Seismic Risk Assessment of Bacon Island Levees.....	223
5.7 Risk Assessments of Bacon Island Under other Hazards.....	227
CHAPTER 6: Conclusions and Recommendations.....	229

6.1 Conclusions.....	229
6.2 Recommendations for Future Research.....	233
APPENDIX A: CPT Profiles for Northern and Southern Levees.....	236
APPENDIX B: Selected Unscaled Ground Motions for Simulating Levee Fragility Functions	239
REFERENCES .....	265

## LIST OF FIGURES

<b>Figure 2.1</b> Schematic of a site, nearby faults, and a scenario earthquake event. ....	9
<b>Figure 2.2</b> <i>PGV</i> -based hazard curve for a single site in the Delta region. ....	10
<b>Figure 2.3</b> Map showing the site of interest, Bacon Island, the Delta region, and surrounding faults.....	14
<b>Figure 2.4</b> <i>PGA</i> -based hazard curve of the given site of interest. ....	15
<b>Figure 2.5</b> <i>SA</i> (1.0)-based hazard curve of the given site of interest. ....	16
<b>Figure 2.6</b> Deaggregation of <i>PGV</i> of the site at return period of 475 years. ....	18
<b>Figure 2.7</b> Deaggregation of <i>PGV</i> of the site at return period of 2475 years. ....	19
<b>Figure 2.8</b> <i>PGV</i> -based Hazard map of the Delta region for the return period of 2475 years. ....	20
<b>Figure 2.9</b> <i>PGV</i> -Based hazard map of the Delta Region given an occurrence of rupturing of Midland Fault.....	22
<b>Figure 2.10</b> <i>PGV</i> -Based hazard map of the Delta Region given an occurrence of rupturing of San Andreas Fault. ....	23
<b>Figure 2.11</b> $V_{S30}$ histogram of sites used in NGA-West2 model and at Delta sites. (Buckreis, 2022) .....	29
<b>Figure 2.12</b> Map of the Greater Delta Area, showing the locations of Delta and non-Delta stations. (Buckreis, 2022) .....	30
<b>Figure 2.13</b> Plots comparing the fit of ergodic model and region-specific model to observe linear site term versus $V_{S30}$ for (a) <i>PGV</i> and (b) <i>PGA</i> . (Buckreis. 2022) .....	31
<b>Figure 2.14</b> Locations of earthquakes, stations, and paths used in developing regional path model. The ten study subregions are outlined by solid black lines. Inset shows outline of Geysers region from Viegas and Hutchings (2010) and locations of Geysers events.	

(Buckreis et al. 2023).....	33
<b>Figure 2.15</b> Map of the Delta Region, showing the locations of 7 example sites, the Great Valley (Midland) fault trace, and its surface projection. ....	35
<b>Figure 2.16</b> Predicted median $PGA$ versus $R_{JB}$ distance of 7 example sites with 4 various site conditions ( $V_{S30} = 50, 100, 150,$ and $200$ m/s) under the Great Valley (Midland) fault rupture with $M = 5$ computed from original BSSA14 and BSSA14 with updated site and path models. ....	37
<b>Figure 2.17</b> Predicted median $PGV$ versus $R_{JB}$ distance of 7 example sites with 4 various site conditions ( $V_{S30} = 50, 100, 150,$ and $200$ m/s) under the Great Valley (Midland) fault rupture with $M = 5$ computed from original BSSA14 and BSSA14 with updated site and path models. ....	38
<b>Figure 2.18</b> Map of the Delta Region, showing the locations of 7 selected sites, the Healdsburg fault trace, and its surface projection. ....	39
<b>Figure 2.19</b> Predicted median $PGA$ versus $R_{JB}$ distance of 7 example sites with $V_{S30}$ equaling to 760 m/s under the Great Valley (Midland) fault rupture ( $M = 5$ ) and Healdsburg fault rupture ( $M = 6.8$ ) computed from original BSSA14 and BSSA14 with updated site and path models. ....	40
<b>Figure 2.20</b> Predicted median $PGV$ versus $R_{JB}$ distance of 7 example sites with $V_{S30}$ equaling to 760 m/s under the Great Valley (Midland) fault rupture ( $M = 5$ ) and Healdsburg fault rupture ( $M = 6.8$ ) computed from original BSSA14 and BSSA14 with updated site and path models. ....	41
<b>Figure 2.21</b> $PGV$ -based hazard curves of one site on Bacon Island computed from original and BSSA14 with updated site and path models. ....	42

<b>Figure 3.1</b> Map of digital elevation model (DEM) created by lidar point and bathymetry data for Bacon Island.....	45
<b>Figure 3.2</b> Levee reach, CPT, and boring log locations on Bacon Island. ....	46
<b>Figure 3.3</b> Southern levee cross-section geometry visualization at different reaches. ....	47
<b>Figure 3.4</b> Eastern levee cross-section geometry visualization at different reaches.....	48
<b>Figure 3.5</b> Northern levee cross-section geometry visualization at different reaches. ....	48
<b>Figure 3.6</b> Western levee cross-section geometry visualization at different reaches. ....	49
<b>Figure 3.7</b> Visualizations of LiDAR and bathymetric data of selected (a) northern levee cross-section and (b) southern levee cross-section.....	52
<b>Figure 3.8</b> CPT (BI-CPT-01-1) profile through northern levee crest.....	53
<b>Figure 3.9</b> Boring log (dwp-bi-ba5) profile through northern levee crest, Part I.....	54
<b>Figure 3.10</b> Boring log (dwp-bi-ba5) profile through northern levee crest, Part II. ....	55
<b>Figure 3.11</b> Boring log (dwp-bi-ba5) profile through northern levee crest, Part III. ....	56
<b>Figure 3.12</b> CPT (dwp-bi-ba20-cpt) profile through southern levee crest. ....	58
<b>Figure 3.13</b> Boring log (dwp-bi-ba1) profile through southern levee crest, Part I. ....	59
<b>Figure 3.14</b> Boring log (dwp-bi-ba1) profile through southern levee crest, Part II. ....	60
<b>Figure 3.15</b> Cross-section, soil stratigraphy of southern levee, boring log, and CPT locations. .	61
<b>Figure 3.16</b> Cross-section, soil stratigraphy of northern levee, boring log, and CPT locations. .	61
<b>Figure 3.17</b> Shear wave velocity and resistivity profile visualization in the northern levee. ....	63
<b>Figure 3.18</b> Shear wave velocity and resistivity profile visualization in the southern levee. ....	64
<b>Figure 3.19</b> Measured Rayleigh wave velocity at 5 m wavelength for Bacon Island levees.....	65
<b>Figure 3.20</b> Shear wave velocity and peat thickness profile of Sacramento-San Joaquin Delta region (Kwak et al. 2021). ....	67

<b>Figure 3.22</b> Comparison of backbone curves of clay acquired from Darendeli’s model and Yee’s hybrid model. ....	77
<b>Figure 3.24</b> Locations of four examples representative levee reach midpoints on Bacon Island levees.....	83
<b>Figure 3.25</b> (a) <i>PGA</i> -based hazard curves; (b) <i>PGV</i> -based hazard curves of four reach midpoint examples. ....	84
<b>Figure 3.26</b> <i>PGV</i> -based disaggregation results of the midpoint of Reach 2 for a return period of 10 years. ....	86
<b>Figure 3.27</b> <i>PGV</i> -based disaggregation results of the midpoint of Reach 2 for a return period of 50 years. ....	86
<b>Figure 3.28</b> <i>PGV</i> -based disaggregation results of the midpoint of Reach 2 for a return period of 100 years. ....	87
<b>Figure 3.29</b> <i>PGV</i> -based disaggregation results of the midpoint of Reach 2 for a return period of 225 years. ....	87
<b>Figure 3.30</b> <i>PGV</i> -based disaggregation results of the midpoint of Reach 2 for a return period of 475 years. ....	88
<b>Figure 3.31</b> <i>PGV</i> -based disaggregation results of the midpoint of Reach 2 for a return period of 2475 years. ....	88
<b>Figure 3.32</b> Response spectra of selected ground motions, compared to the target response spectra distribution computed by BSSA14 model with (a) magnitude = 6.5, distance = 10km, $V_{S30}$ =350 m/s; (b) magnitude = 8.3, distance = 90 km, $V_{S30}$ =350 m/s.....	90
<b>Figure 3.33</b> One input ground motion record and its spectral acceleration of Chi-Chi earthquake (RSN=1244) with magnitude 7.62, Taiwan, 1999. ....	91

<b>Figure 3.34</b> One input ground motion record and its spectral acceleration of Chuetsu-Oki earthquake (RSN=4875) with magnitude 6.8, Japan, 2007. ....	91
<b>Figure 3.35</b> One input ground motion record and its spectral acceleration of Darfield earthquake (RSN=6886) with magnitude 7, New Zealand, 2010. ....	92
<b>Figure 3.36</b> Comparison of ground accelerations of unscaled and scaled ground motion with amplifying factor equaling to 4 from 1989 Loma Prieta Earthquake. ....	93
<b>Figure 3.37</b> Magnitude histogram plot of unscaled and scaled ground motions. ....	94
<b>Figure 3.38</b> Levee input PGV histogram plot resulted from unscaled and scaled ground motions. ....	94
<b>Figure 3.39</b> Levee input PGA histogram plot resulted from unscaled and scaled ground motions. ....	95
<b>Figure 3.40</b> Steady-state finite element seepage analysis of northern levee.....	97
<b>Figure 3.41</b> Steady-state finite element seepage analysis of southern levee.....	98
<b>Figure 3.42</b> Finite element mesh configuration of northern levee generated by GiD.....	99
<b>Figure 3.43</b> Finite element mesh configuration of southern levee generated by GiD .....	99
<b>Figure 3.44</b> 4-node quadrilateral element with SSP and UP. ....	100
<b>Figure 3.45</b> Northern levee mesh configuration with Lysmer-Kuhlemeyer dashpot.....	102
<b>Figure 3.46</b> von Mises yield surfaces in 3-D stress space (Gu et al., 2011) .....	104
<b>Figure 3.47</b> Modulus reduction curves of organic peat based on Wang et al. (2022).....	105
<b>Figure 3.48</b> Cyclic shear stress ratio versus number of uniform loading cycles derived from direct simple shear (DSS) PDMY03 model simulations (Khosravifar et al.2018).....	110
<b>Figure 3.49</b> $K\sigma$ relationships derived from model simulations compared to relationships by Idriss and Boulanger (2008) (Khosracifar et al.2018).....	111



<b>Figure 3.50</b> Experimental trends for different $(N_1)_{60}$ values and $\sigma_v' < 3$ atm from Harder and Boulanger (1997) and model generated static shear stress correction factors ( $K_\alpha$ ) for $\sigma_{vc}' = 1$ atm.....	112
<b>Figure 3.51</b> Drucker-Prager and Mohr-Coulomb yield surfaces. (Chaitanya, 2017).....	113
<b>Figure 3.52</b> 1-D ground response analysis model mesh extracted from the original northern levee model mesh configuration.....	120
<b>Figure 3.53</b> Simulation software in ‘Tools and Applications’ module on the DesignSafe portal. ....	122
<b>Figure 3.54</b> Input settings for running parallel simulations using OpenSeesMP on Stampede 2 on DesignSafe. ....	123
<b>Figure 3.55</b> Vertical displacement contour plots of southern levee at the end of (a) gravity analysis; (b) ground shaking; (c) post-shaking reconsolidation phases under the ground motion (RSN =4875) from 2007 Chuetsu-Oki earthquake.....	125
<b>Figure 3.56</b> Pore water pressure distribution plots of southern levee at the end of (a) gravity analysis; (b) ground shaking; (c) post-shaking reconsolidation phases under the ground motion (RSN =4875) from 2007 Chuetsu-Oki earthquake.....	127
<b>Figure 3.57</b> An example of the directory containing completed simulation results of the northern levee model on DesignSafe portal. ....	128
<b>Figure 3.58</b> Levee crest settlement versus surface $PGV$ from 1-D model without liquefaction under unscaled and scaled ground motions for (a) southern levee; (b) northern levee. ....	133
<b>Figure 3.59</b> Levee crest settlement versus input $PGV$ under unscaled and one group of scaled ground motions for (a) southern levee; (b) northern levee. ....	134
<b>Figure 3.60</b> Input $PGV$ versus levee crest surface $PGV$ under unscaled and scaled ground	

motions of a 1-D vertical soil column extracted from (a) southern Levee; (b) northern levee. .....	135
<b>Figure 3.61</b> Southern Levee crest settlement versus levee (a) input <i>PGA</i> ; (b) input <i>PGV</i> under unscaled and scaled ground motions.....	136
<b>Figure 3.62</b> Magnitude versus residuals computed from regressed lines for simulation results of (a) southern levee; (b) northern levee under unscaled ground motions.....	137
<b>Figure 3.63</b> Levee crest settlement versus input <i>PGV</i> under unscaled and two groups of scaled ground motions for (a) southern levee; (b) northern levee. ....	138
<b>Figure 3.64</b> Input <i>PGV</i> versus levee crest settlement and linear fitting results including linear regression equation and standard deviation of residuals for (a) northern levee, (b) southern levee. ....	139
<b>Figure 3.65</b> Q-Q plots of standardized errors obtained from (a) northern levee, and (b) southern levee. ....	140
<b>Figure 3.66</b> Histogram and kernel density estimation curve of the regressed residuals computed from the southern levee model.....	141
<b>Figure 3.67</b> Standardized residuals versus independent variable input <i>PGV</i> of (a) northern levee, and (b) southern levee.....	143
<b>Figure 3.68</b> Input <i>PGV</i> versus levee crest settlement and piecewise linear fitting line with a breaking point input <i>PGV</i> equaling 50cm/s.....	144
<b>Figure 3.69</b> Finite element model of southern levee showing material region of levee fill. ....	146
<b>Figure 3.70</b> (a) Shear wave velocity $V_{S5}$ of levee versus crest settlement given a ground motion time series from 1994 Northridge earthquake, and (b) normalized $V_{S5}$ and crest settlement in log scales and fitted polynomial function. ....	147

**Figure 3.71** *PGV* and  $V_{SS}$ -based seismic fragility functions of levee reach 15 on northern levee.  
..... 150

**Figure 3.72** *PGV* and  $V_{SS}$ -based seismic fragility functions of levee reach 1 on southern levee.  
..... 151

**Figure 4.1** A scheme of rank reduction transformation from a rank-3 tensor (with indices  $l, j, k$ )  
to a rank-1 tensor (with index  $q$ ) for a target total hazard from all considered seismic  
sources..... 160

**Figure 4.2** A scheme of rank reduction transformation from a rank-4 tensor (with indices  $l, j, k, i$ )  
to a rank-2 tensor (with indices  $q, i$ ) for hazard produced by three events..... 161

**Figure 4.3** A schematic plot of (a) disaggregation of the seismic hazard by magnitude and  
distance, (b) marginal magnitude distribution, and (c) corresponding cumulative sum of  
marginal magnitude distribution. (Wang et al., 2023) ..... 165

**Figure 4.4** Map showing hazard-consistent event selection results and four target example sites  
of the Bacon Island levee system in the central Delta region (Liu et al, 2022). ..... 169

**Figure 4.5** Hazard curves for full PSHA and for event subset at four reach locations on Bacon  
Island (Liu et al., 2022)..... 170

**Figure 4.6** Map showing locations of study region, 157 target sites, and three example target  
sites. .... 171

**Figure 4.7** Mean of absolute arithmetic relative errors versus number of selected events for *PGV*  
hazard matching of the Delta region without preservation of magnitude and distance  
distributions..... 174

**Figure 4.8** Locations of the 42 selected events (36 selected rupture events and 6 selected point  
source events) of *PGV* hazard matching without magnitude and distance preservation

generated by LASSO regression. ....	176
<b>Figure 4.9</b> True and recovered hazard curves for <i>PGV</i> by the 42 selected events from the LASSO regression method without preservation of magnitude and distance distributions hazard matching of three example sites. ....	179
<b>Figure 4.10</b> Mean of absolute arithmetic relative errors versus number of selected events for <i>PGA</i> hazard matching of the Delta region without preservation of magnitude and distance distributions.....	180
<b>Figure 4.11</b> Locations of the 44 selected events (10 selected rupture events and 34 selected point source events) of <i>PGA</i> hazard matching generated without magnitude and distance preservation by LASSO regression.....	181
<b>Figure 4.12</b> True and recovered hazard curves for <i>PGA</i> by the 44 selected events from the LASSO regression method without preservation of magnitude and distance distributions hazard matching of three example sites. ....	184
<b>Figure 4.13</b> Mean of absolute arithmetic relative errors versus number of selected events for <i>PGA</i> hazard matching of the Delta region after excluding points sources with magnitude larger than 6.5. ....	185
<b>Figure 4.14</b> Locations of the 42 reselected events (19 selected rupture events and 23 selected point source events) of <i>PGA</i> hazard matching generated by LASSO regression after excluding points sources with magnitude larger than 6.5.....	186
<b>Figure 4.15</b> True and recovered hazard curves for <i>PGA</i> by the 42 reselected events from the LASSO regression method of three example sites. ....	188
<b>Figure 4.16</b> Mean of absolute arithmetic relative errors versus number of selected events for <i>PGA</i> hazard matching of the Delta region with preservation of magnitude distributions..	190

**Figure 4.17** Locations of the 82 selected events (35 selected rupture events and 47 selected point source events) of *PGA* hazard matching with magnitude preservation generated by LASSO regression. .... 191

**Figure 4.18** True and recovered hazard curves for *PGA* by the 82 selected events from the LASSO regression method without preservation of magnitude and distance distributions hazard matching of three example sites. .... 195

**Figure 4.19** Marginal distribution plots for *PGA* hazard at three sites with respect to magnitude. The results apply for 10, 50, 100, 225, 475, and 2475-year return periods. Results shown in the figure apply for 82 selected events by the LASSO regression method configured to match true hazard curves for both intensity measures and true magnitude distributions. .. 195

**Figure 4.20** Mean of absolute arithmetic relative errors versus number of selected events for *PGA* hazard matching of the Delta region with preservation of magnitude distributions after excluding points sources with magnitude larger than 6.5. .... 196

**Figure 4.21** Locations of the 65 selected events (29 selected rupture events and 36 selected point source events) of *PGA* hazard matching with magnitude preservation generated by LASSO regression after excluding points sources with magnitude larger than 6.5. .... 197

**Figure 4.22** True and recovered hazard curves for *PGA* by the 65 reselected events from the LASSO regression method of three example sites. .... 201

**Figure 4.23** Marginal distribution plots for *PGA* hazard at three sites with respect to magnitude. The results apply for 10, 50, 100, 225, 475, and 2475-year return period. Results shown in the figure apply for 65 reselected events by the LASSO regression method configured to match true hazard curves for both intensity measures and true magnitude distributions. .. 201

**Figure 5.1** Terminology in system reliability analysis framework. (Zimmaro et al., 2013) ..... 205

**Figure 5.2.** Overview of the Delta area, location of the three selected faults and Bacon Island.  
..... 209

**Figure 5.3** (a) Measured  $V_{S5}$  and smoothed  $V_{S5}$  using gaussian window function along the southern levee; (b) Required  $PGV$  values to achieve 30cm crest settlement along the southern levee. .... 212

**Figure 5.4** Semi-variogram versus lag distance (m) and fitted gaussian model based required  $PGV$  values to achieve 30 cm crest settlement along the southern levee. .... 215

**Figure 5.5** (a) Measured  $V_{S5}$  and smoothed  $V_{S5}$  using gaussian window function along western levee; (b) Required  $PGV$  values to achieve 30cm crest settlement along western levee.... 216

**Figure 5.6** Semi-variogram versus lag distance (m) and fitted gaussian model based required  $PGV$  values to achieve 30 cm crest settlement along the western levee..... 217

**Figure 5.7** Map showing locations of the Delta, Bacon Island levees, available earthquake stations, and the ruptured faults and epicenter of 1980 Livermore earthquake with ( $M_w = 5.8$ ). .... 219

**Figure 5.8** Observed damage on levee slope on the island side of eastern Bacon Island during the January 24, 1980, Livermore earthquake. (Finch, 1980)..... 221

**Figure 5.9** Map showing locations of the Delta, Bacon Island levees, available earthquake stations, and the ruptured faults and epicenter of 2014 South Napa earthquake ( $M_w = 6.0$ ).  
..... 222

**Figure 5.10** Annual rates of exceedance of various settlements using the selected event subset.  
..... 224

**Figure 5.11** Map of Port Chicago tide gauge where data is served by NOAA  
(<https://tidesandcurrents.noaa.gov/map/index.html>)..... 225

**Figure 5.12** Water elevation at Port Chicago tide gauge from December 16, 2023 through  
January 15, 2024 (<https://tidesandcurrents.noaa.gov/map/index.html>). ..... 226

## LIST OF TABLES

<b>Table 2.1</b> Coefficient values for $c_1$ , $c_2$ , $c$ , $V_1$ , $V_2$ , $V_c$ , and $V_{ref}$ .(Buckreis, 2022).....	31
<b>Table 2.2</b> Subregional anelastic coefficients of $PGA$ and $PGV$ . (Buckreis, 2022).....	34
<b>Table 1.1</b> Fundamental information of available CPT and boring logs on Bacon Island. ....	50
<b>Table 2.2</b> Averaged $V_{S5}$ of 28 reaches of Bacon Island levee system. ....	66
<b>Table 3.3</b> Measured soil parameters of northern levee from lab tests. ....	69
<b>Table 3.4</b> Measured and inferred soil parameters of northern levee from lab tests. ....	69
<b>Table 3.5</b> TCU test of clay samples obtained in northern levee. ....	70
<b>Table 3.6</b> TCU test of peat samples obtained in northern levee. ....	70
<b>Table 3.7</b> Corrected blow counts and relative density of sand layers in the northern levee model. .....	74
<b>Table 3.8</b> Measured and calculated soil parameters of northern levee from field tests. ....	74
<b>Table 3.9</b> Measured and inferred soil parameters of southern levee from lab tests. ....	78
<b>Table 3.10</b> Shear strength ratio and cone factor profile based on CPT and TUU test results. ....	81
<b>Table 3.11</b> Measured and calculated soil parameters of southern levee from field tests. ....	82
<b>Table 3.12</b> Selected magnitude-distance combination scenarios with significant hazard contributions based on the disaggregations for all return periods. ....	89
<b>Table 3.13</b> Undrained shear strength and modeling information of fine-grained soil in northern levee. ....	107
<b>Table 3.14</b> Undrained shear strength and modeling information of fine-grained soil in southern levee. ....	108
<b>Table 3.15</b> Boundary conditions of 6 analysis stages.....	114
<b>Table 3.16</b> Analysis commands used in stage 1, 2, 3, and 4.....	115



<b>Table 3.17</b> Analysis commands used in stage 5. ....	119
<b>Table 3.18</b> Damage level classification (Kwak et al. 2016a). ....	130
<b>Table 3.19</b> Damage level classification of Bacon Island levees.....	131
<b>Table 3.20</b> Kolmogorov-Smirnov and Shapiro-Wilk tests for standardized regression error terms from northern and southern levees.....	142
<b>Table 3.21</b> Means and standard deviations of log-normal CDFs of exceeding various damage levels (DL) for northern and southern levee models. ....	152
<b>Table 4.1.</b> Variables for regional PSHA calculation. ....	157
<b>Table 4.2</b> Selected rupture and point events for <i>PGV</i> hazard matching.....	177
<b>Table 4.3</b> Selected rupture and point events for <i>PGA</i> hazard matching.....	182
<b>Table 4.4</b> Re-selected rupture and point events for <i>PGA</i> hazard matching.....	187
<b>Table 4.5</b> Selected rupture and point events for <i>PGA</i> hazard matching with magnitude preservation.....	192
<b>Table 4.6</b> Re-selected rupture and point events for <i>PGA</i> hazard matching with magnitude preservation.....	198
<b>Table 5.1</b> Probability of exceeding various settlement levels of Bacon Island levee system during 1980 Livermore earthquake. ....	220
<b>Table 5.2</b> Probability of exceeding various settlement levels of Bacon Island levee system during 2014 South Napa earthquake. ....	223
<b>Table 5.3</b> Probabilities of levee failure over various spans of time for this study, and DRMS (2009).....	227
<b>Table 5.4</b> Annual rates of overtopping failure.....	228

## ACKNOWLEDGEMENTS

I would like to express my deepest gratitude to my primary advisor, Professor Scott Joseph Brandenburg, for his unwavering patience, support, guidance, and mentorship throughout my doctoral journey. The invaluable lessons extend far beyond the realm of academia; under Scott's guidance, I have learned what it truly means to be a compassionate, dedicated, and empathetic individual. His unwavering commitment to fostering a supportive academic environment has instilled in me the importance of kindness, collaboration, and mentorship. Through countless meetings, constructive feedback, and shared experiences, Scott has modeled the qualities of an excellent mentor, more importantly, a great person. I am fortunate to have had not only an academic mentor in Scott but also a role model for the kind of person I aspire to be.

I am grateful to Professor Jonathan Paul Stewart and Professor Paolo Zimmaro, thanks so much for your valuable instructions and suggestions during our weekly meetings in the past 4 years. I also thank my committee members, Professor Henry V. Burton and Professor Timu Gallien, for their invaluable insights and constructive feedback. Special thanks to my colleagues Professor Pengfei Wang and Dr. Tristan E. Buckreis, thank you for collaborating and providing many valuable insights and advice.

I want to express my gratitude for the opportunity to work as Dr. Martin Hudson's teaching assistant, which was an enriching experience for me. I would also like to thank the many professionals and researchers who helped me with my research. In a similar manner, I would like to thank the past and present collaborators of the *Geotechnical Research Group* at UCLA, you guys not only provided so much generous help to me for tackling a variety of technical issues but also enriched my life with incredible friendships. I will give a collective "thank you" to all of you

in case omitting anyone.

I acknowledge the Delta Stewardship Council for providing financial support for my research, enabling me to pursue this project. The Department of Civil and Environmental Engineering at UCLA generously offered me teaching opportunities for funding sources that enable me to be able to complete my Ph.D. research.

Finally, I appreciate the support and understanding of my family and friends, whose encouragement kept me motivated during challenging times. Special thanks to my parents, Meiying Fan and Xiaojian Liu. As I reflect on the journey that has led me to this point, I am overwhelmed with gratitude for the unwavering support you have provided. Your love, encouragement, and sacrifices have been the bedrock upon which I have built my dreams.

# CURRICULUM VITA

## Education

M.S., 2019, Civil (Geotechnical) Engineering, University of California, Los Angeles

## Experience

Graduate Student Researcher, University of California, Los Angeles, Department of Civil and Environmental Engineering (2019-2023)

Teaching Assistant, University of California, Los Angeles, Department of Civil and Environmental Engineering, Principles of Soil Mechanics (2022)

Teaching Assistant, University of California, Los Angeles, Department of Civil and Environmental Engineering, Advanced Geotechnical Design (2023)

## Publications

**Liu, Z.**, Wang, P., Brandenburg, S. J., Zimmaro, P., & Stewart, J. P. (2022). Validation of Regression-Based Event Selection for Seismic Risk Assessment of Distributed Levee System in California. In *Proceedings of the 12th National Conference on Earthquake Engineering*.

Wang, P., **Liu, Z.**, Brandenburg, S. J., Zimmaro, P., & Stewart, J. P. (2023). Regression-based scenario earthquake selection for regional hazard-consistent risk assessments. *Earthquake Spectra*, 39(4), 2236-2262.

Brandenburg, S. J., **Liu, Z.**, Wang, P., Zimmaro, P., & Stewart, J. P. (2021). Earthquake event selection for regional seismic hazard analysis of levee systems. In *Proceedings Seismological Society of America 2021 Annual Meeting*.

Pengfei Wang; Linda Al Atik; Nick Gregor; Nicolas Kuehn; Melanie A. Walling; Albert R. Kottke; **Zehan Liu**; Paolo Zimmaro; Yousef Bozorgnia; Scott J. Brandenburg; Jonathan P. Stewart. (2023). GIRS 2023-02: Hazard-Consistent Scenario-Based Correlated Ground Motions For California Gas Pipeline Infrastructure. DOI: 10.34948/N3001C.

Winters, M., M. Delisle, J. Lucey, Y. Kim, **Z. Liu**, K. Hudson, S. Brandenburg, T. Gallien, (2019) "UCLA UAV Imaging", in Ridgecrest, CA earthquake sequence, July 4 and 5, 2019. DesignSafe-CI. <https://doi.org/10.17603/ds2-wfgc-a575> v1

# **CHAPTER 1: Introduction**

## **1.1 Motivation of Research**

The Sacramento-San Joaquin Delta is formed at the western edge of the Central Valley by the confluence of the Sacramento and San Joaquin rivers and lies just east of where the rivers enter Suisun Bay, which flows into San Francisco Bay. The Delta was formed by rising sea level following glaciation, leading to the accumulation of Sacramento and San Joaquin River sediments behind the Carquinez Strait, the sole outlet from the Central Valley to San Pablo Bay. The narrowness of the Carquinez Strait coupled with tidal action has caused the sediment to pile up, forming expansive islands. Geologically, the Delta has existed for about 10,000 years since the end of the Last Glacial Period. According to sediment core analyses (Shlemon and Begg 1975; Atwater 1982), the Delta has been a tidal freshwater marsh, with a network of channels, sloughs, and islands, for more than 6,000 years. The Delta provides at least a portion of the water supply for about two-thirds of California's population, and provides a migratory pathway for four fish that are listed as endangered or threatened pursuant to the federal Endangered Species Act. (Mount and Twiss, 2005)

The Sacramento-San Joaquin Delta encompasses about 3600 km<sup>2</sup> where lowlands are surrounded by 183 km levees. About 630 km are "project" levees which are part of the State Plan of Flood Control, and about 1,200 km are "nonproject" levees which are owned and maintained by local levee management agencies. The levee system is central to aquatic and terrestrial habitat, agriculture, California's water supply system, and other infrastructure investments. The system protects agriculture and infrastructure from flooding and serves as the hub of California's water distribution system. High quality water is pumped from the Delta to central and southern parts of the State for irrigation and drinking water supply. A key function of the Delta levee system is

minimizing salt water intrusion into the Delta to maintain water quality for local irrigation and export, and to maintain aquatic habitats for sensitive species. Currently this is achieved by maintaining a steady flow of fresh water through the Delta into the bay.

The Delta is exposed to numerous natural hazards including sudden shocks imposed by high water events and earthquakes, and long-term stresses imposed by land subsidence and sea level rise. A particularly onerous scenario would occur if multiple Delta levees were to simultaneously breach during a sudden shock. As the open space in the islands fills with water, the predominantly fresh-water Delta channels would become contaminated with salt water drawn in from the West. Understanding the risk posed to the Delta by these natural hazards is critical for making informed decisions about Delta land management, levee maintenance and enhancement, water conveyance, and habitat protection.

Hazard and risk assessment in the Delta has been ongoing for many years and must remain ongoing as new information becomes available and improved analysis methods are developed. The Delta Risk Management Strategy (DRMS, DWR 2009), completed just over a decade ago, provided a comprehensive analysis of the reliability of Delta levee systems to floods, earthquakes, and sunny-day hazard. A key finding of DRMS was that the Delta region is unsustainable in its current configuration due to threats to levee integrity. The DRMS effort was conducted utilizing the best information available at the time of the study. Nevertheless, the following advances were made since DRMS completed, which warrants re-evaluation of risk:

1. A total of over 8000 geotechnical boring logs and over 4000 cone penetration test soundings are now available in the Delta, which marks approximately a 30% increase in available geotechnical data.

2. Significant advances have been made in understanding levee fragility functions based on observations of damage (or lack thereof) to levees that were strongly shaken by earthquakes in Japan and founded on inorganic soils (Kwak et al. 2016a) and organic soil (Tsai et al. 2017).
3. A new system reliability framework has been established for assessing the probability of failure of a system (i.e., an island) given spatially correlated fragility functions and demands (Kwak et al. 2016b, Zimmaro et al. 2018).
4. Advances in non-invasive geophysical testing techniques (Park et al. 2007, Johnson et al. 2010, Uhlemann et al. 2018) and the coupling of their analyses (Hauck et al. 2010, Ivanov et al. 2017, Hayashi et al. 2018) enable high resolution imaging of soil properties within and beneath Delta levees. These soil properties are crucial for characterizing soil properties and their spatial variability.
5. A new hydraulic model allows analysis of short-term effects and longer-term tidal effects on water elevation in the Delta in response to future sea level rise (Andrews et al. 2017).

## **1.2 Research Objectives and Scope**

The purpose of this study is to bring these scientific advances described above to bear on natural hazard risk assessment in the Delta. In this regard, the study directly supports the missions of the Delta Science Program to “provide scientific information and syntheses for the state of scientific knowledge on issues critical for managing the Bay-Delta system” (<https://deltacouncil.ca.gov/delta-science-program/>, accessed January 17, 2022).

The overall objective of the research in this dissertation mainly focuses on seismic hazard analysis and risk assessment of the Bacon Island levee system and elaborates the detailed steps to

accomplish these tasks. I also briefly address flood risk performed by other project team members as a comparison with seismic risk. Bacon Island was selected for my study for the following reasons: (1) it is highly subsided and is therefore important for maintaining fresh water in the Delta, (2) there is ample geotechnical site investigation data available, and (3) it is owned by Metropolitan Water District, who has a shared interest in hazard assessment and is a cooperative stakeholder. I envision that methods developed in the dissertation will also be easily adaptable to other islands in the Delta as part of a future Delta-wide updated risk assessment. The scope of my work may be summarized by the following aspects:

1. Perform Probabilistic Seismic Hazard Analysis (PSHA) to Bacon Island levee system. Adopt the ad hoc linear site model for the Delta (Buckreis et al., 2023) and regional path model (Buckreis et al., 2023) in the Boore et al. (2014; hereafter BSSA14) ground motion model (GMM) utilized in PSHA and explicitly demonstrate the effects to ground motion predictions and hazard curves of Bacon Island levees.
2. Implement comprehensive site characterizations for Bacon Island levees by leveraging a variety of newly available data including LiDAR and Bathymetry data, geotechnical, and geophysical testing data.
3. Establish two-dimensional levee cross-section finite element models according to site characterization results mentioned above and conduct the non-linear finite element analysis for levee models using OpenSees. Perform comprehensive data analysis of the data from dynamic earthquake simulations and develop appropriate reach-based levee fragility functions for Bacon Island levees using statistical modeling approaches.
4. Utilize an efficient LASSO regression-based event selection algorithm to select a manageable and hazard-consistent reduced event subset from the large number of event



scenarios utilized in the probabilistic seismic hazard analysis. Furthermore, develop various reduced event subsets for the entire Delta region to match various ground motion intensity measures and native earthquake parameters to facilitate other future Delta-wide earthquake hazard analysis.

5. Develop spatial correlation lengths of southern and western levee seismic capacity based on shear wave velocity  $V_{S5}$  of levee measured in geophysical test and semi-variogram analysis.
6. Utilize a system reliability analysis framework based on level crossing statistics to quantify probability of failure due to earthquake shaking, overtopping, and seepage analysis performed on two-dimensional cross-sections. Perform seismic risk assessment for Bacon Island levees based on developed fragility functions, the selected event subset, and correlation lengths.
7. Present the levee risk assessments of other natural hazards accomplished by coherent researchers and perform the multi-hazard risk assessment for Bacon Island levee system by integrating all these risk assessment results.

### **1.3 Organization**

The organization of this dissertation is described as follows:

Chapter 2 introduces the traditional Probabilistic Seismic Hazard Analysis (PSHA), and I elaborate the limitations of applying conventional PSHA that generally aims for point-scale analysis to a spatially distributed system such as the Delta levees. Moreover, I present the necessity of event-based analysis in the regional PSHA for the levee system seismic hazard analysis, and I mention an efficient LASSO regression event selection approach that significantly alleviates computing

demands in event-based analyses. In addition, I present the Boore et al. (2014) ground motions models (GMM) with updated Delta-specific linear site term and regional path term by leveraging newly available database (Buckreis. 2022), and I also demonstrate the updated site and path models' effects on ground motion predictions and hazard curves.

Chapter 3 mainly focuses on non-linear finite element simulations and development of fragility functions of Bacon Island levees. Firstly, this chapter presents the site characterization of Bacon Island levees by taking advantage of LiDAR, bathymetry, boring log, laboratory test, cone penetration test, and geophysical data, and levee geometry, soil stratigraphy, and soil properties can be obtained. Additionally, I demonstrate the ground motion selection process for Bacon Island by matching unconditional response spectrum using the method proposed by Baker and Lee (2018). Furthermore, I present the comprehensive non-linear finite element simulation process using OpenSees (McKenna et al., 2000) via high performance computer (HPC) platform to inspect the levees' performance under the previously selected ground motions. Moreover, I also quantify the within and inter cross-section variability of levee system fragility based on additional simulation results. Finally, I implement the post-processing and data analysis for all simulation results to develop reach-based fragility functions of Bacon Island levees to quantify levee seismic capabilities.

Chapter 4 thoroughly introduces the LASSO regression event selection methodology proposed by Wang et al. (2022) and its various applications. Besides, I also develop a variety of reduced event subsets of the Delta region for matching  $PGA$ ,  $PGV$ , and preserving marginal magnitude distributions by means of performing LASSO regression event selection approach, and these reduced event subsets can be directly utilized in various seismic hazard assessments.

Chapter 5 focuses on the system reliability analysis and starts with introducing system reliability framework based on level crossing statistics approach (LCS). I develop correlation lengths of levee system seismic capacity by means of geophysical testing results and semi-variogram analysis. Moreover, I present some case studies to validate this system reliability analysis method computing the probability of failure of Bacon Island levee system under past occurred earthquakes in Northern California. In addition, I assess the seismic risk of Bacon Island levee system using convolving developed fragility functions, selected reduced event subset, and system reliability analysis method. Furthermore, at the end of this chapter, I briefly introduce the risk assessment results of other hazards for Bacon Island levees accomplished by cohort researchers in ‘Next Generation Multi-Hazard Risk Assessment’ project.

Last but not least, Chapter 6 summarizes the scope and major findings from this study, and it provides recommendations for future work based on what I have learned throughout my research.

## CHAPTER 2: Regional Probabilistic Seismic Hazard Analysis

Chapter 2 first introduces traditional probabilistic seismic hazard analysis (PSHA) and then it discusses regional probabilistic seismic hazard analysis (RPSHA) and the comparison of these two methods. The general framework of RPSHA is introduced. Selecting hazard-consistent event scenarios is crucial in RPSHA, and the relevant literatures and methodologies of earthquake event selection from past decades to recent years are demonstrated. In addition, Delta-wide path and site effects in the GMM used in the RPSHA are also discussed at the end of this chapter.

### 2.1 Seismic Hazard Analysis at a Point

An important aspect of earthquake engineering is assessment of design ground motions. Consider the site, nearby faults, and earthquake scenario event shown in Fig. 2.1. Shaking intensity at the site will depend on the earthquake magnitude and style of faulting (source effects), distance to the fault rupture (path effects), and stiffness of the soil beneath the site (site effects). Furthermore, ground motions involve significant uncertainties, which are included as an error term. Eq. 2.1 describes the functional form commonly used to estimate ground motion at a site for a given earthquake scenario.

$$\ln(Y_{ij}) = F_{E_j} + F_{P_{ij}} + F_{S_{ij}} + \varepsilon\sigma_{ij} \quad (2.1)$$

where  $i$  and  $j$  represent the site  $i$  and earthquake  $j$ ,  $F_{E_j}$ ,  $F_{P_{ij}}$ , and  $F_{S_{ij}}$  are source, path, and site terms, respectively.  $\sigma_{ij}$  is the standard deviation of the model and  $\varepsilon$  is a unit normal distribution function.

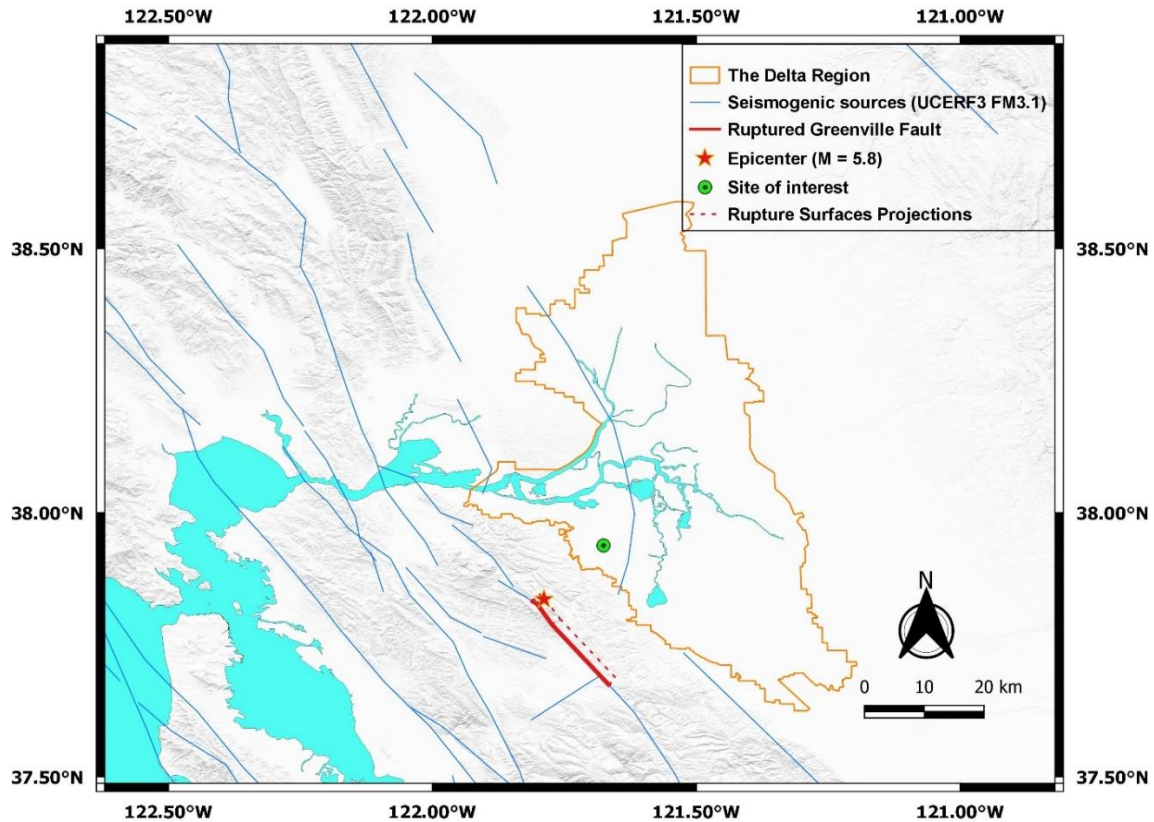


**Figure 2.1** Schematic of a site, nearby faults, and a scenario earthquake event.

A single scenario event is illustrated in Fig. 2.1, but earthquakes can occur at any location on the faults near the site, and for a range of magnitudes with an upper limit constrained by fault geometry. Uncertainties in the location and magnitude of the possible events, and the ground motions arising from them can be handled using probabilistic seismic hazard analysis (PSHA) or deterministic seismic hazard analysis (DSHA). PSHA mathematically combines seismic source model and GMM equations to compute annual rate of exceedance as a function of an earthquake ground motion intensity measure. This relationship is called a hazard curve, as illustrated by Fig. 2.2. Figure 2.2 shows the *PGV*-based hazard curve of a single site in the Delta region and three return-period levels computed using the NSHMP-haz tool (<https://github.com/usgs/nshmp-haz>, last

accessed Dec 20, 2023) for  $V_{S30} = 300$  m/s. Ground motions may be computed by selecting a suitable annual exceedance probability (e.g., 2475 years), and the selected ground motion is then used in design. Alternatively, the hazard curve may be convolved with a probabilistic representation of the engineering response of a system or component to ground shaking, as represented by a fragility function, to obtain a new curve representing annual rate of exceedance versus an engineering response parameter (e.g., system or component damage level). Equations for computing ground motion hazard curves and engineering response hazard curves are discussed later.

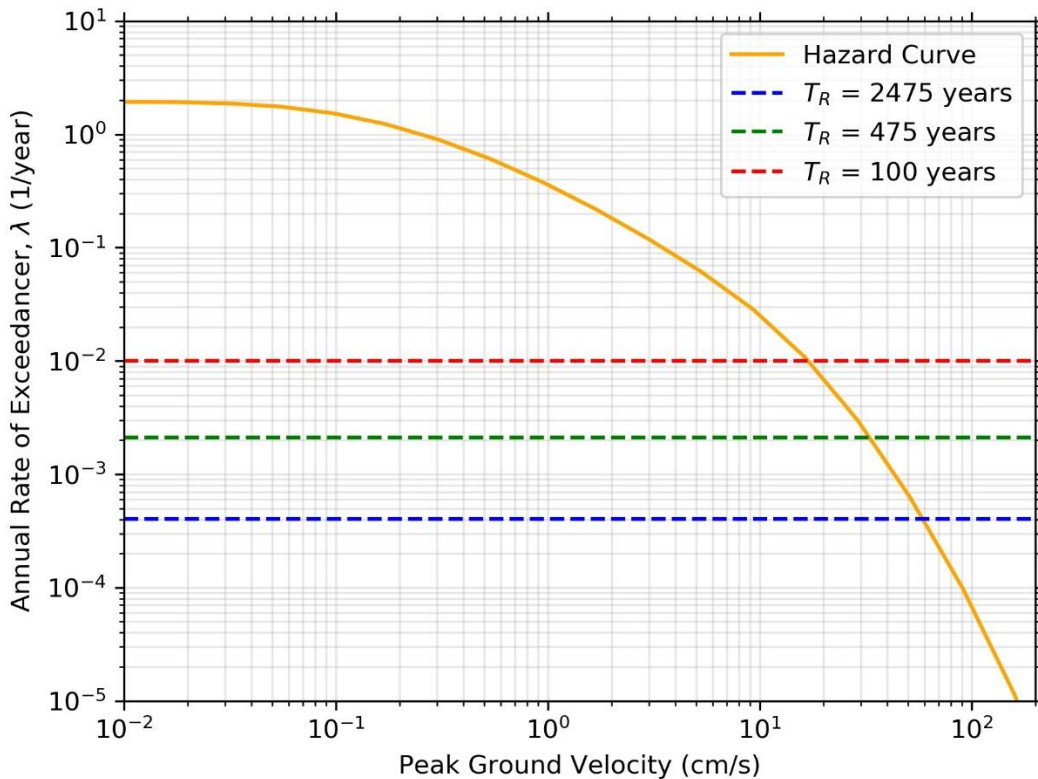


**Figure 2.2** PGV-based hazard curve for a single site in the Delta region.

DSHA selects a single representative earthquake scenario, and the ground motion associated with that scenario is generally selected to be some number of standard deviations above the mean. The probability of exceedance of the resulting ground motion is not computed, and DSHA does not incorporate earthquake rates, nor contributions from all of the faults that contribute to the hazard. Both DSHA and PSHA can play a role in seismic hazard and risk analyses, one method will have priority over the other depending on how quantitative the mitigation decisions are to be made, seismic environment, and the scope of project. Generally, PSHA is preferred to be used in more complex decisions and subtler seismic environments whereas simpler decisions and well-understood seismicity strongly suggest DSHA. PSHA is primarily focused here, so DSHA will not be discussed further.

### **2.1.1 Probabilistic Seismic Hazard Analysis Calculations**

In PSHA, all possible earthquake events, associated rate of occurrence, and resulting ground shaking are considered to calculate the annual rate of exceeding a ground motion intensity measure. There are three main steps in PSHA calculations.

- 1) Identify all possible earthquake sources that might produce damaging ground shaking to the site of interest. Herein, potentially damaging earthquakes are considered those with  $M > 5$  within 300 km of the site.
- 2) Identify the distribution of earthquake magnitude of potentially damaging seismic events, and discretize seismic sources into discrete events each with their own annual rate of occurrence. Herein, the Uniform California Earthquake Rupture Forecast, version 3 (UCERF3; Field et al., 2014) is utilized for this purpose. UCERF3 is the most recent source model for California at the time of writing this thesis. Although Field et al. (2023) proposed updated U.S. Geological Survey time-independent earthquake rupture forecast for the

conterminous United States, the data in this earthquake rupture forecast model was not publicly available yet by the time of writing this thesis.

- 3) Compute the distance between each scenario event and the site, and compute the desired ground shaking intensity measure based on magnitude, distance, and local site conditions, etc. Ground motion intensity is a random variable because the conditioning variables are not perfect predictors.
- 4) Integrate and combine all uncertainties in event magnitude, distance and intensity measure using the total probability theorem.

Earthquake sources can be faults (typically planar surfaces) or areal regions (background seismicity) in Step 1. The distribution of event magnitudes is commonly derived from the Gutenberg-Richter recurrence law, or the characteristic earthquake model. There are various definitions of “distance” used in PSHA depending on the GMMs. Joyner-Boore distance  $R_{jb}$  is commonly used for shallow crustal earthquakes, and is defined as the closest distance to the surface projection of the rupture plane. According to the total probability theorem and assuming that event magnitude and distance are statistically independent, for a single site of interest the probability of exceedance of intensity measure  $IM$  level  $im$  from a single source can be expressed as:

$$P(IM > im) = \int_{m_{min}}^{m_{max}} \int_{r_{min}}^{r_{max}} P(IM > im | m, r) f_M(m) f_R(r) dm dr \quad (2.2)$$

where  $P(IM > im | m, r)$  can be computed using a given GMM,  $f_M(m)$  and  $f_R(r)$  are the probability distribution functions of magnitude and distance. In reality, magnitude and distance are not statistically independent because a larger magnitude event has a higher probability of rupturing closer to a site. In practice, the joint distribution  $f_{M,R}(m, r)$  is substituted for the product  $f_M(m)f_R(r)$  in Eq. 2.2.



The annual rate of occurrence of earthquakes on the given source is also required in the PSHA calculation. Therefore, for a single site, the rate of intensity measure  $IM$  exceeding a certain level  $im$  for a single source can be written as:

$$\lambda(IM > im) = \lambda(M > m_{min}) \int_{m_{min}}^{m_{max}} \int_{r_{min}}^{r_{max}} P(IM > im | m, r) f_M(m) f_R(r) dm dr \quad (2.3)$$

where  $\lambda(M > m_{min})$  is the rate of occurrence of events greater than  $m_{min}$ . Eqs. 2.2 and 2.3 are applicable for a single source, but all possible sources must be considered in PSHA. The rate of  $IM > im$  for all possible sources can be simply calculated as the sum of the rates of  $IM > im$  for each individual source. Additionally, in practice, the integrals are generally converted to discrete summations over  $N_m$  and  $N_R$ , which are the number of discrete magnitudes  $m_j$  and discrete distances  $r_k$ . Therefore, the rate of  $IM > im$  for all possible sources can be written as,

$$\lambda(IM > im) = \sum_{i=1}^{N_s} \lambda(M > m_{min}) \sum_{j=1}^{N_m} \sum_{k=1}^{N_R} P(IM > im | m_j, r_k) P(M_i = m_j) P(R_i = r_k) \quad (2.4)$$

where  $N_m$  is the number of considered sources. Note that statistical dependence between  $M$  and  $R$  is achieved in this discretization by selecting discrete earthquake events, and computing the distance between each event and the site.

An example PSHA calculation for a single site on Bacon Island in the Sacramento and San Joaquin Delta Region is performed to demonstrate the PSHA calculations and outputs. Figure 2.3 shows the site and surrounding rupture faults in Fault Model 3.1 of UCERF3. Hazard curves can be computed for different intensity measures, including peak ground acceleration ( $PGA$ ), peak ground velocity ( $PGV$ ), and 5%-damped pseudo-spectral acceleration ( $S_a$ ) at a desired oscillator period. Figure 2.4 and figure 2.5 show hazard curves for  $PGA$  and  $S_a(T=1s)$ .

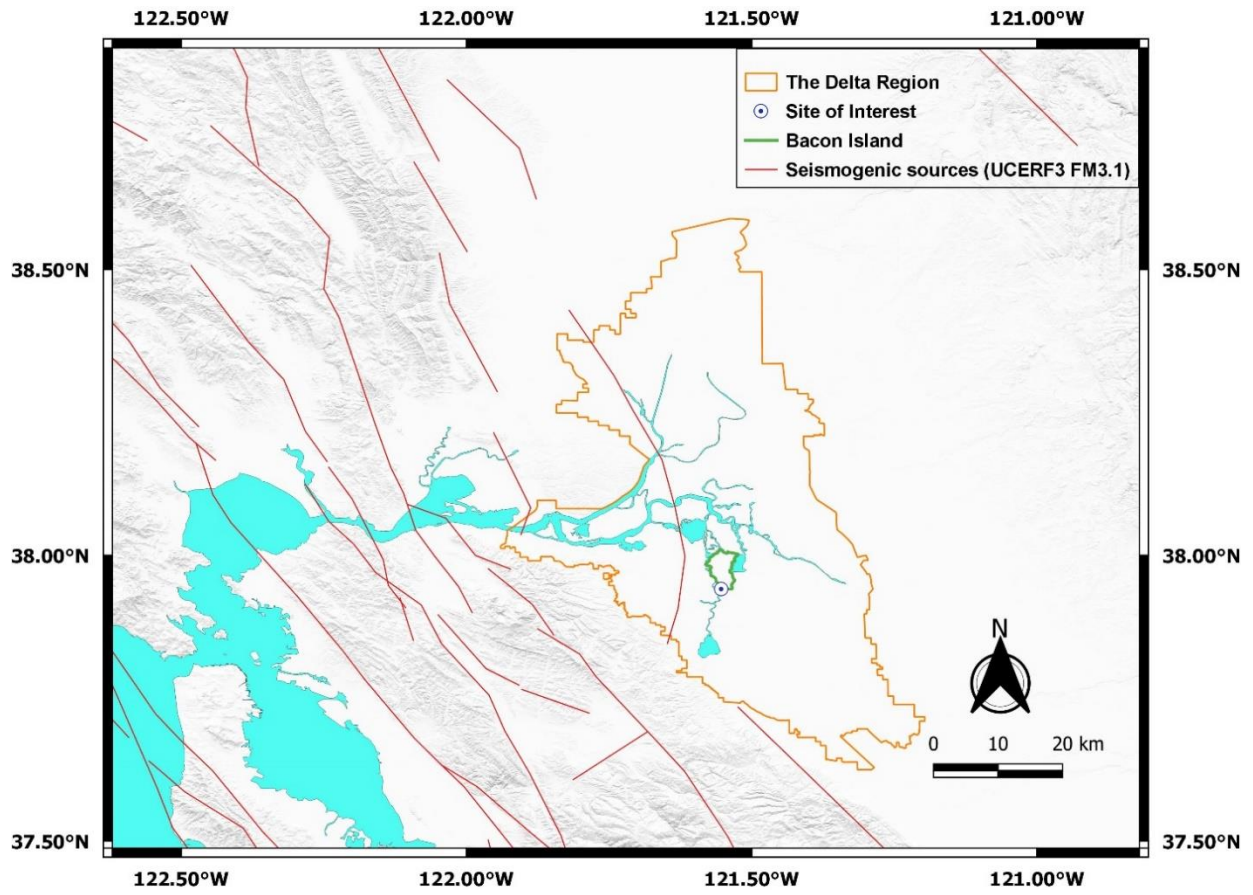


**Figure 2.3** Map showing the site of interest, Bacon Island, the Delta region, and surrounding faults.

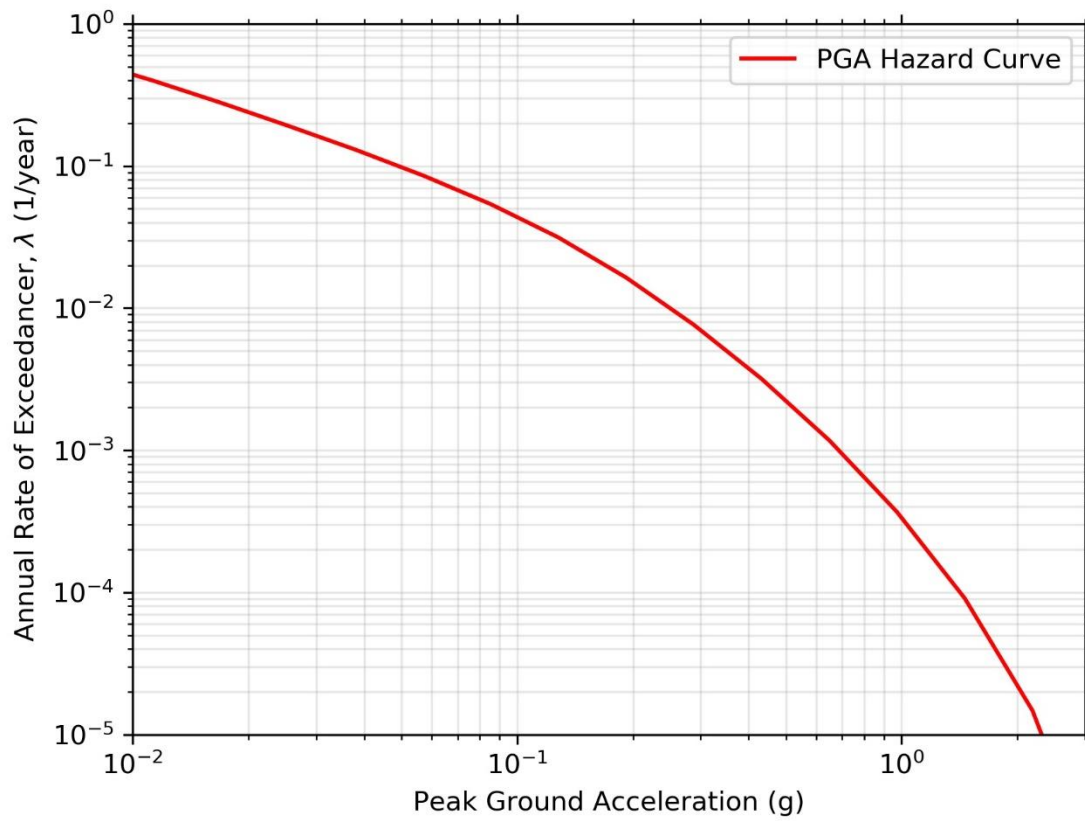


**Figure 2.4** PGA-based hazard curve of the given site of interest.

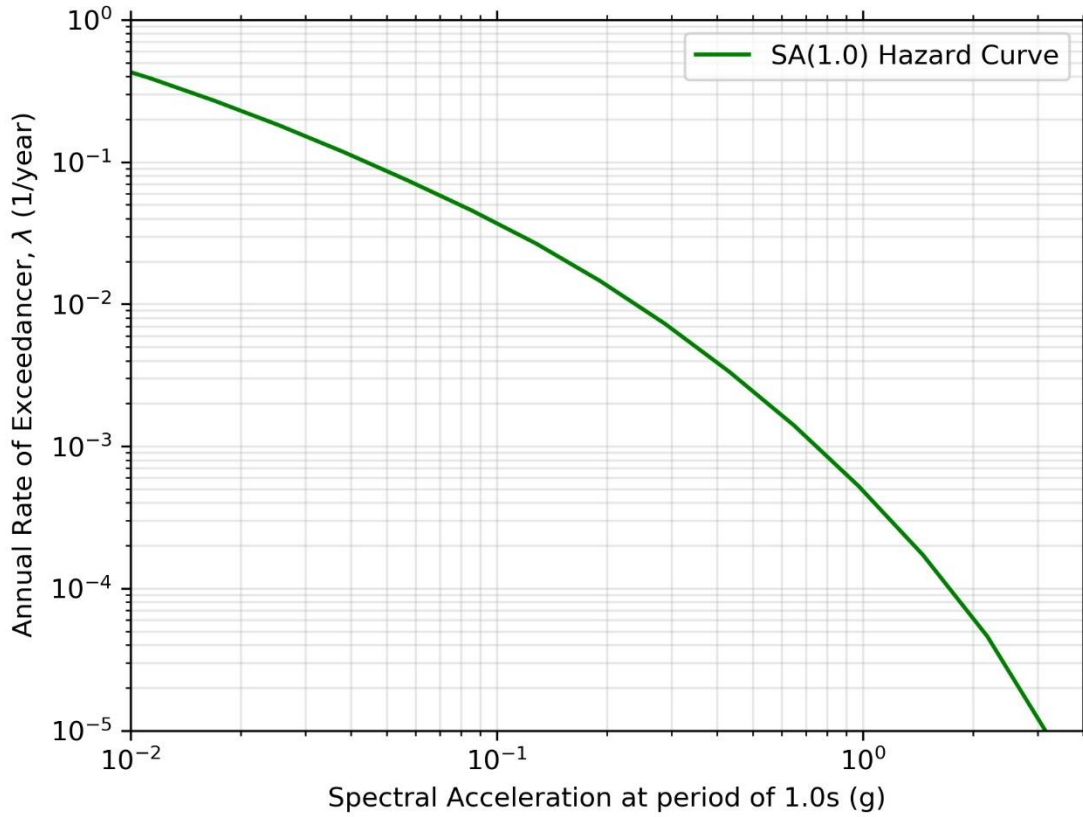


**Figure 2.5** SA (1.0)-based hazard curve of the given site of interest.

Understanding the contribution to the hazard from different earthquake scenarios is also an important aspect of PSHA because PSHA involves all possible event scenarios. De-aggregation provides the relative contributions of various earthquake scenarios with different source-to-site distance and magnitude at a particular return period, or intensity measure level. The marginal probability of exceedance of an intensity measure level ( $IM > x$ ) conditioned on a particular magnitude  $m$  and distance  $r$  is expressed by:

$$P(M = m, R = r | IM > im) = \frac{\lambda(IM > im | M = m, R = r)}{\lambda(IM > im)} \quad (2.5)$$

where the denominator is the exact result of equation 2.4 and the numerator can be written as,

$$\lambda(IM > im, M = m, R = r) = \sum_{i=1}^{N_s} \lambda(M > m_{min})P(IM > im|m, r)P(M_i = m)P(R_i = r)(2.6)$$

Equation 2.6 is derived from Equation 2.4 in PSHA but is summed over M and R that lie within prescribed bins rather than being summed over all events. Figures 2.6 and 2.7 show the results *PGV* de-aggregation for a site in the Bacon Island for 475-year and 2475-year return periods, and  $\varepsilon$  represents the number of standard deviations from the median ground motion as predicted by GMM. In Fig. 2.7, as a result of de-aggregation of *PGV* for 2475 years return periods, it clearly indicates that close fault and median magnitude (e.g.  $M=6.5$ ) have the greatest contribution to the hazard. However, de-aggregation of *PGV* with return period of 475 years reveals that long distance and large magnitude dominate the hazard in that case. This is because more distance faults in the Bay Area (e.g., the San Andreas and Hayward faults) have higher slip rates, and are more likely to shake the Delta at short return periods, whereas nearby faults are less active, but are more likely to strongly shake the Delta. Figure 2.6 reflects that moderate magnitude and close fault contribute mostly to hazard while large magnitude and long-distance fault still account for much contribution of hazard.

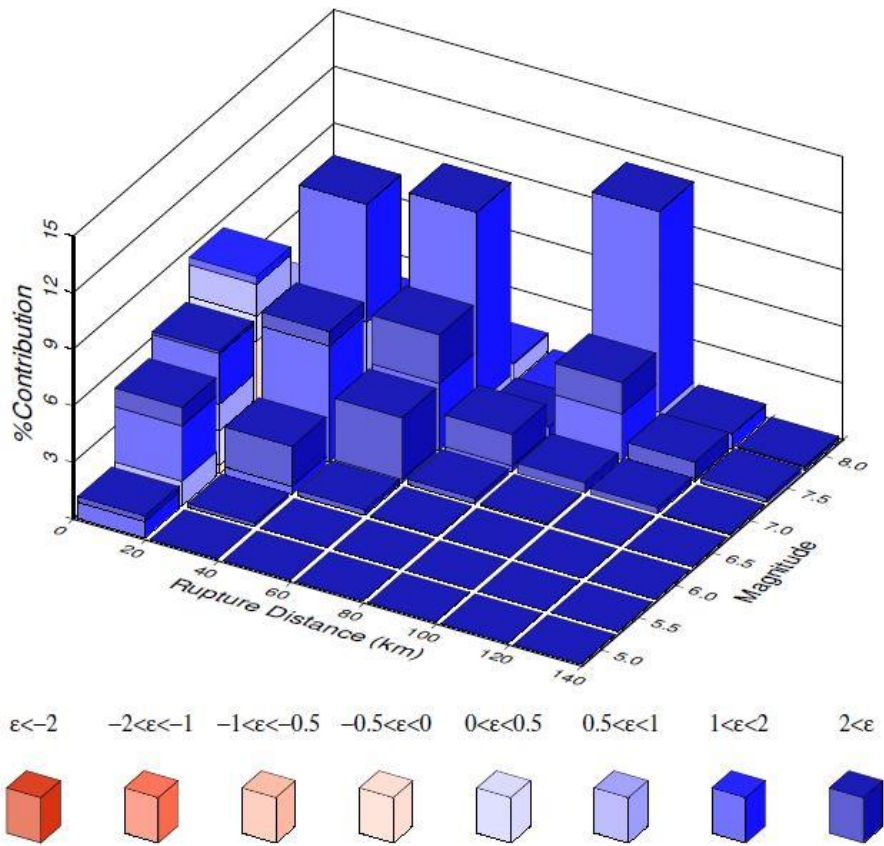


**Figure 2.6** Deaggregation of *PGV* of the site at return period of 475 years.

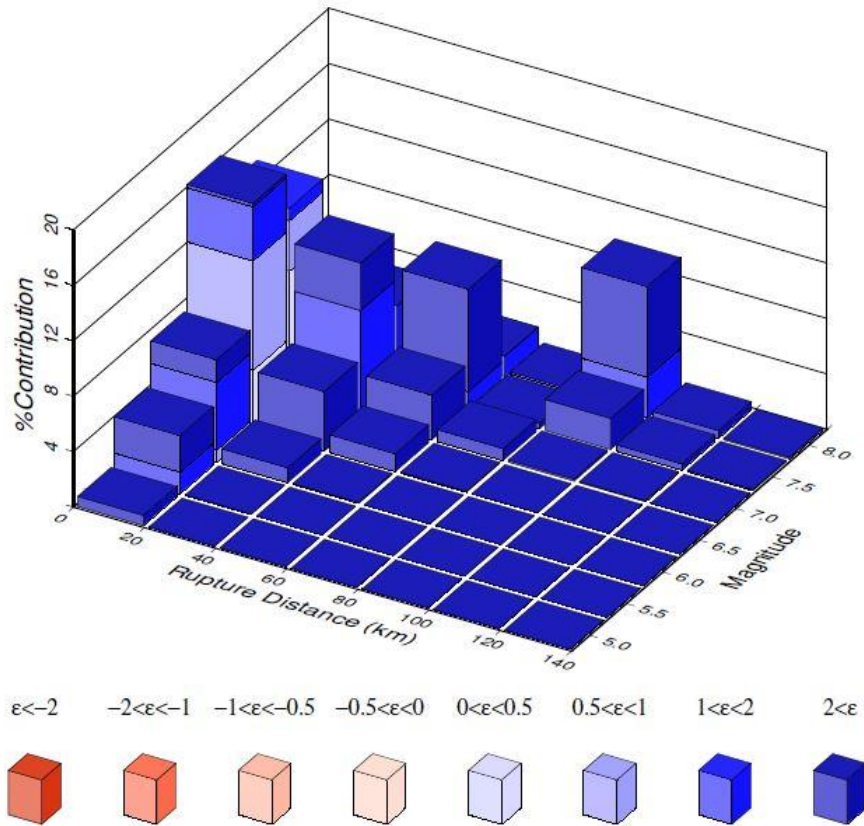


**Figure 2.7** Deaggregation of *PGV* of the site at return period of 2475 years.

If the hazard curve calculation performed for Bacon Island is repeated for many sites within a region, results can be represented by a hazard map depicting ground motion intensity at a specified return period. Fig. 2.8 shows the *PGV*-based hazard map of the Delta region for 2475-year return period, and this hazard map illustrates the overall regional seismic demand. Apparently, the *PGV* hazard varies spatially in the Delta region, with higher hazard in the west and hazard decreasing toward the east.

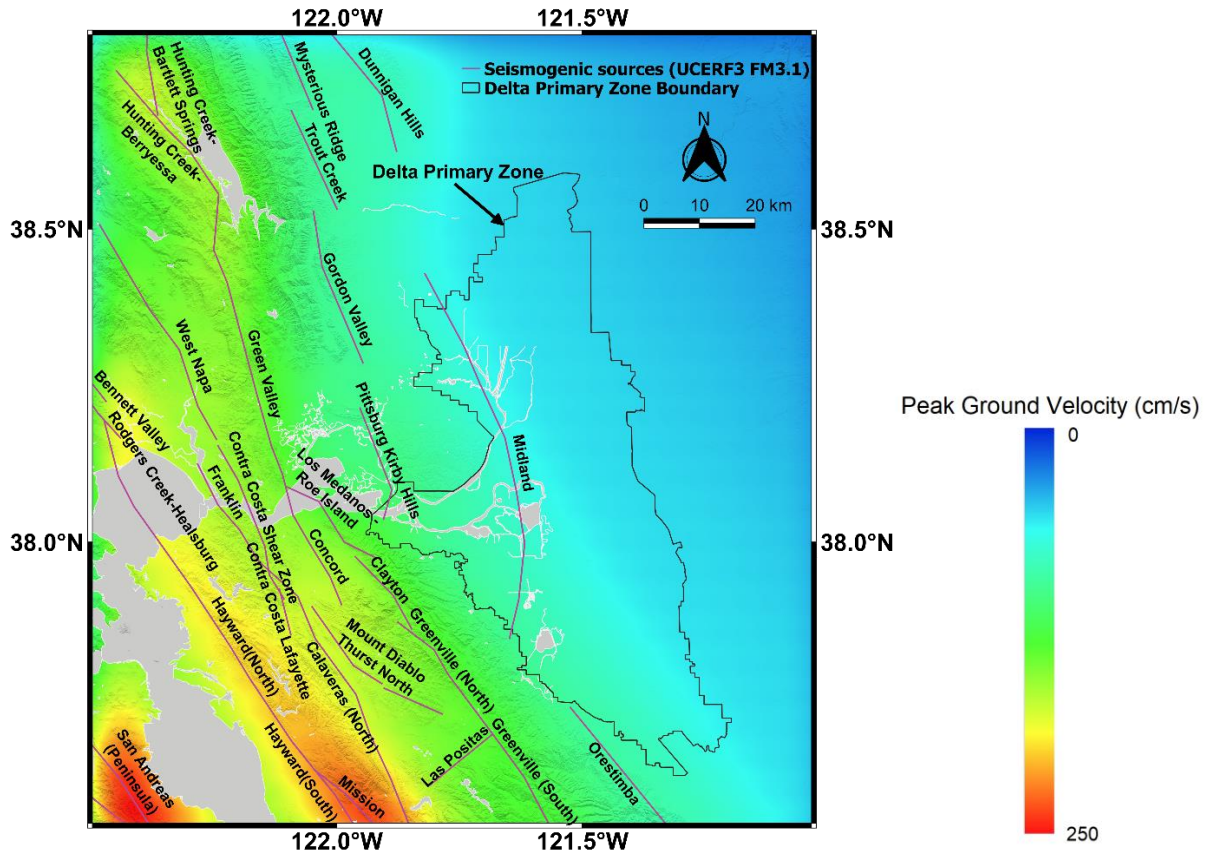


**Figure 2.8** PGV-based Hazard map of the Delta region for the return period of 2475 years.

An important aspect of hazard maps is that many different earthquakes contribute to the hazard at each point, and the hazard curve calculations are performed for each single site in the region independently. No single earthquake event, on its own, will produce uniform hazard level ground shaking simultaneously across an entire region. Uniform hazard maps are therefore useful for evaluating individual points on a particular map (e.g., the location of an individual building). However, uniform hazard maps are inappropriate for analyzing spatially distributed infrastructure systems like Delta levees, aqueducts, pipelines, etc. because each event will exhibit spatial



variability of shaking intensity. Regional PSHA which considers each event one at a time should be used for the spatially distributed system in risk or hazard analyses.

## **2.2 Regional Probabilistic Seismic Hazard Analysis Framework**

In the regional probabilistic seismic hazard analysis (RPSHA) for a spatially distributed system such as Delta levees, the hazard produced by each individual event should be analyzed. The main reason that RPSHA must utilize scenarios events rather than uniform hazard maps calculated from PSHA is that no single event will simultaneously produce uniform hazard shaking at every point in the system. Spatial correlations of ground shakings which cause different ground motion severities in different components of a system should be considered in a particular event.

An example can be used to demonstrate the spatially different ground shakings of a distributed system given an occurrence of a single earthquake event. Fig. 2.9 shows the *PGV*-based hazard map of the Delta region given the Great Valley (Midland) fault ruptures with a magnitude of 5.8. It is worth pointing out that the area with the strongest ground shaking is not centered around the fault trace because it is a reverse fault rupture with a  $47^\circ$  dipping angle. The BSSA14 GMM is utilized and a constant time-averaged shear wave velocity value at the depth of 30-meter  $V_{s30} = 300$  cm/s is assigned for the whole region to predict median *PGV*. Apparently, the median *PGV* varies spatially significantly within the Delta region. The area near the fault experiences severe ground shaking whereas the further area has slight ground shaking or even zero shakings. Fig. 2.10 presents the hazard map of the Delta region given a less frequent (higher return period) scenario where San Andreas Fault (Peninsula) ruptures with a magnitude of 8. The zone with the largest *PGV* is basically centered around the fault trace because the fault is the strike-slip type with a  $90^\circ$  dipping angle. There is not much difference of *PGV* intensity within the entire Delta region during

this event scenario. Spatial distributions of *PGV* intensities within the Delta region from these above two hazard maps are significantly different. Thus, it is not applicable to utilize uniform return period hazard maps computed across multi-sites in seismic analysis for a spatially distributed system.

As for the correlations of spatially distributed ground motions intensities, Jayaram and Baker (2009) estimated some spatial correlation models of different intensity measures at various spectral periods by assessing their semi-variograms of within-event residuals of observed ground motions from past seven earthquakes in California. These correlation models can be seen as general California ground shaking spatial correlation models, so they are feasible to be utilized in the RPSHA for the levee system in the Delta.

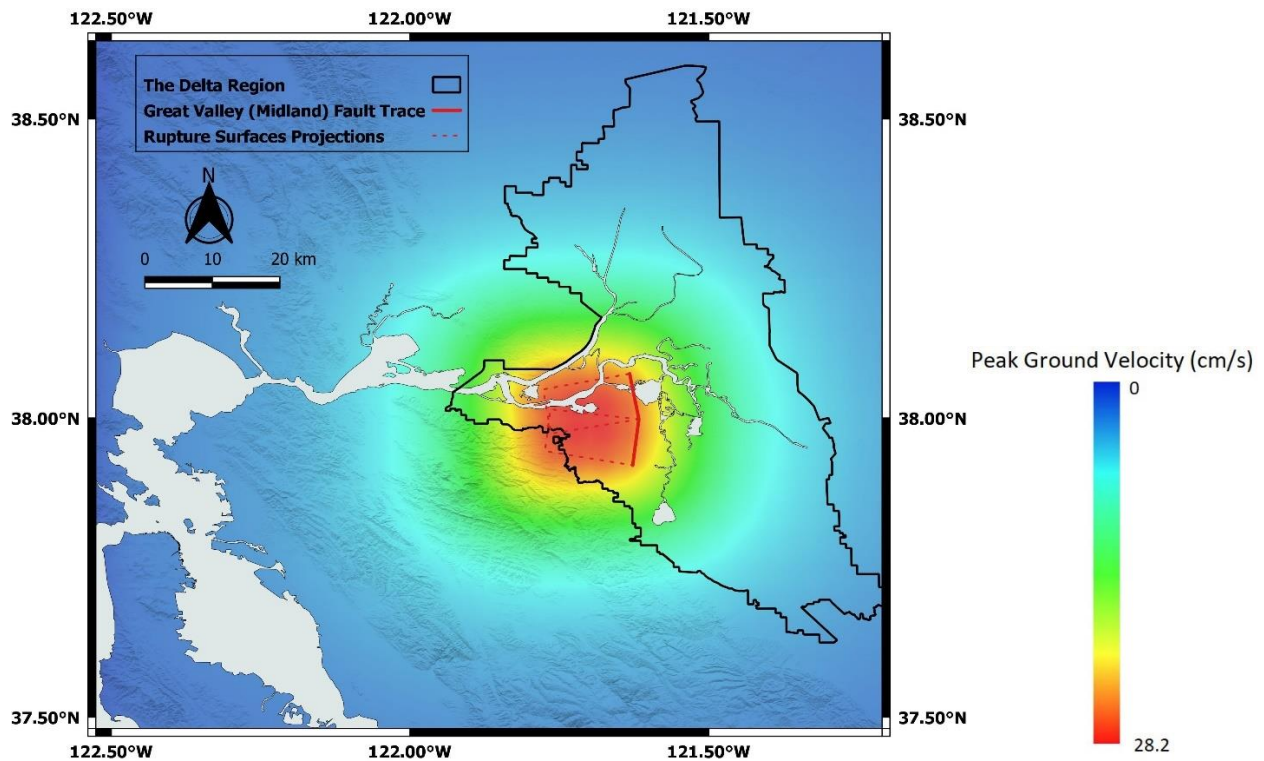


**Figure 2.9** *PGV*-Based hazard map of the Delta Region given an occurrence of rupturing of Midland Fault.

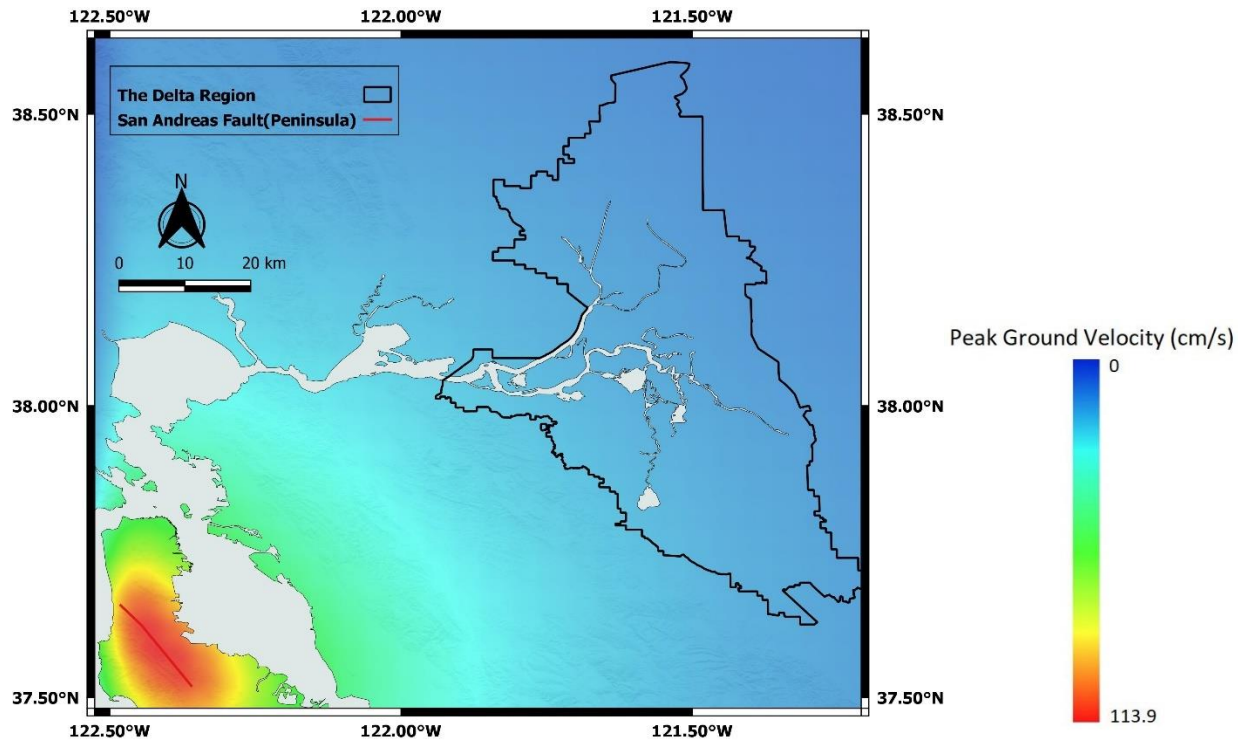


**Figure 2.10** PGV-Based hazard map of the Delta Region given an occurrence of rupturing of San Andreas Fault.

However, event-based analysis sometimes can be relatively computationally expensive when there are a huge amount of event scenarios needing to be considered. For instance, UCERF3 is commonly used as the source model in seismic hazard analysis in California. There are over hundreds of thousands of earthquake scenarios in this model, and even more ground motion realizations will be generated if they are sampled from earthquake scenarios. Ground motion realizations are generally used in the seismic risk analysis for a spatially distributed infrastructure. In addition, hazard or risk analysis for an entire system in a single event is not trivial. Thus, all event scenarios in UCERF3 are too many to be considered in system hazard and risk assessment.

Intuitively, event selection which selects a manageable and hazard and/or risk-consistent event subset should be implemented in RPSHA or RPSRA (regional probabilistic risk analysis) for a system to alleviate computational demanding.

Many researchers proposed various methodologies to deal with event selection problems in the past two decades. Chang et al. (2000) proposed a pre-knowledge and optimization-based event selection methodology to select representative scenarios. First, this methodology requires some judgement calls or/and pre-knowledge from users to define a potential event subset incorporating maximum credible event scenarios. Then, iterations of adjusting probabilities of occurrences of pre-defined event scenarios are implemented until (1) the hazard curves computed from the pre-defined event subset and the full event set are matching across some target sites; and (2) the hazard maps produced from the pre-defined event subset and the full event set are collectively consistent. A case study was implemented in their paper, this methodology was performed to select events for risk analysis of Los Angeles County network infrastructure. 47 earthquake scenarios were selected based on their knowledge and they ran the iteration to adjust the associated probabilities of these events. These probabilities are finally determined when the hazard curves matching across Los Angeles City Hall and hazard maps matching the hazard level of 10 percent probability of exceedance in 50 years are sufficiently consistent. This methodology provided some good initial thoughts of event selection in risk assessment for a spatially distributed system. However, the generality of this methodology is not robust enough. In other words, this method is relatively subjective and hard to apply in other cases analysis since the selected event subset is heavily dependent on the users' pre-knowledge and judgment calls.

Campbell and Seligson (2003) addressed 'subjective' issues of the method above and introduced a quantitative method to develop a subset of hazard-consistent earthquake events. They mainly

select events with high hazard contributions for multi points in a grided region and a certain range of ground motion values. (called a “bin”, e.g. 0.145g—0.284g, where  $g = 981\text{cm/s}^2$ ) The ratio of the probability of a ground motion value in this bin is from a certain event and the total probabilities of all events’ ground motion will fall in the bin is defined as the hazard contribution. They showed two case studies for applying this method to two hypothetical lifeline systems where one is geographically concentrated whereas the other is geographically diverse in southern California. Reasonable subsets of hazard-consistent earthquake events can be produced in both cases. However, this method can only deal with one single intensity measure with a specified short range of ground motion levels, which is very limited in the practical applications. In seismic engineering design, a boarder range of intensity measure levels are generally needed to be considered.

Kiremidjian et al. (2007) and Jayaram and Baker (2010) proposed an event reduction methodology using importance sampling to preferentially sample ‘important’ events such as earthquakes with large magnitudes. They fundamentally performed Monte Carlo Simulation to generate events from given earthquake sources rather than selecting events from a given full set such as UCERF3. Moreover, they did not consider the hazard consistency of these generated events, so these generated events might not be able to well represent the actual overall hazard of a certain region.

Vaziri et al. (2012) and Han and Davidson (2012) introduced an optimization-based method to select a hazard-consistent event subset for PSHA of spatially distributed infrastructure to address issues above. They implemented mixed-integer linear optimization method to select events and minimize the hazard error for a single intensity measure, multiple sites within a region and a variety of return periods. They demonstrated the effectiveness of reduction and achieving good hazard-consistency this method by performing a RPSHA for city of Los Angeles. Soleimani et al. (2021) used this optimization-based method and added some new constraints in it to produce an ensemble

of multi-hazard scenarios that can be used for spatially distributed infrastructure, and each multi-hazard scenario incorporates a possible realization of ground motion contours, liquefaction contours and locations of surface fault rupture. Despite the effectiveness of significant event reduction and hazard consistency of this mixed-integer linear optimization, this method is not very efficient and flexible. For a large-scale region, for example the entirety California, this optimization-based method generally took several days to complete the calculation. Moreover, it is not easy to add more objectives and constraints in the optimization function. In some cases, multi-intensity measures are anticipated to be simultaneously matched for a seismic hazard analysis, or magnitude and distance distributions are also expected to be preserved when selecting event subset. For instance, in seismic liquefaction and landslide displacement risk analysis, magnitude and intensity measures are all important.

Wang et al. (2022) proposed a LASSO regression-based event selection methodology which aims to select a manageable and hazard-consistent event subset for various intensity measures more efficiently. Additionally, this method is relatively flexible and can be used in a variety of event scenario selection with different objectives and constraints. LASSO regression is also called L1 regularization which is a regularization technique aiming for preventing overfitting for the model, and it adds “absolute value of magnitude” of coefficients as a penalty term to the loss function. It is good for variable selection since it can shrink coefficients to 0. This method can ultimately produce the events and adjusted associated rate of occurrence. Earthquake events with 0 coefficients indicates these events are not selected in matching overall regional hazard. Wang et al. 2022 illustrated and proved that this methodology is much more efficient than the mixed-integer linear optimization method especially for complex and large-scale infrastructure. Liu et al. (2022) validated this LASSO regression-based scenario selection method worked perfectly for both

seismic and risk assessment of the spatial distributed infrastructure. They implemented a comprehensive case study for a levee system within Bacon Island in the Delta region in California, and they found that both hazard and risk of the levee system calculated from the selected subset and the entire event set are considerably close. Considering the comparably high efficiency and low implementing complexity, this LASSO regression-based event selection method will be utilized to select earthquake scenarios in regional probabilistic seismic hazard and risk analysis in subsequent chapters.

After event selection, for each single event  $i$ , ground motion realizations within the infrastructure system can be simply simulated using GMM and spatial correlation model of ground motion. Additionally, each event  $i$  and the adjusted associated rate of occurrence  $\beta_i$  of event  $i$  is used to calculate the rate of exceedance a certain level of intensity measure under the single event  $i$ , which is written as,

$$\lambda_i(IM > im) = \beta_i \cdot P(IM > im|i) \quad (2.7)$$

where  $P(IM > im|i)$  probability of ground motion exceedance if event  $i$  occur, which can be simply calculated by the normal density function defined by the GMM.

### **2.3 Updated Site and Path Models for the Delta Region**

GMMs are critical components for PSHA and RPSHA. Existing GMMs, such as those developed for the NGAWest2 project (Bozorgnia et al. 2014), are ergodic because they utilize a spatially distributed worldwide dataset, and application of those GMMs inherently assumes that the stochastic processes that give rise to ground motion variability are stationary in space and time. However, regional variations in earthquake ground motions have been observed in which a particular region exhibits path or site effects that differ in a statistically significant manner from

the ergodic GMMs. In such cases, regional corrections are often formulated to improve model predictions in a particular region.

There is ample evidence that the Delta region differs from ergodic GMMs. First, there is a large amount of very soft organic peaty soil with  $V_{S30}$  values that are significantly lower than represented in the dataset from which the NGWest2 GMMs were derived. My colleague, Tristan Buckreis, utilized earthquake ground motion records in the Delta to develop non-ergodic site response factors. Their study is currently under review. Furthermore, my colleague, Pengfei Wang is utilizing ground response analyses to develop a nonlinear site response model for the Delta. His study is under active development and is not yet published or submitted for publication. Second, Erdem et al. (2019) studied 14 earthquakes in the San Francisco Bay area and found that earthquake ground motions attenuate more quickly with distance for those events compared with the ergodic GMMs. Subsequently, Buckreis et al. (2023) developed a subregional anelastic attenuation model in which crustal damping factors were derived for subregions developed based on surface geology, and confirmed certain aspects of Erdem et al. (2019). Specifically, earthquakes originating in the north coast subregion exhibit significantly more attenuation than indicated by ergodic GMMs.

In this section, I describe the linear site response model (Buckreis 2022) and subregional anelastic attenuation model Buckreis (2023), and subsequently assess the influence of these models on seismic hazard in the Delta. These site and path models replace the ergodic models in the BSSA14 GMM to demonstrate their effects on site responses and hazard curves in different cases.

### **2.3.1 Site Models for the Delta Region**

The site response term in BSSA14 is applicable globally for all active tectonic regions. Nevertheless, Landwehr et al. (2016), Nweke et al. (2022), and Wang et al. (2022a) observed some



site response discrepancies after investigating regional site effects at a more local scale. There are two issues that motivate researchers to develop a Delta-specific site model in the existing GMM. Firstly, The  $V_{S30}$  values of peaty soils in the Delta generally range from 60 m/s to 200 m/s, which is smaller than the lower limit for the site BSSA14 response model. Figure 2.11 shows the  $V_{S30}$  distributions of sites utilized in NGA-West2 models and at Delta sites.

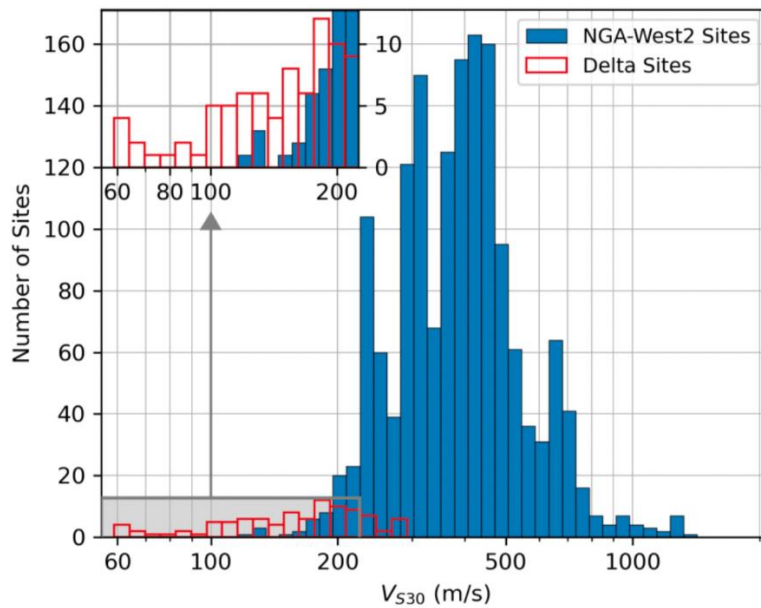


**Figure 2.11**  $V_{S30}$  histogram of sites used in NGA-West2 model and at Delta sites. (Buckreis, 2022)

In addition, the inorganic soils underlying the soft peaty soils in the Delta are significantly stiffer, creating a strong impedance contrast that may give rise to resonances at modal frequencies. Site terms in BSSA14 smooth over such resonances, and may therefore be inadequate predictors of site responses for sites with such resonance effects.

BSSA14 utilizes site response equations developed by Seyhan and Stewart (2014), and consist of linear and non-linear components. Buckreis (2022) expanded the ground motion database to

include many records in and around the Delta region to assess empirical site response in the Delta, and he developed a linear site amplification model using weak ground motions, where significant nonlinear effects are not expected. To be more specific, a  $V_{S30}$ -scaling model is developed by observing the trends of linear amplification versus  $V_{S30}$  for a variety of intensity measures with different return periods using the in the ground motion recording stations shown in Fig. 2.12.

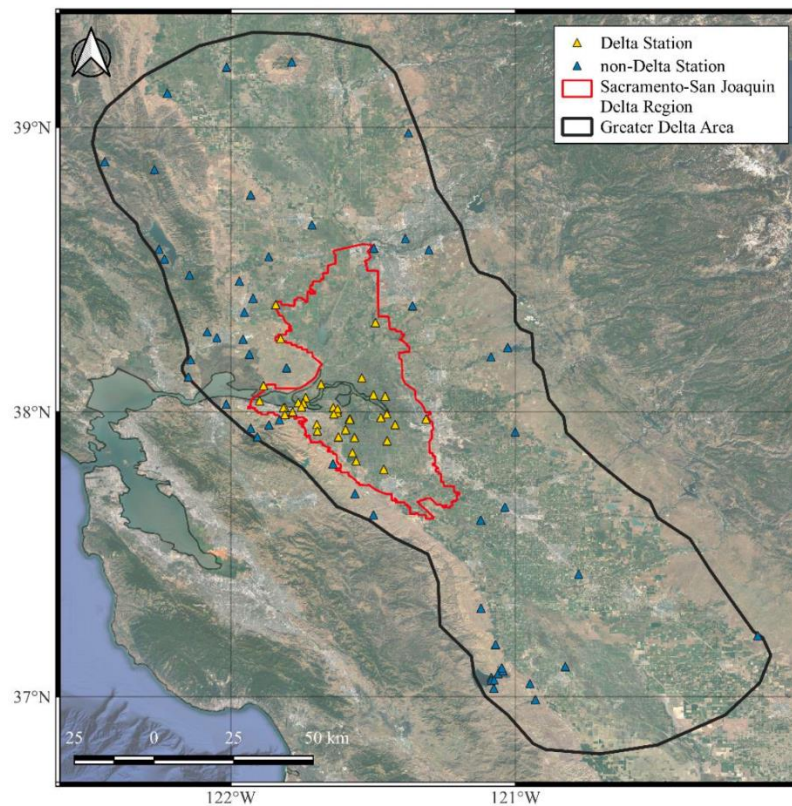


**Figure 2.12** Map of the Greater Delta Area, showing the locations of Delta and non-Delta stations. (Buckreis, 2022)

The linear site model with  $V_{S30}$ -scaling proposed by (Buckreis, 2022) is given by Eq. 2.7-2.10.

$$F_{lin}(V_{S30}) = \begin{cases} c_1 \ln\left(\frac{V_{S30}}{V_1}\right) + c_2 \ln\left(\frac{V_1}{V_2}\right) + c \ln\left(\frac{V_2}{V_{ref}}\right) & V_{S30} < V_1 & (2.7) \\ c_2 \ln\left(\frac{V_{S30}}{V_2}\right) + c \ln\left(\frac{V_2}{V_{ref}}\right) & V_1 < V_{S30} < V_2 & (2.8) \\ c \ln\left(\frac{V_{S30}}{V_{ref}}\right) & V_2 < V_{S30} < V_c & (2.9) \\ c \ln\left(\frac{V_c}{V_{ref}}\right) & V_c \leq V_{S30} & (2.10) \end{cases}$$

where  $c_1$ ,  $c_2$ , and  $c$  are  $V_{S30}$ -scaling coefficients,  $V_1$ ,  $V_2$ , and  $V_c$  are limiting velocities, and  $V_{ref}$  is the reference site condition, taken as 760 m/s. These coefficients of  $PGV$  and  $PGA$  are presented in Table 2.1.

**Table 2.1** Coefficient values for  $c_1$ ,  $c_2$ ,  $c$ ,  $V_1$ ,  $V_2$ ,  $V_c$ , and  $V_{ref}$ .(Buckreis, 2022)

Intensity Measure	$c_1$	$c_2$	$c$	$V_1$ (m/s)	$V_2$ (m/s)	$V_c$ (m/s)	$V_{ref}$ (m/s)
$PGV$	-0.20509	-1.07806	-0.84000	221.47	491.32	1300.00	760
$PGA$	0.00000	-0,45979	-0.60000	135.82	760	1500.00	760

Figure 2.13 shows the fit comparison of ergodic model and region-specific model to observed linear amplification (linear site term)  $(f_1)_j$  versus  $V_{S30}$  for  $PGV$  and  $PGA$ .

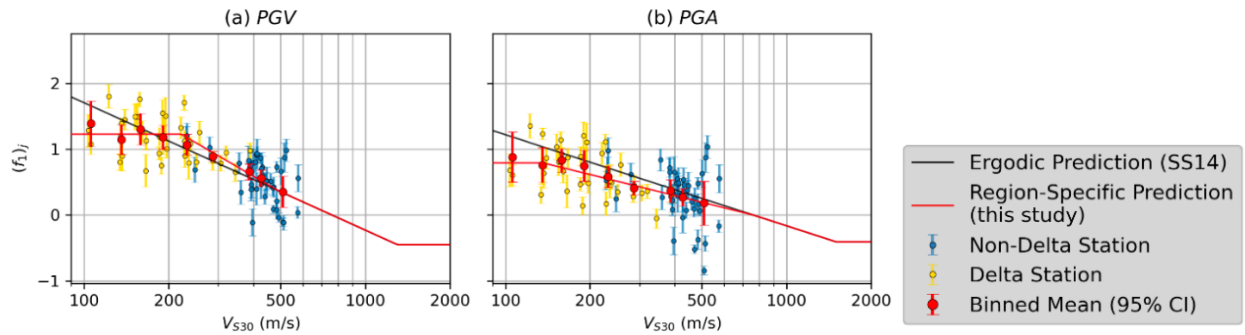


**Figure 2.13** Plots comparing the fit of ergodic model and region-specific model to observe linear site term versus  $V_{S30}$  for (a)  $PGV$  and (b)  $PGA$ . (Buckreis, 2022)

The last two equations match the BSSA14 model, and the first two equations reflect the  $V_{S30}$ -scaling for soft and soft-to-moderate site conditions in the Delta.

### **2.3.2 Path Models for the Delta Region**

Regional path adjustment terms in NGA-West2 GMMs were developed for broad geopolitical regions such as California, Japan, and China. However, attenuations rates of ground motion may vary at a more granular level resolution of area, facilitating the possibility for subregional path models to improve GMMs. Buckreis et al. (2022) proposed a subregional path model for California that significantly reduces path bias relative to BSSA14. Fig. 2.14 shows the subregions, locations of earthquakes, stations, and event-station paths used in developing subregional path models.

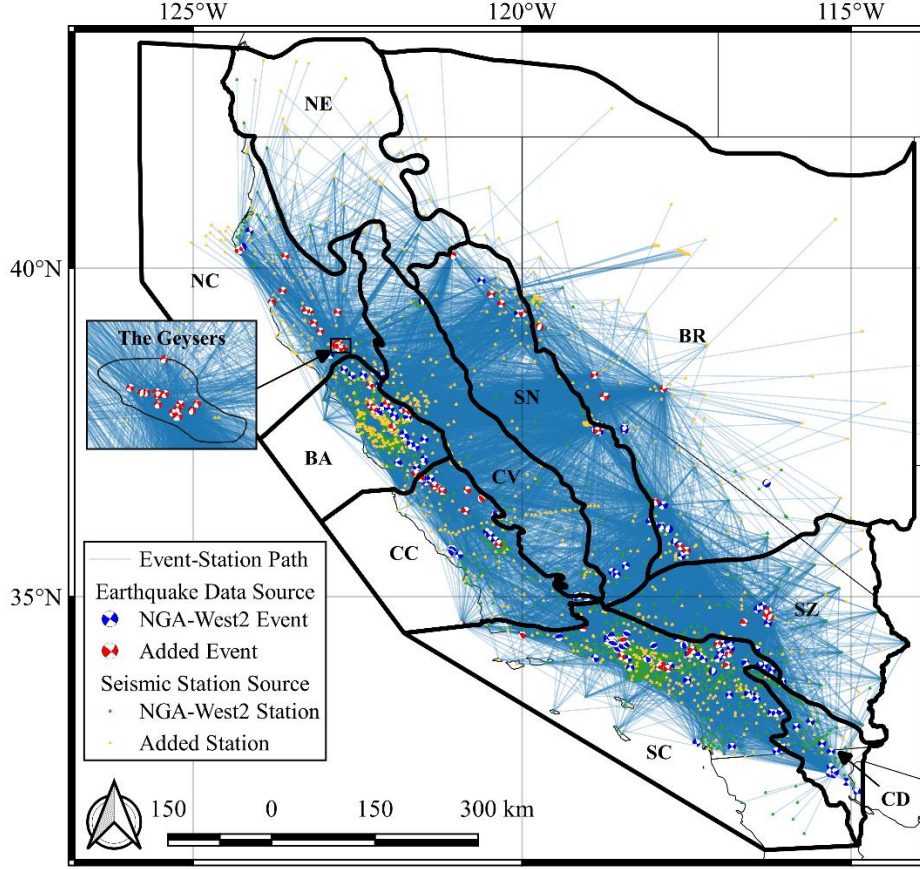


**Figure 2.14** Locations of earthquakes, stations, and paths used in developing regional path model. The ten study subregions are outlined by solid black lines. Inset shows outline of Geysers region from Viegas and Hutchings (2010) and locations of Geysers events. (Buckreis et al. 2023)

The suggested subregional path model is expressed by:

$$F_P(R_{JB}, \mathbf{M}, region) = [c_1 + c_2(\mathbf{M} - \mathbf{M}_{ref})] \ln(R/R_{ref}) + (c_3 + \Delta c_3^*)(R - R_{ref}) + \Delta c_{0,r} \quad (2.11)$$

where the first component remains same as in BSSA14,  $\Delta c_{0,r}$  is taken as the value for the subregion where the event originates, and the parameter  $\Delta c_3^*$  in the anelastic attenuation term is computed for a particular source-site path as,

$$\Delta c_3^* = \sum_{r=1}^{10} \Delta c_{3,r} W_r \quad (2.12)$$

where  $\Delta c_{3,r}$  comprise subregional anelastic coefficients ( $r$  is an index from 1:10),  $W_r$  indicates the proportion of the total path which traverses subregion  $r$ , and  $\sum_{r=1}^{10} W_r = 1$ . Weights  $W_r$  are computed from a linear source-to-site path drawn from the closest point on the surface projection of the fault to the site; using that line the proportion of the path in each subregion is computed.  $\Delta c_{3,r}$  of  $PGA$  and  $PGV$  for 10 defined subregions are shown in Table 2.2, the smallest and largest anelastic coefficients occur in ‘North Coast’ and ‘Sierra Nevada’ subregions, which reveals the strongest high and low ground motion attenuation effects.

**Table 2.2** Subregional anelastic coefficients of  $PGA$  and  $PGV$ . (Buckreis, 2022)

Subregion	Ground Shaking Intensity Measure	
	$PGV$	$PGA$
Basin and Range	-0.00183	-0.00229
Bay Area	-0.00156	-0.00193
Central Coast	-0.00065	-0.00156
Central Valley	-0.00196	-0.00162
Colorado Desert	-0.00048	-0.00291
Eastern California Shear Zone	0.000533	0.000673
North Coast	-0.00439	-0.00902
Northeastern California	-0.00297	-0.00482
Sierra Nevada	0.002161	0.002848
South Coast	-0.00061	-0.00054

### 2.3.3 Site and Path Model Implementation

Previous seismic hazard calculations presented in this dissertation utilized the USGS NSHMP-haz tool in conjunction with existing GMMs. However, the Delta-specific site and path models have not yet been implemented in that tool. For this reason, Liu (2023b) implemented these models into BSSA14 using the OpenQuake Engine (Pagani et al. 2014) using a Python script. I then ran updated seismic hazard calculations using these models to study their effects on seismic hazard in the Delta. To study site and path effects, seven points within the Delta were randomly selected, and two

events are used to demonstrate the modifications relative to BSSA14. The first event is a **M5** rupture of the Great Valley (Midland) fault (Fig. 2.15), and the 2<sup>nd</sup> is a **M6.8** event on the Healdsburg fault (Fig. 2.18).

**(a) Site model effects on ground motion predictions**

Figures 2.16 and 2.17 show the predicted *PGA* and *PGV* versus distance  $R_{JB}$  corresponding to 4 different site conditions with  $V_{S30} = 50, 100, 150,$  and  $200$  m/s. Points are plotted for the original BSSA14 model as well as BSSA14 plus site and path models. Path effects are insignificant for the Midland fault rupture because distances are less than 100 km, where the path model differences are small. I therefore focus on this event for the purpose of illustrating the influence of site effects.

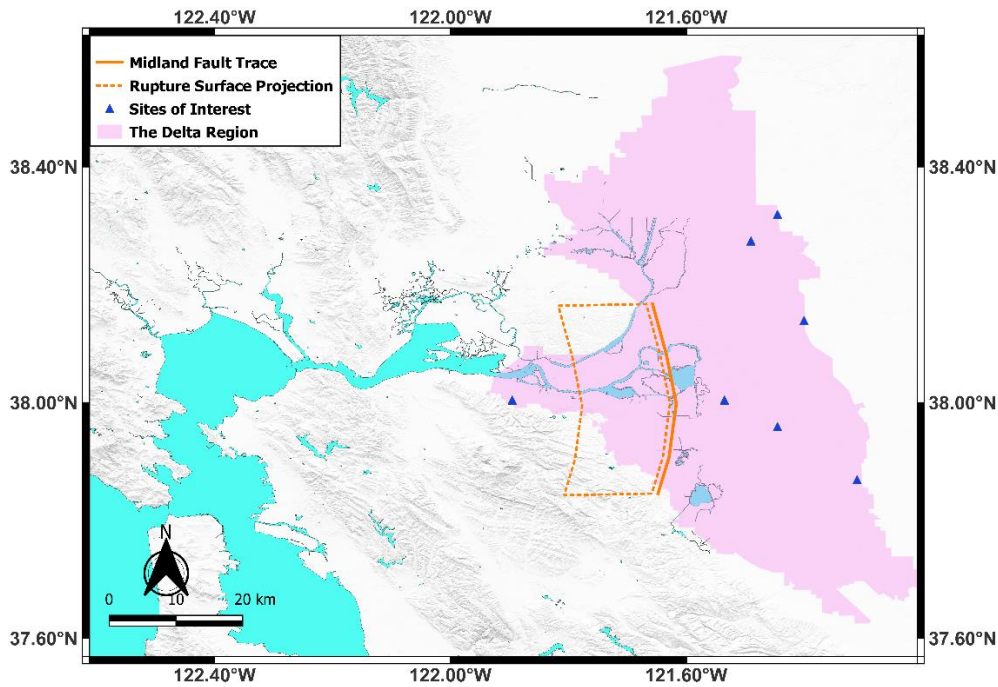


**Figure 2.15** Map of the Delta Region, showing the locations of 7 example sites, the Great Valley (Midland) fault trace, and its surface projection.

The updated site model results in lower predictions of *PGA* and *PGV* relative to the original

BSSA14 model. Differences are largest for  $V_{S30}=50\text{m/s}$ , and decrease as  $V_{S30}$  increases. The BSSA14 model is not constrained at such low  $V_{S30}$  values, nor for organic soils, so it is not surprising that the updated model is different. A potential reason why the updated model is lower than BSSA14 is that peat tends to exhibit higher damping at small strains compared with inorganic soils. As an example, Tokimatsu and Sekiguchi (2006) found that ground motions at peat sites were lower than at nearby stations on inorganic soils when shaking intensity was small (i.e., when site response is linear). However, they also found that shaking intensity was highest at the recording station on peat for the stronger shaking intensities. They attributed this finding to peat being relatively linear at high strains, whereas nonlinear site response more significantly influences inorganic soils. For this reason, the findings presented in Figs. 2.16 and 2.17 should not be extrapolated to large ground motions. Pengfei Wang is currently studying nonlinear site response effects, and I anticipate that a nonlinear site response model will be released soon. However, it was not available at the time of the writing of this thesis.



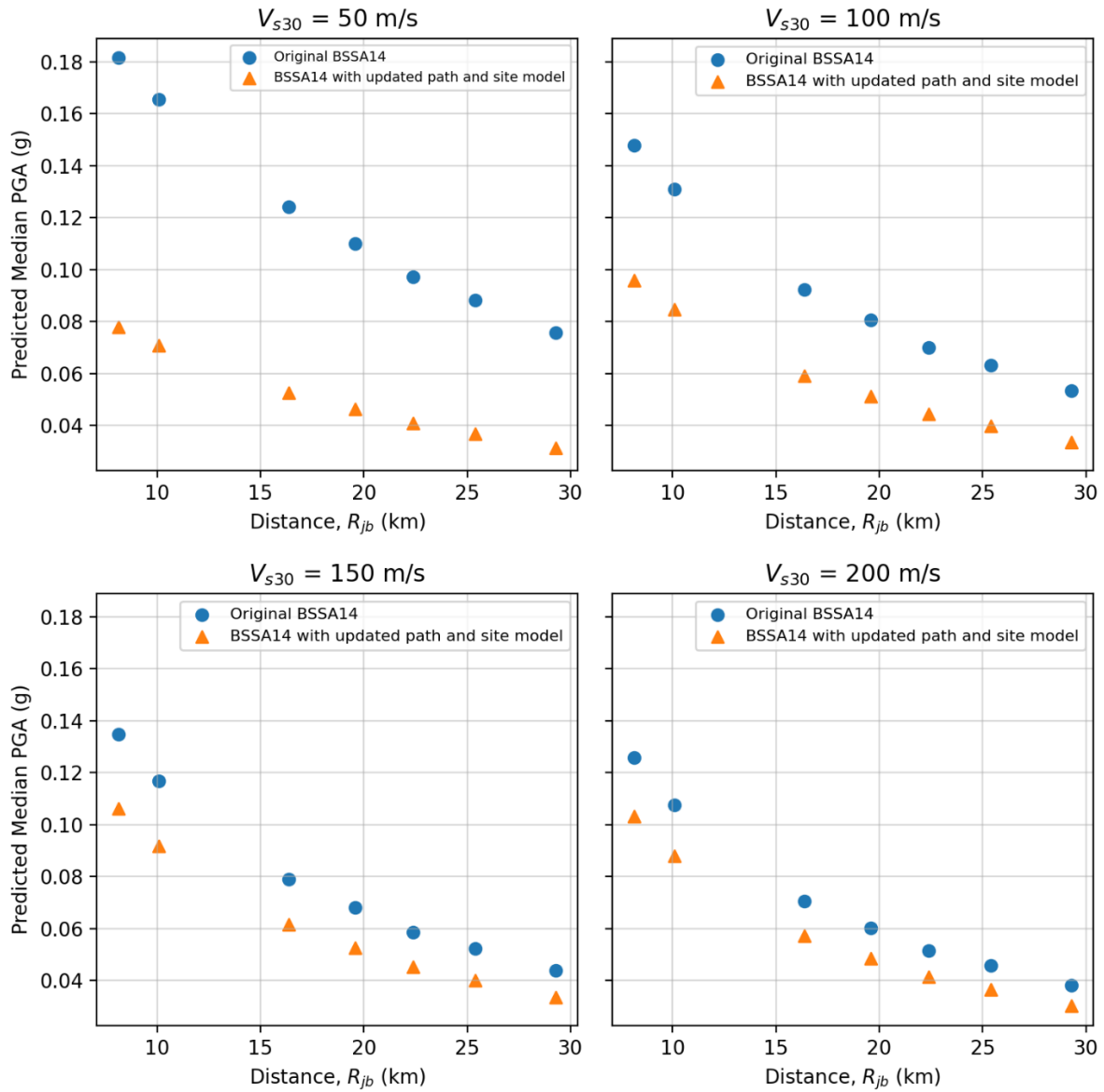


**Figure 2.16** Predicted median  $PGA$  versus  $R_{JB}$  distance of 7 example sites with 4 various site conditions ( $V_{s30} = 50, 100, 150,$  and  $200$  m/s) under the Great Valley (Midland) fault rupture with  $M = 5$  computed from original BSSA14 and BSSA14 with updated site and path models.

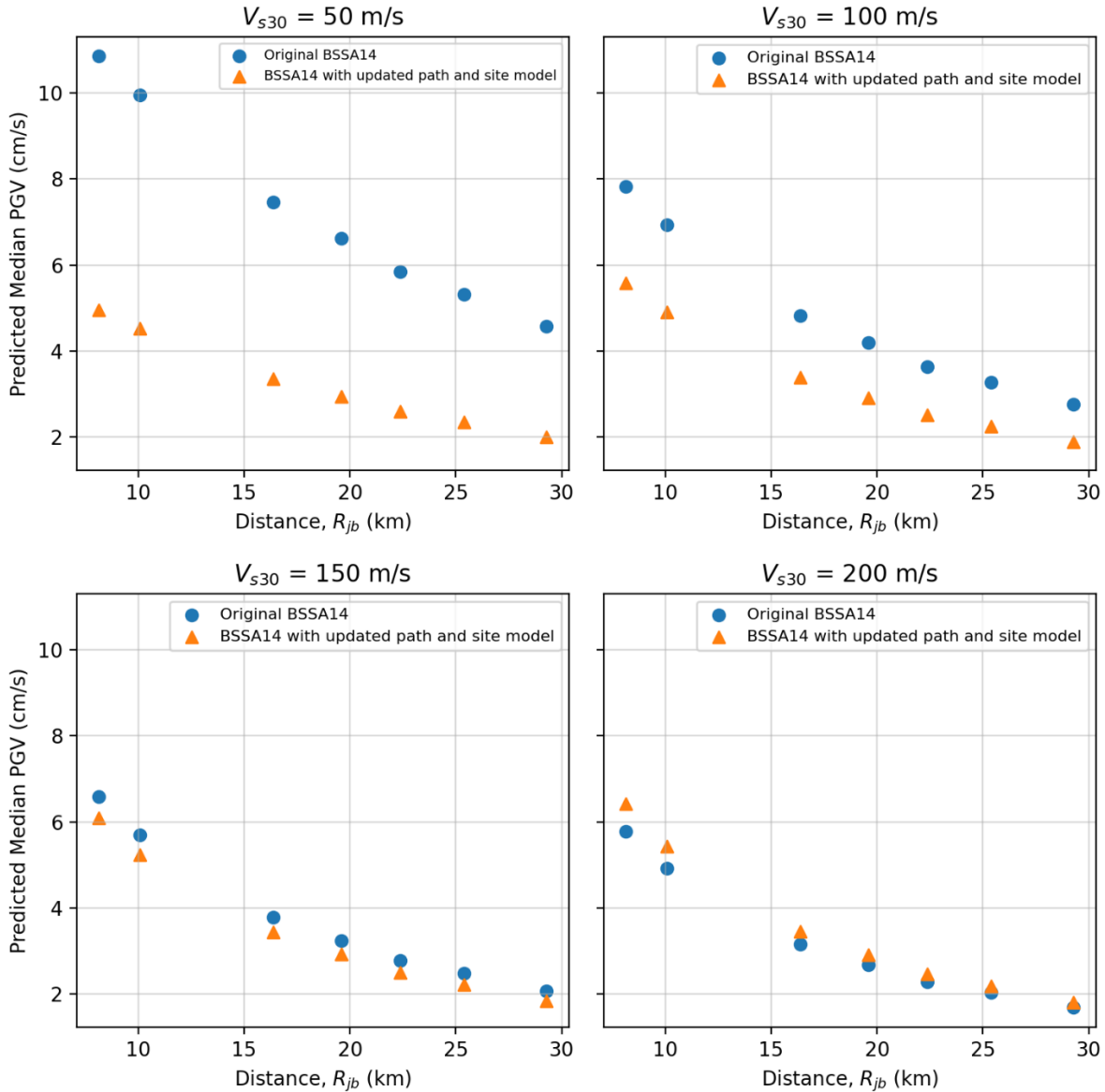


**Figure 2.17** Predicted median  $PGV$  versus  $R_{JB}$  distance of 7 example sites with 4 various site conditions ( $V_{S30} = 50, 100, 150,$  and  $200$  m/s) under the Great Valley (Midland) fault rupture with  $M = 5$  computed from original BSSA14 and BSSA14 with updated site and path models.

**(b) Path model effects on ground motion predictions**

To demonstrate the path model effects, I incorporate the Healdsburg fault rupture scenario in the Santa Rosa area with a magnitude of 6.8 for comparisons, as shown in Figure 2.18. The Healdsburg

rupture was selected because it originates in the north coast subregion, where crustal attenuation was observed to be significant by Buckreis et al. (2023), and because it is further from the Delta than the Midland fault rupture, and path effects are therefore anticipated to be more significant. I selected  $V_{S30} = 760$  m/s in this case to isolate path effects from site effects, and ran the original BSSA14 and the BSSA14 plus updated site and path models to estimate  $PGA$  and  $PGV$ .

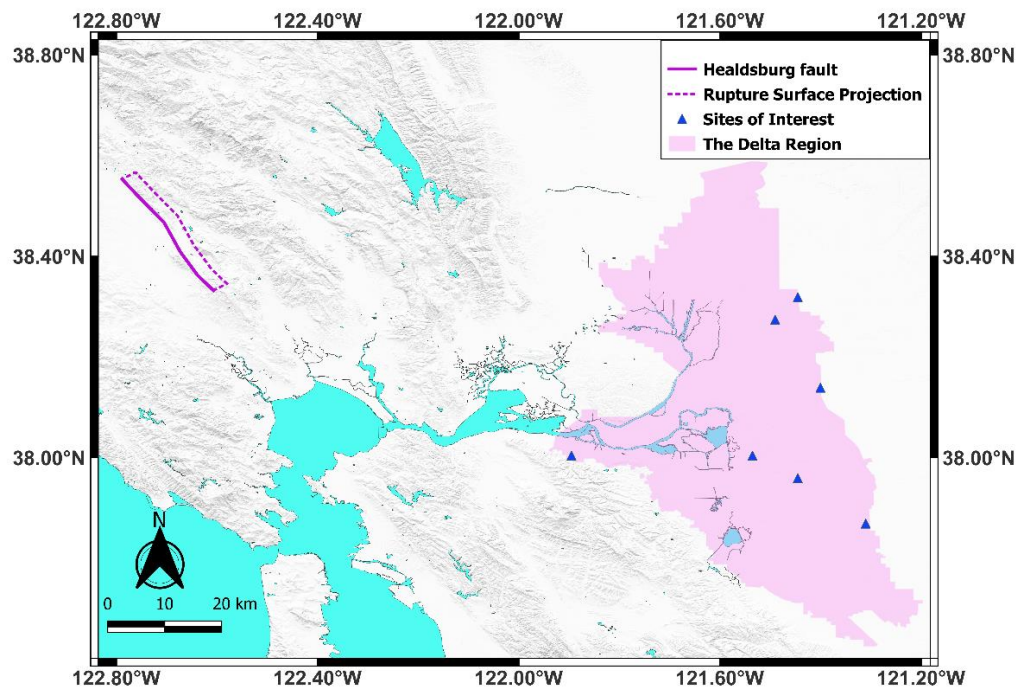


**Figure 2.18** Map of the Delta Region, showing the locations of 7 selected sites, the Healdsburg fault trace, and its surface projection.

Figures 2.19 and 2.20 illustrate the predicted  $PGA$  and  $PGV$  values. Path effects for the Midland fault rupture are very small because source-to-site distances are small. Path effects are more significant for the Healdsburg fault rupture, with the updated path model producing a significant

reduction in shaking intensity at the Delta sites. This is similar in nature to the reduction in ground motion observed by Erdem et al. (2019).

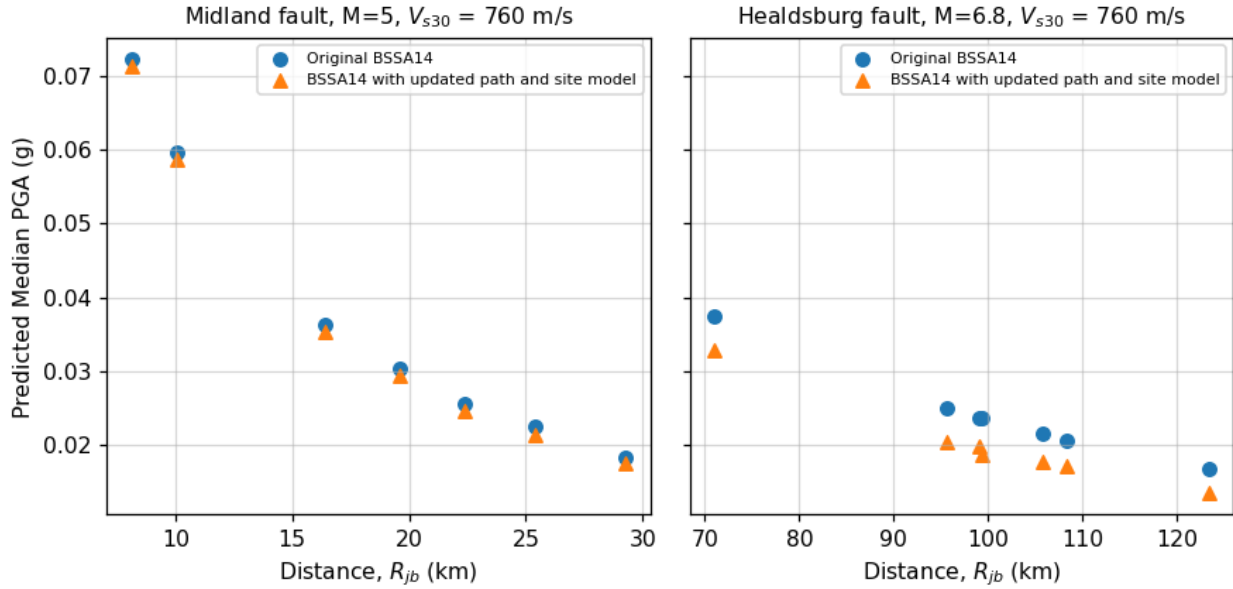


**Figure 2.19** Predicted median  $PGA$  versus  $R_{JB}$  distance of 7 example sites with  $V_{S30}$  equaling to 760 m/s under the Great Valley (Midland) fault rupture ( $M = 5$ ) and Healdsburg fault rupture ( $M = 6.8$ ) computed from original BSSA14 and BSSA14 with updated site and path models.

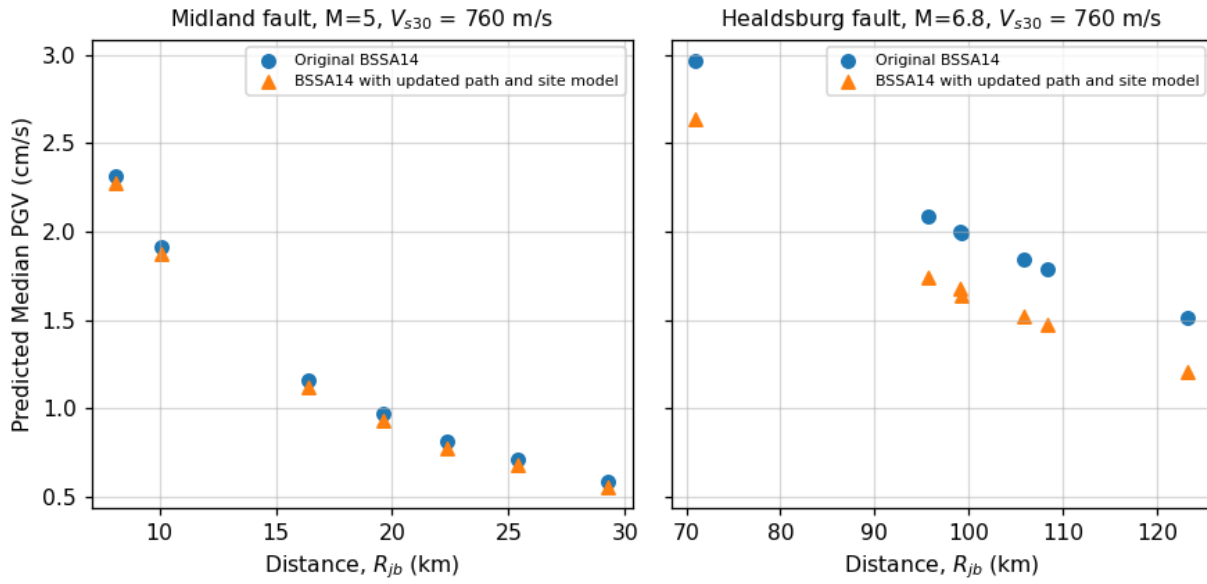


**Figure 2.20** Predicted median  $PGV$  versus  $R_{JB}$  distance of 7 example sites with  $V_{S30}$  equaling to 760 m/s under the Great Valley (Midland) fault rupture ( $M = 5$ ) and Healdsburg fault rupture ( $M = 6.8$ ) computed from original BSSA14 and BSSA14 with updated site and path models.

**(c) Hazard curve**

Given that site and path effects influence ground motion in the Delta relative to ergodic GMMs, I also compare the hazard curves produced by original BSSA14 and BSSA14 with updated site and path models. Figure 2.21 presents the  $PGV$ -based hazard curve comparison derived from the two models for a site on Bacon Island with two different  $V_{S30}$ , and the hazard curves are produced from a hazard-consistent event subset rather than all events in the source model. The  $V_{S30}$  of the site in Figure 2.21 (a) is assigned to 100 m/s, because that is a typically common site condition in the Delta. According to Fig 2.21 (a), the hazard curve derived by the updated model is consistently lower than the one derived by BSSA14 from low to high return periods. I attribute this to the faster ground motion attenuations for relatively soft site conditions produced in updated site model. In Fig. 2.21 (b), I selected  $V_{S30} = 350$  m/s because that is consistent with site conditions for the inorganic soils that underlie the peat deposits, which is the elevation where ground motions are

imposed in the finite element models presented later in this thesis. In general, these two hazard curves look similar whereas the rate of exceedance calculated from the BSSA14 with updated site and path models is slightly smaller when  $PGV$  is less than 40 cm/s. I conclude that the difference is because at long return periods, the hazard has significant contributions from moderate magnitude events near the Delta, and larger magnitude events on more distant faults such as San Andreas and Hayward faults. Path effects are not significant for short source-to-site distances, and paths from the Hayward and San Andreas faults have anelastic attenuation coefficients that are similar to the BSSA14 path model. Therefore, the two hazard curves in Fig. 2.21 are almost overlapping at large return period region.

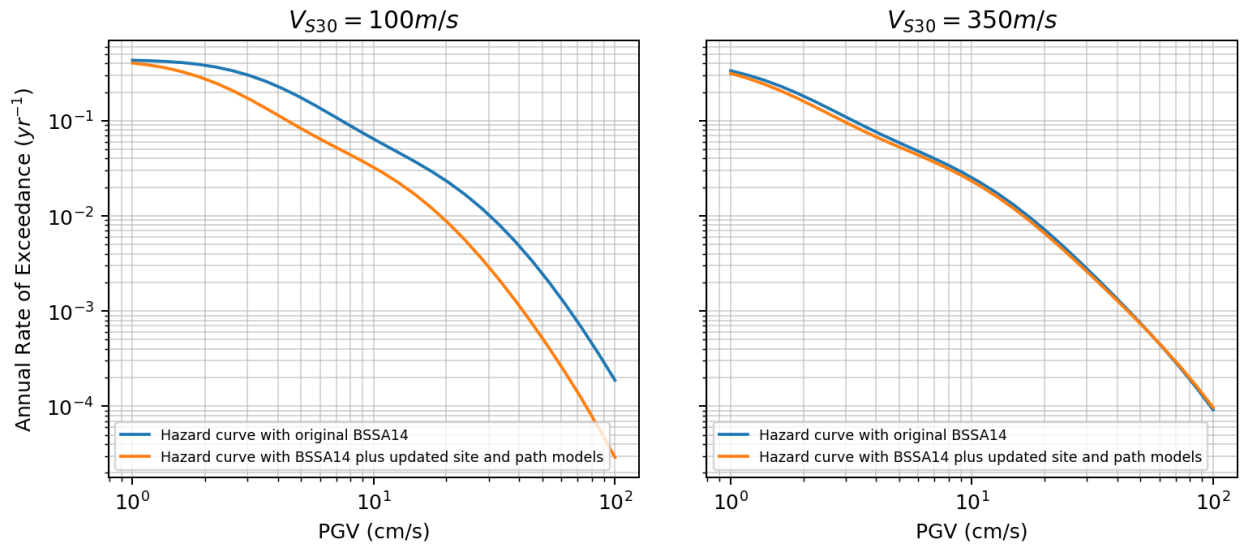


**Figure 2.21**  $PGV$ -based hazard curves of one site on Bacon Island computed from original and BSSA14 with updated site and path models.

## **CHAPTER 3: Fragility Functions of Bacon Island Levee System**

This chapter presents fragility functions for Bacon Island levees in the central Delta. Bacon Island was selected for this study because: (1) it is highly subsided and is therefore crucial for retaining fresh water in the Delta, (2) there is sufficient geotechnical site investigation data available, and (3) it is owned by Metropolitan Water District, who has a shared interest in risk assessment and is a cooperative stakeholder.

Levee seismic fragility functions define the probability of exceedance of a specified damage threshold as a function of shaking intensity. Different fragility functions are defined for different reaches within Bacon Island based on the types of soils encountered and levee geometry. Two representative levee cross-sections on southern and northern Bacon Island are selected to build 2-D finite element models and develop fragility functions based on earthquake dynamic numerical simulations. Western and eastern levee conditions are very similar to the levees in the north but different from southern levees, which are presumably more vulnerable subjected to earthquake shaking due to appreciably larger amount of soft and highly organic peat profile within levee.

This chapter focuses first on-site characterization for Bacon Island levees using geotechnical site investigation data, geophysical studies, as well as LiDAR and bathymetry surveys. I then turn my attention to selecting ground motions for fragility analysis, and performing finite element modeling and analysis to investigate levee performance under ground shaking. Furthermore, I implement data analysis for simulation data to develop levee fragility functions.

### **3.1 Characterization of Bacon Island Levees**

Site characterization is the process of developing an understanding of the geologic, hydrologic,

and engineering properties at the site of interest including the soil, bedrock, and ground water (Benson, 2016), which plays a critical role in quantifying seismic fragility functions of the levee system. Newly available Delta data was leveraged to be used in finite element simulations for better quantifying seismic capacity of the Bacon Island levees, and the process of determining levee geometry and soil properties assignments are discussed in detailed in this section.

### **3.1.1 Levee Geometry**

Light detection and ranging (LiDAR) data collected in 2017 (OCM Partners, 2023) provides the most recent comprehensive digital elevation model for the Delta levees. However, LiDAR is unable to penetrate water. For this reason, the submerged portions of the Delta levees were measured using bathymetry data (Foxgrover et al., 2007). The LiDAR data of the Delta was collected at a nominal pulse spacing (NPS) of 0.35 m, and it contains information about the water table, shape of the earth, and its surface characteristics while bathymetric data includes information of depth and shapes of underwater terrain.

Figures 3.1 show a map of digital elevation model (DEM) created by the merged lidar point data and bathymetry data for Bacon Island, and the datum of the DEM is North American Vertical Datum of 1988 (NAVD 88).



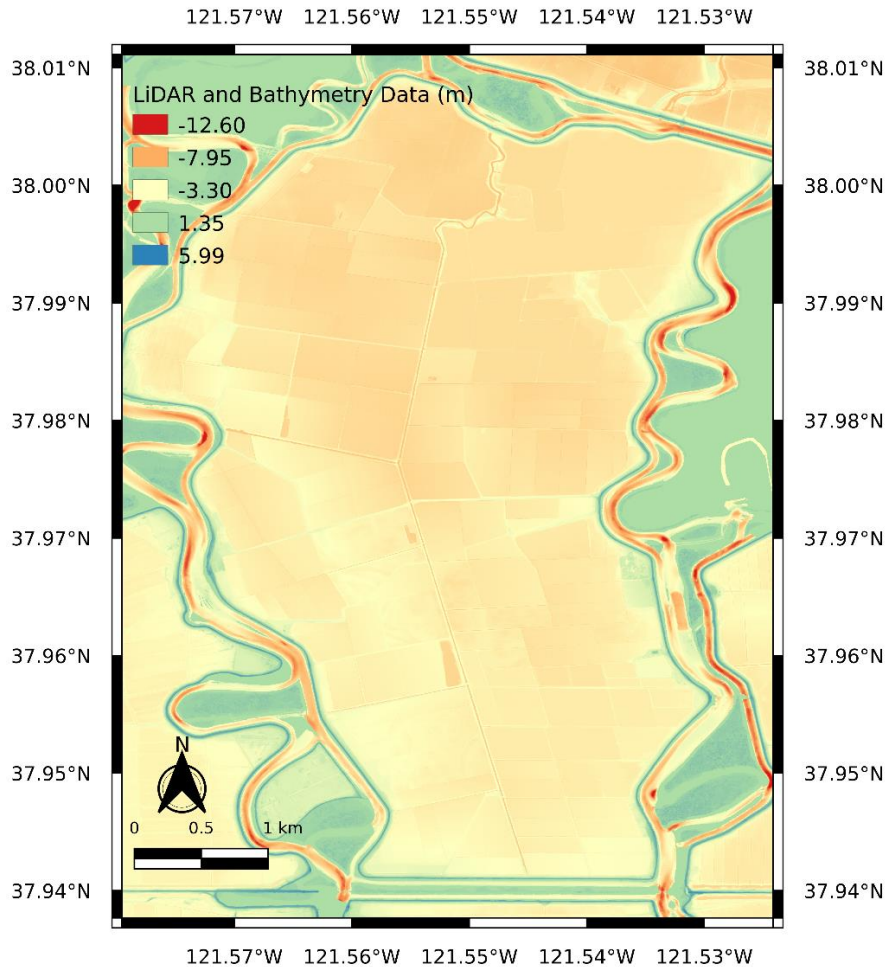


**Figure 3.1** Map of digital elevation model (DEM) created by lidar point and bathymetry data for Bacon Island.

Figure 3.2 presents a map of Bacon Island where the levees have been divided into 28 reaches, each approximately 1 km long with center points of each reach identified with a numbered green circle, and the purpose of this is to facilitate subsequent risk assessment of the levee system. Kwak et al. (2016a) defined a reach as a length of levee for which the levee capacity and demand can reasonably be represented as a stationary random field. Stationary means that mean, standard deviation, and spatial correlation are constant. The determination process of the proper reach

length of Bacon Island levee will be discussed in detail in Chapter 5. I now turn my attention to assessment of capacity based on levee cross-section geometry.

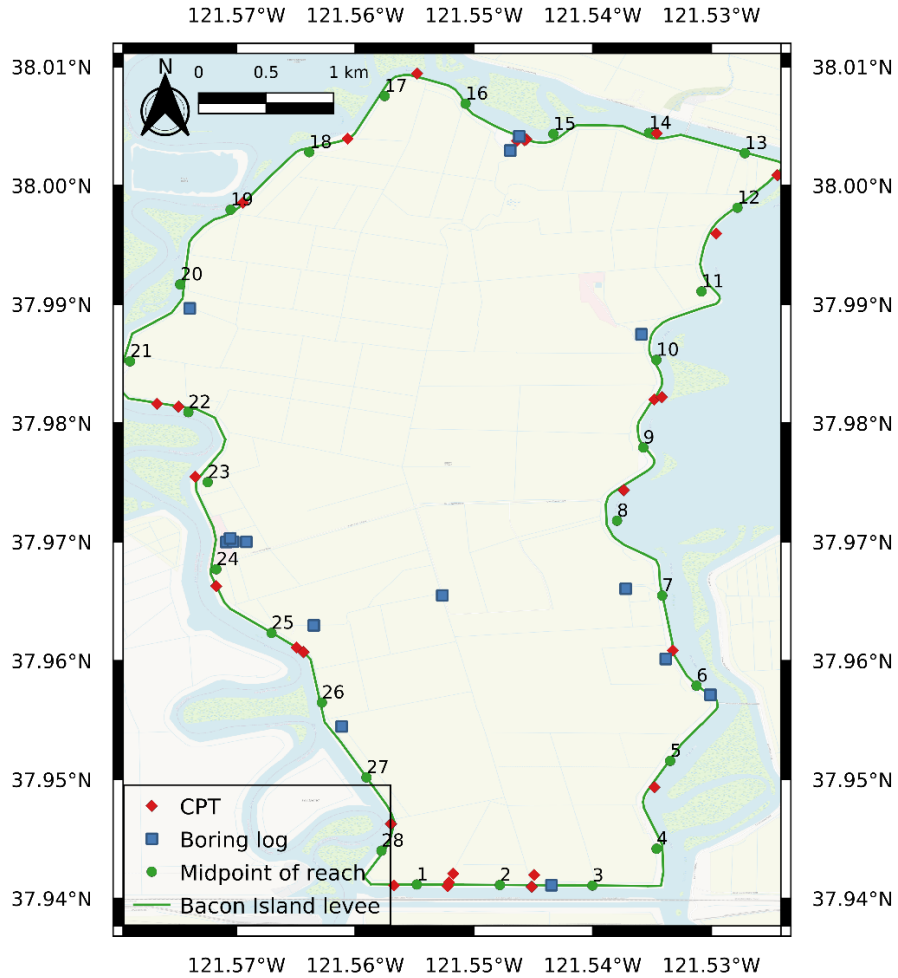


**Figure 3.2** Levee reach, CPT, and boring log locations on Bacon Island.

The cross-section geometry profile of each reach centroid is shown in Figures 3.3 to 3.6 for the southern, eastern, northern, and western reach centroids. Most reaches in the west, east, and north have similar cross-section geometry, though there are variations in the location of the drainage ditch, and riverbed shape. The average width of the levee crest from these areas is approximately

6.5 m and the height of the levee measured from the ditch to the crest is around from 7 m to 10 m. Some shape outliers whose geometry is quite different from its adjacent reaches for each side can also be observed in these figures, for example, reach 4, 11, 23 and 24. This is attributed to the factor that these reach centroids are all in the curvature region of levee system where levee cross-section geometry might be different. As for the southern side, levee geometries are similar to each other as illustrated in Figure 3.3. Furthermore, the geometry of the southern levee is different from the geometry elsewhere on the island. The average width of levee crest is only about 4 m, and the overall cross-section area is also appreciably similar. Therefore, I conclude that the geometry of the eastern, northern, and western levees can be reasonably represented by a single 2-D cross-section levee, while a separate cross-section is required for the south side.

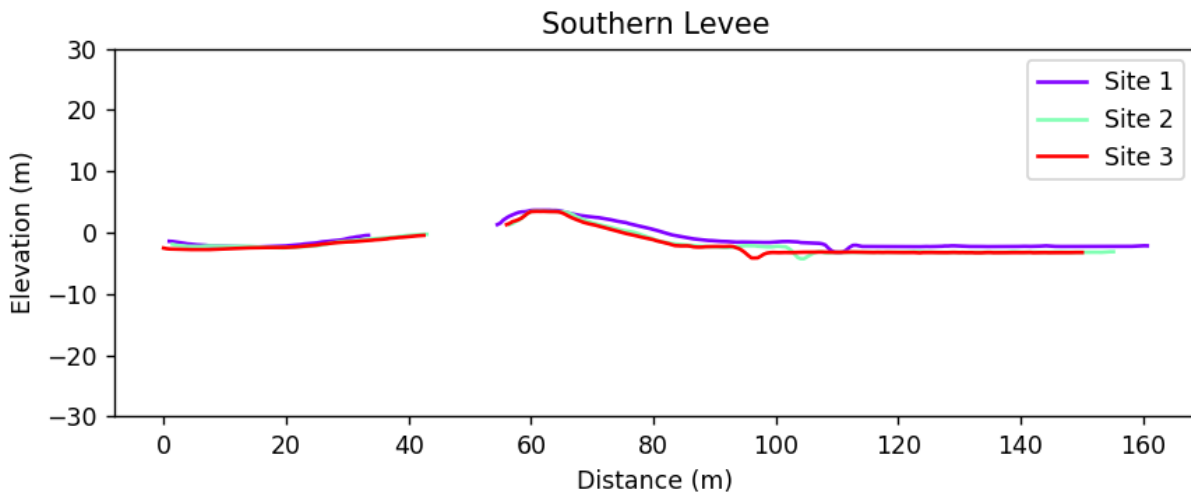


**Figure 3.3** Southern levee cross-section geometry visualization at different reaches.

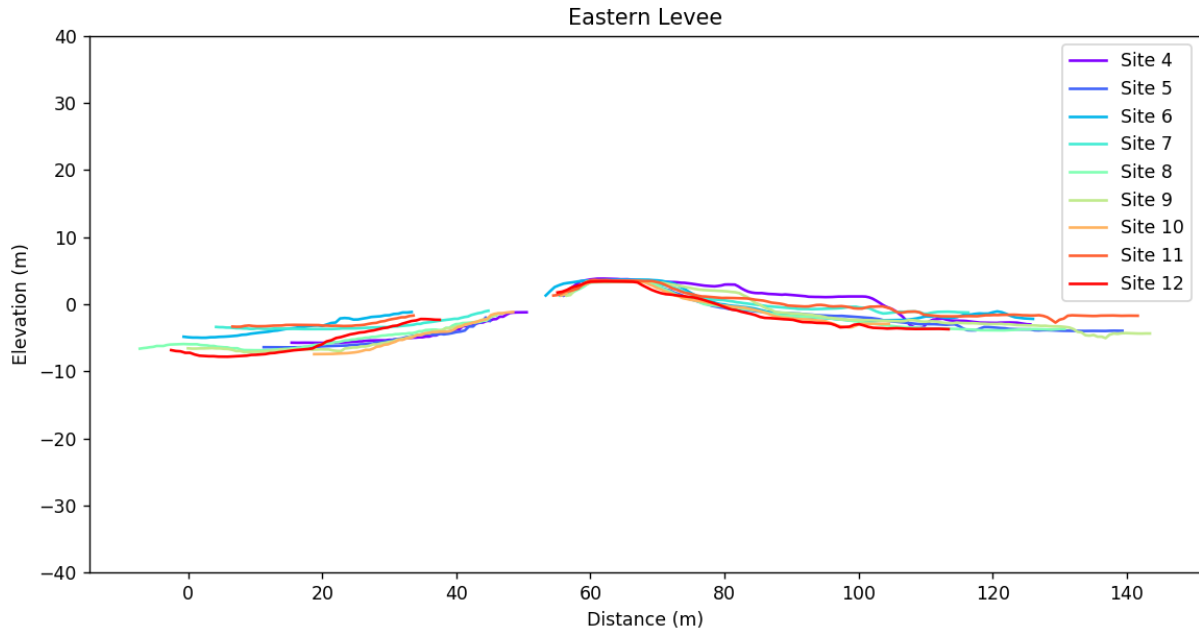


**Figure 3.4** Eastern levee cross-section geometry visualization at different reaches.

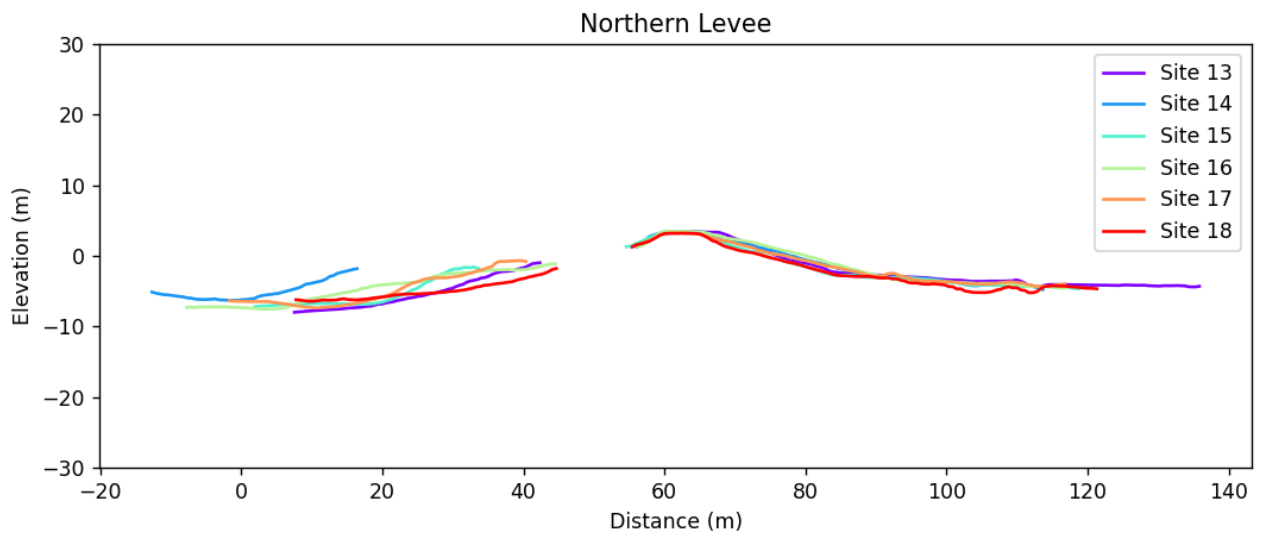


**Figure 3.5** Northern levee cross-section geometry visualization at different reaches.

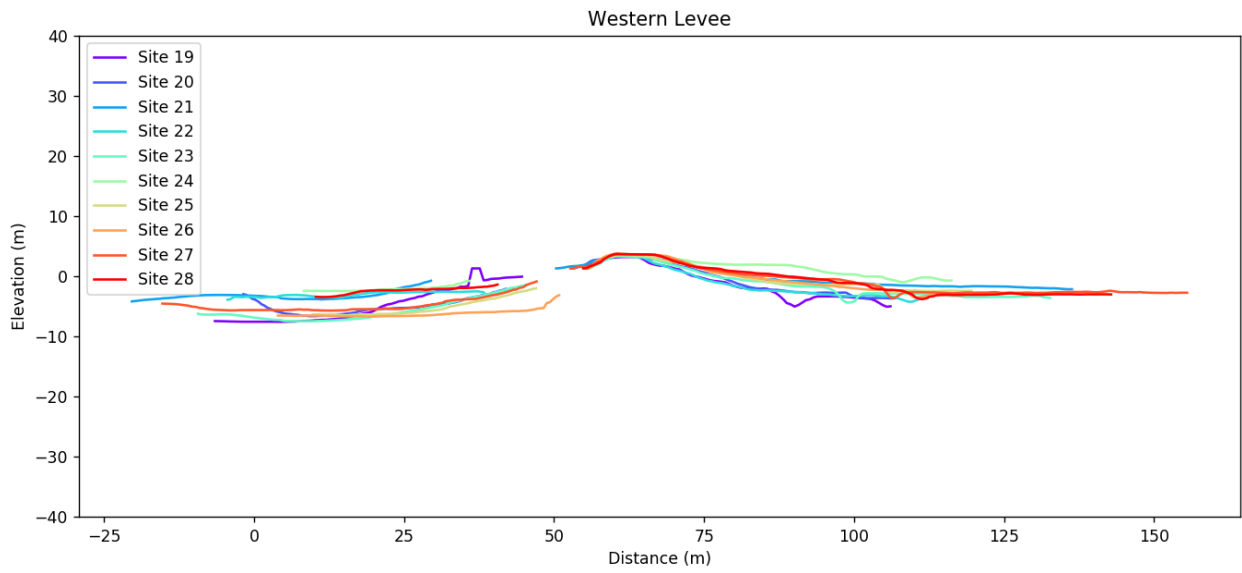


**Figure 3.6** Western levee cross-section geometry visualization at different reaches.

### 3.1.2 Geotechnical Site Investigation Data

Fig. 3.2 also shows the locations of geotechnical site investigation data including CPT and boring log. A total of 28 CPT and 19 boring logs are available, as summarized in Table 3.1.

**Table 1.1** Fundamental information of available CPT and boring logs on Bacon Island.

<b>Boring log</b>			
<b>Number</b>	<b>Name</b>	<b>Year of completion</b>	<b>Name of agency gathered data</b>
1	bac-isl-pge-b-1	2005	NOMELLINI GRILLI MCD
2	bac-isl-pge-b-2	2005	NOMELLINI GRILLI MCD
3	bac-isl-pge-b-3	2005	NOMELLINI GRILLI MCD
4	dwp-bi-ba1	1988	Harding Lawson Associates
5	dwp-bi-ba2	1988	Harding Lawson Associates
6	dwp-bi-ba3	1988	Harding Lawson Associates
7	dwp-bi-ba4	1988	Harding Lawson Associates
8	dwp-bi-ba5	1988	Harding Lawson Associates
9	dwp-bi-ba6	1988	Harding Lawson Associates
10	dwp-bi-ba7	1988	Harding Lawson Associates
11	dwp-bi-ba8	1988	Harding Lawson Associates
12	gm-bn-ba-35	2004	Hultgren-Tillis Engineers
13	scb57-bn-bi-x1	1957	California Department of Water Resources
14	scb57-bn-bi-x2	1957	California Department of Water Resources
15	scb57-bn-bi-x3	1957	California Department of Water Resources
16	scb57-bn-bix1	1957	California Department of Water Resources
17	scb57-bn-bix2	1957	California Department of Water Resources
18	scb57-bn-bix3	1957	California Department of Water Resources
19	scb57-bn-bix4	1957	California Department of Water Resources
<b>Cone Penetration Test</b>			
<b>Number</b>	<b>Name</b>	<b>Year of completion</b>	<b>Name of agency gathered data</b>
1	bi-cpt-01-1	2001	Bureau of Reclamation
2	bi-cpt-01-2	2001	Bureau of Reclamation
3	bi-cpt-01-3	2001	Bureau of Reclamation
4	bi-cpt-01-4	2001	Bureau of Reclamation
5	bi-cpt-01-5	2001	Bureau of Reclamation
6	bi-cpt-01-6	2001	Bureau of Reclamation
7	bi-cpt-01-7	2001	Bureau of Reclamation
8	bi-cpt-01-8	2001	Bureau of Reclamation
9	dwp-bi-ba-1	1988	Harding Lawson Associates
10	dwp-bi-ba-3	1988	Harding Lawson Associates
11	dwp-bi-ba-4	1988	Harding Lawson Associates
12	dwp-bi-ba-5	1988	Harding Lawson Associates
13	dwp-bi-ba-7	1988	Harding Lawson Associates
14	dwp-bi-ba-8	1988	Harding Lawson Associates
15	dwp-bi-ba-9	1988	Harding Lawson Associates
16	dwp-bi-ba-10	1988	Harding Lawson Associates
17	dwp-bi-ba-11	1988	Harding Lawson Associates
18	dwp-bi-ba-12	1988	Harding Lawson Associates

19	dwp-bi-ba-13	1988	Harding Lawson Associates
20	dwp-bi-ba-14	1988	Harding Lawson Associates
21	dwp-bi-ba-15	1988	Harding Lawson Associates
22	dwp-bi-ba-16	1988	Harding Lawson Associates
23	dwp-bi-ba-17	1988	Harding Lawson Associates
24	dwp-bi-ba-18	1988	Harding Lawson Associates
25	dwp-bi-ba-19	1988	Harding Lawson Associates
26	dwp-bi-ba-20	1988	Harding Lawson Associates
27	dwp-bi-ba-21	1988	Harding Lawson Associates
28	dwp-bi-lab	1988	Harding Lawson Associates

Boring logs conducted in the 1950's are sometimes illegible, their precise position is not well known, and they generally do not provide useful information aside from identifying soil types.

There are also some cone penetration tests (CPT) implemented within the Bacon Island levees. A few locations in Bacon Island contain an adequate density of site investigation data to develop geotechnical cross-sections. Two cross-sections are finally chosen, one is from the southern levee, and another is from the northern levee. Figure 3.7 shows the locations of selected levee cross-sections on northern and southern levees and visualizations of LiDAR and bathymetric data of cross-sections, and the red dot represents CPT location while blue dot reflects boring log locations on the island. According to Fig. 3.7, the levee geometry capture from merged LiDAR and bathymetry data is apparently odd and forms the “bench” shape on the river side, because LiDAR and Bathymetry data do not connect. I manually and smoothly connect the LiDAR and Bathymetry data to obtain more reasonable levee geometries for southern and northern levee cross-sections/

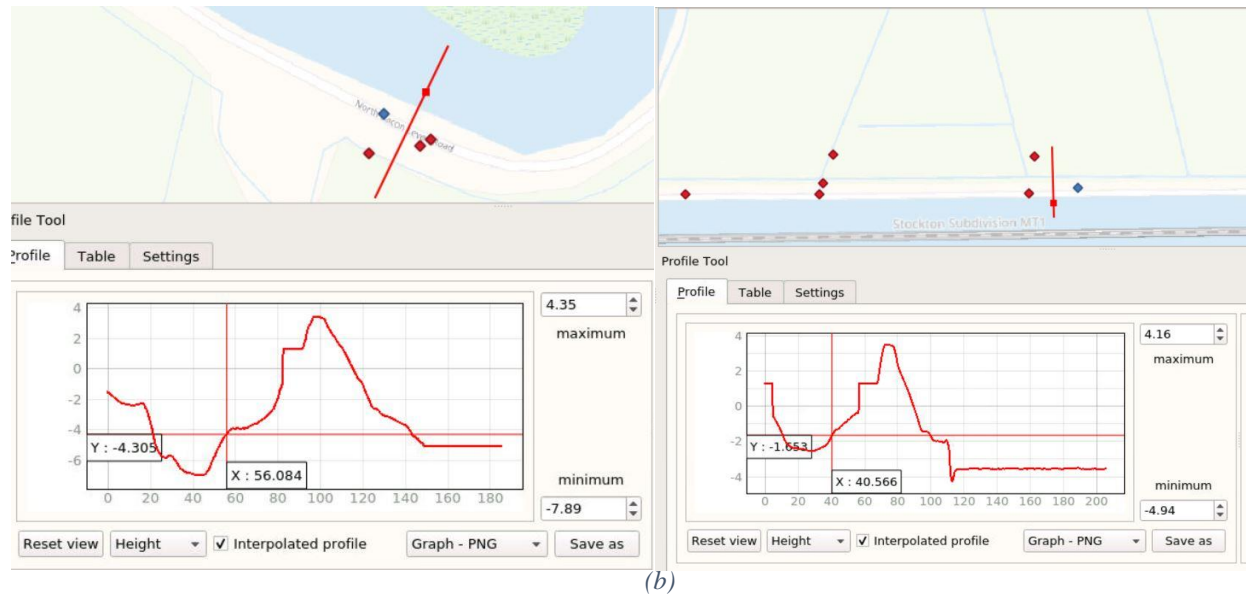


**Figure 3.7** Visualizations of LiDAR and bathymetric data of selected (a) northern levee cross-section and (b) southern levee cross-section

Geotechnical data for BI-CPT-01-1 and dwp-bi-ba5 on northern levee crest are shown in Figures 3.8 to 3.11. CPT provides tip resistance, sleeve friction (or friction ratio), pore pressure, and soil behavior type profile of soil versus depth, so soil stratigraphy of levee can be directly determined and undrained shear strength can also be estimated. Boring logs can be used to determine and calibrate soil stratigraphy within levees. Moreover, some laboratory tests results such as unit weight calculation, permeability test, and triaxial compression test are documented in boring log profile, which is appreciably handfull for effectively estimating soil properties. There are two additional CPT performed on levee slope and free-field area on the island, and they are also used to identify soil stratigraphy and property near the free-field side. The rest of CPT profiles of northern levee are shown in Appendix A.

Boring dwp-bi-ba5 indicates that the levee fill is silty sand, which rests atop high plasticity clay with peat, overlying soft peat. CPT BI-CPT-01-1 also reveals that the levee fill is made by silty



sand associated with large tip resistance and sleeve friction. Consequently, this levee fill is likely susceptible to liquefaction. CPT tip resistance and sleeve friction in the peat is very low as shown in Figure 3.8, indicating that this material is soft and compressible.

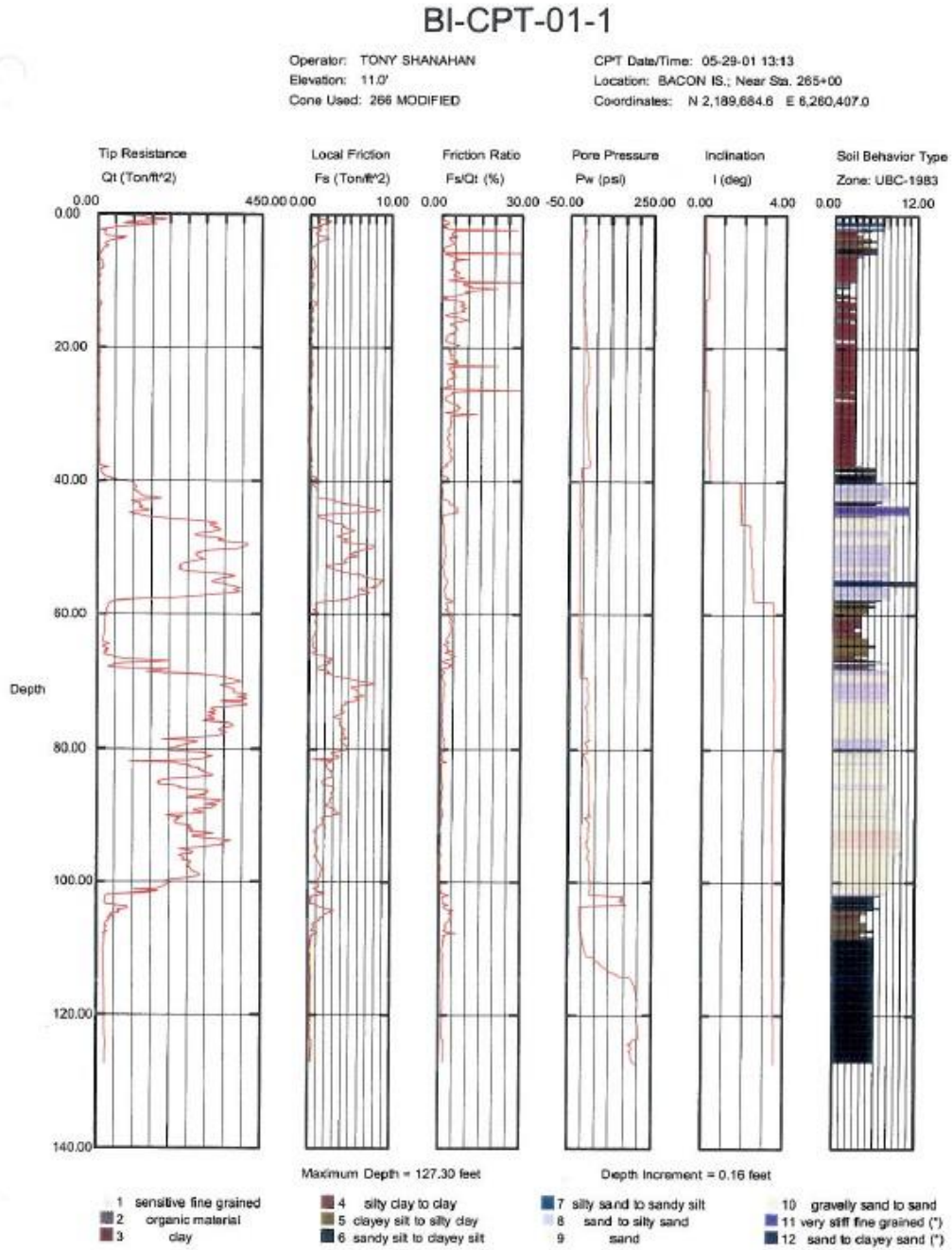


**Figure 3.8** CPT (BI-CPT-01-1) profile through northern levee crest

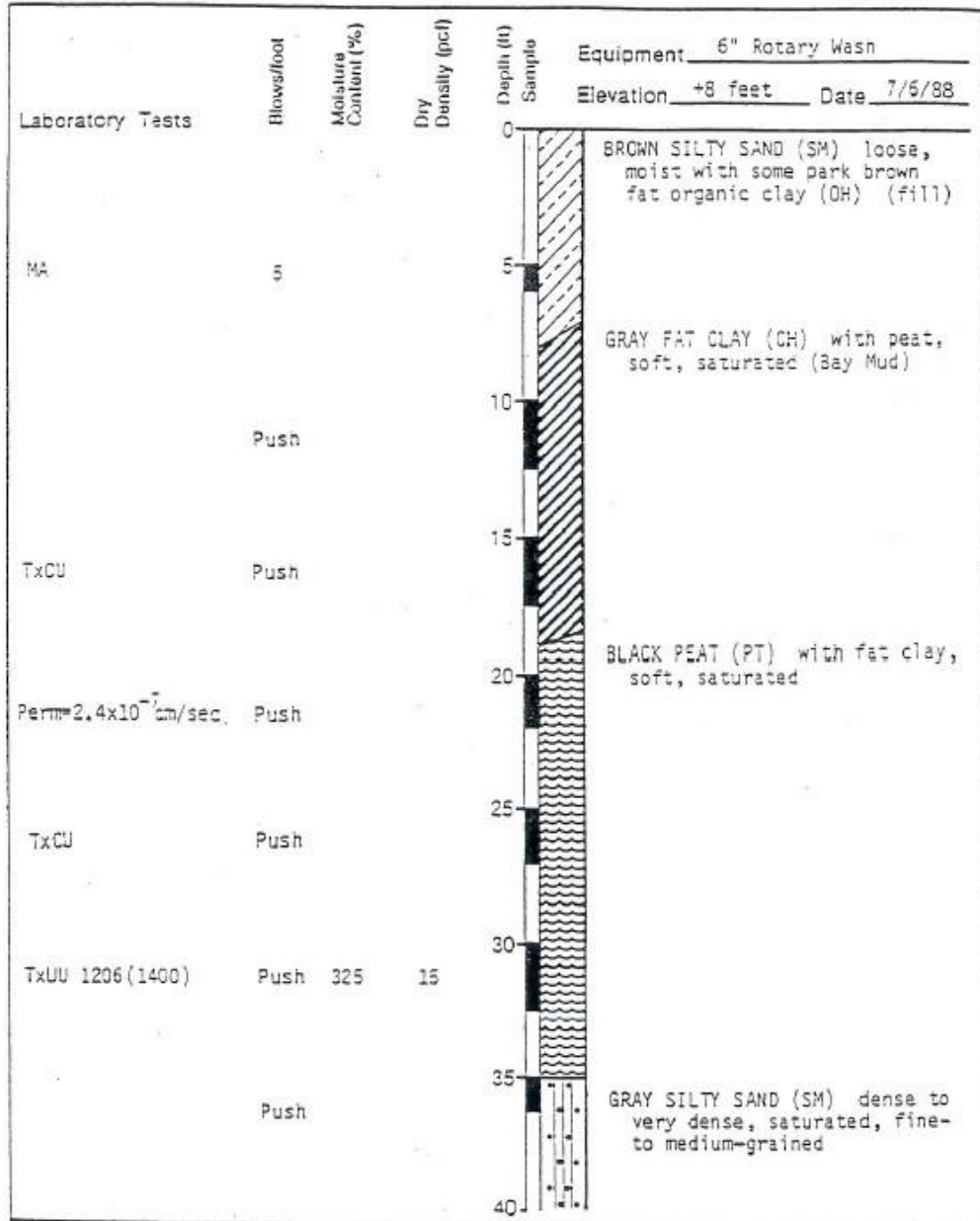


**Figure 3.9** Boring log (dwp-bi-ba5) profile through northern levee crest, Part I.

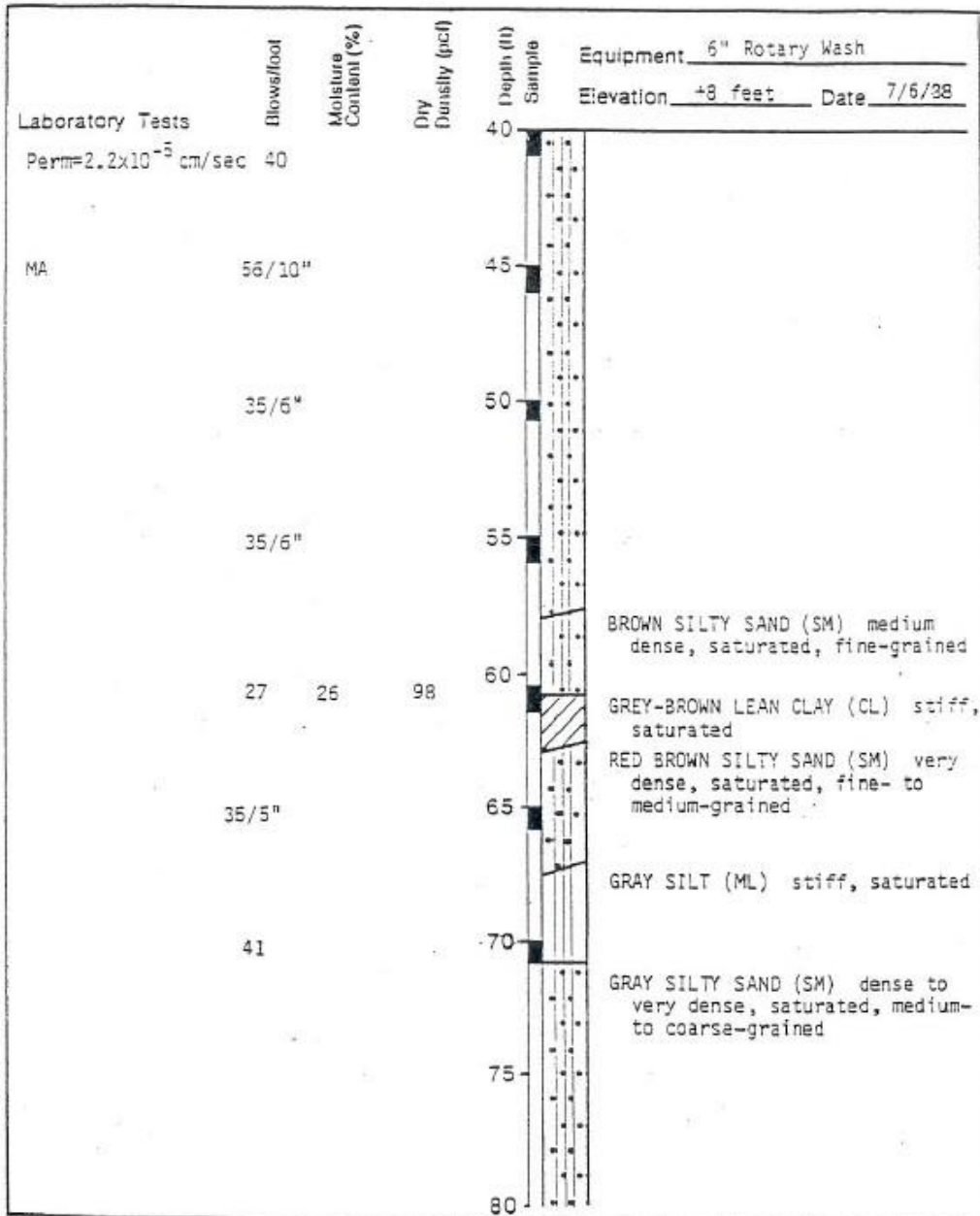
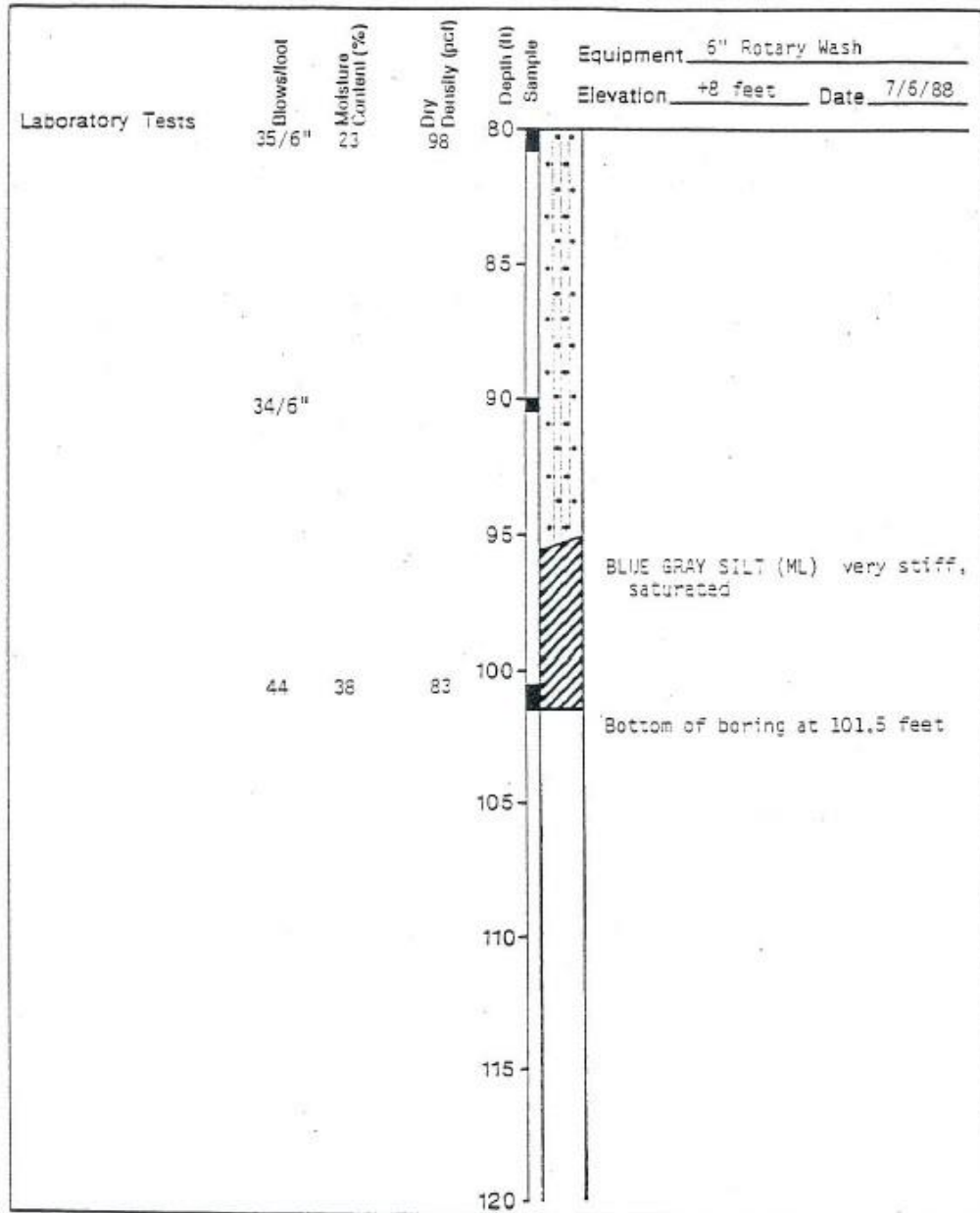


Figure 3.10 Boring log (dwp-bi-ba5) profile through northern levee crest, Part II.



**Figure 3.11** Boring log (dwp-bi-ba5) profile through northern levee crest, Part III.

Likewise, Figures 3.12, 3.13, and 3.14 show the profiles of CPT (dwp-bi-ba20-cpt) and boring log (dwp-bi-ba1) implemented on the top of southern levee. Based on these profiles, the levee is composed of peat resting atop native peat and peat mixtures, which indeed reflects that the southern

levee is essentially made of soft organic peat. The peat is very soft and compressible but is not susceptible to liquefaction or significant strength loss during shaking. It is therefore unclear whether the southern levee is more or less fragile than the northern levee in terms of seismic loading, which is a key aspect studied later in this report. Figure 3.13 shows that peat even starts from the top of the levee crest, which seems 'contradicts' with the result of CPT shown in Figure 3.12. My interpretation is that the peat is desiccated near the crest of the levee, and is therefore stiff, leading to higher cone tip resistance. Another available CPT profiles of southern levee is shown in Appendix A.

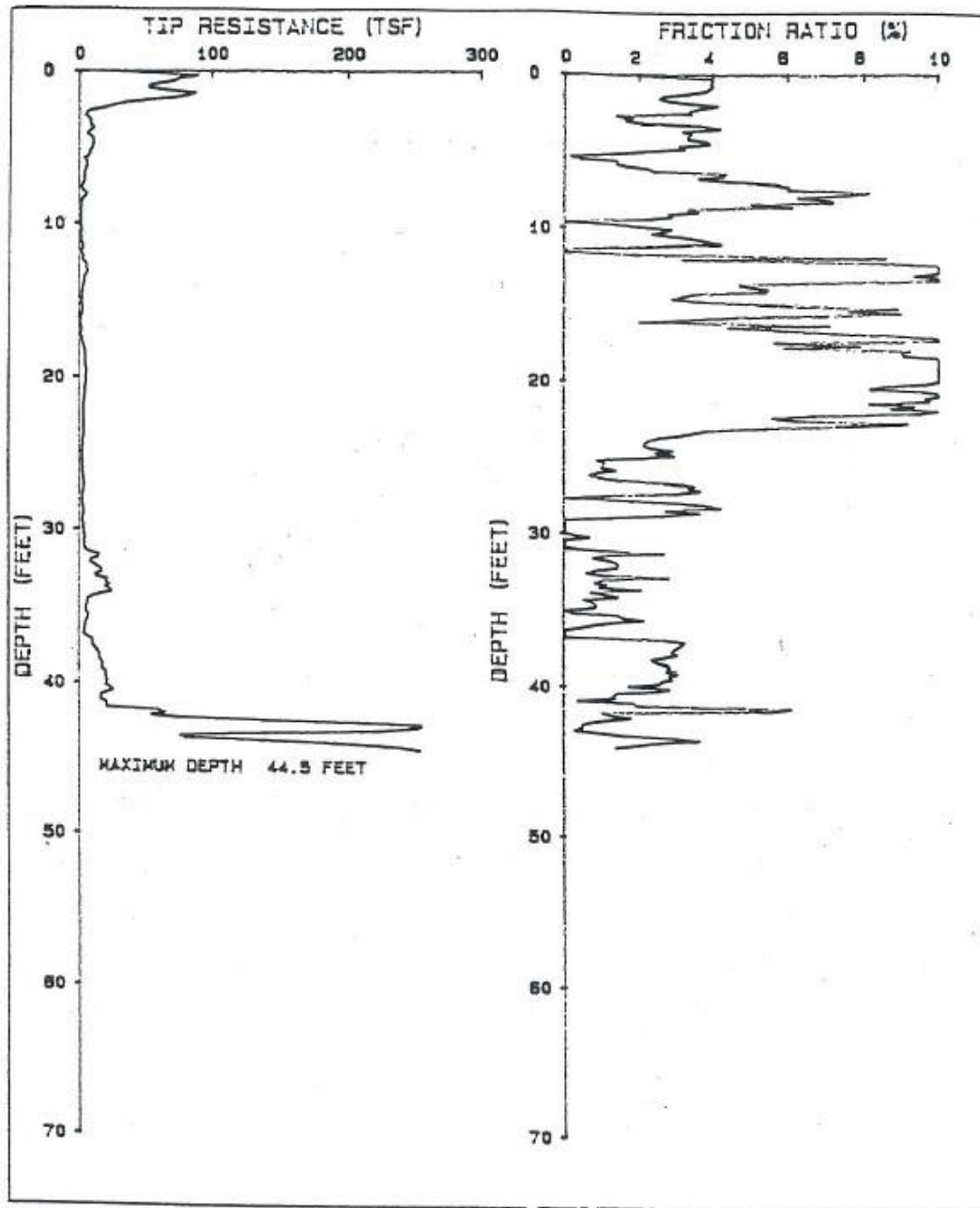


Figure 3.12 CPT (dwp-bi-ba20-cpt) profile through southern levee crest.

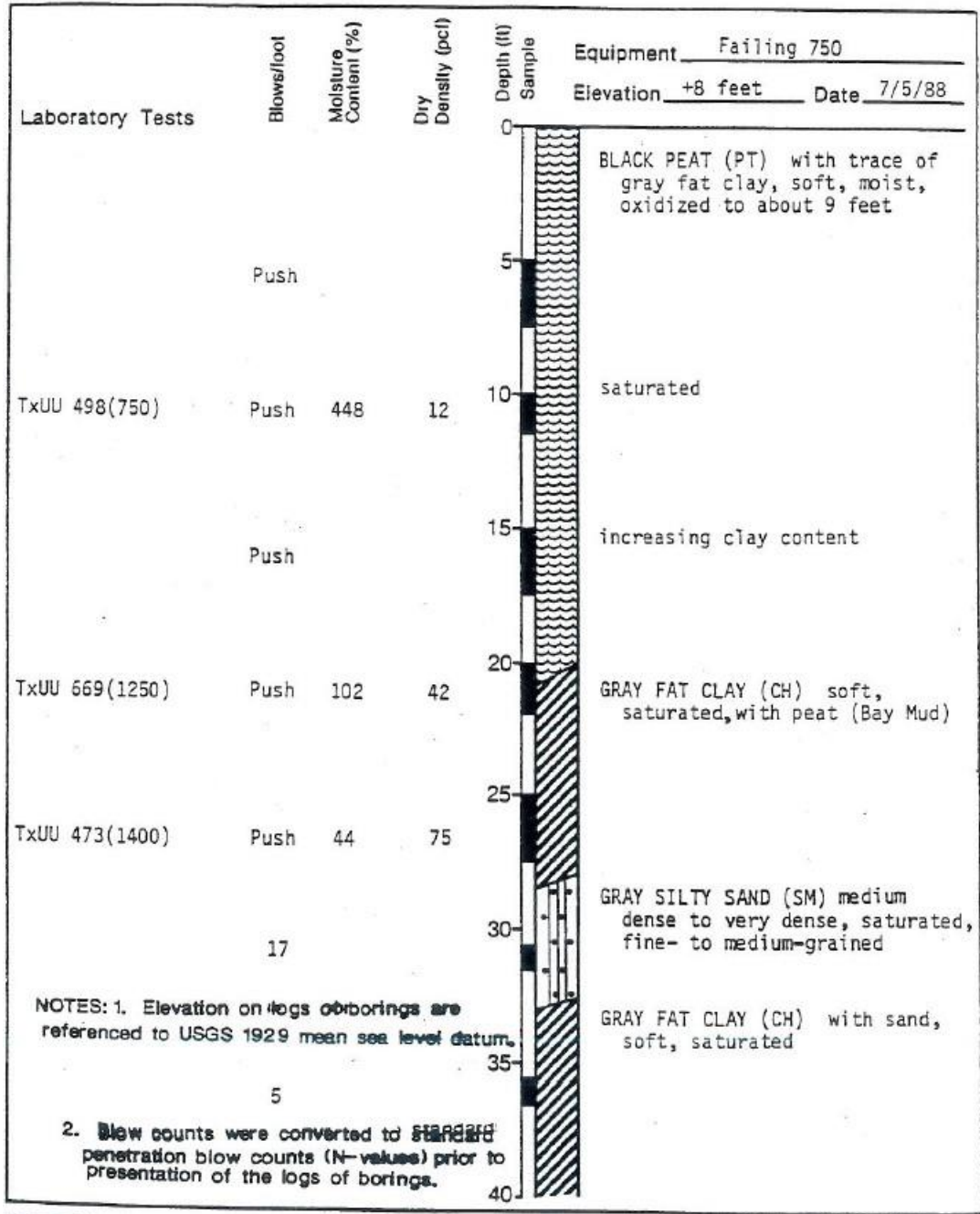
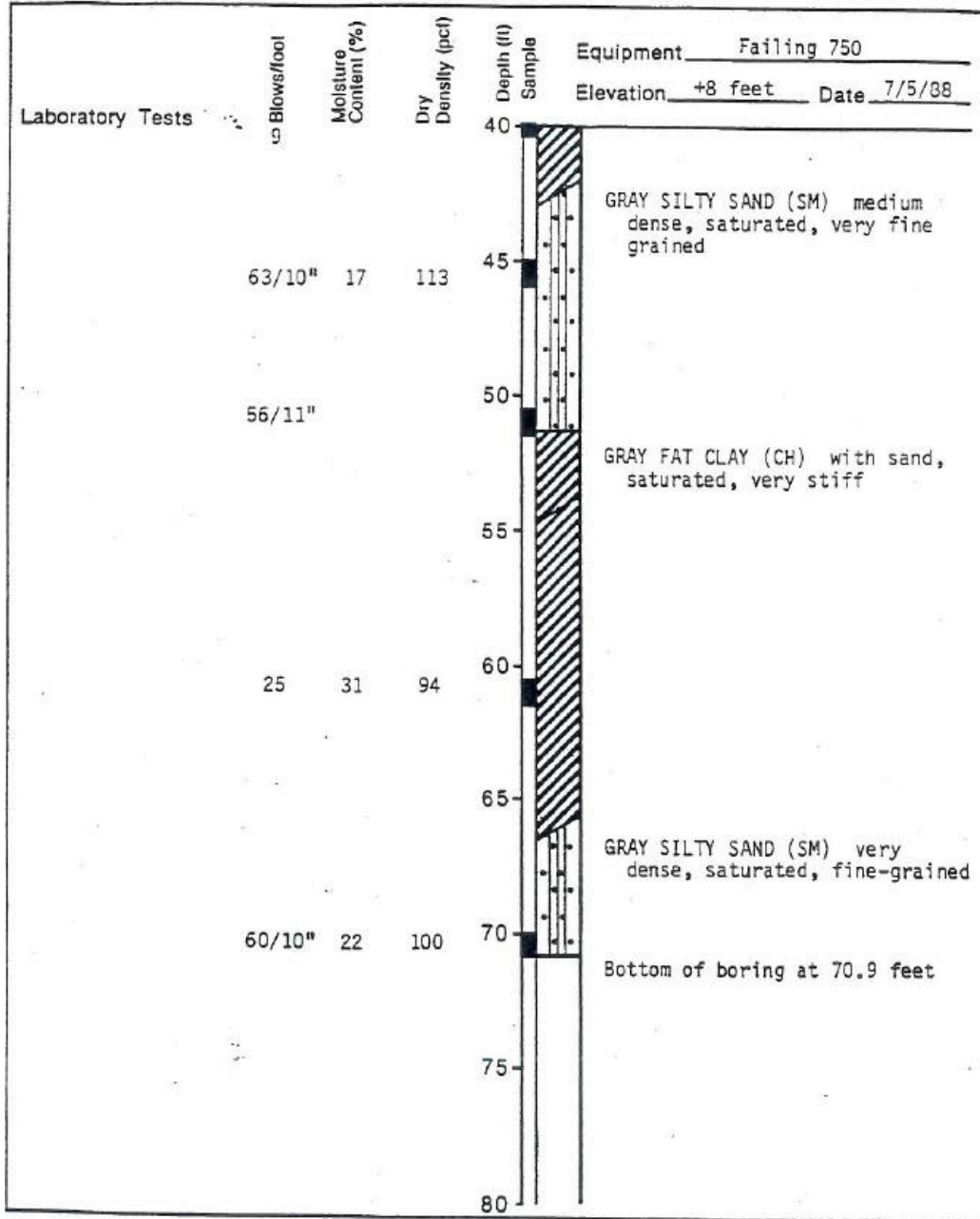


Figure 3.13 Boring log (dwp-bi-ba1) profile through southern levee crest, Part I.



**Figure 3.14** Boring log (dwp-bi-ba1) profile through southern levee crest, Part II.

After interpreting the available LiDAR, bathymetric data, SPT, and CPT results, the geometry and soil stratigraphy for the southern and northern levee cross sections are presented in Figures 3.15 and 3.16, respectively. According to Figure 3.15 and 3.16, levees are essentially composed of levee



fill, silty sand, organic peat and clay and the water tables are approximately 2 m below the levee crest. It is worthwhile to point out another judgement call made in terms of soil stratigraphy of both two cross-sections that silty sand or/and clay are assigned on the riverbed area right below the river, because there are very few peats which are comparatively light-weighted being deposited on the riverbed in light of daily frequent fluvial process.

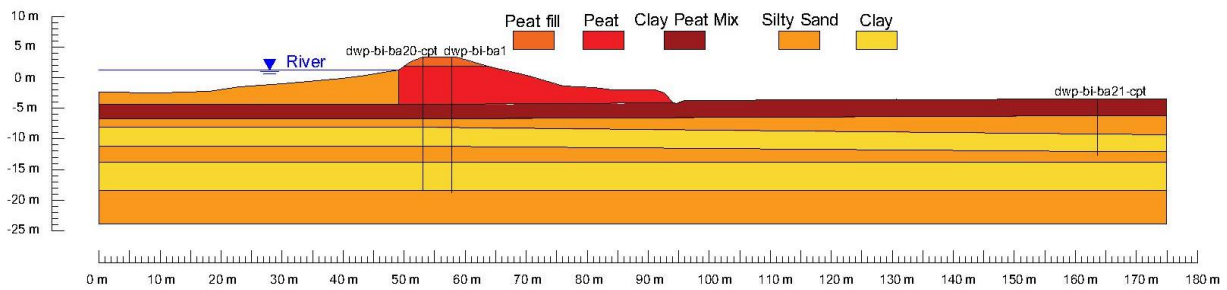


**Figure 3.15** Cross-section, soil stratigraphy of southern levee, boring log, and CPT locations.

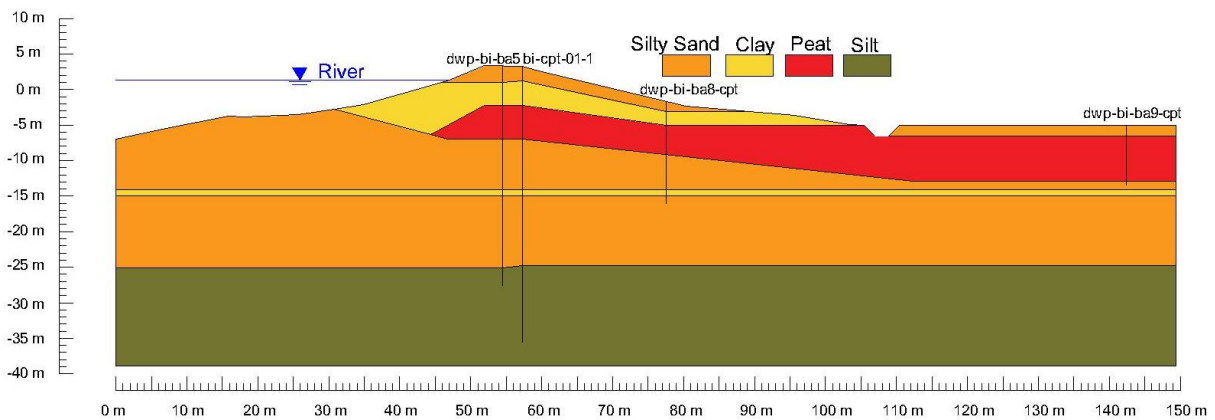


**Figure 3.16** Cross-section, soil stratigraphy of northern levee, boring log, and CPT locations.

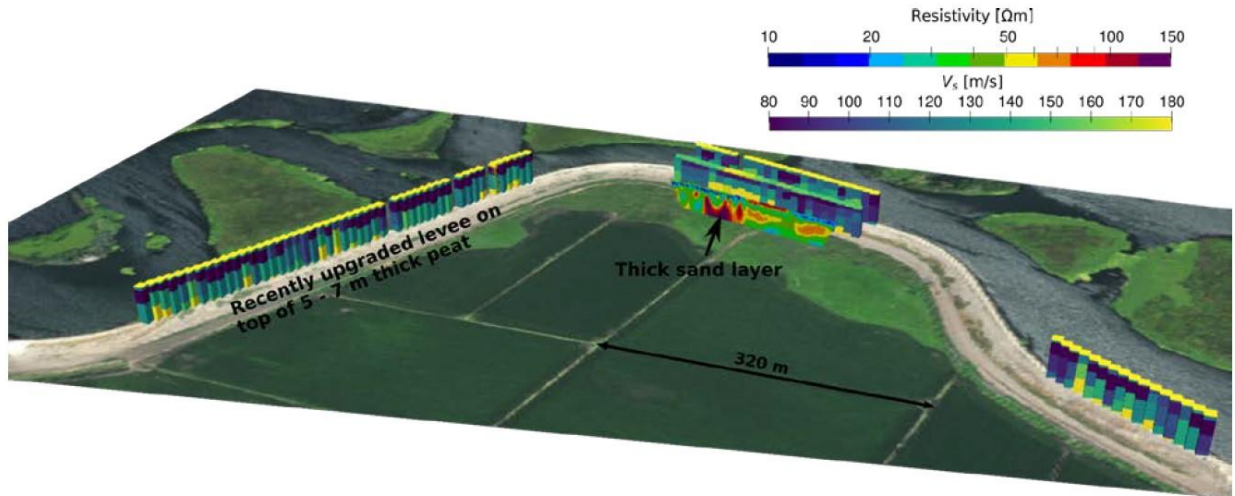
### 3.1.3 Geophysical Data

Secant shear modulus (maximum shear modulus) is a crucial parameter in capturing soil shear-strain relationship under cyclic loading, and it can be calculated by using the following equation,

$$G_{max} = \rho \cdot V_s^2 \quad (3.1)$$

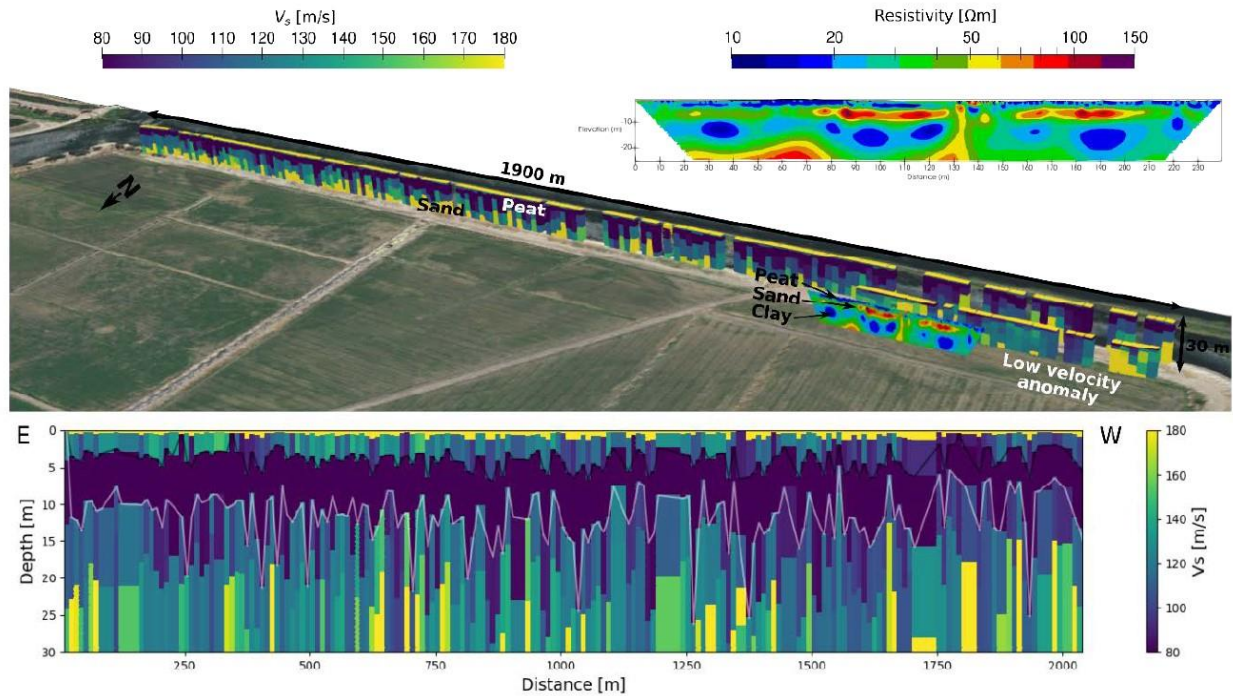
where  $\rho$  is the density and can be calculated based on lab tests;  $V_s$  is the shear wave velocity of the soil.

Researchers from Lawrence Berkeley National Laboratory conducted multichannel analysis of surface waves (MASW) and Electrical Resistivity Tomography (ERT) at various locations on Bacon Island (Uhlemann et al., 2021). These studies were conducted to (1) measure shear wave velocity, thereby enabling estimation of  $G_{max}$ , and (2) to image spatial variability in soil properties within and beneath the levees. Figure 3.17 shows the 3-D presentation of the data acquired in the northern Bacon Island levee, including shear wave velocity and resistivity profile. Based on these measured data, shear wave velocity of soil in northern levee, we observe a relatively stiff levee fill with  $V_s$  near 180 m/s overlying a very soft layer of peat with  $V_s$  as low as 80 m/s. The profile then becomes stiffer with depth beneath the peat. The peat layer is clearly identified in the inverted velocity profiles. Additionally, the ERT data identifies a high resistivity anomaly that is interpreted as a thick sand layer. Considering the fluvial depositional environment, that layer might be a paleochannel, which could contribute significantly to liquefaction hazard.



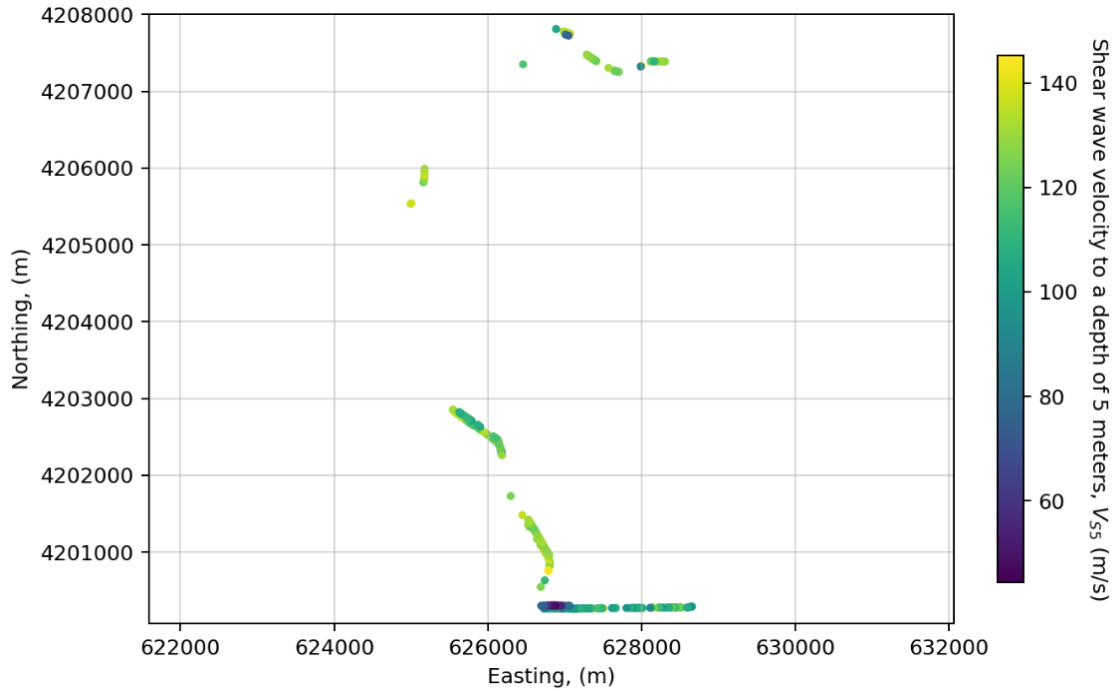
**Figure 3.17** Shear wave velocity and resistivity profile visualization in the northern levee.

Figure 3.18 demonstrates the 3-D visualization of ERT and MASW test results in the southern levee. The shear wave velocity structure for the southern levee is somewhat similar to the northern levee with levee fill soils having  $V_S$  near 140 to 180 m/s, and the underlying peat having  $V_S$  near 80 m/s. The cross section also shows that the stiffness of the peat is relatively similar along the length of the levee, while the levee fill exhibits more significant variability. Zones with high ERT values are also encountered at various locations beneath the levee fill, indicating sandy materials. These sands were not encountered in the CPT and boring log data, and are therefore not independently confirmed.



**Figure 3.18** Shear wave velocity and resistivity profile visualization in the southern levee.

In addition, the Lawrence Berkeley National Laboratory team also performed the geophysical test measuring Rayleigh wave velocity at 5 m wavelength along the Bacon Island levees. Figure 3.19 shows the locations where Rayleigh wave velocity at 5 m wavelength were measured on Bacon Island, and most tests are conducted on the levee crest whereas some tests are performed on the island free field. The wave velocity measured on the levee crest can be defined as the  $V_{S5}$  of levee. According to Fig 3.19, measured wave velocities range from 44 m/s to 145 m/s, and the averaged  $V_{S5}$  of southern levee is significantly lower than the  $V_{S5}$  of northern and western levees.



**Figure 3.19** Measured Rayleigh wave velocity at 5 m wavelength for Bacon Island levees.

Based on Rayleigh wave velocity measured from levee crest, the shear wave velocity  $V_{S5}$  of 28 levee reaches can be either calculated from field tests or inferred from adjacent measurements. I notice there are no measurements on eastern levee, so I use the averaged  $V_{S5}$  of northern and western levees as the  $V_{S5}$  of eastern levee. Table 3.2 presents the averaged  $V_{S5}$  of 28 reaches of Bacon Island levees.

**Table 2.2** Averaged  $V_{S5}$  of 28 reaches of Bacon Island levee system.

<b>Location</b>	<b>Levee Reach</b>	<b>Type of <math>V_{S5}</math></b>	<b>Averaged <math>V_{S5}</math> (m/s)</b>
South	1	Measured	98
South	2	Measured	106.7
South	3	Measured	111.7
East	4	Inferred	125.4
East	5	Inferred	125.4
East	6	Inferred	125.4
East	7	Inferred	125.4
East	8	Inferred	125.4
East	9	Inferred	125.4
East	10	Inferred	125.4
East	11	Inferred	125.4
East	12	Inferred	125.4
North	13	Inferred	124.6
North	14	Inferred	124.6
North	15	Measured	120.6
North	16	Measured	123.7
North	17	Measured	125.5
North	18	Inferred	124.6
North	19	Inferred	124.6
West	20	Measured	132.6
West	21	Inferred	126.8
West	22	Inferred	126.8
West	23	Inferred	126.8
West	24	Inferred	126.8
West	25	Measured	121.3
West	26	Measured	113.8
West	27	Measured	133.4
West	28	Measured	130.5

Furthermore, Kwak et al (2021) also provided the shear wave velocity profile with various peat thickness range at different depth in Sacramento and San Joaquin Delta region, as illustrated in Figure 3.20.

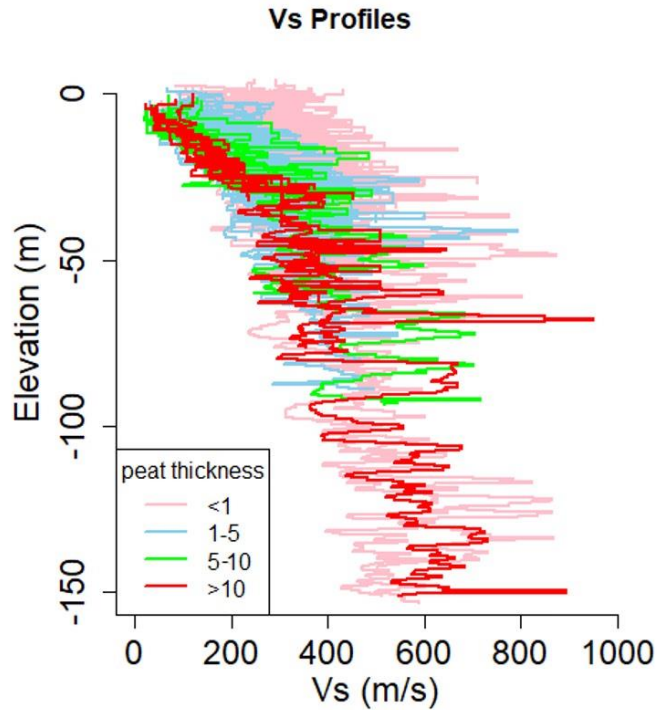


**Figure 3.20** Shear wave velocity and peat thickness profile of Sacramento-San Joaquin Delta region (Kwak et al. 2021).

### 3.1.4 Soil Properties

Ideally, adequate information about soil properties would be available to create detailed levee cross sections at each reach location. However, available data does not permit such detailed analysis, so judgment is needed to synthesize the available geotechnical site investigation data and geophysical. Soil properties within levee cross-sections can be mainly interpreted from tests: (1) lab tests including sieve analysis, permeability test, consolidation test, and triaxial compression tests, (2) penetration resistance from in-situ geotechnical investigations, and (3) geophysical field tests. The laboratory tests and geotechnical data are useful primarily for assigning soil type and strength, while the geophysical data are useful for assigning shear modulus and assessing spatial variability.

#### *a) Northern Levee*

According to soil stratigraphy within the northern levee, there are 3 silty sand layers, 2 clay layers and 1 silt layer in total. There is one boring log (dwp-bi-ba5) implemented on levee crest as indicated in Figure 3.9, 3.10, and 3.11, and various lab tests were performed using log soil sample, which provides a variety of measured soil properties. Some soil layers' properties are not measured in the laboratory tests; therefore, their properties are estimated based on empirical relationships and assumptions instead. Table 3.3 summarizes some measured soil parameters of northern levee from laboratory tests, and these are, on their own, inadequate to develop soil properties for all of the layers. Then I use judgement to combine field and lab test data to infer properties that were not measured. I assume unit weight of silty sand 1 is similar to unit weights of silty sand 2 and 3, so  $18.9 \text{ kN/m}^3$  is assigned to silty sand 1. Poisson ratios for these layers are used empirical values ranging from 0.33 to 0.4. Likewise, the void ratios of silty sand 1 and 2 are assumed to be similar to the void ratio of silty sand 3. The horizontal and vertical hydraulic conductivity of clay should be appreciably lower than sand and peat. Hydraulic conductivity of silty sand 1 should be similar to silty sand 2, and I assume  $k_x$  and  $k_y$  of silt and silty sand 3 are lower than silty sand 2 since they locate at larger depth. Table 3.4 presents the complete soil parameters measured and inferred from laboratory test.



**Table 3.3** Measured soil parameters of northern levee from lab tests.

<b>Soil</b>	<b>Unit Weight <math>\gamma</math> (kN/m<sup>3</sup>)</b>	<b>Poisson Ratio, <math>\nu</math></b>	<b>Void ratio, <math>e</math></b>	<b>Horizontal hydraulic conductivity, <math>k_x</math>(cm/s)</b>	<b>Vertical hydraulic conductivity, <math>k_y</math> (cm/s)</b>
Silty sand 1					
Clay 1	13.1		4		
Peat	10.6		6.69	5.8e-8	5.8e-9
Silty sand 2	19.4			2.2e-7	2.2e-7
Clay 2	19.4		0.73		
Silty sand 3	19.4		0.73		
Silt	17.9		1.05		

**Table 3.4** Measured and inferred soil parameters of northern levee from lab tests.

<b>Soil</b>	<b>Unit Weight <math>\gamma</math> (kN/m<sup>3</sup>)</b>	<b>Poisson Ratio, <math>\nu</math></b>	<b>Void ratio, <math>e</math></b>	<b>Horizontal hydraulic conductivity, <math>k_x</math>(cm/s)</b>	<b>Vertical hydraulic conductivity, <math>k_y</math> (cm/s)</b>
Silty sand 1	18.9	0.35	0.73	3.5e-7	3.5e-7
Clay 1	13.1	0.4	4	2.4e-12	2.4e-12
Peat	10.6	0.38	6.69	5.8e-8	5.8e-9
Silty sand 2	19.4	0.35	0.75	2.2e-7	2.2e-7
Clay 2	19.4	0.4	0.73	2.4e-12	2.4e-12
Silty sand 3	19.4	0.35	0.73	2.2e-9	2.2e-9
Silt	17.9	0.37	1.05	2.2e-9	2.2e-9

There are two triaxial consolidated undrained (TCU) tests performed for peat and clay soil at the depth of about 4.6 m and 7.6 m in the northern levee. Table 3.5 and 3.6 summarize the results of these two triaxial consolidated undrained tests.

**Table 3.5** TCU test of clay samples obtained in northern levee.

Soil	Sample	In-situ effective stress (kPa)	Consolidation pressure (kPa)	$\sigma'_1$ (kPa)	$\sigma'_3$ (kPa)	$(s_u/\sigma'_v)$
Clay	A	42.8	43.6	67.7	5.0	0.72
	B	42.8	64.7	98.4	26.8	0.55
	C	42.8	112.5	143.6	35.3	0.48

**Table 3.6** TCU test of peat samples obtained in northern levee.

Soil	Sample	In-situ effective stress (kPa)	Consolidation pressure (kPa)	$\sigma'_1$ (kPa)	$\sigma'_3$ (kPa)	$(s_u/\sigma'_v)$
Peat	A	50.7	52.2	81.7	14.9	0.64
	B	50.7	81.4	98.2	23.5	0.46
	C	50.7	119.7	114.8	35.6	0.46

According to Table 3.5 and 3.6, for both clay and peat, there are three soil samples confined with increasing consolidation pressure and then these samples are sheared under deviator stresses until reaching to failure states. Consolidation tests for these samples are not available, so it is not possible to know the OCR for these tests. We interpret the normally consolidated strength ratio  $(s_u/\sigma'_v)_{NC}$  to be equal to the measured strength ratio for the test conducted at the highest consolidation pressure. These end up being 0.48 and 0.46 for the clay and peat, respectively.

Figure 3.21 shows unit weight, total stress, and effective stress profile through the northern levee crest interpreted from boring log and laboratory test and the digitized results of CPT through levee

crest. The Soil behavior type index  $I_c$  and undrained shear strength  $s_u$  can be interpreted based on interpreted in-situ vertical stress profiles as well as measured profile of  $q_t, f_s$ , and  $u$  in CPT.

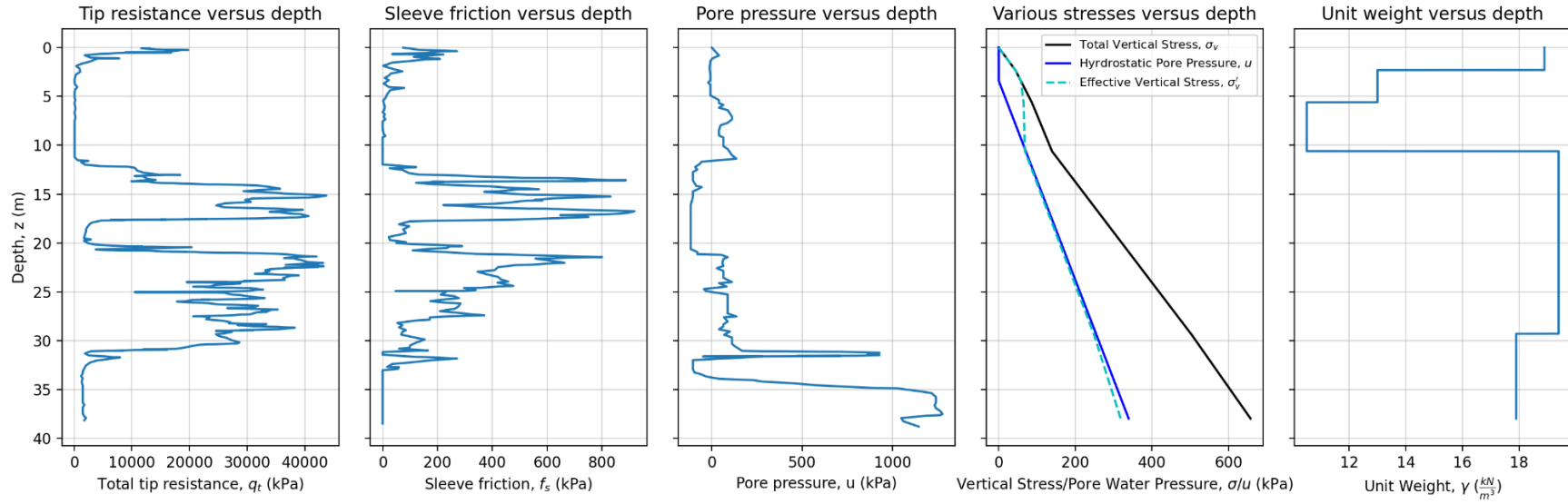


**Figure 3.21** Digitized tip resistance and sleeve friction ratio versus depth profile and interpreted unit weight and computed in-situ total and effective stress versus depth through northern levee crest according to boring logs and associated lab tests.

SPT provides field blow counts  $N$  of soil layers at boring log location, and these blow counts can be corrected to  $N_{60}$  for field procedures based on Skempton (1986) as follow,

$$N_{60} = \frac{E_H C_B C_S C_R N}{0.6} \quad (3.2)$$

where  $E_H$  is Hammer efficiency and is taken as 0.6 for the use of hand dropped donut hammer;  $C_B$  is borehole diameter factor and is taken 1 because the borehole diameter is ranging from 65mm to 115mm;  $C_S$  is the sampler correction and it is 1 because the standard sampler was used; and  $C_R$  is rod length correction and is taken as 1 since the rod length is longer than 10 meters. (BNBC 2015)

Overburden pressure appreciably affects the penetration resistance of cohesionless soils, so the overburden pressure correction factor  $C_N$  is introduced to correct blown counts and corrected blow counts for overburden pressure  $(N_1)_{60}$  can be written as,

$$(N_1)_{60} = C_N N_{60} \quad (3.3)$$

where Liao and Whitman (1986) suggested that  $C_N = \left(\frac{p_a}{\sigma'_v}\right)^{0.5}$ ,  $p_a$  is approximately taken as 100 kPa, and  $\sigma'_v$  is the current vertical effective stress.

Yang (2021) found that the average relative density of sand layers within the levee fill tremendously affects levee seismic fragility functions in the Sacramento-San Joaquin Delta region, so herein it is necessary to estimate average relative density of levee fill. Boulanger and Idriss (2008) proposed that the relative density of sand layer can be estimated based on corrected blow counts for overburden pressure  $(N_1)_{60}$ , it can be expressed as,

$$D_R = \sqrt{\frac{(N_1)_{60}}{46}} \quad (3.4)$$

Table 3.7 summarizes calculation of corrected blow counts and relative density of three sand layers in the northern levee and its foundation.

**Table 3.7** Corrected blow counts and relative density of sand layers in the northern levee model.

Soil	Depth (m)	Field blow count, $N$	Effective stress, $\sigma'_v$ (kPa)	$N_{60}$	$(N_1)_{60}$	Relative density, $D_r$ (%)
Sand layer 1	4.5	5	28.4	5	9	45
Sand layer 2	12.2	40	85.4	40	43	97
Sand layer 2	13.7	56	100.0	56	56	100
Sand layer 2	15.2	35	114.6	35	33	84
Sand layer 2	16.7	35	129.2	35	31	82
Sand layer 3	19.8	35	157.2	35	29	78
Sand layer 3	27.4	34	226.6	34	23	70

Table 3.8 presents the measured and calculated soil properties of northern levee based on field test including boring and geophysical tests.

**Table 3.8** Measured and calculated soil parameters of northern levee from field tests.

Soil	Density, $\rho$ (kg/m <sup>3</sup> )	Shear Wave Velocity, $V_s$ (m/s)	Maximum Modulus, (kPa)	Shear $G_{max}$	Relative Density, $D_r$ (%)
Silty sand 1	1928	160	49371		45
Clay 1	1340	120	19296		/
Peat	1078	80	6899		/
Silty sand 2	1981	160	50707		91
Clay 2	1981	150	44566		/
Silty sand 3	1981	165	53925		74
Silt	1831	180	59312		/

The modulus reduction curve of each soil layer is another important input parameter in nonlinear seismic site response analysis. Menq (2003) and Darendeli (2001) proposed some modulus

reduction unified models using lab testing data for sand and clay. Equation 3.5 demonstrates the hyperbolic form of Menq (2003) and Darendeli (2001) soil modulus reduction model, but different coefficients are utilized in these two models. Shear modulus of soil can be written as a function of shear strain as shown below.

$$\frac{G(\gamma)}{G_m} = \frac{1}{1 + \left(\frac{\gamma}{\gamma_r}\right)^\alpha} \quad (3.5)$$

In Menq (2003) model,  $\alpha = 0.86 + 0.1 \times \log\left(\frac{\sigma'_0}{p_a}\right)$ ,  $\gamma_r(\%) = 0.12 \times C_u^{\varphi_1} \times \left(\frac{\sigma'_0}{p_a}\right)^{\varphi_2}$ ,  $\varphi_1 = -0.6$ ,  $\varphi_2 = 0.5 \times C_u^{-0.15}$ ,  $\sigma'_0$  is the mean effective stress,  $p_a$  represents the atmospheric pressure and generally takes 101 kPa,  $C_u$  is the soil uniformity coefficient, and  $G_m$  is the maximum shear modulus.

In Darendeli (2001) model,  $\alpha = 0.92$ ,  $\gamma_r(\%) = (\varphi_1 + \varphi_2 \times PI \times OCR^{\varphi_3}) \times \left(\frac{\sigma'_0}{p_a}\right)^{\varphi_4}$ ,  $\varphi_1 = 0.0352$ ,  $\varphi_2 = 0.0010$ ,  $\varphi_3 = 0.3246$ ,  $\varphi_4 = 0.3483$ , and  $PI$  is the plasticity index and the unit is %.

Wang et al. (2021) used same hyperbolic form indicated in Equation 3.5 and proposed a shear modulus reduction model specifically for organic peat using results of cyclic tests implemented on peat soil from 6 regions in the world, and these 6 regions are Washington (USA), Sacramento-San Joaquin Delta (USA), New York (USA), Japan, Greece, and Netherland.

In Wang et al. (2021) model,  $\alpha = 0.75$ ,  $\gamma_r(\%) = (\varphi_1 + \varphi_2 \times OC^{\varphi_3}) \times \left(\frac{\sigma'_0}{p_a}\right)^{\varphi_4}$ ,  $\varphi_1 = 0.4572$ ,  $\varphi_2 = 0.0028$ ,  $\varphi_3 = 1.4047$ ,  $\varphi_4 = 0.0831$ , and  $OC$  is the organic content in peat.

However, these models are generally applicable to about the shear strain  $\gamma$  is less or equal to 0.3%, so they basically cannot produce realistic result of nonlinear site response under strong ground

motions. Yee et al. (2013) came up with a procedure to correct the modulus reduction curve in the large strain portion and make the backbone curve asymptotically approach to shear at large strains. The soil shear strain range of interest is set as from  $10e^{-6}$  to 0.1, and 0.1 is generally believed to be the maximum shear strain of soil. For Yee et al. (2013) correction procedure, soil shear strength at failure is assumed to be approximately 0.3 times maximum shear modulus so the transitional strain is taken as 0.3%. Figure 3.22 shows the comparison of backbone curve of clay 2 layer in the northern levee computed from Darendeli's model and Darendeli's model combined with Yee et al. correction procedure, and the shear strength of clay 2 is estimated to be about 74 kPa. Clearly, the red curve computed from the hybrid model does a better job in describing a reasonable relationship between shear strain and shear stress at the large strain part, because the desired shear strength is approximately achieved when the maximum shear strain is reached. Quite similar conclusions can also be drawn from the backbone comparisons of sand and peat soil, and the results are not shown here to avoid redundancy. Thus, for each individual soil material, the corresponding appropriate modulus reduction model combined with this correction procedure is implemented to yield the final desired modulus reduction curve.



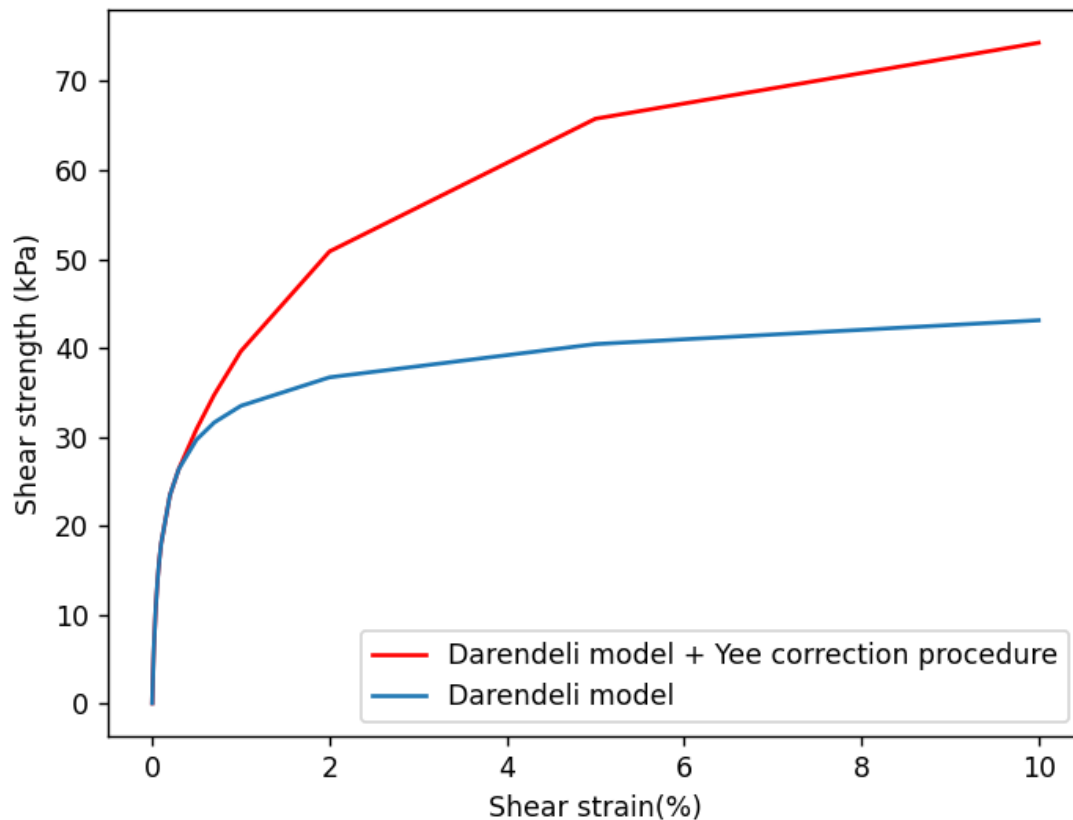


**Figure 3.22** Comparison of backbone curves of clay acquired from Darendeli’s model and Yee’s hybrid model.

***b) Southern Levee***

Likewise, similar analysis calculation and estimation of soil properties are replicated according to laboratory and field test results of southern levee. As illustrated in Figure 3.15, there are 4 sand layers, 2 clay layer, 1 peat layer, 1 peat and clay mix layer, and 1 desiccated peat fill on the top of the levee. Same procedures to infer soil properties based on measured ones from laboratory tests. To avoid redundancy, the inferring process is not elaborated here and measured and inferred soil properties of southern levee from lab test are presented together in Table 3.9. It is interesting to notice that the layer dominated by peat exhibits significantly different permeability in vertical and

horizontal direction due to the unique fiber arrangement in peat soil structure.

**Table 3.9** Measured and inferred soil parameters of southern levee from lab tests.

Soil	Unit Weight $\omega$ (kN/m <sup>3</sup> )	Poisson Ratio, $\nu$	Void ratio, $e$	Horizontal hydraulic conductivity, $k_x$ (cm/s)	Vertical hydraulic conductivity, $k_y$ (cm/s)
Artificial peat fill	15.7	0.34	0.9	6e-9	6e-9
Peat	10.3	0.35	9.50	5.8e-8	5.8e-9
Peat clay mix	17.0	0.37	1.3	3e-9	3e-10
Silty sand 1	18.9	0.35	0.60	8e-9	8e-9
Clay 1	18.5	0.37	1.0	2.4e-12	2.4e-12
Silty sand 2	20.8	0.35	0.5	5e-9	5e-9
Clay 2	19.3	0.37	0.81	2.4e-12	2.4e-12
Silty sand 3	19.2	0.35	0.70	2.2e-9	2.2e-9
Silty sand 4	16.5	0.35	0.6	2.2e-7	2.2e-7

Figure 3.23 shows the interpreted unit weight and stress profile as well as digitized CPT profile.

Sleeve friction ratio  $f_r$  rather than sleeve friction  $f_s$  is recorded in CPT profile, so  $f_s$  can be computed by multiplying measured total tip resistance  $q_t$  and friction ratio  $f_r$ .

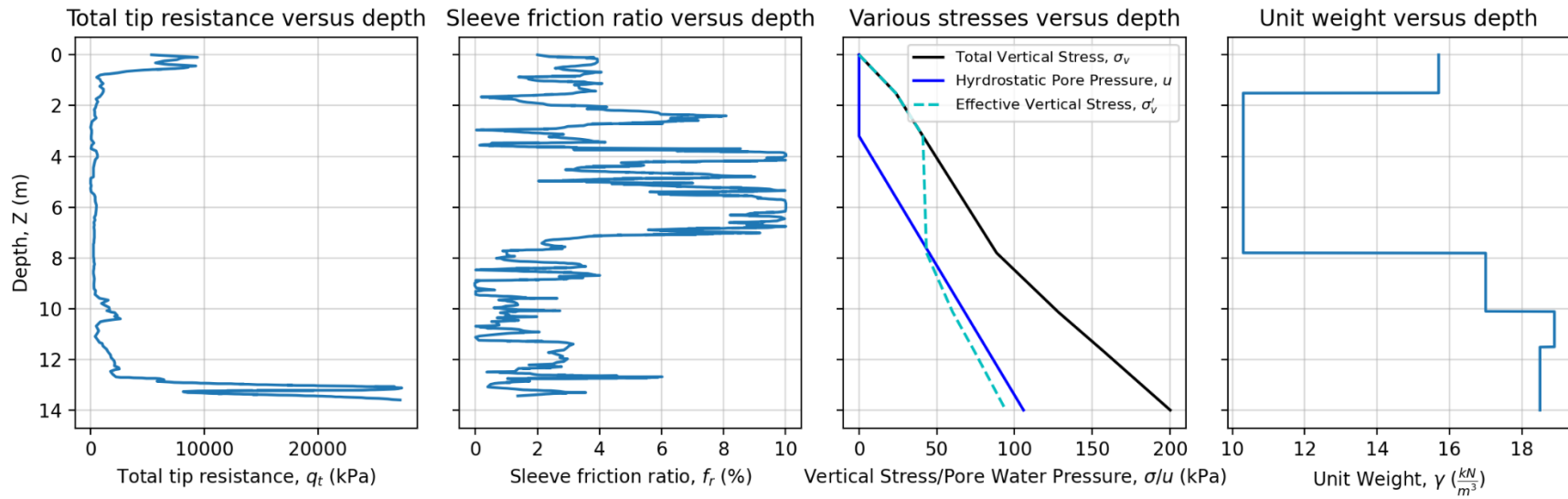


**Figure 3.23** Digitized tip resistance and sleeve friction ratio versus depth profile and interpreted unit weight and computed in-situ total and effective stress versus depth through southern levee crest according to boring logs and associated lab tests.

Due to the relatively quick cyclic loading during earthquake shaking, soil in levees can be assumed to be sheared in the undrained condition. As a corollary, soil undrained shear strength is an important parameter in dynamic earthquake simulation. There are 4 triaxial unconsolidated undrained tests (TUU) for pressure-dependent fine-grained soil, and 3 tests are for southern levee and another one is for northern levee. These tests directly provide laboratory-based undrained shear strength for soil layers at different depths. CPT results can also be used to interpret undrained shear strength of soil at different using the following formula,

$$s_u = \frac{q_t - \sigma_v}{N_{kt}} \quad (3.6)$$

where  $\sigma_v$ ,  $q_t$ ,  $N_{kt}$ , are in-situ total stress, tip resistance, cone factor, respectively. In general,  $N_{kt}$  is treated as a constant and varies from 10 to 18. With lab measured undrained shear strength plugging back in the above equation, the calibrated  $N_{kt}$  can be calculated for each individual soil.

Ladd and Foote (1974) proposed the SHANSEP (stress history and normalized soil engineering properties) model for modeling undrained shear strength of clay soils, and the undrained shear strength of clay soil subjected to a given stress path can be expressed by,

$$s_u = \sigma'_{vc} \cdot S \cdot OCR^m \quad (3.7)$$

where  $\sigma'_{vc}$ ,  $S$ ,  $OCR$ , and  $m$  are in situ effective vertical stress, strength ratio in normally consolidated state, over consolidation ratio, and exponent parameter typically between 0.75 and 1. It is reasonable to assume each pressure-dependent soil layer has constant shear strength ratio, and this ratio can be computed from TUU and CPT. Ali (2016) found that the shear strength ratio obtained from TUU is about 1.5 times larger than the shear strength ratio measured from direct simple shear test (DSS) for fine-grained soil in the Sacramento Delta region. Shear strength ratio

measured from DSS is preferred to be assigned to soils because this test better simulates the realistic soil shearing process during ground shaking events. Table 3.10 shows the calculated shear strength ratio of fine-grained soil and site-specific  $N_{kt}$  values of some peat and clay layers for southern and northern levee based on CPT and TUU. It is clear to observe that peat's shear strength ratio is comparatively larger than ratio of clay, and the clay at depth of 6.1m exhibits a much larger shear strength ratio because it is stemmed from the interface between peat and clay according to Figure 3.13.

**Table 3.10** Shear strength ratio and cone factor profile based on CPT and TUU test results.

Location	Soil type	Depth (m)	Shear Strength $S_u$ (kPa)	Total stress $\sigma_v$ (kPa)	Effective stress $\sigma'_v$ (kPa)	Tip resistance $q_t$ (kPa)	Shear Strength ratio (TUU) $(s_u/\sigma'_v)$	Cone factor $N_{kt}$	Shear Strength ratio (DSS) $(s_u/\sigma'_v)$
North	Peat	9.1	57.7	120.6	50.7	407.1	1.14	5.0	0.76
South	Peat	3.0	23.8	37.6	19.1	103.3	1.25	2.8	0.83
South	Clay	6.1	32.0	73.5	25.2	445.9	1.27	11.6	0.85
South	Clay	7.6	22.6	96.8	33.4	224.3	0.68	5.6	0.45

Table 3.11 summarizes the measured and calculated soil properties of southern levee based on field test including boring and geophysical tests.

**Table 3.11** Measured and calculated soil parameters of southern levee from field tests.

Soil	Density, $\rho$ (kg/m <sup>3</sup> )	Shear wave velocity, $V_s$ (m/s)	Maximum shear modulus, $G_{max}$ (kPa)	Relative Density, $D_r$ (%)
Peat fill	1570	130	26533	/
Peat	1030	80	6592	/
Peat clay mix	1700	110	20570	/
Silty sand 1	1890	130	31941	68
Clay 1	1850	130	31265	/
Silty sand 2	2080	145	43732	100
Clay 2	1930	165	52544	/
Silty sand 3	1920	180	62208	96
Silty sand 4	1650	110	19965	65

Last but not least, similar analyses for determining desired modulus reduction curves of soils under cyclic loading used for northern levee is implemented for soil layers in southern levee. The hybrid model still does a better job in capturing shear-strain relationship reasonably than general modulus reduction model, so it is utilized to produce the modulus reduction curve for each soil layer. To avoid redundancy, the example of showing backbone curve comparison of soil within southern levee computed from different models is not presented here.

### 3.2 Ground Motion Selection

Prior to performing nonlinear finite element simulations to develop fragility functions for levees in Bacon Island, selecting a set of appropriate ground motions that are consistent with the results of seismic hazard analysis is needed. Selecting motions for fragility analysis is a bit different from selecting motions to match a target spectrum, and I need to cover levee response over a wide range of shaking intensity. In addition, I also want the motions to be reasonably consistent with magnitude and distance disaggregation from the seismic hazard. To accomplish this, three critical principles should be followed during ground motion selection procedures: a) Select ground

motions from the earthquakes whose mechanism are consistent with the ones considered in seismic hazard analysis for Bacon Island; b) The intensity measures caused by ground motions ought to have a good cover of the ranges of intensities calculated for a variety of return periods in seismic hazard analyses; c) The combinations of magnitude and distances of event scenarios should be adequately consistent with disaggregation results in PSHA.

Seismic hazard may vary within a spatially distributed infrastructure system due to the different source-to-site distances and site conditions. To explore whether seismic hazard varies significantly within Bacon Island, four locations are selected at the South, East, North, and West side of the levee system and seismic hazard curves are computed at each location. Figure 3.24 shows the locations of four selected sites on Bacon Island levee system.

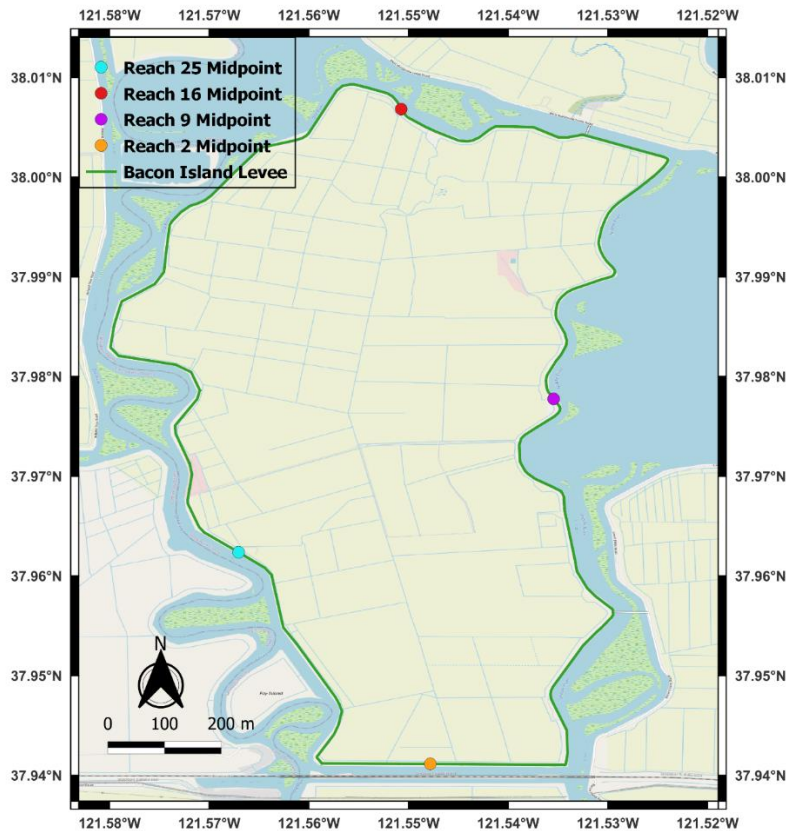


**Figure 3.24** Locations of four examples representative levee reach midpoints on Bacon Island levees.

PSHAs are performed for these 4 representative sites using the National Seismic Hazard Mapping Project Hazard (NSHMP-HAZ) code (USGS, 2022) for  $V_{S30} = 350$  m/s. This site condition is reasonably consistent with the stiffness of the soils underlying the peat in the Delta. UCERF3 is used as the source model and the NGA-West 2 BSSA14 GMM is utilized. Figure 3.25 (a) and (b) shows the calculated *PGA*-based and *PGV*-based hazard curves for those four sites. These hazard curves of four sites are essentially identical, which illustrates that Bacon Island is a relatively small region related to the rate of change of seismic hazard and that the same hazard curve can be used throughout the island.

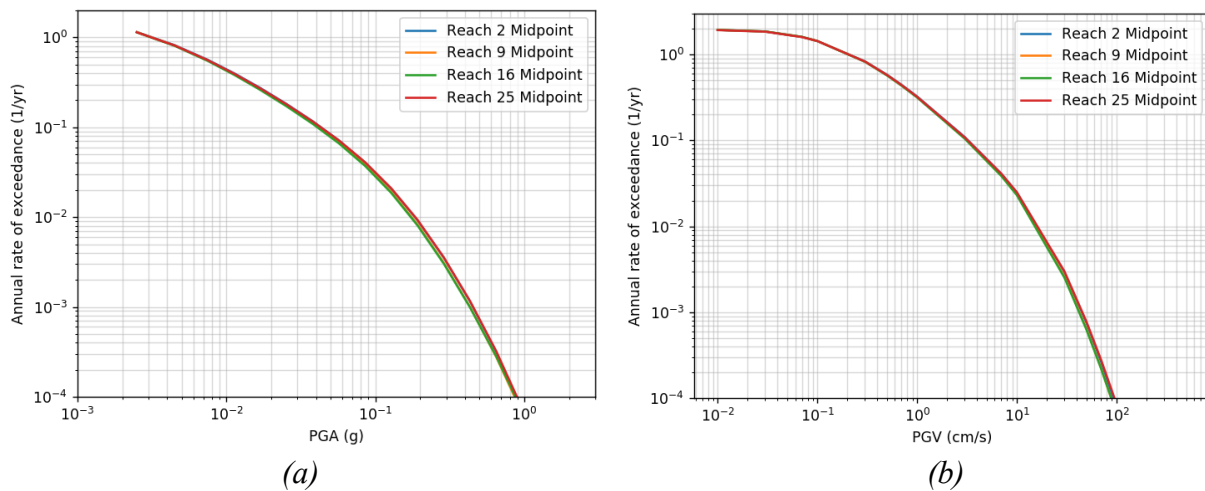


**Figure 3.25** (a) *PGA*-based hazard curves; (b) *PGV*-based hazard curves of four reach midpoint examples.

Deaggregation (also called disaggregation) is one of the extensions of PSHA and it reveals the relative contribution of various earthquake sources and magnitudes to the rate of exceedance of a given ground motion intensity by applying the Bayes' rule. In disaggregation, the probability that an earthquake's magnitude equals to  $m$  and source-to-site distance is  $r$  given that a ground motion  $IM$  is greater than  $x$  is calculated as follow,



$$P(M = m, R = r | IM > x) = \frac{\lambda(IM > x, M = m, R = r)}{\lambda(IM > x)} \quad (3.8)$$

where the denominator  $\lambda(IM > x)$  is exactly what we previously calculated in PSHA, as indicated in the equation 2.4, and the numerator  $\lambda(IM > x, M = m, R = r)$  is a joint distribution and is computed by omitting both summations over magnitude  $M$  and distance  $R$  in the equation 2.4.

Since seismic hazard of these four sites are almost identical, the deaggregation analyses of one of the sites at a series of return periods are reasonably equivalent to the overall deaggregation results of the entire Bacon Island levee. Figure 3.26 to 3.31 show the deaggregation results of reach 2 midpoint at return periods of 10, 50, 100, 225, 475, and 2475 years, respectively. These deaggregations are computed and plotted by using Open-Source Seismic Hazard Analysis (OpenSHA) which is a Java-based platform for conducting seismic hazard analysis developed by USGS. To be consistent with previous PSHA, UCERF3 and BSSA14 are used as source model and GMM, and the reference  $V_{S30}$  is set as 350 m/s as well.

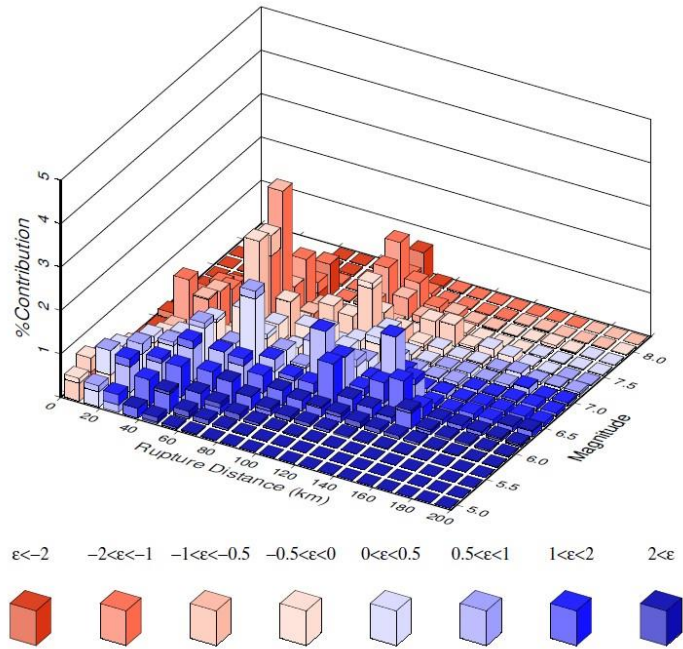


**Figure 3.26** PGV-based disaggregation results of the midpoint of Reach 2 for a return period of 10 years.

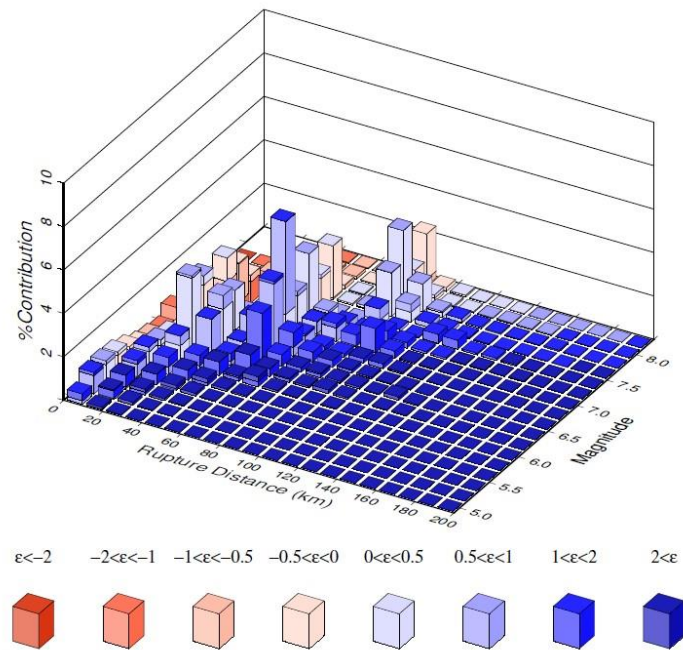


**Figure 3.27** PGV-based disaggregation results of the midpoint of Reach 2 for a return period of 50 years.

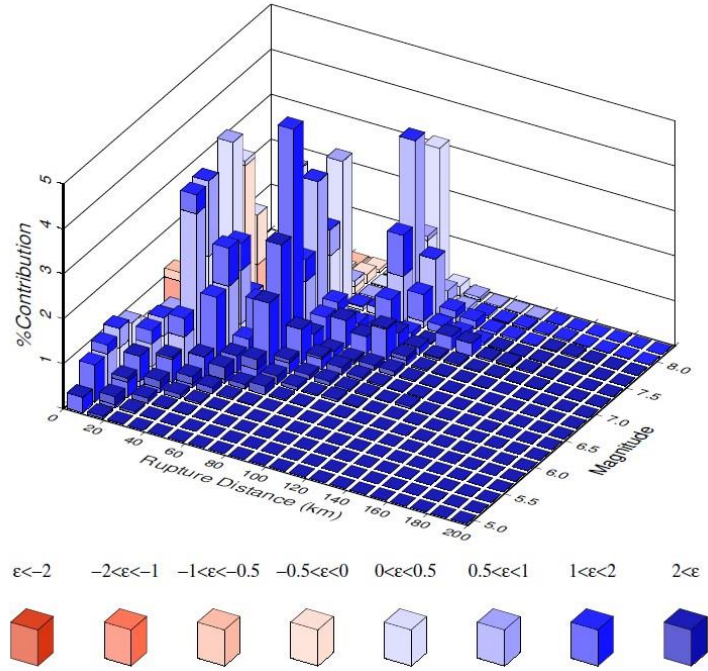


**Figure 3.28** PGV-based disaggregation results of the midpoint of Reach 2 for a return period of 100 years.

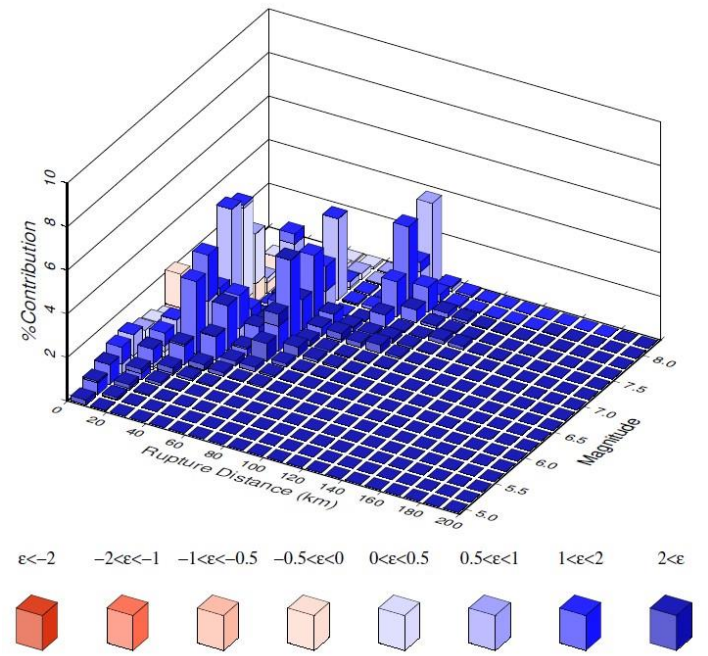


**Figure 3.29** PGV-based disaggregation results of the midpoint of Reach 2 for a return period of 225 years.

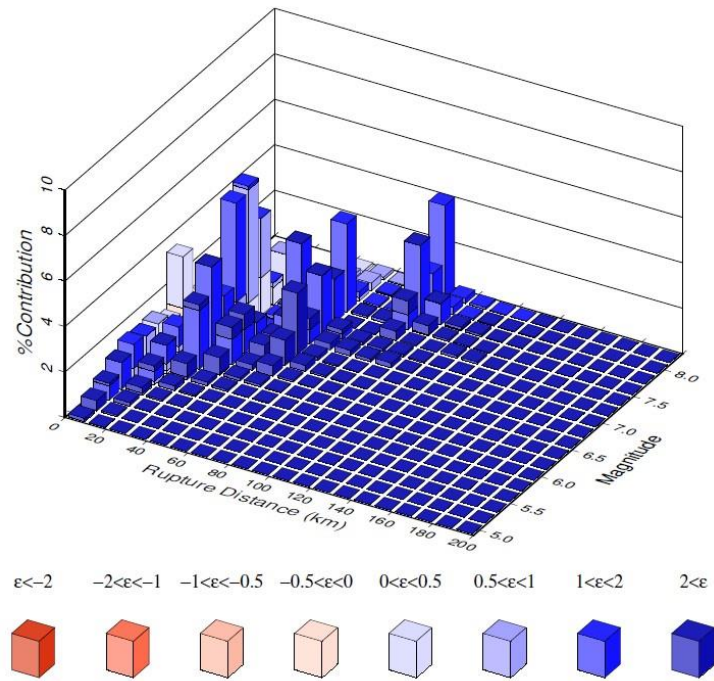


**Figure 3.30** PGV-based disaggregation results of the midpoint of Reach 2 for a return period of 475 years.

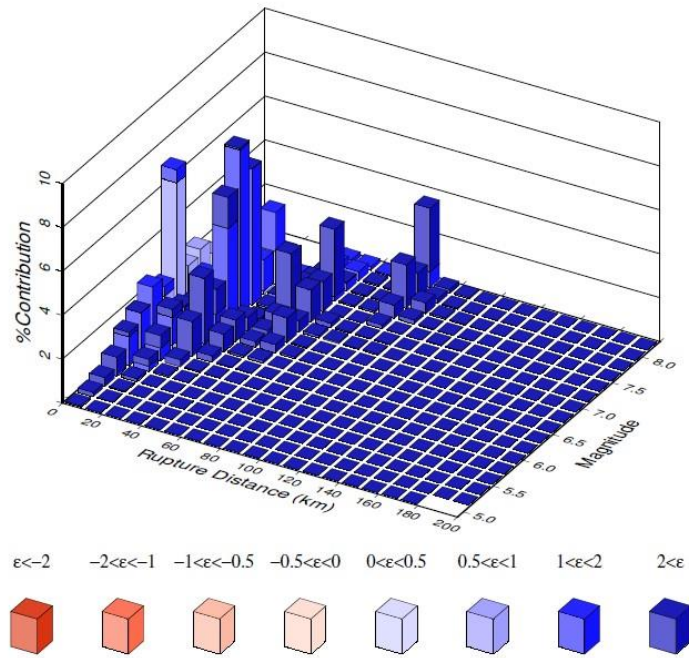


**Figure 3.31** PGV-based disaggregation results of the midpoint of Reach 2 for a return period of 2475 years.

In disaggregation results,  $\varepsilon$  represents the number of standard deviations above or below the median, and positive  $\varepsilon$  indicates above while negative  $\varepsilon$  represents below the median. Based on deaggregations, negative  $\varepsilon$  occurs in shorter return periods while positive  $\varepsilon$  dominates in longer return periods. Moderate magnitude and nearby rupture such as Great Valley Midland fault and background seismicity as well as larger magnitude and more distant seismic events such as Hayward and San Andreas faults are essential seismic hazard contributing sources in Bacon Island.

The magnitude-distance combination scenarios which account for more than 1% contribution of seismic hazard in these 6 return periods of interest are defined as large hazard contributors and selected from disaggregation results, and then 41 scenarios are obtained. Table 3.12 summarizes the selected magnitude-distance combination scenarios with significant hazard contributions based on the disaggregations for all return periods.

**Table 3.12** Selected magnitude-distance combination scenarios with significant hazard contributions based on the disaggregations for all return periods.

<b>Magnitude</b>	<b>Distance (km)</b>
5.2, 5.3, 5.4, 5.5, 5.6, 5.8, 5.9, 6, 6.1, 6.2, 6.3, 6.5	10
6, 6.1, 6.2, 6.3, 6.4, 6.5, 7, 7.1, 7.2	30
7, 7.1, 7.2	50
6.6, 6.7, 6.8, 6.9, 7,	70
7.8, 7.9, 8, 8.1, 8.2, 8.3	90
7.5, 7.6, 7.7	110
7.4, 7.5, 7.6	130

The ground motion selection algorithm by Baker and Lee (2018) was used to select motions for each of the 41 magnitude-distance scenarios to choose a set of ground motions that match the unconditional response spectrum corresponding to each magnitude-distance combination scenario.

Unconditional response spectrum is distinguished from the conditional mean spectrum because it is not conditioned to match specific return period. Ground motions are only selected from the

NGA-West 2 database, so the subduction events are not considered, and the rupture distance is less than 200 km. In addition,  $V_{S30}$  are specified to be less than 500 m/s. 616 unscaled ground motions are finally selected from this algorithm. Figure 3.32 demonstrates response spectra of selected ground motions and the calculated target response spectra distribution from BSSA14 model associated with two magnitude-distance scenarios, and it shows relatively good response spectra matchings at range of 0.01 s to 10 s periods.

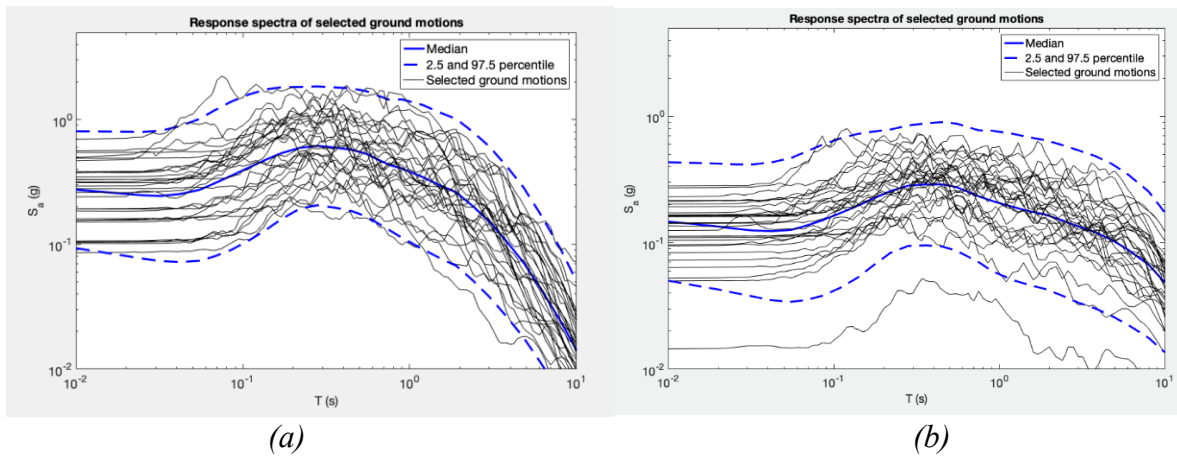


**Figure 3.32** Response spectra of selected ground motions, compared to the target response spectra distribution computed by BSSA14 model with (a) magnitude = 6.5, distance = 10km,  $V_{S30}$  =350 m/s; (b) magnitude = 8.3, distance = 90 km,  $V_{S30}$ =350 m/s.

As illustrated in Section 3.2, 616 ground motion records in NGA-West2 database (Timothy et al. 2014) were applied to the northern and southern levee models for developing seismic fragility functions. From Figure 3.33 to 3.35, three examples input ground motion time series and response spectra are presented. The ground motions have various magnitude, source-to-site distance, peak

ground acceleration, frequency, duration, and spectral responses associated with periods ranging from 0.01s to 20s.

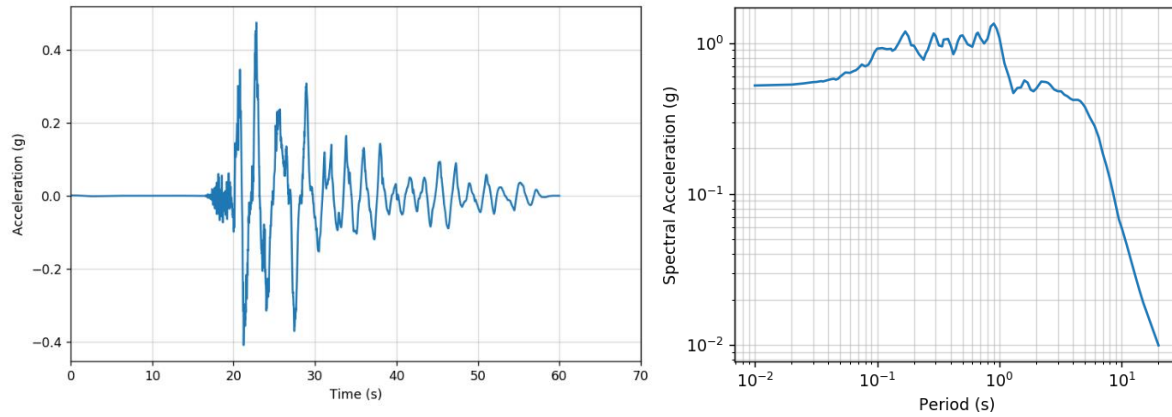


**Figure 3.33** One input ground motion record and its spectral acceleration of Chi-Chi earthquake (RSN=1244) with magnitude 7.62, Taiwan, 1999.

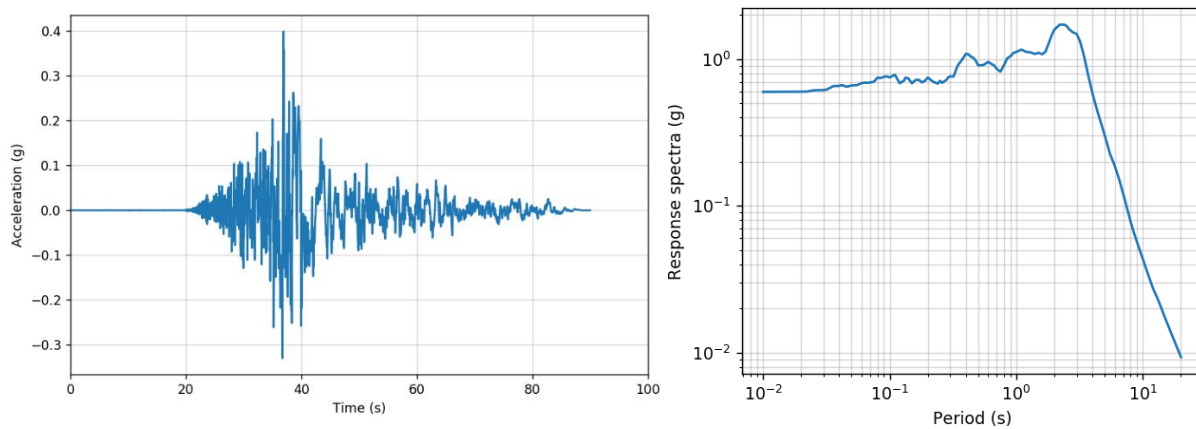


**Figure 3.34** One input ground motion record and its spectral acceleration of Chuetsu-Oki earthquake (RSN=4875) with magnitude 6.8, Japan, 2007.

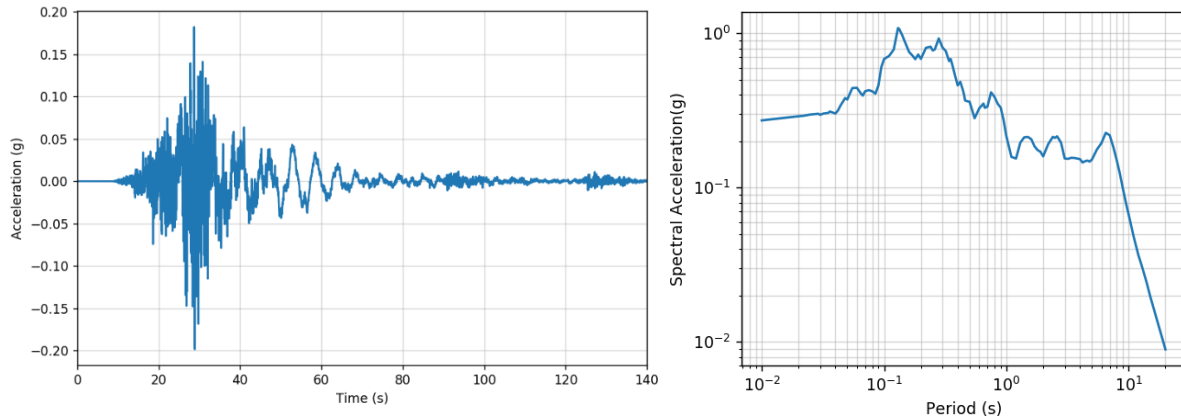


**Figure 3.35** One input ground motion record and its spectral acceleration of Darfield earthquake (RSN=6886) with magnitude 7, New Zealand, 2010.

Additionally, a group of 62 unscaled ground motions are scaled by a factor of 2 and 4 to generate stronger ground motions for developing levee fragility functions. The scaling method is basically to amplify the amplitude of original ground motions by multiplying 2 and 4 to its measured time-series ground accelerations. Figure 3.36 shows an example of a comparison of original unscaled ground motion and scaled ground motion with a amplifying scale factor of 4 from 1989 Loma Prieta earthquake,  $M=6.9$ .



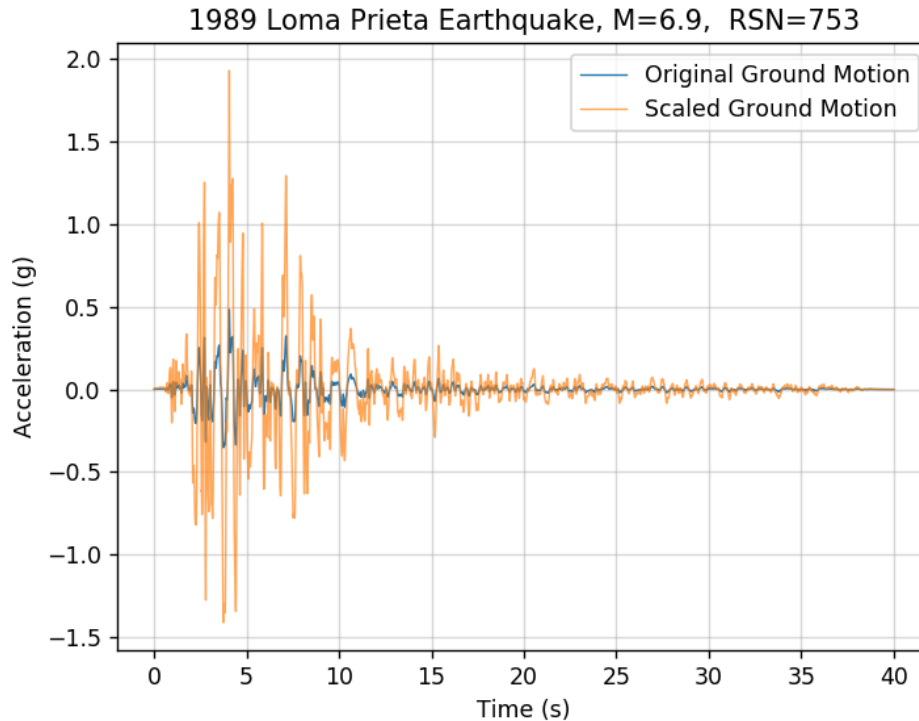


**Figure 3.36** Comparison of ground accelerations of unscaled and scaled ground motion with amplifying factor equaling to 4 from 1989 Loma Prieta Earthquake.

Figures 3.37, 3.38, and 3.39 present the histogram of earthquake magnitude, input *PGV* and input *PGA* of all 740 unscaled and scaled ground motions. Based on Figure 3.37, the unscaled ground motions chosen to be scaled have moderate to large magnitude and the selected magnitudes approximately range from 5 to 7.8. Figures 3.38 and 3.39 illustrate that most *PGV* values resulted from ground motions lie in the range where *PGV* is about from 4 cm/s to 15 cm/s and most *PGA* values are around 0.02 g to 0.6g. The entire *PGV* result ranges from 0.4 cm/s to 500 cm/s while *PGA* varies from 0.004g to 6g. Additionally, the scaled ground motions appreciably extend the levee input *PGV* and *PGA* range beyond the 100cm/s and 1 g, which aims to simulate the levee performance and better assess levee seismic fragility under relatively strong ground motions.

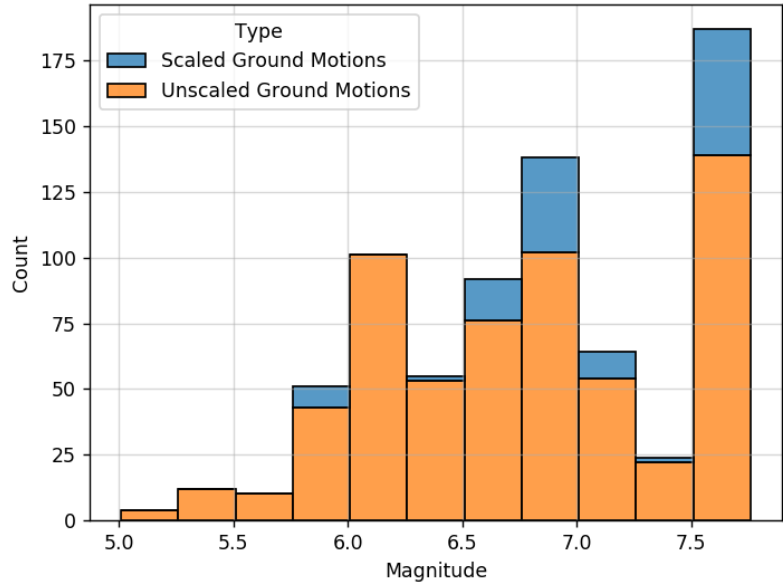


**Figure 3.37** Magnitude histogram plot of unscaled and scaled ground motions.

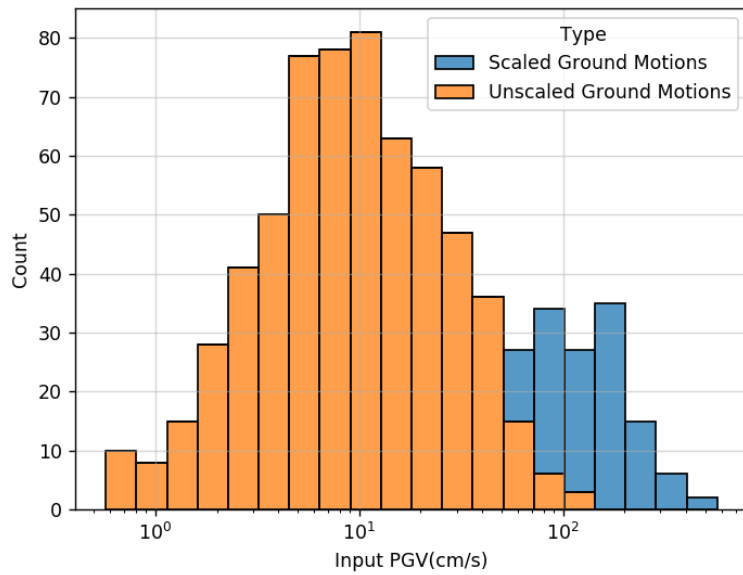


**Figure 3.38** Levee input PGV histogram plot resulted from unscaled and scaled ground motions.

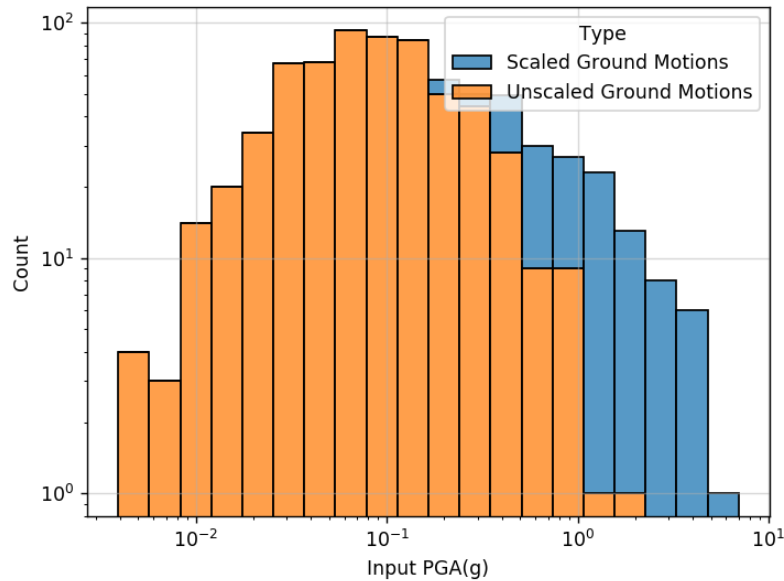


**Figure 3.39** Levee input PGA histogram plot resulted from unscaled and scaled ground motions.

### 3.3 Nonlinear Finite Element Modeling

Nonlinear dynamic finite element simulations have been utilized to develop fragility functions for levees shaken by earthquake ground motions. Tools utilized in the finite element modeling include the Open System for Earthquake Engineering Simulation (OpenSees) for performing the simulations, the pre-processor GiD (Coll et al., 2008) for creating the finite element meshes, the Scientific Toolkit for OpenSees (STKO) for visualization of select simulations, and the Stampede2 supercomputer at the Texas Advanced Computing Center for running parameter sweeps since the simulations are computationally demanding. This section thoroughly elucidates the simulation processes regarding pre-processing, analysis, and post-processing aspects using OpenSees as well as other advanced tools.

#### 3.3.1 Pre-processing

Seepage analysis is needed to determine phreatic surface within the levee. Moreover, a number of

input files must be prepared to define the levee models prior to conducting analyses in OpenSees. For example, nodes, elements, boundary conditions, loads, and material properties must be specified. This section discusses the pre-processing steps utilized to create the models.

#### *a) Seepage Analysis*

As shown in Figure 3.15 and 3.16, the river table is only about 2.3 m below the levee crest in the riverside area for both northern and southern levee, which is a high-water level and validates the Delta levees are indeed constantly impounding water. High water level in levee upstream might moist or even saturate more soil inside levee and alter soil engineering properties. For instance, it might saturate some loose and contractive sand layer within levee and render it more susceptible to liquefaction under rapid ground shakings. As a result, in this case, primary seepage analyses are required to identify the phreatic line within the levee and classify saturated and unsaturated soil layers.

The RS2 which is a 2-D finite element analysis software is used to perform 2-D steady-state seepage analyses for northern and southern levee. Levee upstream and downstream domains are extended to better exhibit seepage results, and the water level at the free field side is assumed to be located right at the bottom of drain ditch, which is about 1.5 m below the ground. Soil density and hydraulic conductivity can be borrowed directly from the previous tests and calculations. Figure 3.40 demonstrates seepage analysis result of northern levee. Small arrows indicate that most water flows through the middle sand layer with a relatively high permeability coefficient and a small part of water also flows through the peat layer. The red line is the calculated phreatic line within the levee, and it almost overlaps with the levee slope near the levee toe part, which is not realistic. This is attributed to the large hydraulic conductivity value uniformly assigned to the silty sand 1 layer which extends from the levee crest to the levee toe. However, in fact, this silty sand

layer on levee slope is supposed to have much smaller permeability coefficients. Therefore, to amend this, the phreatic line near the levee toe is slightly dragged down to make it smoothly connect to the bottom of ditch where the pressure head is zero. The black curve within the levee represents the manually modified phreatic line in the levee slope.

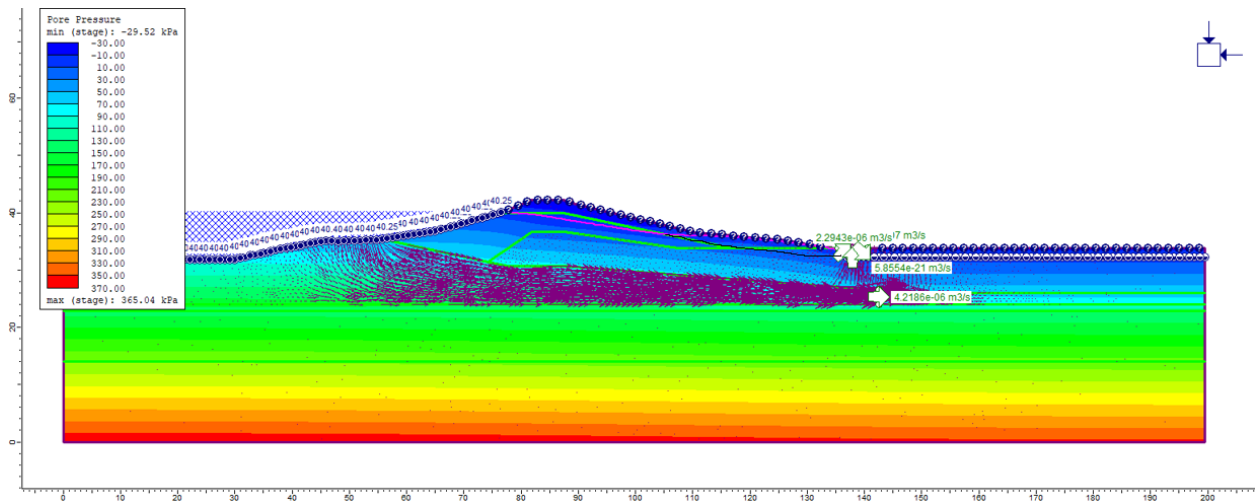


**Figure 3.40** Steady-state finite element seepage analysis of northern levee.

Similar seepage analyses are also performed for southern levee, and Figure 3.41 shows the steady-state seepage analysis result of the southern levee. The red curve represents the computed phreatic line, and most water flows through the peat layer in levee fill while a small part of water flows through the silty sand layer underneath the levee. Similar judgment call is made to modify a part of the unrealistic computed phreatic line near the levee slope in free filled side, and the orange curve represents the modified phreatic line.

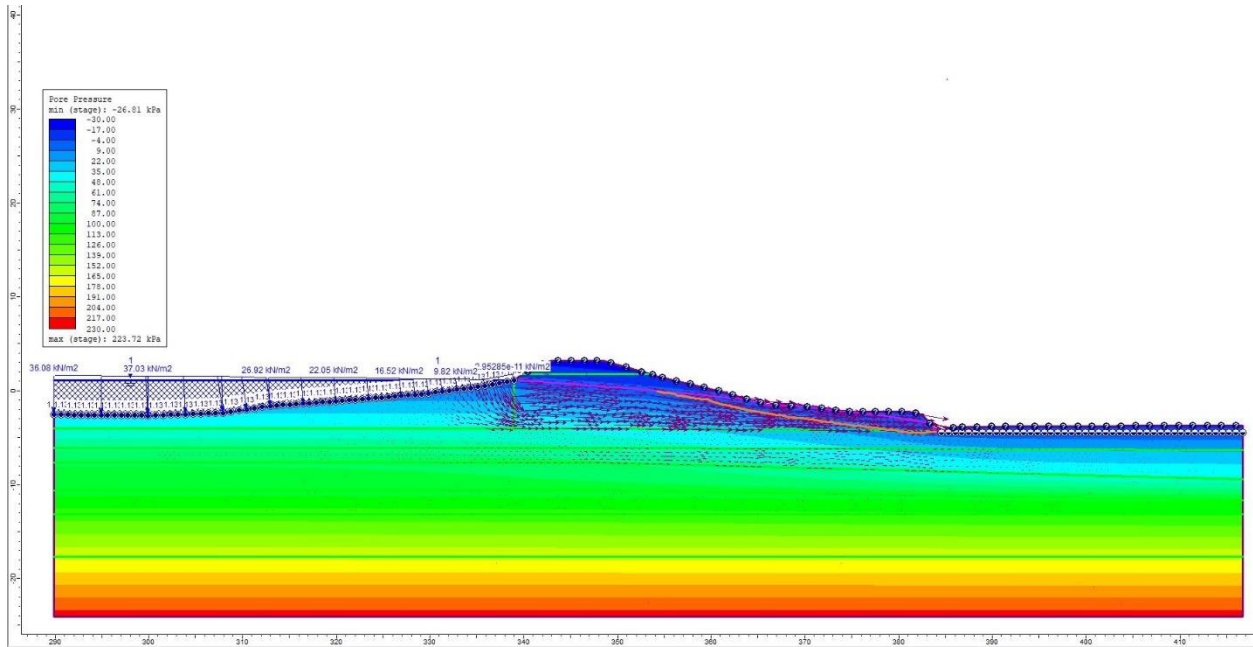


**Figure 3.41** Steady-state finite element seepage analysis of southern levee

***b) Nodes and elements***

GiD, which is an interactive graphical user interface used for the definition, preparation, and visualization of data related to a numerical simulation, is utilized to produce the mesh and retrieve coordination and numbering information of meshed nodes and element. With determined levee geometry, soil stratigraphy profile, and calculated phreatic line of southern and northern levee interpreted in the previous sections, mesh configurations of levees can be generated in GiD where the mesh size is set as 1.3 m. According to spatial Nyquist criterion, 2 elements per wavelength are required, so this mesh is capable of propagating earthquake waves with wavelengths longer than 2.6 m, which is adequate. Figure 3.42 and 3.43 show mesh configurations of northern and southern levee using GiD, respectively. Many different material zones were utilized to capture the influence of consolidation stress on undrained shear strength. For example, in Fig. 3.44 the peat in the levee fill is divided into two different regions due to the different consolidation stresses from

the overlying levee fill. Material properties are discussed later in this section.

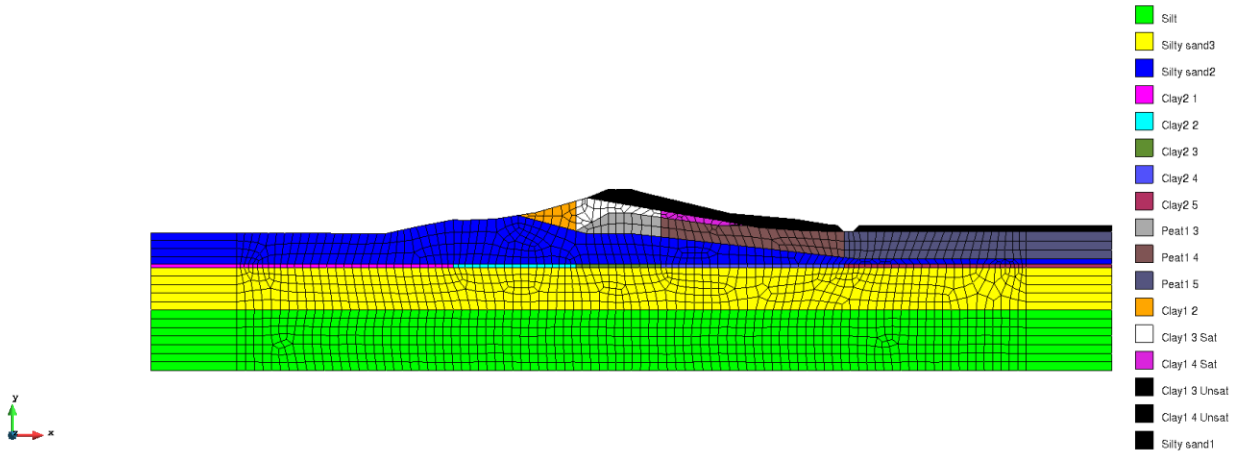


**Figure 3.42** Finite element mesh configuration of northern levee generated by GiD

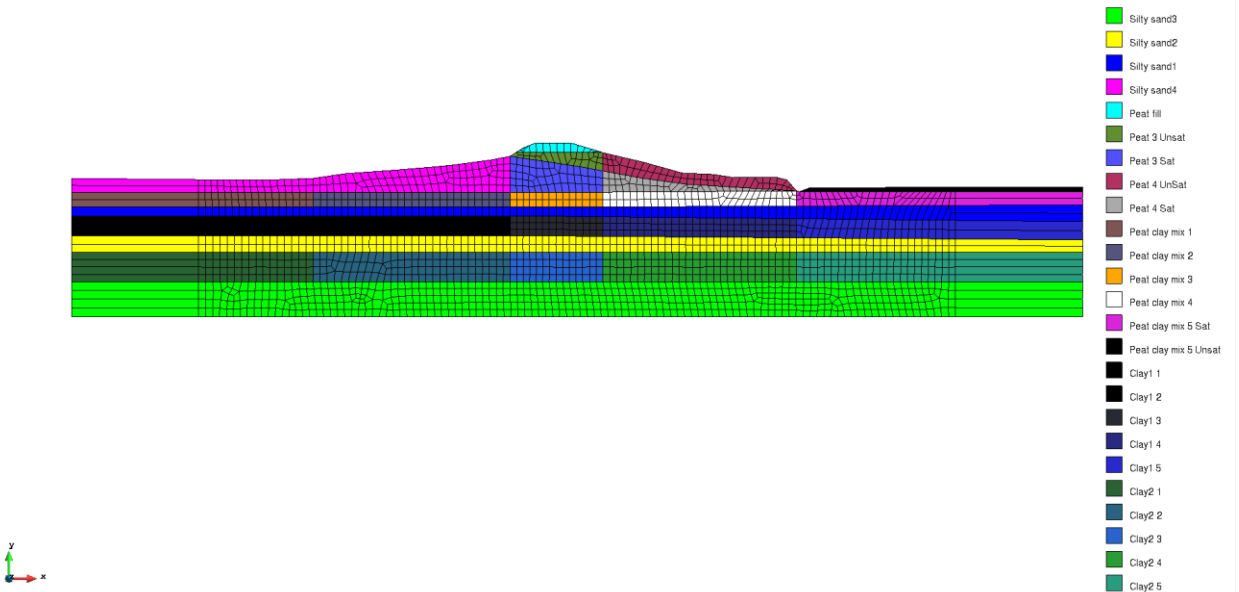


**Figure 3.43** Finite element mesh configuration of southern levee generated by GiD

The model utilizes the *SSPquadUP* element, which is a four-node quadrilateral element using physically stabilized single-point integration (SSP) and a mixed displacement-pressure (UP) formulation. Figure 3.44 shows the *SSPquadUP* element with a gauss point in the middle of the element.

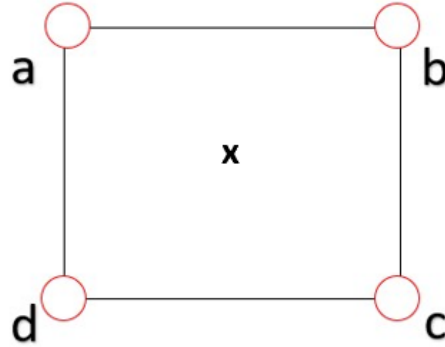


**Figure 3.44** 4-node quadrilateral element with SSP and UP.

McGann et al. (2012) demonstrated that SSP results in an element which does not exhibit volumetric and shear locking, which is a problem known to adversely affect the response of fully integrated quad elements (e.g., four-node quad elements with four Gauss points) when the tangent shear modulus becomes very small relative to the bulk modulus. The UP formulation is based on Biot’s theory of flow through a porous medium (Zienkiewicz and Shiomi 1984). There are three degrees of freedom in each node: DOF 1 and 2 represent solid displacement in horizontal and vertical directions while DOF 3 reflects fluid pressure. Additionally, the stabilizing parameter  $\alpha$  is specified by McGann et al. (2012) as:

$$\alpha = \frac{h^2}{4\rho c^2} \quad (3.9)$$

Where  $h$  represents the element size,  $\rho$  is the mass density of the solid phase, and  $c$  is the shear wave velocity in the solid phase.  $\alpha$  is set as  $6e^{-5} \text{ m}^2/\text{N}$  in this study.



### ***c) Boundary conditions***

Boundary conditions must be specified to constrain either displacements or forces along the external boundaries, as well as fluid pressures. Regarding displacement boundary conditions, a common approach for solving vertical wave propagation problems is to use harmonic boundary conditions in which the opposing vertical side boundaries are constrained to have the same displacement (i.e., using the OpenSees EqualDOF command). However, harmonic boundary conditions are inappropriate for the levee models because the soil profiles on the left and right sides of the model are different. For this reason, boundary conditions along the vertical left and right portions of the domain are connected to free-field soil columns with a large out-of-plane thickness. This approach has been used successfully by others (e.g., McGann and Arduino, 2014, 2015) to impose free-field conditions along the vertical boundaries of the model. The free-field columns are adequately far away from the main levee body region so that effects of wave reflections between main levee mesh and free-field columns on levee seismic vulnerability are negligible. Moreover, to ensure free-field columns are more massive than other regions, the thickness (out of plane direction) of elements in free-field columns are assigned as 10000 m while the element thickness in other areas is 1 m.

The ground motion records measured from earthquake stations are regarded as outcropping motions, and the domain below the model base is treated as an elastic half space. A Lysmer-Kuhlemeyer (1969) dashpot is utilized to model the elastic half space. A single *zeroLength* element is utilized to for dashpot and the dashpot constant is set equal to  $\rho V_S A$ , where  $\rho$  and  $V_S$  are the mass density and shear wave velocity of the half-space, respectively, and A is the total cross-sectional area of the model base (Fig. 3.45). The nodes along the model base are constrained to have the same horizontal displacement, and vertical displacement is fixed.

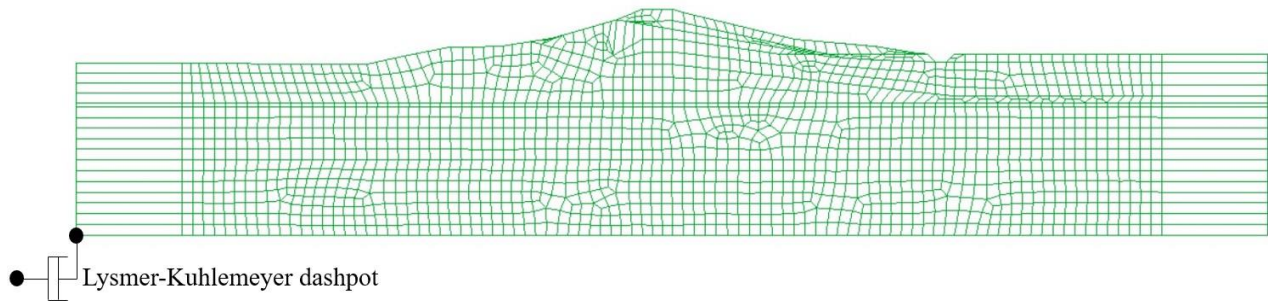


**Figure 3.45** Northern levee mesh configuration with Lysmer-Kuhlemeyer dashpot.

The total heights of northern and southern levee model are measured about 42 m and 27 m, and the peat thickness is approximately from 5 m to 10 m. Thus, according to Figure 3.20 showing shear wave velocity and peat thickness profiles in the Delta, it is reasonable to assign 350 m/s to the shear wave velocities of medium underlying both northern and southern levee models.

Regarding pore pressure boundaries, the position of the phreatic surface is determined using a steady state finite element analysis using the Slide program by Rocscience. Slide was utilized instead of OpenSees because it can provide steady state seepage solutions, whereas OpenSees uses a transient solve and is inefficient for steady state problems. The position of the phreatic surface is assumed to remain unchanged during and after earthquakes. Pore pressures of are set as 0 above the phreatic surface. The side vertical sides and base of the model are zero-flow boundaries. Displacement boundary conditions vary in gravity analysis, earthquake shaking analysis, and post-shaking reconsolidation analysis. Initially, the horizontal and vertical displacement are fixed for all base nodes and horizontal displacement of side nodes are fixed as well, so the models cannot move in gravity analysis stage. As for two free-field columns in each model, the side nodes on each column are given equal displacements in both horizontal and vertical direction. Boundary

conditions alterations in other analysis stages will be discussed and summarized in detail in the subsequent section.

#### ***d) External loads***

Vertical body forces representing gravity loading are imposed on the model based on the mass density specified for each element. The acceleration of gravity is set as  $9.81 \text{ m/s}^2$ . Pondered water on the channel side of the levee is represented by pressure distributions acting normal to the external boundaries. These pressures are assumed to be static. Hydrodynamic effects of water-levée interaction are ignored in these models. Normal stresses are required to prevent negative effective stresses from developing in the soil below the pondered water.

#### ***e) Material model***

Material model selection is a crucial aspect of numerical modeling, and OpenSees offers many different material models for soil. The guiding principle here is to select the most appropriate and updated material model for the dynamic response of soils in the levees. The ideal material model would be capable of capturing modulus reduction and damping behavior, liquefaction of sand-like soils, and cyclic softening of clay-like soils. In this study, the *PressureIndependentMultiYield* (PIMY) material model was used for clay-like soils and peat, while the *PressureDependMultiYield* (PDMY) material model was used for sand. These models were developed by Elgamal et al. (2003).

The PIMY material model simulates the response of material whose shear behavior does not rely on the confinement stress, and is therefore appropriate for cohesive soils modeled using an undrained shear strength (e.g., clay, silt, and peat). The PIMY utilizes nested von Mises type yield surfaces. The undrained shear strength is controlled by the size of the outer surface, which does not translate or rotate (i.e., no hardening). The smaller yield surfaces exhibit kinematic hardening

laws in which the surfaces translate, and the hardening parameters for each surface can be set to match a desired modulus reduction curve. The PIMY model follows Masing's rules, which are known to over damp soils at high strains (Kwok et al. 2008).

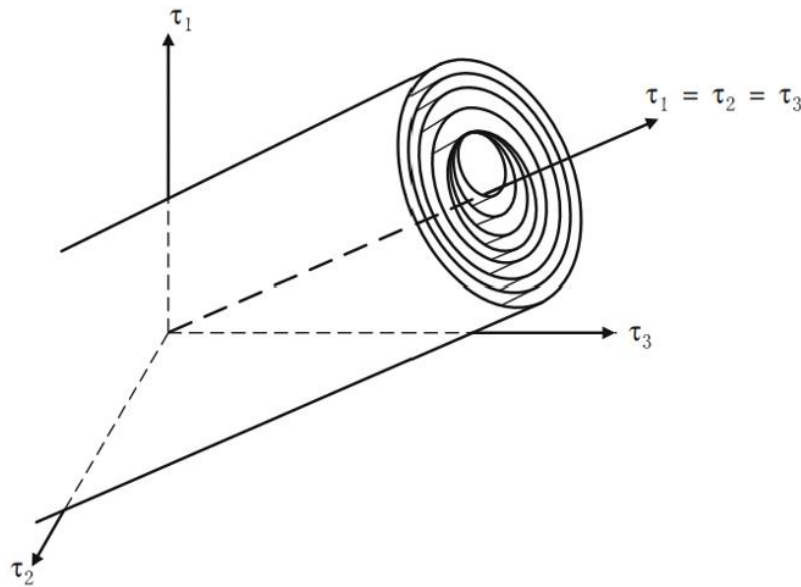


**Figure 3.46** von Mises yield surfaces in 3-D stress space (Gu et al., 2011)

As discussed in the previous site characterization section, Darendeli (2001) unified modulus reduction model combined with Yee et al. (2013) correction was used to calculate the modulus reduction curves for clay and silt while the Wang et al. (2022) model and Yee et al. (2013) correction were selected to determine modulus reduction curves of peat soil with shear strain ranging from 0.0001% to 10%.

Figure 3.47 presents the modulus reduction curves of peat soil based on the Wang et al. (2022)

model. As demonstrated in Figure 3.26, the modulus reduction curves shift to the right as the overburden pressure and organic content increase, meaning soil is more linear. Organic content of peat is needed to implement Wang et al (2022) model, and this can be roughly estimated according to boring logs and Deverel et al (2016). The organic contents of the selected northern and southern levee cross-section are approximately estimated as 41% and 28%.

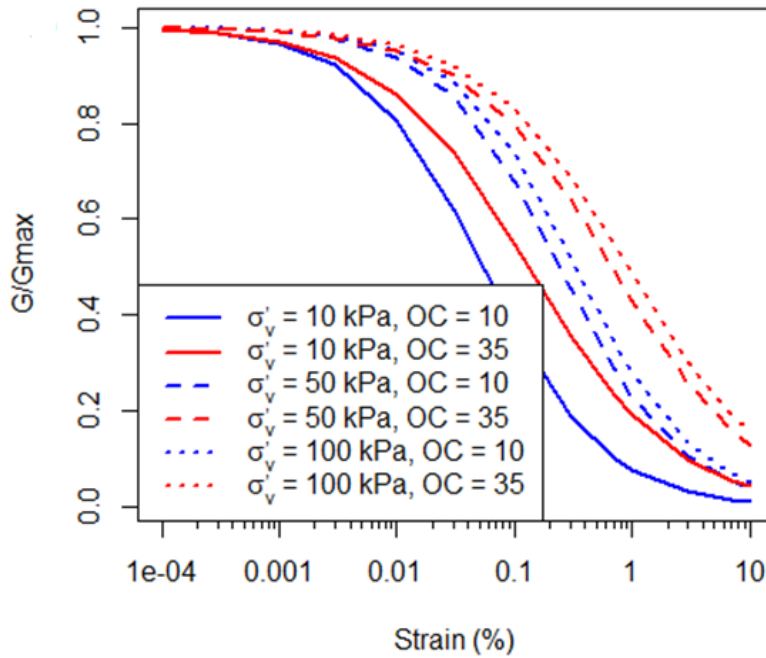


**Figure 3.47** Modulus reduction curves of organic peat based on Wang et al. (2022)

In OpenSees, the inputs of maximum shear modulus, bulk modulus, and modulus reduction curve are the calibrated values under a reference mean confining pressure and this reference pressure is generally set as 1 atm (101.325 kPa). The expression for shear modulus for the PIMY and PDMY material models can be written as,

$$G = G_r \left( \frac{p'}{p_r} \right)^d \quad (3.10)$$

where  $G$  is the measured or estimated shear modulus based on site characterization,  $G_r$  is the reference shear modulus,  $p'$  is the in-situ mean effective stress,  $p'_r$  is the reference pressure and it is generally equal to 101 kPa, and  $d$  is the pressure dependent coefficient. For PIMY, I adopt  $d = 0$ , while for PDMY I adopt  $d = 0.5$ .

Shear strength of soil is required to be specified when applying Yee et al correction (2013) in determining modulus reduction curves. Although the PIMY model is pressure independent, the assigned value of undrained shear strength should consider effective consolidation stress and overconsolidation ratio. Because consolidation stresses vary within the levee cross-section, the levee was divided into different regions within which the undrained shear strength was modeled as being constant. As indicated in Figure 3.42 and 3.43, levee cross-sections are roughly divided into five regions: river-side free field, river-side slope, levee body, island-side slope, and island side free field, which are denoted as zone 1, 2, 3, 4 and 5, respectively. The soil materials are named using a numbering convention that corresponds to soil type and to zone. For example, 'Clay 1\_2' represents clay 1 in zone 2. Undrained shear strengths in different zones are calculated according to in-situ effective stress and shear strength ratios computed in the site characterization portion. Table 3.13 and 3.14 summarize calculated undrained shear strengths and other modeling information of fine-grained soils within different zones of northern and southern levees.

**Table 3.13** Undrained shear strength and modeling information of fine-grained soil in northern levee.

<b>Zone</b>	<b>Soil</b>	<b>Undrained shear strength (kPa)</b>	<b>Material Model</b>	<b>Pressure Dependent Coefficient, d</b>	<b>Modulus reduction and damping model</b>
1	Clay 1_1	47.1	PIMY	0	Darendeli (2001) + Yee et al. (2013)
2	Clay 1_2	8.6	PIMY	0	Darendeli (2001) + Yee et al. (2013)
	Clay 2_2	67.3	PIMY	0	Darendeli (2001) + Yee et al. (2013)
3	Clay 1_3	35.7	PIMY	0	Darendeli (2001) + Yee et al. (2013)
	Peat 1_3	33.5	PIMY	0	Darendeli (2001) + Yee et al. (2013)
	Clay 2_3	86.6	PIMY	0	Darendeli (2001) + Yee et al. (2013)
4	Clay 1_4	29.4	PIMY	0	Darendeli (2001) + Yee et al. (2013)
	Peat 1_4	25.2	PIMY	0	Darendeli (2001) + Yee et al. (2013)
	Clay 2_4	56	PIMY	0	Darendeli (2001) + Yee et al. (2013)
5	Peat 1_5	17.6	PIMY	0	Darendeli (2001) + Yee et al. (2013)
	Clay 2_5	30.5	PIMY	0	Darendeli (2001) + Yee et al. (2013)

**Table 3.14** Undrained shear strength and modeling information of fine-grained soil in southern levee.

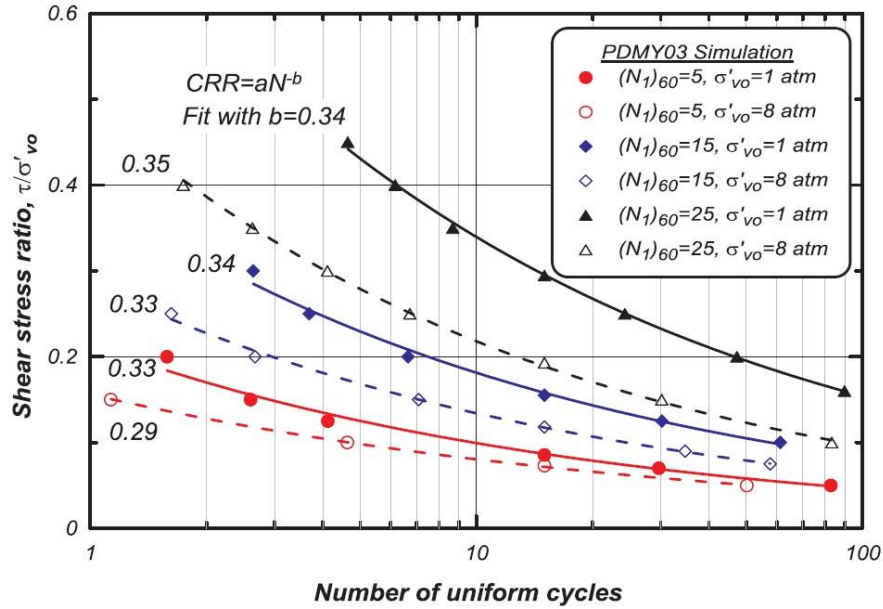
<b>Zone</b>	<b>Soil</b>	<b>Undrained shear strength (kPa)</b>	<b>Material Model</b>	<b>Pressure Dependent Coefficient, d</b>	<b>Modulus reduction and damping model</b>
1	Peat clay mix 1_1	15.5	PIMY	0	Darendeli (2001) + Yee et al. (2013)
	Clay 1_1	38	PIMY	0	Darendeli (2001) + Yee et al. (2013)
	Clay 2_1	79.8	PIMY	0	Darendeli (2001) + Yee et al. (2013)
2	Peat clay mix 1_2	24.5	PIMY	0	Darendeli (2001) + Yee et al. (2013)
	Clay 1_2	47.1	PIMY	0	Darendeli (2001) + Yee et al. (2013)
	Clay 2_2	88.8	PIMY	0	Darendeli (2001) + Yee et al. (2013)
3	Peat 1_3	34.2	PIMY	0	Darendeli (2001) + Yee et al. (2013)
	Peat clay mix 1_3	33.1	PIMY	0	Darendeli (2001) + Yee et al. (2013)
	Clay 1_3	55.6	PIMY	0	Darendeli (2001) + Yee et al. (2013)
	Clay 2_3	97.4	PIMY	0	Darendeli (2001) + Yee et al. (2013)
4	Peat 1_4	17.3	PIMY	0	Darendeli (2001) + Yee et al. (2013)
	Peat clay mix 1_4	20.8	PIMY	0	Darendeli (2001) + Yee et al. (2013)
	Clay 1_4	44.8	PIMY	0	Darendeli (2001) + Yee et al. (2013)
	Clay 2_4	85.6	PIMY	0	Darendeli (2001) + Yee et al. (2013)
5	Peat clay mix 1_5	11.3	PIMY	0	Darendeli (2001) + Yee et al. (2013)
	Clay 1_5	40.6	PIMY	0	Darendeli (2001) + Yee et al. (2013)
	Clay 2_5	78.2	PIMY	0	Darendeli (2001) + Yee et al. (2013)



Based on Table 3.13 and 3.14, fine-grained soils in Zone 3 have largest undrained shear strengths compared to soils in other zones while shear strengths of soils are smallest in Zone 1 and 5 due to smaller overburden pressure.

PressureDependMulti03 (PDMY03) material model (Khosravifar et al. 2018) is used to simulate sandy material and it is the most updated version of PDMY. There are two previous versions of pressure-dependent multi-yield surface constitutive models called PDMY and PDMY02. The PDMY material model was originally developed to capture cyclic mobility and post-liquefaction accumulation of shear strains and generally for simulating the essential response characteristics of pressure sensitive soils subjected to general loading conditions. However, the model was not formulated to capture the effects of overburden stress and static shear stress on liquefaction behavior. PDMY02 is formulated to better capture the  $K_\sigma$  effect, and PDMY03 captures both  $K_\sigma$  and  $K_\alpha$  effects. This model has been improved with new flow rules to better capture contraction and dilation in sands.

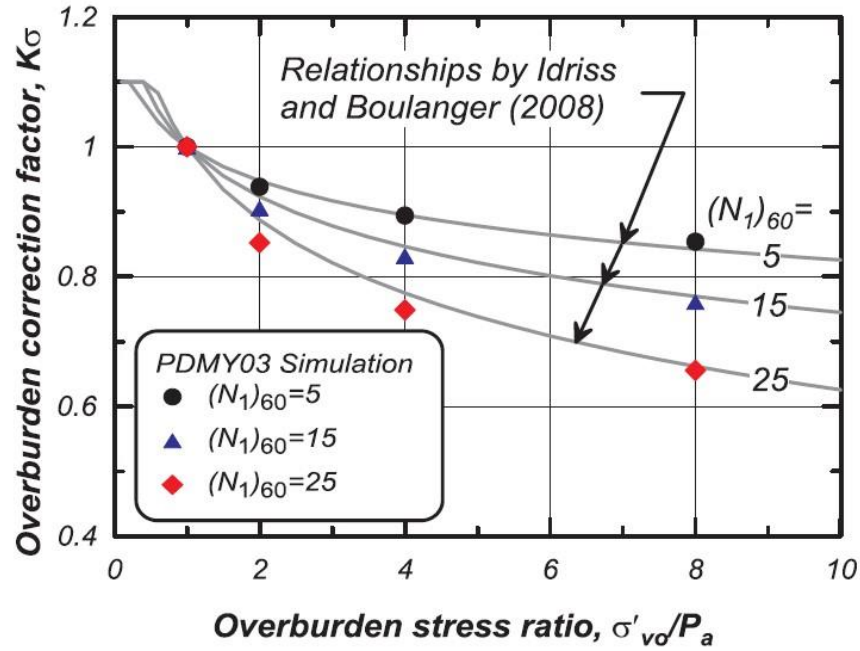
Figure 3.48 shows cyclic stress ratio to trigger liquefaction versus the number of loading cycles based on DSS simulation of PDMY03 model with various  $(N_1)_{60}$  values and confining pressures. Each curve is fitted with a power function and the power value (b value) ranges from 0.29 to 0.35, which results in a reasonable agreement of b values with experimental results implemented by Yoshimi et al (1984).



**Figure 3.48** Cyclic shear stress ratio versus number of uniform loading cycles derived from direct simple shear (DSS) PDMY03 model simulations (Khosravifar et al.2018).

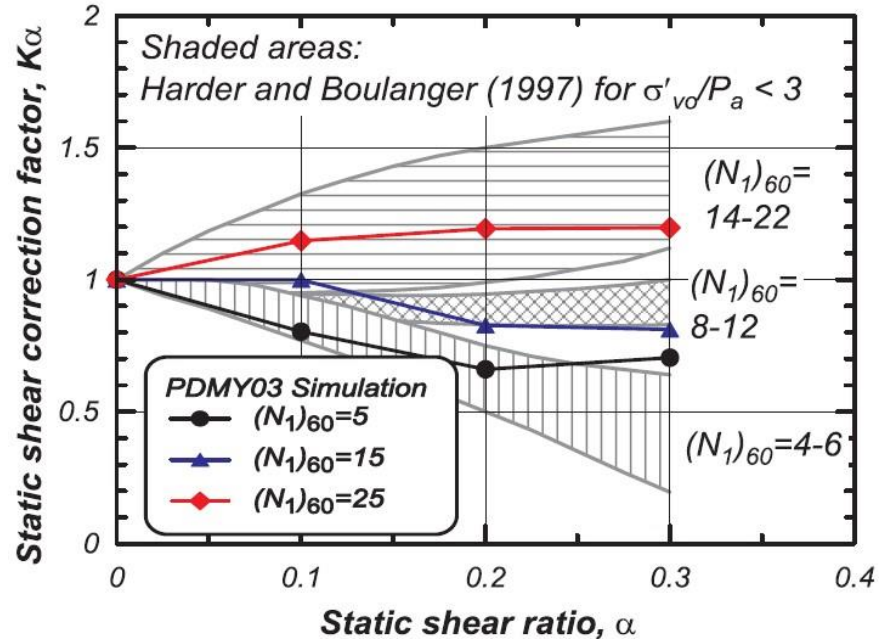
Figure 3.49 shows  $K_\sigma$  from simulation results for effective overburden stresses ranging from 1 to 8 atm for sands with  $(N_1)_{60}$  values of 5, 15, and 25, and is defined as  $K_\sigma = CRR_{\sigma'_v} / CRR_{\sigma'_v=1 \text{ atm}}$ .

As indicated in the figure, the model response aligns well with the recommended values across a wide range of effective overburden stresses.



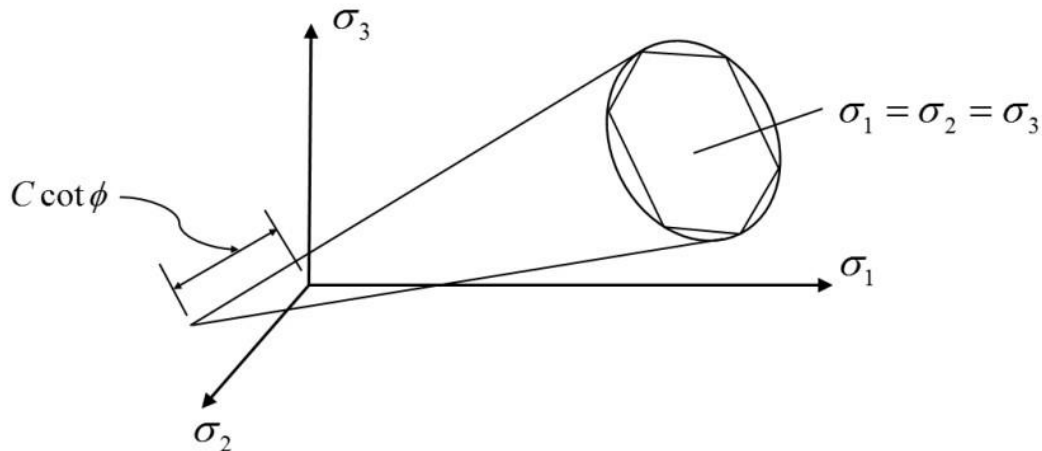
**Figure 3.49**  $K_\sigma$  relationships derived from model simulations compared to relationships by Idriss and Boulanger (2008) (Khosracifar et al.2018).

Figure 3.50 shows the  $K_\alpha$  factors derived from simulations compared to experimental results from Harder and Boulanger (1997), and  $K_\alpha$  is used to characterize the influence of the static shear stress on liquefaction resistance and is defined as  $K_\alpha = CRR_\alpha / CRR_{\alpha=0}$  based on Seed and Idriss (1982). In general, an increase in the static shear stress ratios  $\alpha$  contributes to a decrease in a decrease for loose sands and an increase for dense sand.



**Figure 3.50** Experimental trends for different  $(N_1)_{60}$  values and  $\sigma'_v < 3$  atm from Harder and Boulanger (1997) and model generated static shear stress correction factors ( $K_\alpha$ ) for  $\sigma'_{vc} = 1$  atm.

The yield surfaces for PDMY03 model are of the Drucker-Prager type. Figure 3.51 shows the comparison of Drucker-Prager and Mohr-Coulomb yield surfaces. Mohr-Coulomb is arguably the most common yielding criterion for soils and is formulated based solely on the major and minor principal stresses, while the intermediate principal stress is ignored. As a result, the yield surface is represented by a hexagonal cone in a 3-D stress space shown in Figure 3.51. The sharp corners of the Mohr-Coulomb model complicate return mapping algorithms, and can lead to numerical instabilities. The Drucker Prager yield surface is a smooth circular cone in a 3-D space presented in Figure 3.31. The Drucker Prager model (Drucker and Prager, 1952) does not have sharp corners, and therefore does not suffer the same numerical instabilities.



**Figure 3.51** Drucker-Prager and Mohr-Coulomb yield surfaces. (Chaitanya, 2017)

As discussed in the previous levee characterization section, unified modulus reduction model proposed by Menq (2003) and Yee et al (2013) correction procedure is implemented to determine the modulus reduction curves of sandy materials (PDMY03 materials). Equation 3.10 is implemented to calculate reference maximum shear modulus and modulus reduction curves which are used as inputs in OpenSees, and the pressure dependent coefficient  $d$  is generally set as 0.5.

After creating the mesh in GiD and setting up boundary conditions and material models, a script is used to translate the mesh into tool command language (TCL) files in the format required by OpenSees.

### 3.3.2 Finite element analysis

This section explains the analysis stages imposed on the levees and illustrates example model responses for each stage. The models are computationally demanding and were run in parallel using high performance computing (HPC) on Stampede 2 at the Texas Advanced Computing Center (TACC) through the DesignSafe portal. The approach adopted for the HPC runs is also

discussed.

Six loading stages are imposed on the models during the simulations, as summarized in Table 3.15.

Boundary conditions vary in these different stages based on the needs for each stage with respect to displacements and seepage conditions.

**Table 3.15** Boundary conditions of 6 analysis stages.

Stage number	Stage name	Model base boundary conditions			Model sides boundary conditions		
		Horizontal	Vertical	Seepage	Horizontal	Vertical	Seepage
1	Gravity (elastic)	Fixed	Fixed	Zero flow	Fixed	Free	Zero flow
2	Gravity (plastic)	Fixed	Fixed	Zero flow	Fixed	Free	Zero flow
3	Seepage (uniform k)	Fixed	Fixed	Zero flow	Fixed	Free	Zero flow
4	Seepage (nonuniform k)	Fixed	Fixed	Zero flow	Fixed	Free	Zero flow
5	Shaking	Lysmer-Kuhlemeyer	Fixed	Zero flow	Harmonic for free-field columns	Free	Zero flow
6	Post-shaking reconsolidation	Lysmer-Kuhlemeyer	Fixed	Zero flow	Harmonic for free-field columns	Free	Zero flow

Analysis commands must be specified in OpenSees before running simulations. Same analysis commands are utilized in gravity and seepage analysis, and Table 3.16 demonstrates a set of analysis commands used in the stage 1, 2, 3, and 4.

**Table 3.16** Analysis commands used in stage 1, 2, 3, and 4.

<b>Analysis command type</b>	<b>Analysis command selection</b>
<i>Constraints</i>	Transformation
<i>Test</i>	NormDispIncr 1e <sup>-3</sup> 30 1
<i>Algorithm</i>	Newton
<i>Numberer</i>	RCM
<i>System</i>	ProfileSPD
<i>Integrator</i>	Newmark 0.6 0.3
<i>Analysis</i>	Transient

The *constraints* command is used to determine how the constraint equations are enforced in the analysis, and the transformation method is chosen here. The *test* command specifies the convergence test object which determines if convergence can be achieved at the end of the iteration step, and the norm displacement increment test is utilized in this study, and it uses the norm of the left-hand side vector solution vector of the matrix equation to judge if convergence has been reached. Generally, the vector solution vector of the matrix equation is equal to the displacement increments that are to be applied to the model. 1e<sup>-3</sup> is the convergence tolerance and 30 is the max number of iterations to check before returning failure condition. The Newton-Raphson algorithm is used to solve the nonlinear residual equation, which is the most widely used and robust method in solving non-linear equations. RCM numberer where nodes are assigned degree-of-freedom using Reverse Cuthill-McKee algorithm (Cuthill and McKee, 1969) is chosen to determine how degree-of-freedom are numbered. ProfileSPD specifies the linear system of equations and linear solver to store and solve the system of equations in the analysis. As the name implies, the profileSPD is basically used for symmetric positive definite matrix systems. The Newmark integrator, which is generally applied in transient analysis, is used to determine the meaning of the terms in the system of equations. Two ad hoc numerical parameters  $\gamma$  and  $\beta$ , which control both the stability of the method and the amount of numerical damping introduced into the system, need

to be specified in the Newmark method. Artificial damping is introduced when  $\gamma > 0.5$  and damping is not formed when  $\gamma = 0.5$ . For gravity and seepage analysis stages, the models are undamped systems which are unconditionally stable if  $\gamma \geq 0.5$  and  $\beta \geq 0.25(\gamma + 0.5)^2$ . In order to introduce damping to models and ensure stability of the method,  $\gamma$  and  $\beta$  are take as 0.6 and 0.3 in gravity and seepage analysis. Finally, the Transient analysis is used for gravity and seepage stages since the analysis time step is constant.

#### ***a) Gravity Analysis Stages***

Gravity analysis is chosen as the first step of analysis, and levee settlement is basically induced by elastic settlement and soil consolidation because of levee weights. In the initial gravity stage, soil elements are elastic, which is achieved by setting the material stage to be 0 in OpenSees using *updateMaterialStage* command. Cohesionless materials may struggle to converge if they are modeled plastically during gravity analysis, and it is therefore more stable to model them as elastic to initialize effective stresses, and subsequently update the material to plastic after this elastic initialization. Because a UP formulation is utilized, excess pore pressures develop during gravity analysis, and a large number of time steps may be required for the model to consolidate, particularly when layered soil profiles with different hydraulic conductivities are present in the model. To ensure the hydrostatic conditions occur quickly after the application of gravity in the model, the permeability for all soil elements is assigned as 1m/s for stage 1 and subsequently updated after a steady state condition has been reached.

In stage 2, and the material stage is updated to be 1 such that the material switches from elastic to plastic. Hydraulic conductivity is kept equal to 1m/s for all material models during stage 2. Models



sometimes struggle to converge to converge in this phase, so the time steps for analysis usually should start with some smaller time steps (e.g.,  $5e^{-3}$  s) aiming to secure convergence. At the end of gravity analysis stage, *nodeDisp* command is utilized to record induced displacement and settlement of levee crest nodes and base nodes to define a reference condition against which shaking-induced deformations are measured.

### ***b) Seepage Analysis Stages***

In stage 3, seepage boundary conditions are imposed on the model to create a steady-state condition. Hydraulic conductivities remain 1 m/s for this stage. After a steady state seepage condition is reached, hydraulic conductivities are updated to their desired values (Table 3.1 and 3.6) using the *updateParameter* command in OpenSees. The purpose of this is to reach a new steady-state seepage condition consistent with the non-uniform hydraulic conductivities prior to shaking.

### ***c) Shaking and Post-shaking Reconsolidation Analysis Stages***

In stage 5, shaking is imposed on the bottom of the model. This study imposed suites of earthquake ground motions on each model corresponding to a horizontal component of the ground motion. Vertical ground motion was not imposed, and since the models are 2D rather than 3D, only a single horizontal component was imposed in each simulation. As presented in Table 3.10, the horizontal constraints of model base nodes required during gravity analysis are removed to accommodate the translation of the model based due to shaking. The vertical constraints of model base nodes remain fixed. Both ends of the Lysmer-Kuhlemeyer dashpot were fixed in stages 1-4, and the fixity is removed in stage 5 and an earthquake ground motion imposed on the free-end of the dashpot. The base nodes are constrained to have the same horizontal displacement. An issue for these simulations is that the levees are persistently pushed to the right by the impounded water on the river side. After removing the horizontal displacement constraints of base nodes during shaking

and post-shaking stages, the levee model slowly translates in the direction of imposed force. To remove this potential issue, horizontal reaction forces at the end of Stage 4 are recorded, and imposed on the base nodes. Nonlinearity in the model during shaking may influence the forces required to stabilize the model, so permanent base displacement is subtracted from the model in post-processing.

The *nodeDisp* command is used in OpenSees to record displacements and settlements of crest and base nodes during each individual earthquake event. In addition, *recorder Node* command is also used to record velocity and acceleration of crest nodes and the base nodes. The entire model response is not recorded because (1) file input/output operations slow the simulations, and (2) the resulting files would contain many data quantities that are not utilized in developing the fragility functions.

Small-strain material damping is not included in the material model formulation, so it is introduced using a two-point Rayleigh damping model formulation. Two parameters  $a_0$  and  $a_1$  need to be specified so as to determine Rayleigh damping, and they can be written as below,

$$a_0 = \frac{2\xi\omega_l\omega_h}{\omega_l+\omega_h} \quad (3.11)$$

$$a_1 = \frac{2\xi}{\omega_l+\omega_h} \quad (3.12)$$

where  $\xi$  is the target damping ratio and it equals to 0.05 in this study,  $\omega_l$  and  $\omega_h$  represent low and high angular frequency associated with the target damping ratio and they are equal to  $0.4\pi$  and  $40\pi$  radians/s in this study.

Rayleigh damping then can be expressed by these two parameters and frequency as shown in Eq. 3.13.

$$\xi_R = \frac{a_0}{2\omega} + \frac{a_1\omega}{2} \quad (3.13)$$

Table 3.17 shows analysis commands used in the shaking analysis, and they are very similar to the commands implemented in the previous analysis stages except *Analysis* and *Integrator* parameters.  $\gamma$  and  $\beta$  are set as 0.5 and 0.25 to avoid additional damping in the Newmark method. *VariableTransient* which allows the time step to be divided when the convergence is not achieved is utilized instead in the shaking analysis stage.

**Table 3.17** Analysis commands used in stage 5.

<b>Analysis Command Type</b>	<b>Analysis Command Selection</b>
<i>Constraints</i>	Transformation
<i>Test</i>	NormDispIncr 1e-3 30 1
<i>Algorithm</i>	Newton
<i>Numberer</i>	RCM
<i>System</i>	ProfileSPD
<i>Integrator</i>	Newmark 0.5 0.25
<i>Analysis</i>	VariableTransient

After shaking is complete, excess pore pressures have developed in the material model. These excess pore pressures are allowed to dissipate in Stage 6, resulting in additional settlements. Reconsolidation strains are known to be under-predicted by material models that do not include a damage formulation because reconsolidation strains are assumed to be elastic. I therefore consider the post-cyclic volumetric strains to be approximate, but nevertheless important to model.

#### ***d) 1-D Ground Response Analysis Model without Liquefaction Effects***

For the purpose of developing fragility functions a ground motion intensity measure is required and must be consistent with PSHA utilized in the risk assessment. A number of different intensity measures were tested, including (1) PGA and PGV input to the base of the model, (2) PGA and PGV at the levee crest, and (3) PGA and PGV that would exist at the top of a level ground profile

in the absence of liquefaction. Of these options, (2) was eliminated because it includes 2D topographic effects and is therefore inconsistent with PSHA models. I discuss the suitability of options (1) and (3) in the next chapter, and focus my attention here on describing how the 1D numerical simulations were performed for option (3).

To model the surface motion that would exist for free-field conditions in the absence of liquefaction, a vertical column is extracted through levee crest as shown in Fig. 3.52. The 2-D mesh is irregular and not vertical, so a vertical 1-D mesh with the same soil properties was created. To eliminate the liquefaction effects in this model, the bulk modulus of the pore fluid is set equal to that of air, which prevents development of excess pore pressures. Similar gravity, shaking, and post-shaking analyses are implemented for this 1-D soil column model as for the 2-D model, and *recorder Node* is used to record the velocities and accelerations of the base node and surface node in OpenSees. All the ground motions imposed on the 2-D model were also imposed on the base of the 1-D model. Harmonic boundary conditions were utilized to constrain the vertical sides of the 1-D mesh.

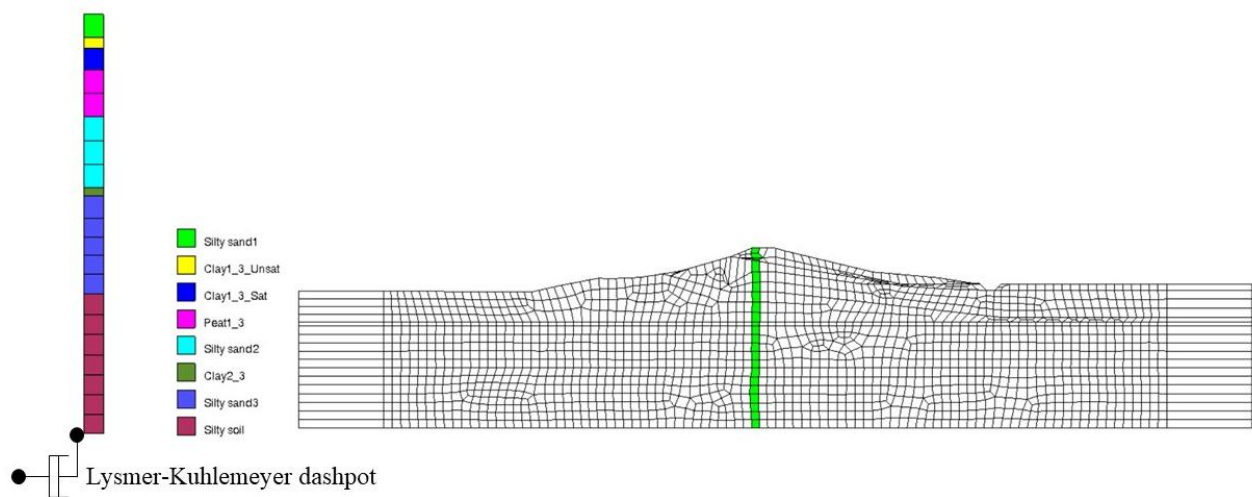


**Figure 3.52** 1-D ground response analysis model mesh extracted from the original northern levee model mesh configuration.

*e) Perform parallel finite element simulations using HPC in TACC through DesignSafe portal*

Each dynamic simulation requires hours to complete, with more nonlinear model responses taking longer. The models were therefore run in parallel using HPC by creating a loop command that sends one ground motion at a time to a core until all 616 ground motions are completed. Parallel calculation in HPC systems enables distributing the workload across multiple processors/nodes. It harnesses the collective power of multiple processors and resources, allowing time-consuming simulations to be completed much more quickly. DesignSafe is utilized as the platform to conduct parallel dynamic finite element simulations using OpenSeesMP. DesignSafe (Rathje et al. 2017) is a comprehensive cyberinfrastructure providing cloud-based tools to manage, analyze, understand, and publish critical data for research to understand the impacts of natural hazards. TACC provides the computational and storage infrastructure that supports DesignSafe's research platform, and DesignSafe relies on TACC's high performance computing resources and expertise to enable researchers in the field of natural hazards engineering to perform complex simulations, process data, and conduct computational research. Figure 3.53 shows the main page of tools and applications module on the DesignSafe portal, and OpenSees and OpenSees-STKO are in the 'Simulation' folder. OpenSees-STKO adds pre and postprocessor capabilities to OpenSees and yields a database file (with a '.mpco' extension) that stores all model response quantities. OpenSees-STKO was utilized for a select number of ground motions for the purpose of illustrating model responses. OpenSeesMP was used for the bulk of the simulations presented here, with much more limited information stored for each simulation to facilitate fragility function development.

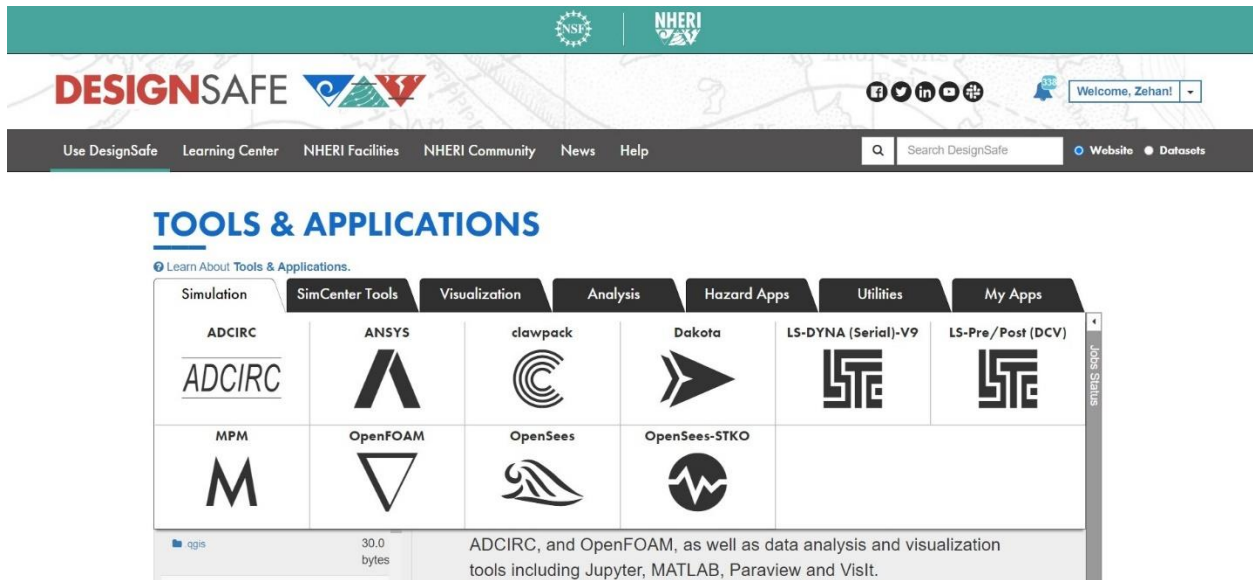


**Figure 3.53** Simulation software in ‘Tools and Applications’ module on the DesignSafe portal.

Figure 3.54 shows the input pre-settings for performing parallel simulation using OpenSeesMP via DesignSafe portal. Firstly, a version of OpenSees and associated HPC should be specified so OpenSeesMP (STAMPEDE 2) - V3.2 is chosen as shown in Figure 3.39. Secondly, input files including files directory and the executable file are supposed to be assigned. Finally, the parameters associated with job running ought to be determined. The maximum job running time is 48 hours and node count as well as processor per node can be assigned according to specific total workload. Essentially, the computation efficiency is optimal when assigned total number processors are greater or equal to the required total number of simulation tasks. In Fig. 3.54, a single node with 48 processors is specified, which is the default number. For the simulations presented here, 11 nodes and 616 processors were requested such that each simulation is performed on its own processor.

Select a version of OpenSees from the dropdown:  
 OpenSeesMP (Stampede2) - v3.2

### RUN OPENSEESMP (STAMPEDE2) - V3.2 ver. 3.2.0

OpenSeesMP is an OpenSees interpreter intended for high performance computers for performing finite element simulations with parametric studies and very large models on parallel machines. OpenSeesMP requires understanding of parallel processing and the capabilities to write parallel scripts. OpenSeesMP runs on up to 12 KNL Nodes on Stampede2, with 64 cores per Node.

#### Inputs

**Input Directory**  
 Select agave://designsafe.storage.default/zhliu23/A\_Result\_NL\_0113\_2023 ✓

The directory containing your OpenSees input files as well as your OpenSees TCL script. You can drag the link for the directory from the Data Browser on the left, or click the 'Select Input' button and then select the directory. To try out sample data copy and paste 'agave://designsafe.storage.community/app\_examples/opensees/FreefieldAnalysisEffective/' above.

**TCL Script**  
 main1.tcl

The filename only of the OpenSees TCL script to execute. This file should reside in the Input Directory specified. To try this out copy and paste in 'freeFieldEffective.tcl'.

#### Job details

**Maximum job runtime**  
 48:00:00

In HH:MM:SS format. The maximum time you expect this job to run for. After this amount of time your job will be killed by the job scheduler. Shorter run times result in shorter queue wait times. Maximum possible time is 48:00:00 (hrs:min:sec).

**Job name**  
 opensees-mp-3.2.0u14\_2023-10-19T23:46:08

A recognizable name for this job.

**Job output archive location (optional)**  
 Select zhliu23/archive/jobs/\${YYYY-MM-DD}/\${JOB\_NAME}-\${JOB\_ID}

Specify a location where the job output should be archived. By default, job output will be archived at: zhliu23/archive/jobs/\${YYYY-MM-DD}/\${JOB\_NAME}-\${JOB\_ID}.

**Node Count**  
 1

Number of requested process nodes for the job. Default number of nodes is 1.

**Processors Per Node**  
 48

Number of processors (cores) per node for the job. e.g. A selection of 16 processors per node along with 4 nodes will result in 4 nodes with 16 processors each, 64 processors total. Default number of processors per node is 48.

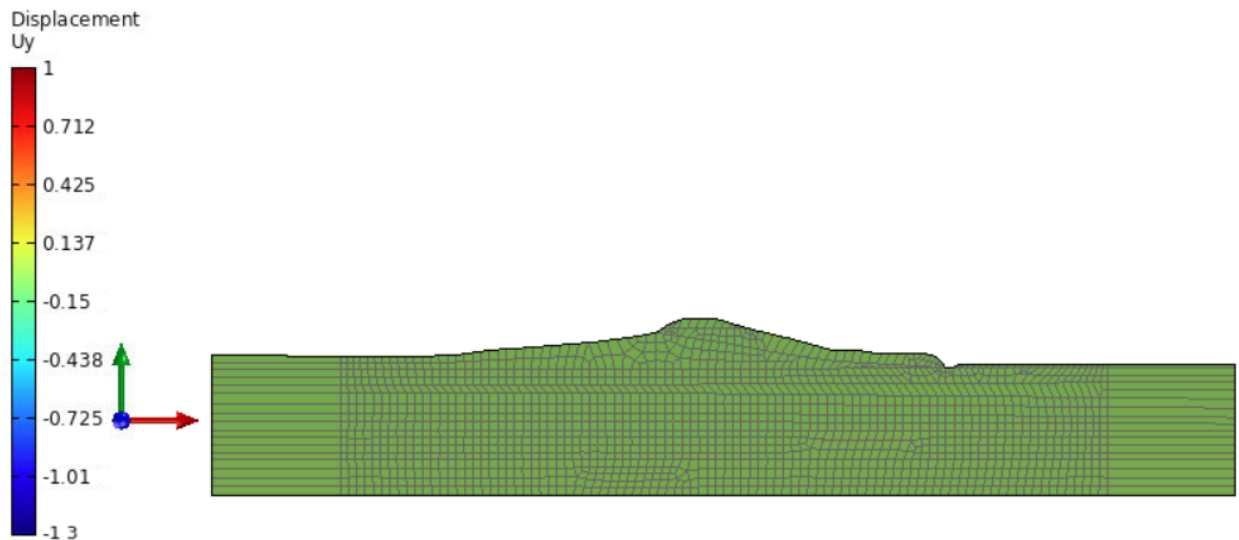
**Figure 3.54** Input settings for running parallel simulations using OpenSeesMP on Stampede 2 on DesignSafe.

### 3.3.3 Post-processing

This section presents procedures utilized to post-process simulations performed in OpenSees-STKO (Petracca et al., 2017) as well as those performed in OpenSeesMP through the DesignSafe portal.

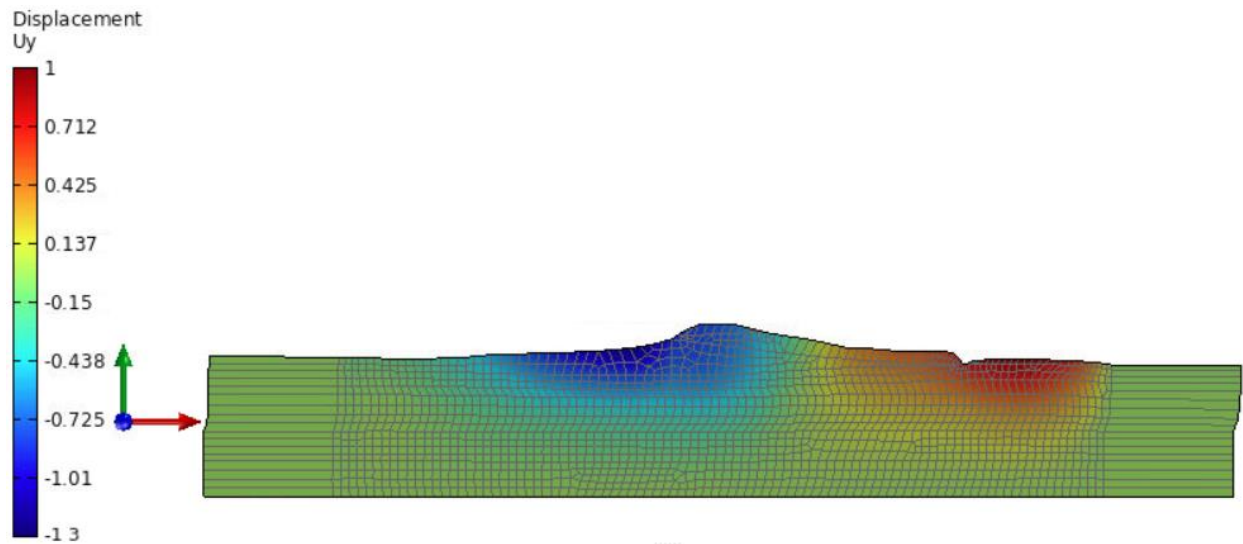
***a) Results from OpenSeesMP-STKO***

STKO was utilized for a handful of simulations to illustrate key aspects of the model responses, and to check that the simulations were configured correctly before proceeding with the OpenSeesMP batch runs. Figure 3.55 shows the vertical displacement contours for different analysis stages when applying the measured ground motion (RSN=4875) from 2007 Chuetsu-Oki earthquake as reflected in Fig. 3.34, and the plots are presented on STKO with deformation scale equal to 1. The levee crest settled 0.043 m, but it is difficult to read from Figure 3.55 (a) due to color setting in the legend bar in the plot. For shaking phase, the largest (more than 1m) settlement occurs on the upstream levee slope area due to the liquefaction of sand within the levee slope. Moreover, large upward vertical displacement occurs on the ditch and free field on the island side due to distortion of levee as a result of levee deformations. Permanent vertical deformations are formed in the shaking phase and these deformations remain almost unchanged after post-shaking reconsolidation phase as shown in Figure 3.55 (c).

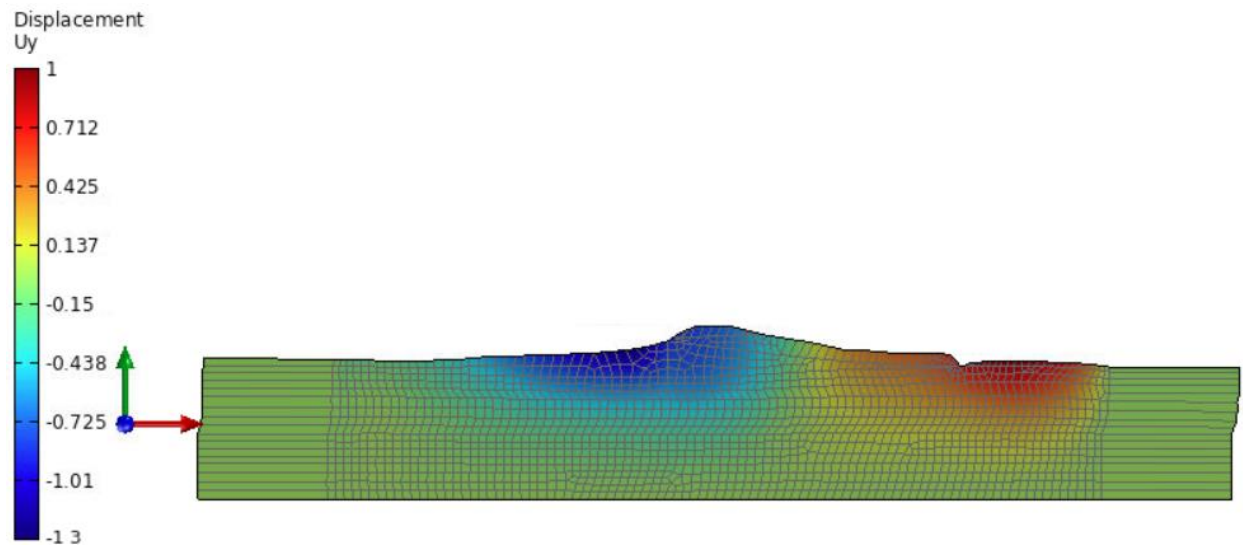


(a)





(b)



(c)

**Figure 3.55** Vertical displacement contour plots of southern levee at the end of (a) gravity analysis; (b) ground shaking; (c) post-shaking reconsolidation phases under the ground motion (RSN =4875) from 2007 Chuetsu-Oki earthquake

Figure 3.56 shows pore water pressure contours for the southern levee in various phases under the same ground motion. Note that although the legend shows angular velocity, in fact, it represents the pore water pressure with units of kPa because OpenSees assigns the title “angular velocity” to

the third degree of freedom for 2D elements, and pore pressures are stored in the 3rd degree of freedom for the UP elements. Initially, the pore pressures correspond to a steady state condition with higher pore pressures beneath the channel and lower on the land-side of the. During shaking the pore water increases to around 450 kPa. After the post-shaking phase, pore water pressure gradually decreases, and its distribution is more even and uniform within the levee model. Nonetheless, the average pore water pressure within the model is still comparatively higher than pore pressure in the initial gravity analysis phase. The reason for this is that the analysis time I assigned for stage 6 is 100,000 seconds (about 11 days), which is not adequate for complete dissipation of pore pressure within fine-grained soils.

As a result, I did not complete the post-shaking reconsolidation analysis for levees, and this would underpredict the final levee crest settlements. Moreover, even if I correctly perform the post-shaking reconsolidation analysis, the crest settlement results will not be accurate, because no constitutive model in OpenSees can account for the reconsolidation consolidation settlements in a good manner so far.

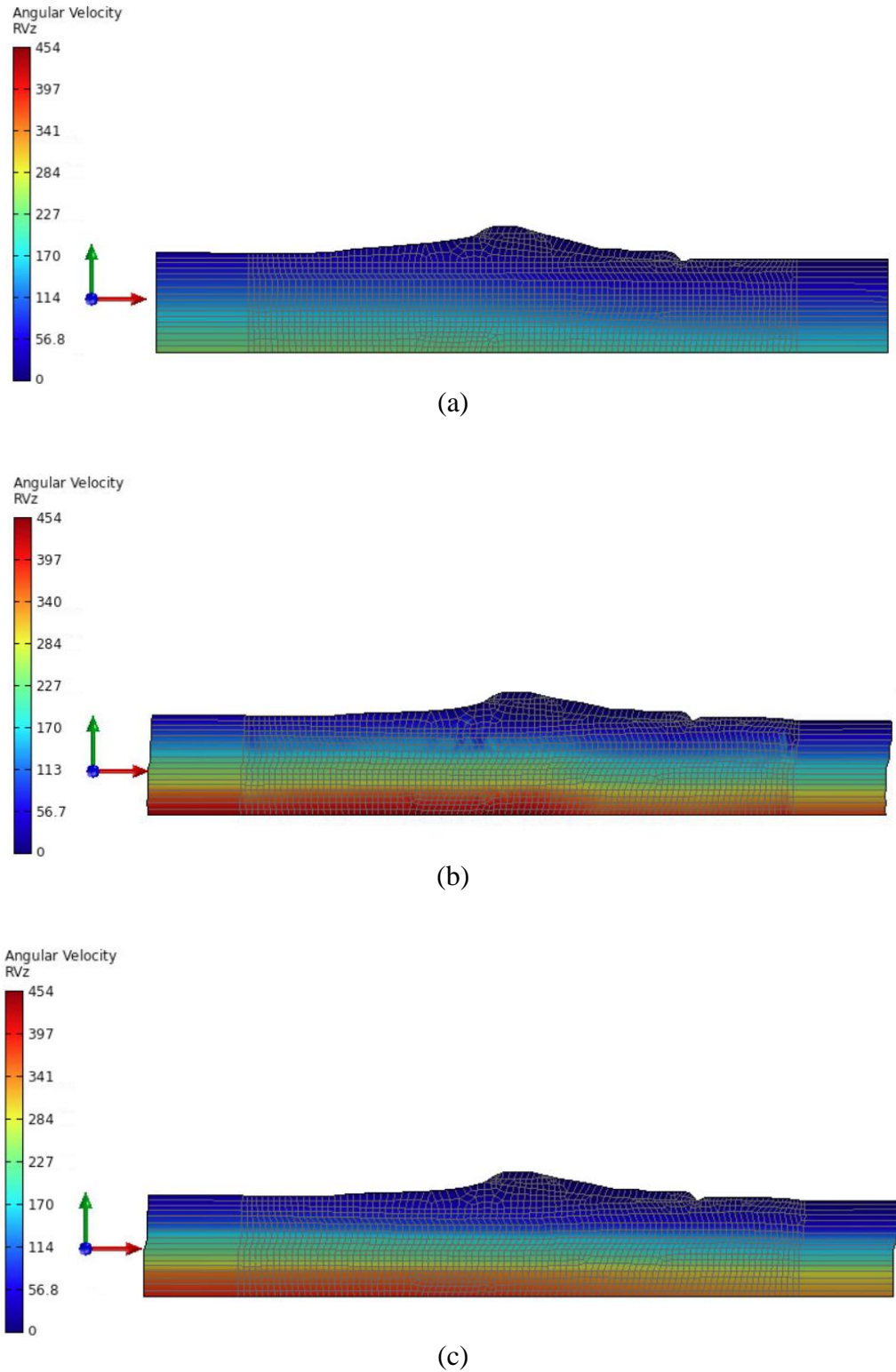
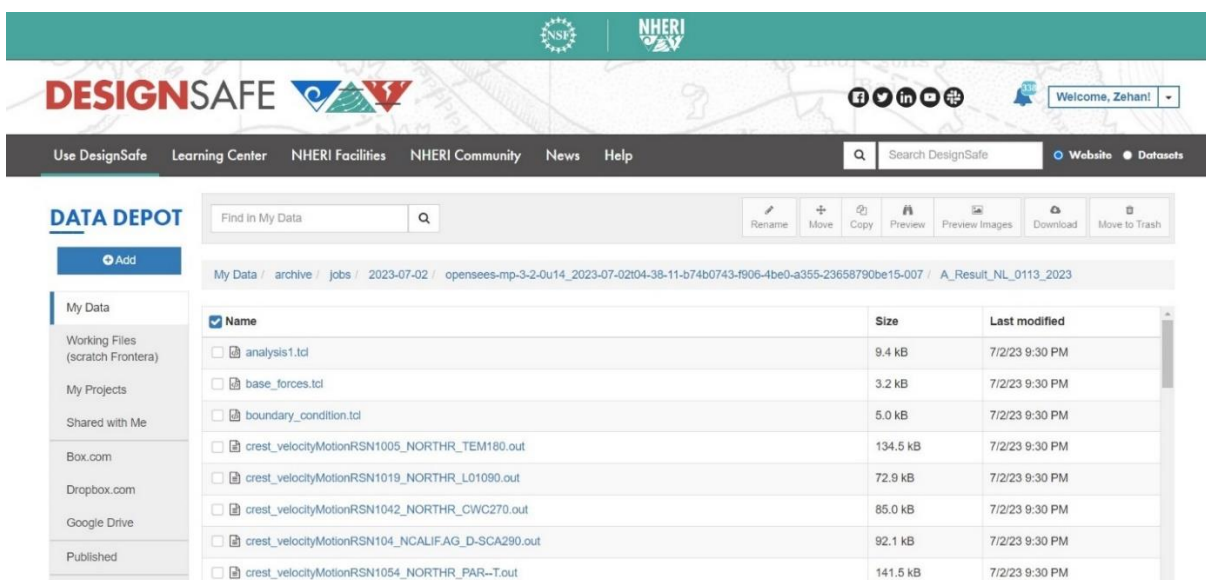


**Figure 3.56** Pore water pressure distribution plots of southern levee at the end of (a) gravity analysis; (b) ground shaking; (c) post-shaking reconsolidation phases under the ground motion (RSN =4875) from 2007 Chuetsu-Oki earthquake.

## b) Results from OpenSeesMP

There is a job status bar on the right side of the main page on DesignSafe portal showing the submitted job running status, and the simulations results can be accessed as shown in Figure 3.57 if clicking ‘More Information’ button of the task in the job status bar. Figure 3.57 shows an example of the directory containing completed simulation results of the northern levee model.

In this study, the displacements (both horizontal and vertical direction) of nodes on the levee crest versus time at a variety of analysis phases are recorded and the average levee crest settlement is computed. Moreover, ground motions time series at the model base such as ground acceleration and velocity over time are also recorded during shaking, and therefore the input *PGA* and *PGV* which are potential levee fragility predictors can be obtained accordingly. Looping over this directory and processing simulations results from a variety of selected ground motions provide levee crest settlements conditioned on various ground motion intensity measures that are utilized in subsequent development of levee fragility functions.



The screenshot displays the DesignSafe portal interface. At the top, there is a navigation bar with the DesignSafe logo and various utility links. Below this, a search bar and a 'Welcome, Zehan!' message are visible. The main content area is titled 'DATA DEPOT' and shows a directory structure for a specific job. The directory path is: My Data / archive / jobs / 2023-07-02 / opensees-mp-3-2-0u14\_2023-07-02t04-38-11-b74b0743-f906-4be0-a355-23658790be15-007 / A\_Result\_NL\_0113\_2023. A table lists the files in this directory, including their names, sizes, and last modified dates.

Name	Size	Last modified
analysis1.tcl	9.4 kB	7/2/23 9:30 PM
base_forces.tcl	3.2 kB	7/2/23 9:30 PM
boundary_condition.tcl	5.0 kB	7/2/23 9:30 PM
crest_velocityMotionRSN1005_NORTHR_TEM180.out	134.5 kB	7/2/23 9:30 PM
crest_velocityMotionRSN1019_NORTHR_L01090.out	72.9 kB	7/2/23 9:30 PM
crest_velocityMotionRSN1042_NORTHR_CWC270.out	85.0 kB	7/2/23 9:30 PM
crest_velocityMotionRSN104_NCALIFAG_D-SCA290.out	92.1 kB	7/2/23 9:30 PM
crest_velocityMotionRSN1054_NORTHR_PAR--T.out	141.5 kB	7/2/23 9:30 PM

**Figure 3.57** An example of the directory containing completed simulation results of the northern levee model on DesignSafe portal.

### 3.4 Seismic Fragility Function Development

This section presents seismic fragility functions for Bacon Island levees developed from the finite element simulation results presented in the previous section for both southern and northern levee models. Two intensity measures, *PGA* and *PGV*, are evaluated at two different locations: surface ground motions for 1-D ground response analysis in the absence of liquefaction, and the input motions imposed on the base of the models. Earthquake magnitude is also investigated as a secondary predictor variable. After a variety of comparisons, the *PGV* input at the base of the model is the best feature. This section also explores different fragility function models for fitting the numerical simulations results.

#### 3.4.1 Literature Review

A fragility function quantifies a structure's probability of collapse, or exceeding a limit state of interest, as a function of some ground intensity measures. A lognormal cumulative distribution functions is often used to a fragility function:

$$P (C|IM = x) = \Phi \left[ \frac{\ln(\frac{x}{\theta})}{\beta} \right] \quad (3.14)$$

where  $P (C|IM = x)$  is the probability that a ground motion equaling to  $x$  will cause the structure collapse or fail,  $\Phi$  is the standard normal cumulative distribution function;  $\theta$  is the median of fragility function and  $\beta$  is the standard deviation of  $\ln (IM)$ . Fragility functions obtained from structural analysis results are increasingly popular in structural assessment procedures (e.g., Applied Technology Council 2012; Federal Emergency Management Agency 2009). A variety of approaches are utilized to develop fragility functions, such as field observations, static and dynamic structural analyses, or judgement. (Kennedy and Ravindra 1984; Kim and Shinozuka

2004; Calvi et al. 2006; Villaverde 2007; Porter et al. 2007; Shafei et al. 2011; Baker 2015)

Delta Risk Management Strategy (DRMS) project developed levee fragility functions by means of utilizing Monte Carlo simulations of levees categorized by a set of vulnerability classes using factors that differentiate the performance of the levees (Salah-Mars et al. 2008). Rosidi (2007) performed 2-D finite element analysis for levee cross-sections to develop levee seismic fragility curves to facilitate levee risk assessment.

Kwak et al. (2016a) developed *PGA* and *PGV* based fragility functions using field performance data of flood control levees that are founded on sands and gravels with low fines content along the Shinano River in Japan under two shallow crustal earthquakes. Kwak et al. (2016a) categorized various damage levels based on levee crest subsidence as indicated in Table 3.18.

**Table 3.18** Damage level classification (Kwak et al. 2016a).

Damage Level	Subsidence (cm)	Crack (cm)	depth	Crack width (cm)	Description
0	0	0		0	No damage reported
1	0-10	0-100		0-10	Slight damage, small cracks
2	10- 30	100-200		10-50	Moderate damage, cracks, or small lateral spreading
3	30- 100	200-300		50-100	Severe damage, lateral spreading
4	>100	>300		>100	Levee collapse

In addition, Tsai (2018) empirically developed *PGA*-based fragility functions using field performance of levees with organic peat and inorganic soil foundations along the Kushiro and Tokachi Rivers, and she found that levees resting on peat were more fragile than levees resting on inorganic soils. She did not develop *PGV*-based fragility functions because a suitable GMM for *PGV* for subduction events in Japan was not available at the time of her work.

Similar to damage level categorization of levee proposed by Kwak et al. (2016a), I define four damage levels for Bacon Island levees with crest settlement larger than 1 cm, 10 cm, 30 cm, and 100 cm as damage state 0, 1, 2, and 3, respectively. Table 3.19 shows the levee damage classification used in this study.

**Table 3.19** Damage level classification of Bacon Island levees.

Damage Level	Settlement, $S_t$ (cm)
1	$S_t \geq 1$
2	$S_t \geq 10$
3	$S_t \geq 30$
4	$S_t \geq 100$

Yang (2021) utilized a linear model to fit  $\ln(PGV)$  at the surface of a 1-D soil column without liquefaction vs. levee crest settlement obtained from finite element simulations for McDonald Island levees. He obtained slope and intercept coefficients of the regressed line from statistical inference using ordinary least squares regression. This fitted linear model was then used to calculate the probability of exceeding a certain levee crest settlement given  $PGV$ . The linear model is shown as follows,

$$\ln(S) = m_1 \cdot \ln(PGV) + m_0 + \varepsilon \quad (3.15)$$

where  $S$  is the levee crest settlement,  $m_1$  and  $m_0$  are coefficients, and  $\varepsilon$  is the error term.

One of the critical assumptions in linear regression is normality of residual, which means the error term should follow a normal distribution. If this assumption is valid, then the prediction error of a follows a normal distribution with mean 0 and standard deviation  $\sigma$ . The standardized expression  $\frac{\log(S_t) - m_1 \cdot \log(PGV_i) - m_0}{\sigma}$  follows a standard normal distribution. Therefore, the probability of exceeding levee settlement  $S_t$  conditioned on a  $PGV_i$  can be written as,

$$P(S > S_t) = 1 - \Phi\left(\frac{\ln(S_t) - m_1 \cdot \ln(PGV_i) - m_0}{\sigma}\right) \quad (3.16)$$

where  $\Phi$  is the cumulative density function of a standard normal distribution.

Eq. 3.16 and simulation result are used to derive fragility functions for Bacon Island levees in this study. Fragility functions are plotted for  $S_t = 1\text{cm}, 10, 30\text{cm},$  and  $100\text{ cm}$ , which spans a wide range of damage levels.

### 3.4.2 Ground Motion Selection for Levee Crest Settlement

In this section, various types of ground motion intensity measures are studied as a primary predictor of levee crest settlement, and earthquake magnitude is also studied as a secondary predictor. Considered ground motion types involve *PGA* and *PGV*, and ground motion sources consist of scaled and unscaled (measured from earthquake station) as well as input ground motions and ground motions from the surface of 1-D ground response analysis of a vertical soil column.

#### *a) Ground motions sources*

Yang (2021) utilized the *PGV* at the surface of 1-D ground response simulations of a vertical soil column through the levee crest without liquefaction effects as the predictor variable for McDonald Island fragility functions. His motivation was that the input ground motion intensity measure should represent the site conditions, including nonlinear site response effects. However, recent work by Bullock et al. (2019) demonstrated that the rock outcrop motion is a better predictor of settlement of structures supported by shallow foundations resting on liquefiable layers. A primary reason for their finding is that nonlinear site response causes ground motions to saturate, such that increasing the input motion no longer increases the surface motion beyond a threshold. Nevertheless, energy entering the base of a model is anticipated to cause more damage, even if it doesn't translate to increased surface motion. For this reason, I conducted an assessment of



whether the input outcrop motion is a better predictor of levee settlement than the surface motion in the absence of liquefaction.

Figure 3.58 shows the southern and northern levee settlement versus surface  $PGV$  from 1-D vertical soil column models for the 616 unscaled ground motions, and for an additional 62 scaled motions. The unscaled motions had relatively few occurrences with high  $PGV$  values, which might cause unreliable assessment of levee seismic capacity under strong ground motions. Therefore, the 62 strongest motions were scaled by a factor of 4 and input to the numerical simulations.

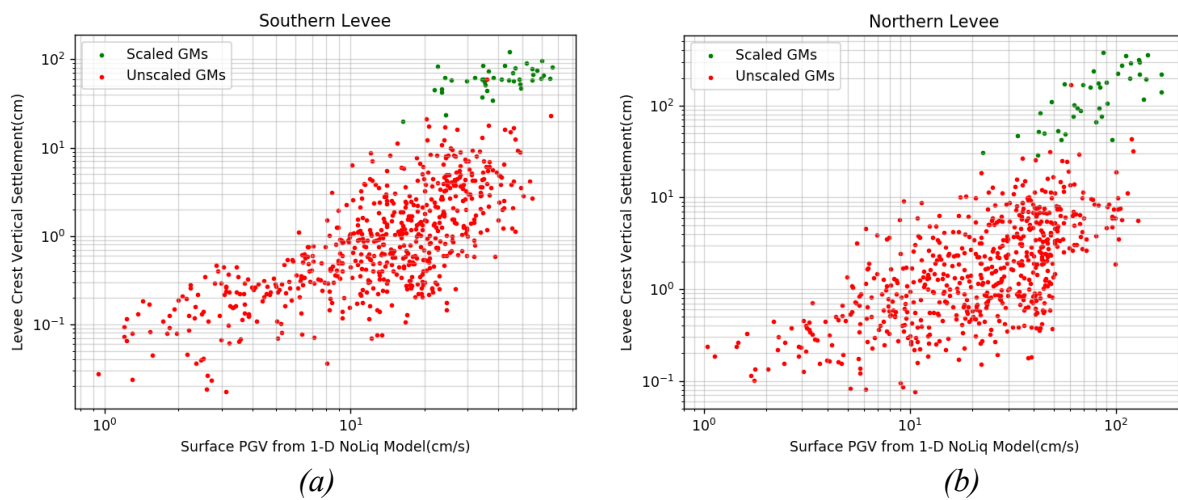


**Figure 3.58** Levee crest settlement versus surface  $PGV$  from 1-D model without liquefaction under unscaled and scaled ground motions for (a) southern levee; (b) northern levee.

The data in Figure 3.59 exhibits significant scatter, and shows a saturation effect in which the points curve upward as  $PGV$  increases. Furthermore, the green dots do not exhibit a corresponding 4sx increase in terms of surface  $PGV$  of the 1-D vertical soil column as crest settlements increase, especially for southern levee model. In addition, data points from unscaled grounds motions

indicated as red dots are considerably scattered and demonstrate a non-linear trend between levee settlement and surface  $PGV$ . Therefore, an alternative settlement predictor --- the original input  $PGV$  is considered as the input variable in levee seismic fragility function.

Figure 3.59 shows the simulation results of levee crest settlement versus input  $PGV$  for southern and northern levees. The data points are comparatively less scattered and more linear, indicating that the input outcrop  $PGV$  is indeed a superior intensity measure for predicting levee settlement. Furthermore, the saturation effect is not apparent in these data since the input motion is used instead of the surface motion. Data points obtained from scaled ground motions of northern levee are slightly non-linear, and heteroskedastic with the dispersion increasing as  $PGV$  increases, which is attributed to the likely occurrence of liquefaction under fairly strong ground motions in northern levee which consists of considerably more sandy soil layers compared to southern levee.

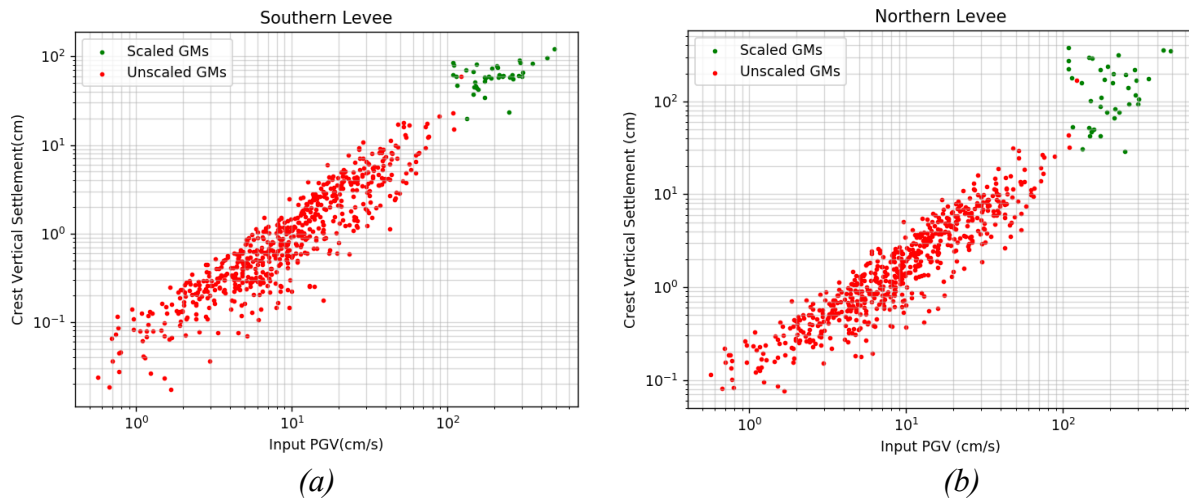


**Figure 3.59** Levee crest settlement versus input  $PGV$  under unscaled and one group of scaled ground motions for (a) southern levee; (b) northern levee.

To further explore the influence of nonlinear site response, Figure 3.60 plots the input  $PGV$  vs.

surface  $PGV$  from the 1-D site response simulations. For both the southern and northern levees, the surface motion saturates at large input  $PGV$ . The trend is more pronounced for the southern levee, which is the result of the wave propagation through the very soft peat soils, which are more prevalent for the southern levee.

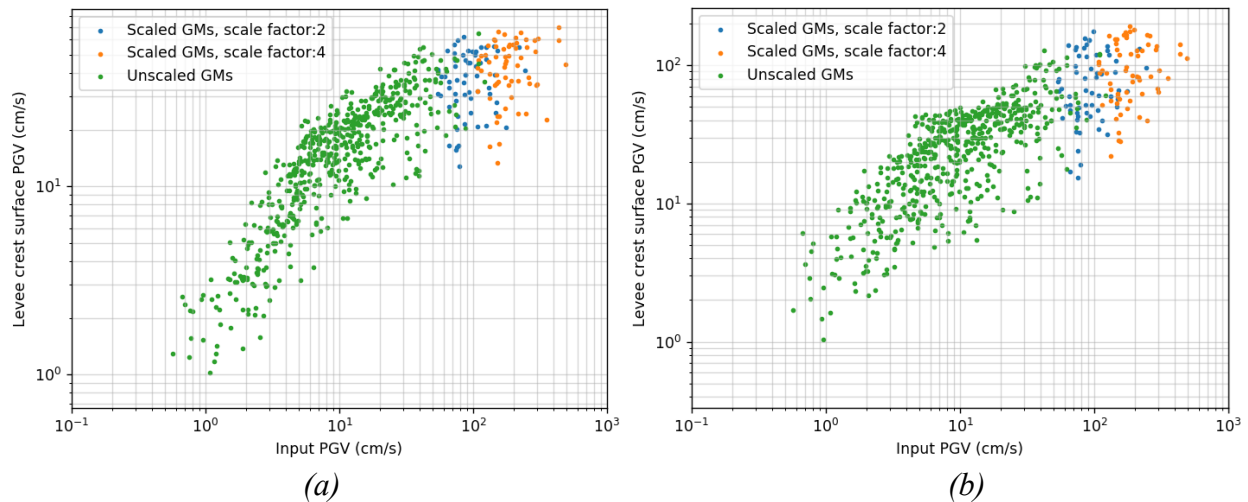


**Figure 3.60** Input  $PGV$  versus levee crest surface  $PGV$  under unscaled and scaled ground motions of a 1-D vertical soil column extracted from (a) southern Levee; (b) northern levee.

***b) Ground motion type***

Kwak et al. (2016a) and Yang (2021) utilized  $PGV$  as the predictor to estimate levee crest settlement as they believed that  $PGV$  instead of  $PGA$  is a better predictor in levee fragility functions. A validation regarding the better ground motion type is implemented as indicated in Fig. 3.61, and it demonstrates southern levee settlement versus input  $PGA$  and input  $PGV$ . Generally speaking, data points in Fig. 3.61 (a) have higher dispersion about the mean trend, indicating that  $PGA$  is a less efficient predictor than  $PGV$ . Hence, this validates that  $PGV$  is a better option for predicting levee settlement, and I have opted to utilize it.

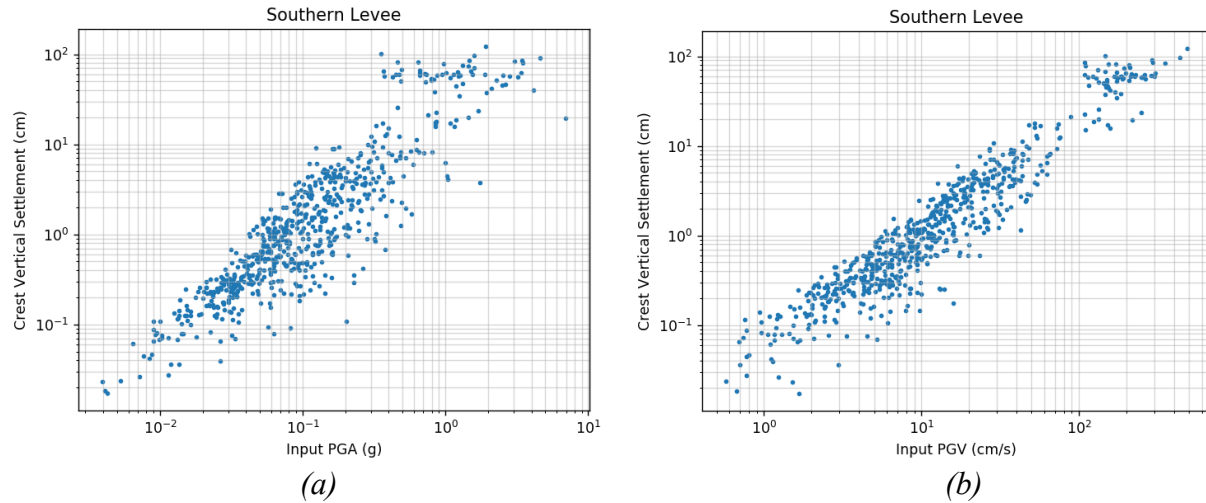


**Figure 3.61** Southern Levee crest settlement versus levee (a) input *PGA*; (b) input *PGV* under unscaled and scaled ground motions.

### *c) Magnitude*

Yang (2021) found that earthquake magnitude had a minor influence on levee crest settlements because, for a given shaking intensity, a larger magnitude earthquake has more loading cycles and would be expected to cause more settlement. He therefore developed fragility functions where *PGV* and magnitude are simultaneously utilized as predictors for McDonald Island levee settlement. Magnitude is also investigated here to study its suitability as a secondary predictor for Bacon Island levees. Residuals, defined as the data point minus a linear model for levee settlement vs  $\ln(PGV)$ , are plotted vs. magnitude in Figure 3.62. The residuals have a slight negative trend for the Southern Levee, indicating that, for a given shaking intensity, larger magnitude events cause slightly less settlement than lower magnitude events. This is a counterintuitive trend that may be caused by sampling bias in the selected events. The northern levee residuals exhibit essentially zero trend with magnitude.

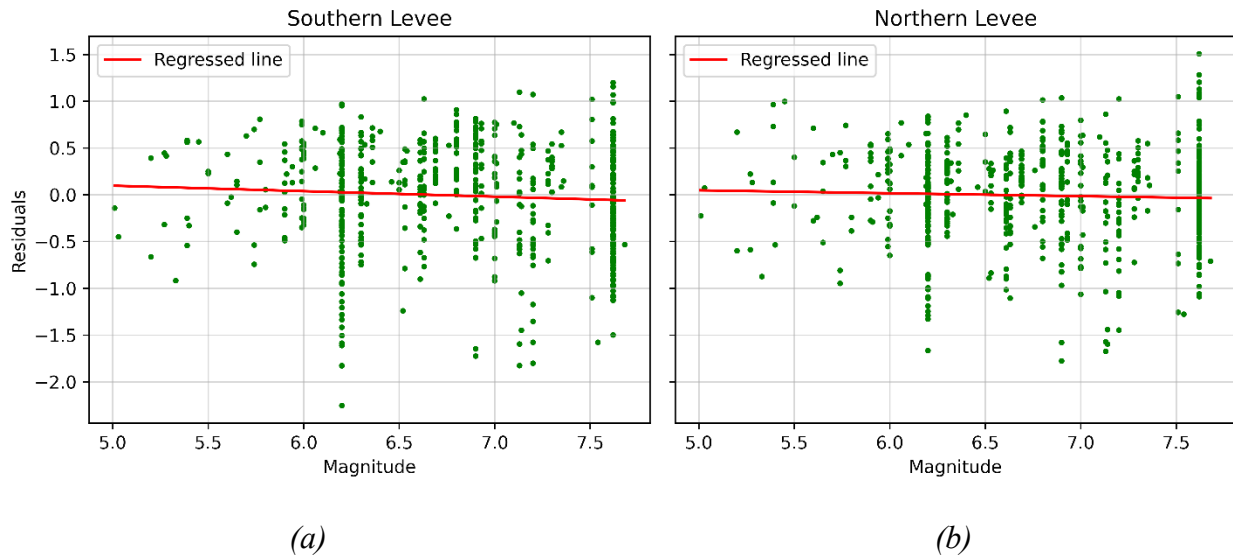


**Figure 3.62** Magnitude versus residuals computed from regressed lines for simulation results of (a) southern levee; (b) northern levee under unscaled ground motions.

Sampling bias can mask true causal relationships among data quantities. In the perspective of causal inference,  $IM$ , crest settlement, and magnitude are considered as treatment, outcome, and confounding variables. Burton and Baker (2023) proposed a semi-parametric model that employs double machine learning (Chernozhukov et al., 2018) to estimate causal effect of various  $IMs$  to engineering demand parameters after controlling other confounding variables including magnitude. I did not attempt to utilize causal inference to study the true influence of magnitude on levee settlement. Rather I simply opted to exclude magnitude from the fragility functions since the trends are weak.

#### ***d) Additional Scaled Motions***

A gap exists between data points in Fig. 3.44 between the unscaled and scaled ground motions. Furthermore, there is less data at high shaking intensity, which could bias the least squares regression at high shaking amplitude, which is particularly important for levee damage. For this

reason, another group of scaled ground motions with an amplification factor of 2 were imposed on the OpenSees models. Figure 3.63 demonstrates the simulations results implementing unscaled ground and two groups of scaled ground motions for both levee models in *OpenSees*. This is the ground motion set I ultimately utilized to develop the fragility functions.

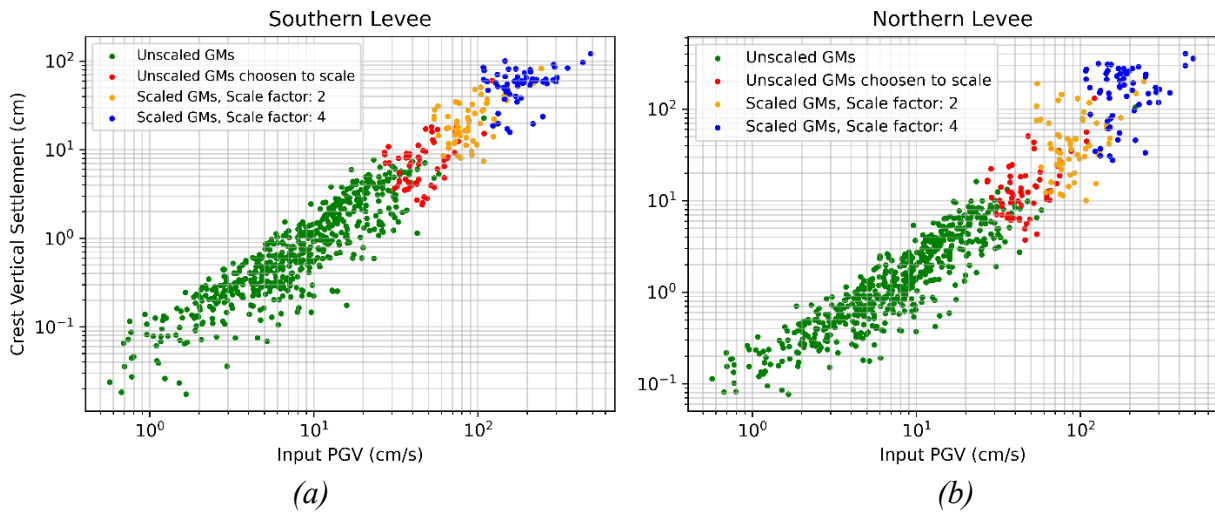


**Figure 3.63** Levee crest settlement versus input *PGV* under unscaled and two groups of scaled ground motions for (a) southern levee; (b) northern levee.

### 3.4.2 Model for levee settlement vs. *PGV*

This section presents the model fit to the numerical simulation data points to represent levee crest settlement as a function of *PGV*. Key considerations addressed in this section are (1) whether a linear fit is adequate, or a piecewise-linear fit should be used, particularly for the northern levee, and (2) whether the residuals are homoscedastic, or whether a *PGV*-dependent standard deviation model is needed.

#### a) *Linear fitting*

The numerical simulations interest many realizations of very small settlements that are lower than the range of engineering interest. To avoid having these inconsequentially small settlements exert

significant influence on the regression, I opted to exclude data points with  $PGV \leq 10$  cm/s in the regression, which corresponds to settlements that are less than 1 cm. Fig. 3.64 shows the data points used in the regression along with a linear fit and associated equation for southern and northern levees.

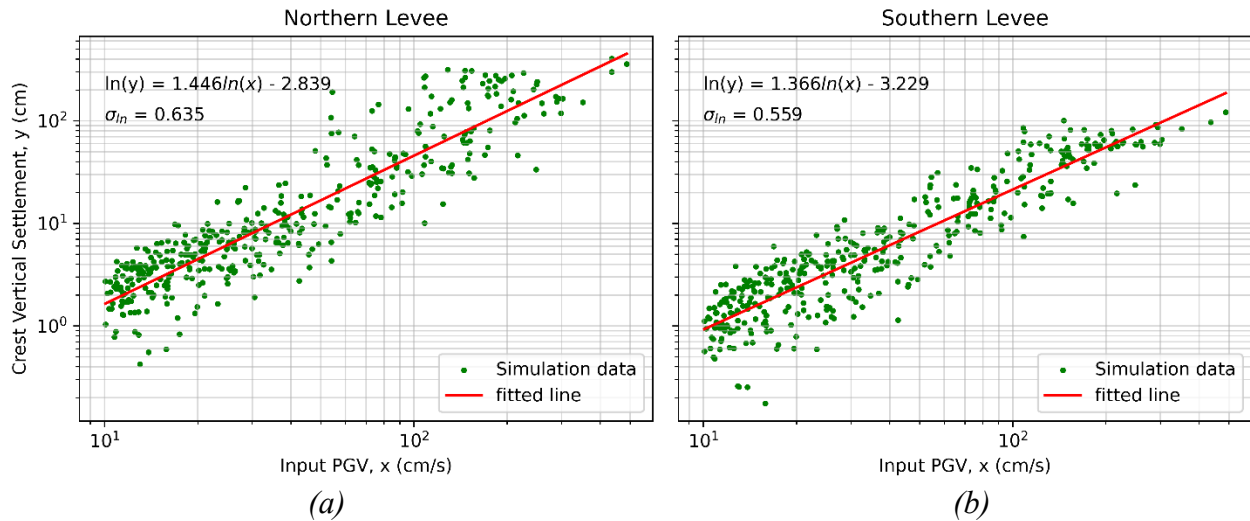


**Figure 3.64** Input  $PGV$  versus levee crest settlement and linear fitting results including linear regression equation and standard deviation of residuals for (a) northern levee, (b) southern levee.

The fitted line from the northern levee is higher and steeper than the one from southern levee. I postulate that this is due to the effects of liquefaction of the sands within the northern levee that are not present in the southern levee. This finding is somewhat surprising since the southern levees rest on softer, more compressible soils.

***b) Normality of error terms***

The normality of error that is a critical assumption in linear regression states that the error terms (residuals) from the model follow a normal distribution function. If error terms are non-normally distributed, errors may propagate through predictive models. To evaluate normality, I utilize the

Q-Q (quantile-quantile) plots shown in Figure 3.65. A normally distributed random variable will have Q-Q plot ordinates that lie along a 1:1 line. I conclude that the northern levee error term is normally distributed since the datapoints closely follow the 45-degree line (red lines shown in the plot). However, datapoints for the southern levee deviate from the red line, which suggests that the errors are a bit left skewed with long left tail as reflected in Fig. 3.66. Figure 3.66 shows the histogram and its kernel density estimation curve of the regressed residuals from southern levee model.

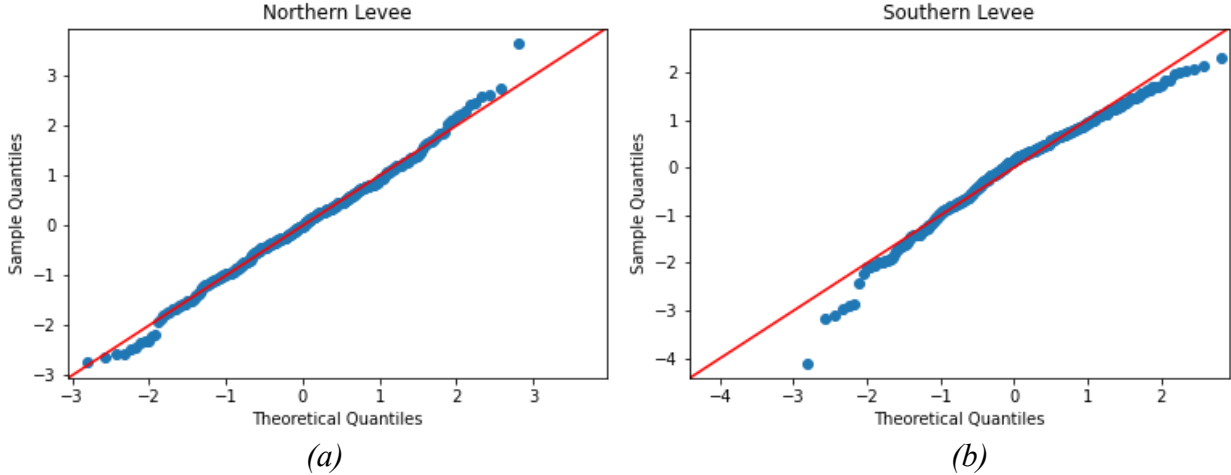


**Figure 3.65** Q-Q plots of standardized errors obtained from (a) northern levee, and (b) southern levee.



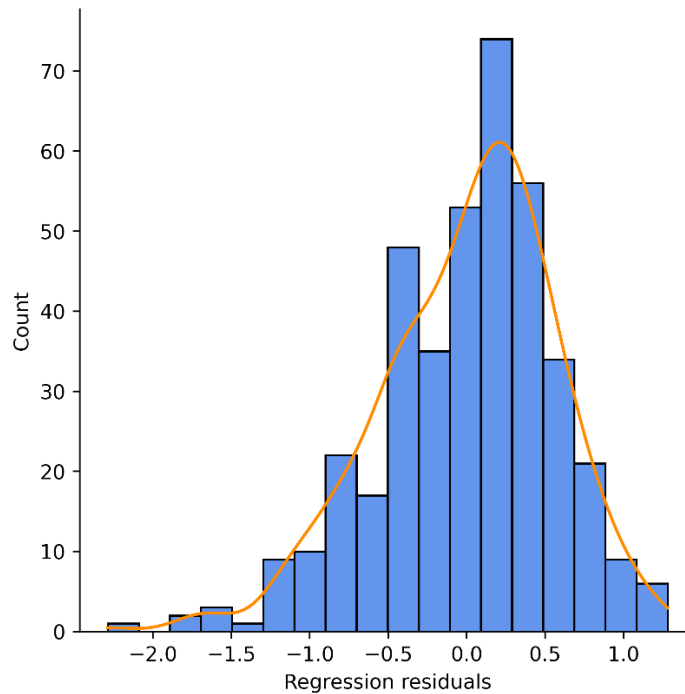


**Figure 3.66** Histogram and kernel density estimation curve of the regressed residuals computed from the southern levee model.

In addition, performing statistical tests of normality can also help validate the assumption. Table 3.20 summarizes the Kolmogorov-Smirnov and Shapiro-Wilk test results of standardized errors from northern and southern levee models. If the desired significance level for the hypothesis test  $\alpha$  is 0.05, which is a widely used value and reflects the 95% level of confidence, then the calculated  $p$ -values from tests can be used to reject or accept null hypothesis by means of comparing with  $\alpha$ . If  $p$ -value is less than  $\alpha$ , then the null hypothesis stating that standardized errors are normally distributed is rejected, and vice versa. Kolmogorov-Smirnov and Shapiro-Wilk test results demonstrate that standardized errors of northern levee are normally distributed, but standardized errors of southern levee are not normally distributed at a 95% confidence level.

**Table 3.20** Kolmogorov-Smirnov and Shapiro-Wilk tests for standardized regression error terms from northern and southern levees.

		Standardized regression error term from Northern levee	Standardized regression error term from Southern levee
<b>Kolmogorov-Smirnov test</b>	test statistics	0.0347	0.0740
	<i>p</i> -value	0.7053	0.0235
<b>Shapiro-Wilk test</b>	test statistics	0.9953	0.9783
	<i>p</i> -value	0.2693	1.0089e-5

To remediate non-normally distributed errors for the southern levee, a Box-Cox transformation was performed on *PGV* and levee settlements. The Box-Cox transformation is similar to a log-transformation (in fact, the log transformation is a subset of Box-Cox), and utilized Eq. 3.17 below,

$$w(\lambda) = \begin{cases} \frac{y^\lambda - 1}{\lambda}, & \text{if } \lambda \neq 0 \\ \log y, & \text{if } \lambda = 0 \end{cases} \quad (3.17)$$

where  $w$  is the transformed variable and  $\lambda$  is an exponent parameter selected to optimize the normality of  $w$ .

However, I found that the Box-Cox transformations did not significantly improve normality of the residuals. Therefore, the added complexity of the Box-Cox transformation and more complicated fragility functions is not worthwhile, and I suggest using the assumption that the residuals are normally distributed.

### ***c) Homoscedasticity***

Homoscedasticity represents the presence of constant variance in the residuals at every level of the independent variable, and it is also an important assumption in linear regression. Non-constant variance (i.e., heteroscedasticity) may result in errors in model predictions that assume homoscedasticity. To assess whether the residuals are homoscedastic, residuals are plotted vs. *PGV*

in Figure 3.67 with binned means reflecting the standard deviation. The figure illustrates that residuals do not have a systematic tendency to spread or narrow as  $PGV$  changes, so I conclude that the assumption of homoscedasticity is valid in linear fitting for both northern and southern levee.

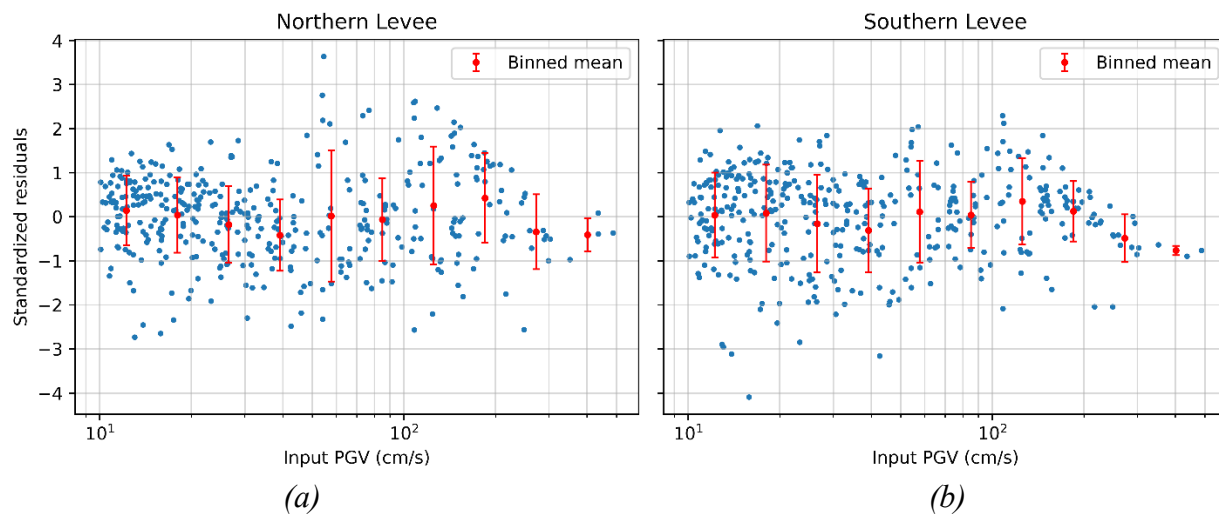


**Figure 3.67** Standardized residuals versus independent variable input  $PGV$  of (a) northern levee, and (b) southern levee.

**d) Piecewise linear fitting**

The northern levee data exhibit a slight nonlinearity, or bend, in the residuals at  $PGV$  near 50 cm/s. I therefore considered an alternative fitting method, piecewise linear fitting, to capture this trend. Figure 3.68 shows the piecewise linear fitting results with the breakpoint at 50 cm/s. The trendline bends slightly upward to with large ground motions. However, the bend is very slight, and I opt to utilize linear fitting since it results in a much simpler fragility model.

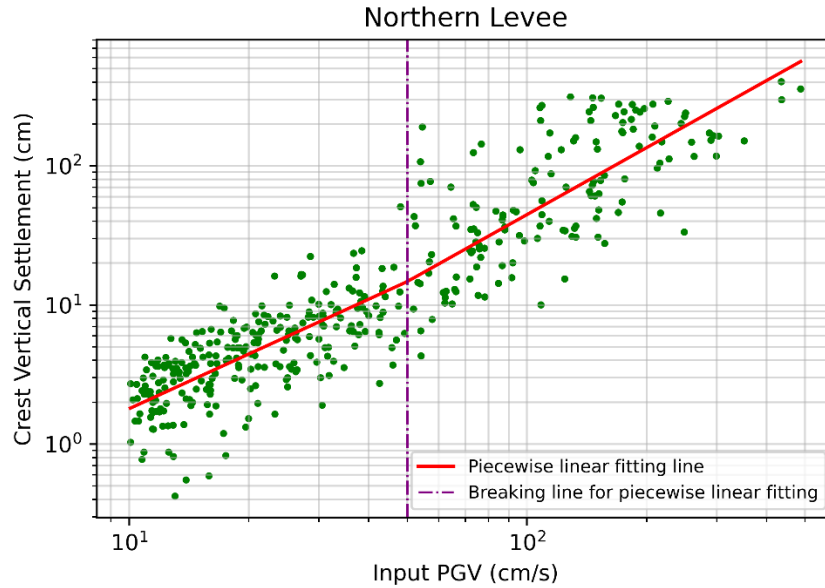


**Figure 3.68** Input *PGV* versus levee crest settlement and piecewise linear fitting line with a breaking point input *PGV* equaling 50cm/s.

***e) Additional Uncertainty from Spatial Variability of Soil Properties***

The OpenSees simulations reasonably capture the influence of motion-to-motion variability on levee fragility, but not several other sources of uncertainty. For example, the levee cross-sections include uniform soil properties within each layer, whereas real soil profiles exhibit spatial variability. Additionally, the section-to-section variability is another type of source of uncertainty, which reflects that mean value of the soil properties within a cross-section vary with distance along the length of the levee.

***i) Within-Section Spatial Variability***

Yang (2021) used random field realizations of soil properties to show that spatial variability of soils introduces additional uncertainty that tends to shift the fragility functions to the left (i.e., decrease the mean) and make them flatter (i.e., increase the standard deviation). The adjusted term  $\Delta m_0$  for the intercept  $m_0$  and the within-section spatial variability  $\sigma_{sp}$  are found to be 0.81 and

0.24 for McDonald Island levees, and I adopt these results to the fragility functions of Bacon Island levees to quantify within-section spatial variability. Thus, the updated intercept is  $\Delta m_0 + m_0$ , and

the standard deviation is calculated as  $\sqrt{\sigma_{m2m}^2 + \sigma_{sp}^2}$ .

### ***ii) Inter-Section Spatial Variability***

In addition, the inter-section (section-to-section) spatial variability of Bacon Island levee fragility functions is also quantified in this research. I firstly validate the  $V_{S5}$  of levee fill and levee fragility are highly correlated. Then I derive the relationship between  $V_{S5}$  of levee and levee vulnerability according to simulations results, and I incorporate additional  $V_{S5}$ -dependent terms in Equation 3.15 to calibrate the fragility functions to be relying on  $PGV$  and  $V_{S5}$ .

Shear wave velocity of levee fill is presumably assumed to be highly correlated with levee seismic vulnerability which is assessed by maximum vertical levee crest settlement in this study, and there are two reasons behind this assumption: 1) Shear wave velocity explicitly reflects the stiffness of soil in levee fill; 2) The squared shear wave velocity is proportional to the maximum shear modulus of soil, so it directly affects soil shear strength. Levee  $V_{S5}$ , which is defined as the shear wave velocity at a depth of 5m measured from levee crest, can be regarded as a good representation of the averaged shear wave velocity of levee fill. Proving levee  $V_{S5}$  and levee seismic capacity are significantly correlated requires further study, therefore, a series of additional simulation tests are anticipated to help validate this assumption using OpenSeesMP.

Here is the framework of simulation tests:

- a) Selecting the southern levee as the object of interest, and the initial southern levee original setups remain identical as before. One ground motion data (RSN =1054) from 1994 Northridge earthquake is used as ground motion input to shake the levee model.

- b) Shake levees with a variety of shear wave velocity of levee fill using the ground motion. Figure 3.69 shows the finite element model of southern levee and its levee fill zone. Change the levee fill shear wave velocity by multiplying a set of ratios, and ratios are 0.5, 0.75, 1, 1.25, 1.5, and 2, respectively.
- c) The time-averaged shear wave velocity at a depth of 5 m can be computed for each simulation based on the finite element model. The initial  $V_{S5}$  of levee model is about 92 m/s.
- d) Record the maximum vertical settlement of levee crest after ground shaking in each scenario and perform a statistical hypothesis test to investigate if levee seismic capacity and  $V_{S5}$  of levee model are significantly correlated.

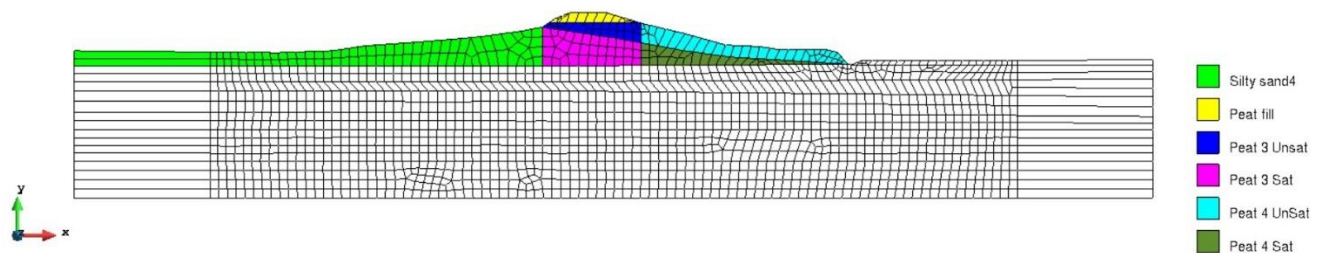


**Figure 3.69** Finite element model of southern levee showing material region of levee fill.

Figure 3.70 (a) presents the results of 7 simulations tests, and it shows that levee  $V_{S5}$  indeed influences crest settlement. Given the same ground shaking level, larger  $V_{S5}$  of levee causes less crest settlement, and vice versa. Based on simulation test results, Spearman correlation coefficient (also called Spearman's rank correlation coefficient) test is conducted. Spearman correlation coefficient is a non-parametric measure of the strength and direction of the monotonic relationship between two variables, and it is particularly useful when the relationship between the variables is not linear. (Spearman, 1961). Spearman correlation coefficient is calculated using the following equation,

$$\rho = 1 - \frac{(6 * \sum d_i^2)}{n * (n^2 - 1)} \quad (3.18)$$

where,  $\sum d_i^2$  is the sum of squared differences between the ranks of the paired observations,  $n$  is the number of paired observations.

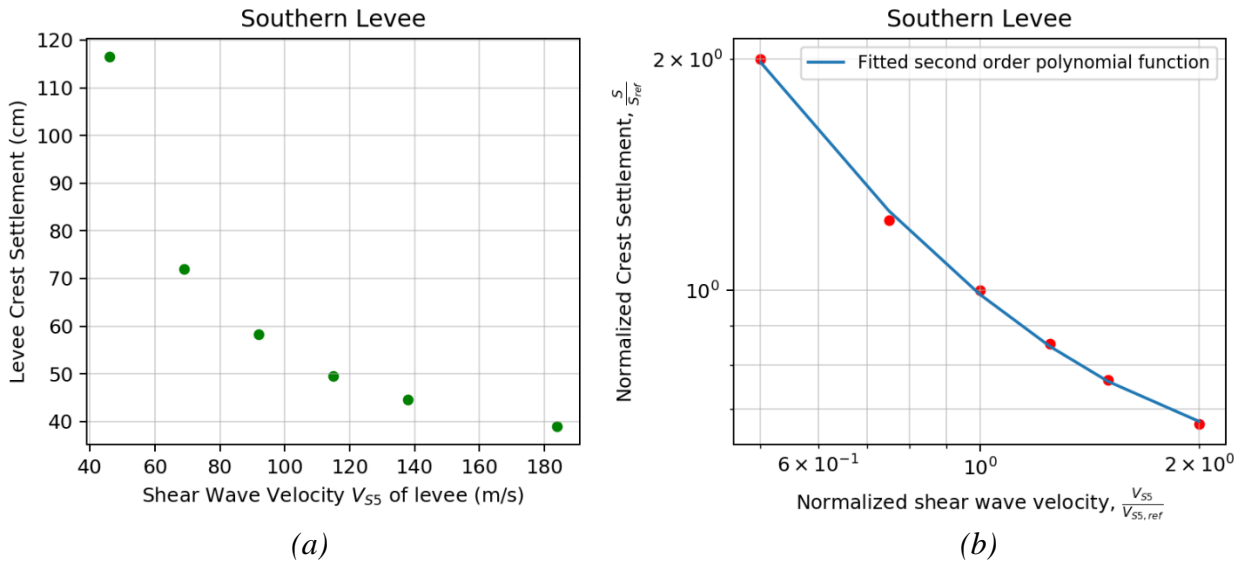


**Figure 3.70** (a) Shear wave velocity  $V_{S5}$  of levee versus crest settlement given a ground motion time series form 1994 Northridge earthquake, and (b) normalized  $V_{S5}$  and crest settlement in log scales and fitted polynomial function.

After calculation, the correlation coefficient  $\rho$  is about 1, which reflects a perfectly positive monotonic relationship. However, p-value should be assessed to determine whether this correlation is statistically significant or not.

The null hypothesis  $H_0$  and alternative hypothesis  $H_1$  are proposed as follow:

$H_0$ : levee seismic vulnerability and levee fill shear wave velocity are not highly correlated.

$H_1$ : levee seismic vulnerability and levee fill shear wave velocity are highly correlated.

In addition, the desired significance level for the hypothesis test is set as 0.05.

The  $t$  statistic is calculated based on calculated correlation coefficient  $\rho$  by the following equation,

$$t = \frac{\rho \cdot \sqrt{N-2}}{\sqrt{1-\rho^2}} \quad (3.19)$$

where  $N$  is the sample size and  $N$  is 6 in this case.

The calculated  $t$ -value is infinite, and it corresponds to the  $p$ -value equaling to 0 based on  $t$  distribution.

In summary, the  $p$ -value is less than significance level  $\alpha$ , therefore, null hypothesis  $H_0$  should be rejected, which concludes that levee seismic vulnerability and levee fill shear wave velocity are highly correlated.

I decide to quantify the effects of  $V_{S5}$  exerted on crest settlement and add adjustment terms for intercept  $m_0$  in Eq. 3.15. Figure 3.71 (b) shows the normalized  $V_{S5}$  and crest settlement in logarithmic scales and fitted second order polynomial function, and the  $V_{S5,ref}$  for southern levee model is 92 m/s. The updated levee crest settlement can be written as,

$$\ln(S) = m_0 + \Delta m_0 + m_1 \cdot \ln(PGV) + m_2 \cdot \left[ \ln\left(\frac{V_{S5}}{V_{S5,ref}}\right) \right]^2 + m_3 \cdot \ln\left(\frac{V_{S5}}{V_{S5,ref}}\right) + m_4 + \varepsilon \quad (3.20)$$

where  $m_2$ ,  $m_3$ , and  $m_4$  are 0.3278, -0.7771, and -0.0118, respectively. These additional  $V_{S5}$ -dependent terms are also applied for eastern, northern, and western levees, and the  $V_{S5,ref}$  is 135.6 m/s for these levees.

Subsequently, I plan to develop reach-based fragility functions accounting for inter-section spatial  $V_{S5}$  variability based on the aforementioned  $V_{S5}$  of levee reaches derived from the geophysical field tests, which generate more granular and specific fragility functions for the levee system.



### 3.4.3 Construct Levee Seismic Fragility Functions

Based on fitted models between crest settlement, input  $PGV$ , and  $V_{S5}$ , the  $PGV$  and  $V_{S5}$ -based fragility curves and functions can be constructed using Eq. 3.16 for both northern levee and southern levee models. The moments of the log-normal CDFs of the fragility curves can be written as,

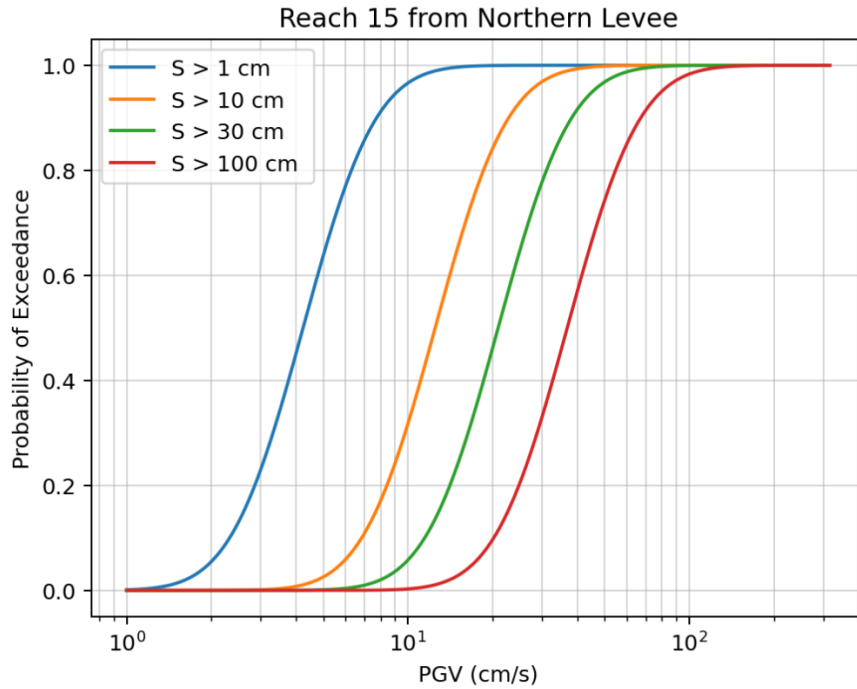
$$\mu = \frac{\ln(S_t) - m_0 - \Delta m_0 - m_2 \cdot \left[ \ln\left(\frac{V_{S5}}{V_{S5,ref}}\right) \right]^2 - m_3 \cdot \ln\left(\frac{V_{S5}}{V_{S5,ref}}\right) - m_4}{m_1} \quad (3.21)$$

$$\beta = \frac{\sqrt{\sigma_{m2m}^2 + \sigma_{sp}^2}}{m_1} \quad (3.22)$$

where  $\mu$  and  $\beta$  are the mean and standard deviation of the log-normal CDF for the fragility curve.

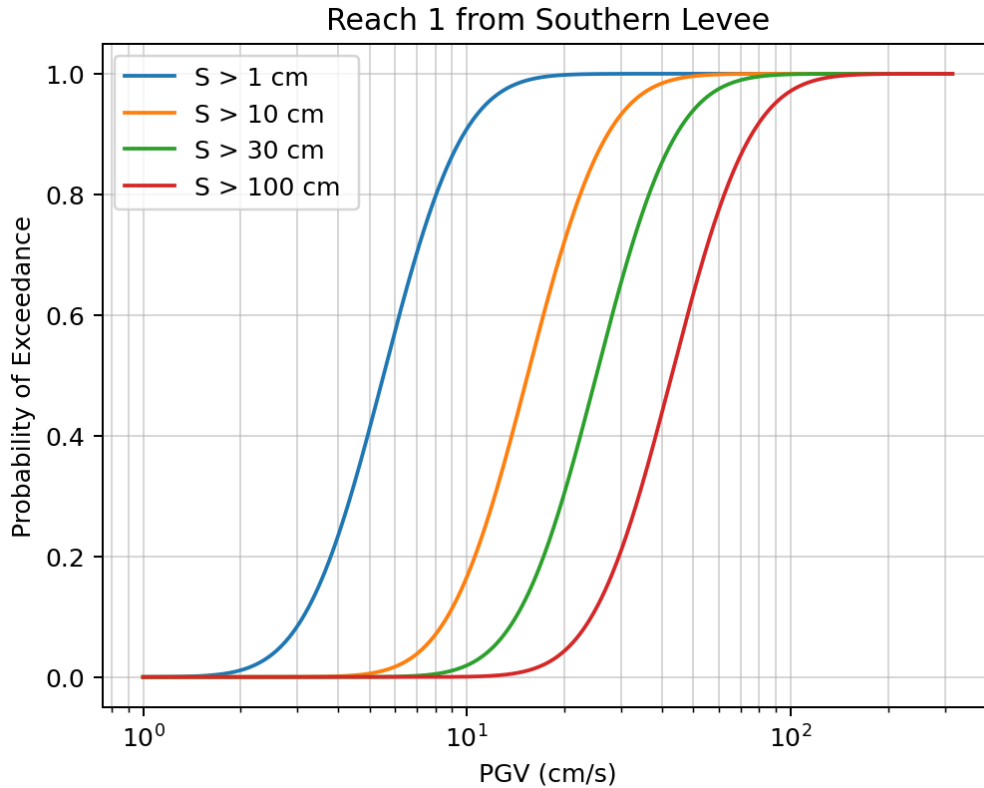
This section summarizes a variety of seismic fragility curves and functions for 28 levee reaches and these reach-based fragility functions will be utilized in ensuing risk assessment.

Figure 3.71 represents the fragility curves of reach 15 on northern levee exceeding four selected settlement levels, and the averaged  $V_{S5}$  of reach 1 is 120.6 m/s. The curves show that  $PGV$  values less than about 4 cm/s are unlikely to cause more than 1 cm of settlement, which is a threshold that would likely not be noticed in a post-earthquake field reconnaissance mission. Furthermore, the curves illustrate that shaking stronger than 100 cm/s is likely to cause large settlements that could result in a breach.



**Figure 3.71** PGV and  $V_{S5}$ -based seismic fragility functions of levee reach 15 on northern levee.

Figure 3.72 presents the fragility curves for the levee reach 1 on southern levee, and the averaged  $V_{S5}$  of reach 1 is 98 m/s. Compared to fragility curves of the reach 15 presented in Fig. 3.71, the reach 1 fragility curves move towards to the right a bit while curve slopes remain nearly same.



**Figure 3.72** PGV and  $V_{S5}$ -based seismic fragility functions of levee reach 1 on southern levee.

Table 3.21 summarizes the moments of log-normal CDFs of exceeding four damage levels for 28 levee reaches. The means of log-normal CDFs  $e^\mu$  of northern levee are smaller than the ones of southern levee while the standard deviations  $\beta$  are similar to each other, which corroborates that the northern levee model is prone to be more vulnerable than southern levee model under earthquakes.

**Table 3.21** Means and standard deviations of log-normal CDFs of exceeding various damage levels (DL) for northern and southern levee models.

Reach	Damage Level	Mean, $\mu$	Exponential Mean, $e^\mu$ (cm/s)	Standard Deviation, $\beta$
1	0	1.81	6.1	0.45
	1	3.50	33.1	0.45
	2	4.30	73.7	0.45
	3	4.94	139.8	0.45
2	0	1.86	6.4	0.45
	1	3.54	34.5	0.45
	2	4.35	77.5	0.45
	3	5	148.4	0.45
3	0	1.88	6.6	0.45
	1	3.57	35.5	0.45
	2	4.37	79	0.45
	3	5.03	152.9	0.45
4	0	1.93	6.9	0.47
	1	3.62	37.3	0.47
	2	4.42	83.1	0.47
	3	5.1	164	0.47
5	0	1.93	6.9	0.47
	1	3.62	37.3	0.47
	2	4.42	83.1	0.47
	3	5.1	164	0.47
6	0	1.93	6.9	0.47
	1	3.62	37.3	0.47
	2	4.42	83.1	0.47
	3	5.1	164	0.47
7	0	1.93	6.9	0.47
	1	3.62	37.3	0.47
	2	4.42	83.1	0.47
	3	5.1	164	0.47
8	0	1.93	6.9	0.47
	1	3.62	37.3	0.47
	2	4.42	83.1	0.47
	3	5.1	164	0.47
9	0	1.93	6.9	0.47
	1	3.62	37.3	0.47
	2	4.42	83.1	0.47
	3	5.1	164	0.47
10	0	1.93	6.9	0.47
	1	3.62	37.3	0.47

	2	4.42	83.1	0.47
	3	5.1	164	0.47
11	0	1.93	6.9	0.47
	1	3.62	37.3	0.47
	2	4.42	83.1	0.47
	3	5.1	164	0.47
	0	1.93	6.9	0.47
12	1	3.62	37.3	0.47
	2	4.42	83.1	0.47
	3	5.1	164	0.47
13	0	1.93	6.9	0.47
	1	3.62	37.3	0.47
	2	4.42	83.1	0.47
	3	5.1	164	0.47
14	0	1.93	6.9	0.47
	1	3.62	37.3	0.47
	2	4.42	83.1	0.47
	3	5.1	164	0.47
15	0	1.92	6.8	0.47
	1	3.6	36.6	0.47
	2	4.41	82.3	0.47
	3	5.08	160.8	0.47
16	0	1.93	6.9	0.47
	1	3.61	37	0.47
	2	4.42	83.1	0.47
	3	5.1	164	0.47
17	0	1.93	6.9	0.47
	1	3.62	37.3	0.47
	2	4.42	83.1	0.47
	3	5.11	165.7	0.47
18	0	1.93	6.9	0.47
	1	3.62	37.3	0.47
	2	4.42	83.1	0.47
	3	5.1	164	0.47
19	0	1.93	6.9	0.47
	1	3.62	37.3	0.47
	2	4.42	83.1	0.47
	3	5.1	164	0.47
20	0	1.96	7.1	0.47
	1	3.64	38.1	0.47
	2	4.45	85.6	0.47
	3	5.14	170.7	0.47
21	0	1.94	7	0.47
	1	3.62	37.3	0.47
	2	4.43	83.9	0.47

	3	5.11	165.7	0.47
22	0	1.94	7	0.47
	1	3.62	37.3	0.47
	2	4.43	83.9	0.47
	3	5.11	165.7	0.47
23	0	1.94	7	0.47
	1	3.62	37.3	0.47
	2	4.43	83.9	0.47
	3	5.11	165.7	0.47
24	0	1.94	7	0.47
	1	3.62	37.3	0.47
	2	4.43	83.9	0.47
	3	5.11	165.7	0.47
25	0	1.92	6.8	0.47
	1	3.6	36.6	0.47
	2	4.41	82.3	0.47
	3	5.08	160.8	0.47
26	0	1.89	6.6	0.47
	1	3.58	35.9	0.47
	2	4.38	79.8	0.47
	3	5.04	154.5	0.47
27	0	1.96	7.1	0.47
	1	3.64	38.1	0.47
	2	4.45	85.6	0.47
	3	5.14	170.7	0.47
28	0	1.95	7	0.47
	1	3.63	37.7	0.47
	2	4.44	84.8	0.47
	3	5.13	169	0.47

The standard deviations of the fragility functions derived herein are smaller than those proposed by Yang (2021), which is great because the uncertainty is reduced. I believe the cause of the smaller standard deviation is that Yang utilized the surface motion, which introduces significantly more scatter in the relationship compared with utilizing the base input motion.

## **CHAPTER 4: Event Selection Algorithm for Delta Region Levee**

### **Risk Assessment**

The regional PSHA of the system should be completed prior to performing risk assessment of a spatially distributed infrastructure system. The uniform hazard map such as the one presented in Figs 2.8 represents the outcome of repeating PSHA calculation at many points of interest, and subsequently interpolating the results to form a map. Each PSHA calculation is performed at a point and contains contributions from many different earthquake scenarios. While these uniform hazard maps are appropriate for evaluating or designing infrastructure at a point, they are inappropriate for analyzing seismic demands on spatially distributed infrastructure systems. As an example, a moderate magnitude earthquake might generate strong shaking at point A, weak shaking at point B, whereas a different scenario might generate strong shaking at point B, but weak shaking at point A. These events both contribute to the seismic hazard at points A and B, but no single event will generate uniform hazard shaking intensities at both points A and B. For this reason, spatially distributed infrastructure systems, such as levees, must be analyzed using carefully selected scenario events rather than uniform hazard maps.

This Chapter describes the LASSO regression-based event selection methodology developed by my colleague, Professor Pengfei Wang, that efficiently selects a manageable event subset to match the hazard, in a least-squares sense, at many locations. It also has the capability of matching magnitude and source-to-site distance distributions. I then implementing this methodology to select an event subset from UCERF3 source for evaluating the Sacramento-San Joaquin Delta levee system.

### **4.1 LASSO Regression-Based Event Selection Methodology**

A robust approach to perform regional PSHA for spatially distributed infrastructure systems is to analyze the systems separately for each individual event considered in the seismic source model utilized in the PSHA. However, this approach is potentially computationally expensive and sometimes not practical to implement, especially when hundreds of thousands of scenario events are considered such as UCERF3 model, which consists of two model branches containing more than 1.5 million scenario events. Furthermore, evaluation of the response of a levee to earthquake ground shaking can sometimes involve simple equations (like the fragility functions utilized herein), but sometimes involve more complicated time-consuming simulations. I adopt a LASSO regression-based event selection methodology proposed by Wang et al. (2023) to select a manageable event set that, in aggregate, approximately matches the hazard for different levels of single or multiple ground motion intensity measures across a certain region while preserving contributions of various magnitudes and distances in PSHA disaggregation. Wang et al. (2023) also demonstrated the scalability, flexibility, and efficiency of this LASSO-regression based event selection method compared to other event selection algorithms. Therefore, this approach basically serves as a tool to select appropriate and manageable events for regional PSHA and risk assessments.

Before introducing the event selection methodology, PSHA and Regional PSHA are reviewed first. When the event magnitude and distance are given, the PSHA formula for a single site as indicated by Eq. 2.3 can be written as follows,

$$\lambda(IM > x) = \sum_{i=1}^{N_E} (v_i P(IM > x | M_i, R_i)) = \sum_{i=1}^{N_E} \Lambda_i(IM > x) \quad (4.1)$$

where  $IM$  is log-normally distributed random variable whose median and standard deviation are



specified by GMMs,  $x$  is a specific value of  $IM$ ,  $\lambda(IM > x)$  is the annual rate at which  $IM$  exceeds  $x$  due to all considered events,  $N_E$  is the total number of considered events,  $v_i$  is the annual occurrence rate of the  $i$ -th event,  $P(IM > x | M_i, R_i)$  is the probability that  $IM$  exceeds  $x$  given the event with magnitude  $M_i$  and site-to-source distance  $R_i$ . The product of annual occurrence rate and exceedance probability is herein defined as  $\Lambda_i(IM > x)$ , which represents the annual ground motion exceedance rate produced by event  $i$ , which can also be conceptualized as an event-specific hazard curve. Uniform hazard maps are computed by simply repeating Eq. 4.1 for a large number of sites within the region of interest and aggregating the results for a particular return period into a map. Essentially, there are 6 variables that need to be considered in regional PSHA calculation, as summarized in Table 4.1.

**Table 4.1.** Variables for regional PSHA calculation.

Variable names	Index of variables	Number of variable elements
Event	$i$	$N_E$
Site	$j$	$N_S$
Intensity measure type	$k$	$N_T$
Intensity measure level	$l$	$N_X$
Magnitude bin	$b$	$N_M$
Distance bin	$d$	$N_R$

Some tensor variables are defined here to describe the LASSO methodology. Assuming the hazard curve at a site is constructed by integrating  $N_X$  separate  $x$  values (various intensity measure levels), rank-1 and rank-2 tensors  ${}^1\lambda_l$  and  ${}^2\Lambda_{l,i}$  can be defined to represent the total hazard curve and the hazard curve produced by each event  $i$ . The left superscripts 1 and 2 of  ${}^1\lambda_l$  and  ${}^2\Lambda_{l,i}$  indicate the ranks of the tensors, which reflects the number of *indices*. Therefore, Eq. 4.1 can be represented for one intensity measure type at one site by Eq. 4.2.

$${}^1\lambda_l = \sum_{i=1}^{N_E} {}^2\Lambda_{l,i} \quad (4.2)$$

For regional PSHA,  ${}^1\lambda_l$  and  ${}^2\Lambda_{l,i}$  must be computed at  $N_S$  different sites within a region (from  $j =$

1 to  $j = N_S$ ), which can be represented by adding an index  $j$  ( $j \in \{1, \dots, N_S\}$ ), thereby increasing the tensor ranks, as defined by Eq. 4.4.

$${}^2\lambda_{l,j} = \sum_{i=1}^{N_E} {}^3\Lambda_{l,j,i} \quad (4.3)$$

Similarly, a variety of types of intensity measures (e.g., *PGA*, *PGV*, and pseudo-spectral acceleration, PSA at different oscillator periods) can be involved by introducing an index  $k$  ( $k \in \{1, \dots, N_T\}$ ), thereby further increasing the tensor ranks as defined by Eq. 4.4.

$${}^3\lambda_{l,j,k} = \sum_{i=1}^{N_E} {}^4\Lambda_{l,j,k,i} \quad (4.4)$$

#### 4.1.1 LASSO Regression

The LASSO regression is short for ‘Least Absolute Shrinkage and Selection Operator’ regression and is also known as regression with L1 regularization. It is proposed by Tibshirani (1996) and is essentially a regularized method which is usually used to perform feature selection, reduce dimensionality to alleviate ‘curse of dimensionality’, and improve overfitting in regression. Compared to the general linear regression which seeks the coefficients that minimize the sum of squared residuals, LASSO regression minimizes the sum of squared residuals plus a penalty term with respect to the sum of the model coefficients. The LASSO regression formula and its objective are provided by Eqs. 4.5 and 5.6:

$$\mathbf{y} = \mathbf{X}\boldsymbol{\beta} + \boldsymbol{\varepsilon} \quad (4.5)$$

$$\arg \min_{\boldsymbol{\beta}} (\mathbf{y} - \mathbf{X}\boldsymbol{\beta})^T (\mathbf{y} - \mathbf{X}\boldsymbol{\beta}) + \gamma \|\boldsymbol{\beta}\|_1 \quad (4.6)$$

where  $\mathbf{y}$  is the target response vector (i.e., a column of values),  $\mathbf{X}$  is the predictor matrix,  $\boldsymbol{\beta}$  is the coefficient vector,  $\boldsymbol{\varepsilon}$  is the error term (which is assumed to follow a multivariate normal distribution),  $\|\cdot\|_1$  is L1 norm (sum of absolute values),  $(\mathbf{y} - \mathbf{X}\boldsymbol{\beta})^T (\mathbf{y} - \mathbf{X}\boldsymbol{\beta})$  is the error value, which is calculated as the inner product of  $(\mathbf{y} - \mathbf{X}\boldsymbol{\beta})$  (or sum of squared errors), and  $\gamma$  is a

parameter to tune the model. On the one hand, larger  $\gamma$  will reduce the sum of squared errors since this term will have a larger contribution to the total objective function, which results in more sparsity in solution (more zeros in  $\boldsymbol{\beta}$ ), where zeros indicate the corresponding features (events) are unselected. On the other hand, smaller  $\gamma$  leads to fewer zeros in  $\boldsymbol{\beta}$  but a better fit for a smaller sum of squared residuals. LASSO regression and ordinary least squares regression coincide when  $\gamma = 0$ .

For regional PSHA considering multiple intensity measure as indicated in Eq. 4.4, I wish to use LASSO regression to solve for an appropriate linear combination of  ${}^4\Lambda_{l,j,k,i}$ . To be more specific, event selection and calculation of their rates can be simultaneously obtained by LASSO regression, which achieves my objectives. LASSO regression is implemented by substituting  $\mathbf{y}$  with  ${}^3\lambda_{l,j,k}$  and  $\mathbf{X}$  with  ${}^4\Lambda_{l,j,k,i}$ . However,  ${}^3\lambda_{l,j,k}$  and  ${}^4\Lambda_{l,j,k,i}$  are rank-3 and rank-4 tensors, respectively, whereas  $\mathbf{y}$  and  $\mathbf{X}$  in LASSO must be a vector (rank-1 tensor) and a matrix (rank-2 tensor). Thus, a rank reduction transformation is required before conducting LASSO regression for event selection.

#### 4.1.2 Tensor Rank Reduction Transformation

${}^3\lambda_{l,j,k}$  and  ${}^4\Lambda_{l,j,k,i}$  are used to illustrate the transformation method adopted for tensor rank reduction. This transformation method is also feasible for high-order rank reductions that are required when magnitude and distance distributions are included in the algorithm. As shown in Figure 4.1, the rank reduction transformation is conducted to transform a rank-3 tensor  ${}^3\lambda_{l,j,k}$  to a rank-1 tensor  ${}^1\lambda_q$ , where  $q$  is an index counter for the resultant rank-1 tensor.  ${}^3\lambda_{l,j,k}$  is analogous to a total hazard (i.e., the annual exceedance rates of ground motion) with three IM types ( $N_T=3$ ) for three IM levels ( $N_X=3$ ) at three sites ( $N_S=3$ ), and each 3 by 3 block indicates

regional total hazard curves for three different IM types (i.e.,  $k = \{1, 2, 3\}$ ). Each column in the block represents the total hazard curve at various sites (i.e.,  $j = \{1, 2, 3\}$ ), and entries in the three rows for each column correspond to annual exceedance rates at three different IM levels (i.e.,  $l = \{1, 2, 3\}$ ). The ank-3 tensor  ${}^3\lambda_{l,j,k}$  is transformed to the rank-1 tensor  ${}^1\lambda_q$  according to Eq. 4.7.

$$q = l + (j - 1) \times N_X + (k - 1) \times N_X \times N_S \quad (4.7)$$

Equation 4.7 introduces a re-arranging rule for transforming rank-3 tensor to rank-1 tensor by stacking hazard curves for each site and then stacking by each intensity measure type.

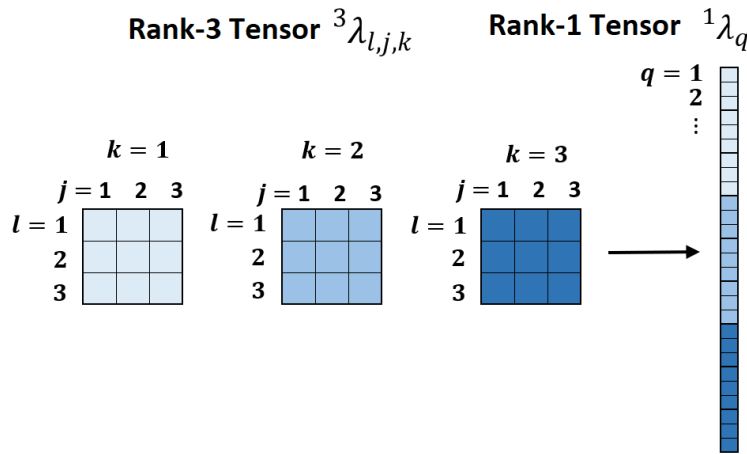


**Figure 4.1** A scheme of rank reduction transformation from a rank-3 tensor (with indices  $l, j, k$ ) to a rank-1 tensor (with index  $q$ ) for a target total hazard from all considered seismic sources.

Figure 4.2 demonstrates another example of rank reduction of a rank-4 tensor, which includes an additional index  $i$  representing the events. Each  $3 \times 3$  block reflects the regional hazard curves produced by each single event  $i$ , and three events (i.e.,  $i = \{1, 2, 3\}$ ) are considered in the example in Figure 4.2, thus there are three  $3$  by  $3$  blocks for each IM type. The array consisting of three columns on the right represents the transformed rank-2 tensor, and each column corresponds to the hazard produced by a single event.

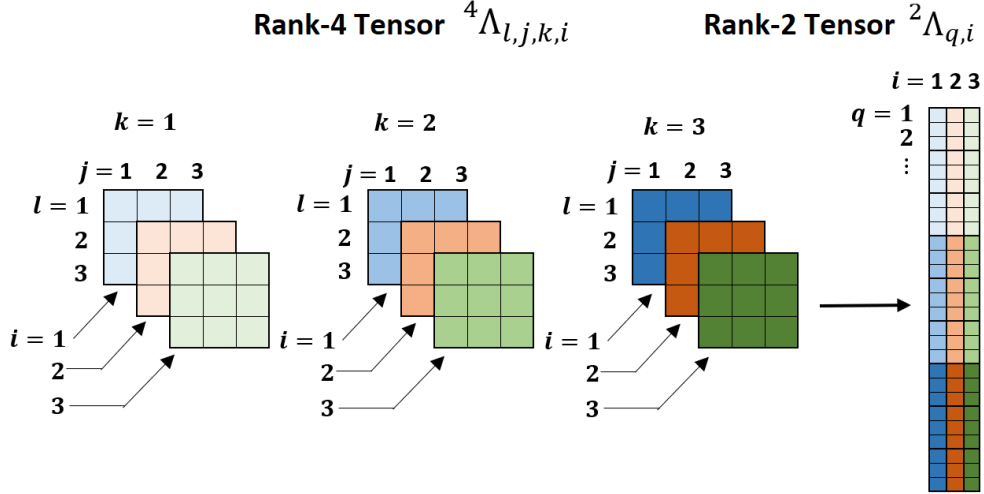


**Figure 4.2** A scheme of rank reduction transformation from a rank-4 tensor (with indices  $l, j, k, i$ ) to a rank-2 tensor (with indices  $q, i$ ) for hazard produced by three events.

#### 4.1.3 Event Selection

With the introduction of tensor rank reduction, the event selection algorithm using LASSO regression can be defined as follows,

$$\lambda = \Lambda\beta + \varepsilon \tag{4.8}$$

$$\arg \min_{\beta} (\lambda - \Lambda\beta)^T W (\lambda - \Lambda\beta) + \gamma \|\beta\|_1 \text{ and subject to } \beta \geq \mathbf{0} \tag{4.9}$$

Compared to Equation 4.5 and 4.6, the target response vector  $\mathbf{y}$  is replaced by rank-1 total hazard  ${}^1\lambda_q$ , and the predictor matrix  $\mathbf{X}$  is replaced by the rank-2 hazard matrix in Equation 4.8 and 4.9. The column vector  $\beta$  represents the rate adjustment multipliers of events in  $\Lambda$ , and  $\varepsilon$  demonstrates the hazard misfit. Elements in  $\beta$  are constrained to be non-negative to ensure adjusted rates of occurrence are physically meaningful. A weighted LASSO regression is utilized, and  $\mathbf{W}$  is a weighting diagonal matrix with main diagonal elements equaling to  $\frac{1}{\lambda}$  and this weighting method is also utilized by Miller and Baker

(2015).

Eqs. (9) and (10) are fully general and can be applied for full PSHA without reducing the number of events by using all  $N_E$  events to develop  $\mathbf{\Lambda}$ , in which case  $\boldsymbol{\beta} = \mathbf{1}$  (all elements in  $\boldsymbol{\beta}$  are 1) and  $\boldsymbol{\varepsilon} = \mathbf{0}$  (all elements in  $\boldsymbol{\varepsilon}$  are 0). For event selection, we seek a subset of  $n$  events ( $n$  columns in  $\mathbf{\Lambda}$ ) from the complete set of  $N_E$  events ( $n < N_E$ ) and the corresponding rate adjustments in  $\boldsymbol{\beta}$  that, in aggregate, are consistent with the total hazard  $\lambda$  at all sites, for all  $IM$  types, and all  $IM$  levels within certain error bounds represented by  $\boldsymbol{\varepsilon}$ . The regressed  $\boldsymbol{\beta}$  is generally greater than 1 since rates of events in the reduced set must be higher than those in the original full set to compensate for the omission of the unselected events. In addition, the number of selected events is equal to the number of positive elements in  $\boldsymbol{\beta}$ , which can be tuned by altering parameter  $\gamma$ .

For a large region or a region where the seismicity is complex, the number of considered events ( $N_E$ ) for PSHA is large (e.g., about 560,000 rupture events and about 960,000 grid point source scenarios for background seismicity from two branches modeled by UCERF3 in California). The number of columns in  $\mathbf{\Lambda}$  is equal to the number of events and inverting  $\mathbf{\Lambda}$  to solve for  $\boldsymbol{\beta}$  can therefore become computationally expensive. However, many of the events are unlikely to significantly influence seismic hazard at sites of interest, and with a modest degree of approximation they can be excluded from the  $\mathbf{\Lambda}$  matrix before performing LASSO regression. The pre-selection of events can be conducted based on seismic hazard disaggregation results (Bazzurro and Cornell, 1999), in which only events that contribute more than a certain amount (e.g., 5%) to the hazard for any intensity measure at any site are included, as demonstrated subsequently.

The output vector in LASSO consists of regularized coefficients, so the rate adjustments for the selected events are not optimal values to solely minimize hazard misfit. Thus, an additional refit (linear regression without penalty term) is performed to refine the rates for the selected events.

To summarize, the complete event selection process can now be summarized as follows:

- i.* Run a traditional PSHA to calculate the total hazard  $\lambda$  at each site for each intensity measure;
- ii.* Use a pre-selected set of events that contribute significantly to the hazard based on disaggregation results to develop  $\Lambda$ ;
- iii.* Run constrained ( $\beta \geq \mathbf{0}$ ) weighted LASSO regression using Eq. (10) for a specified  $\gamma$  to obtain a regularized coefficient vector, which is denoted  $\widehat{\beta}_L$ ;
- iv.* After selecting the event subset in *iii*, re-optimize Eq. (10) without the  $\gamma\|\beta\|_1$  term (i.e., weighted least square) to obtain the updated regressed coefficient vector,  $\widehat{\beta}_R$ . This regression is subject to the constraint that each element of  $\widehat{\beta}_R$  is positive;
- v.* Repeat steps *iii* – *iv* for a series of different  $\gamma$  values to produce an error plot and then determine the best number of selected events (by looking at how errors decrease as the number of selected events increase).

#### **4.1.4 Including Magnitude and/or Source-to-Site Distance**

The above proposed event selection algorithm is capable of matching hazard curves for a variety of sites, intensity measure types, and return periods. However, the selected event set might not match the contributions of magnitude and source-to-site distance in the deaggregation results of the PSHA. In some engineering applications, preserving magnitude and/or source-to-site distance is important. For instance, earthquake magnitude is considered along with shaking intensity in soil liquefaction analysis because larger magnitude earthquakes generally produce ground motions with longer duration and therefore more cycles to induce liquefaction. The LASSO methodology is amenable to modification to match magnitude and distance distributions. Magnitude and distance distribution to total hazard is formulated as a vector and contributions from considered events as a matrix can then be included in

the regression equations.

The disaggregation derived from PSHA provides the target distributions of magnitude and distance which are joint distribution, as indicated in Figure 4.3(a). The heights of the blue bars indicate the relative contributions to a specified hazard level (i.e., intensity measure type and exceedance rate or return period) for binned values of magnitude and distance. The joint distribution of magnitude and distance for a given site, intensity measure, and return period is a rank-2 tensor  ${}^2P_{b,d}$ , where  $b$  and  $d$  are the magnitude and distance bin indices, respectively. Its dimension is  $N_M$  by  $N_R$ , where  $N_M$  and  $N_R$  represent the number of considered magnitude and distance bins, respectively.

Alternatively, marginal distributions can also be used as the target distribution when either magnitude or distance distribution is solely anticipated to be preserved, as illustrated by Figure 4.3(b) for magnitude. The benefit of using marginal distributions is that the target distribution size is reduced from  $(N_M \times N_R)$  to  $(N_M + N_R)$ , thereby alleviating computational demand. Nevertheless, the drawback of using marginal distributions is that the joint distribution of magnitude and distance may not be preserved accurately.

Marginal magnitude and distance distributions are calculated by summing the joint magnitude and distance disaggregation bars, shown in yellow and red columns in Figure 4(a). The marginal magnitude distribution is taken as an example and replotted in Figure 4(b), in which the magnitude bin is denoted as  $m_b$  and bar heights are denoted as  $P(m_b)$ , which represents the relative contribution to hazard from the magnitude bin,  $m_b$ . We can also calculate the cumulative sum,  $F(m_b) = \sum_{z=1}^b P(m_z \geq m_b)$  where  $z$  is the running index and plot  $F(m_b)$  as in Figure 4.3 (c). The cumulative sum  $F(m_b)$  provides a form that is consistent with the hazard curves, which are also cumulative distribution functions. Similarly, the marginal distance distribution  $P(r_d)$  (where  $r_d$  is the  $d$ -th distance bin) and cumulative sum of marginal distance distribution  $F(r_d) = \sum_{z=1}^d P(r_z \geq r_d)$  can also



be calculated. We adopt the notation  ${}^1P_b$  and  ${}^1P_d$  (rank-1 tensors) to represent the marginal magnitude and distance distributions and  ${}^1F_b$  and  ${}^1F_d$  (rank-1 tensors) to represent the marginal cumulative magnitude and distance distributions.

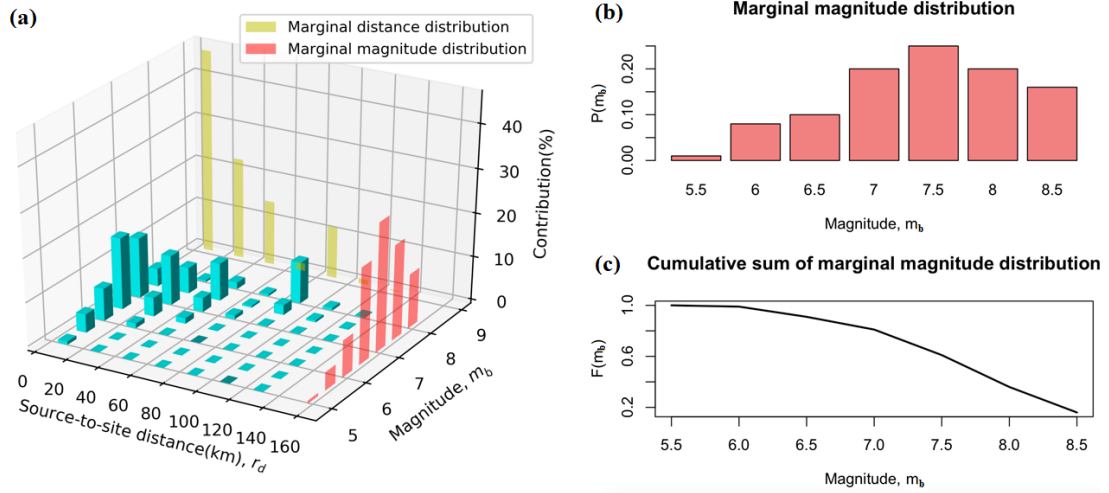


**Figure 4.3** A schematic plot of (a) disaggregation of the seismic hazard by magnitude and distance, (b) marginal magnitude distribution, and (c) corresponding cumulative sum of marginal magnitude distribution. (Wang et al., 2023)

The joint distribution  ${}^2P_b$  and marginal distribution  ${}^1P_b$  and  ${}^1P_d$  are derived from disaggregation results for one site, *IM* type, and *IM* level. If a regional multi-*IMs* hazard is analyzed, the calculation must be replicated for all sites, *IM* types, and *IM* levels. A rank-5 tensor  ${}^5P_{b,d,l,j,k}$  is used to represent the relative hazard contribution at *IM* level *l* for *IM* type *k* at site *j* from the magnitude *b* and distance *d* bin. Two rank-4 tensors  ${}^4P_{b,l,j,k}$  and  ${}^4P_{d,l,j,k}$  are used to represent the marginal magnitude and distance distributions for the magnitude *b* bin and distance *d* bin, respectively, at *IM* level *l* for *IM* type *k* at site *j*. These distributions then must be multiplied by the corresponding annual exceedance rate  $\lambda_{l,j,k}$  to obtain the absolute hazard contribution distributions before incorporating them into LASSO

regression. The reason for multiplication is to assign equal weights to magnitude and distance distributions as well as the ground motion hazard when optimizing the LASSO objective function.

Therefore,  ${}^4\lambda_{b,l,j,k}$  and  ${}^4\lambda_{d,l,j,k}$  can be written as indicated by Eqs. 4.10 and 4.11:

$${}^4\lambda_{b,l,j,k} = {}^4P_{b,l,j,k} \circ \lambda_{l,j,k} \quad (4.10)$$

$${}^4\lambda_{d,l,j,k} = {}^4P_{d,l,j,k} \circ \lambda_{l,j,k} \quad (4.11)$$

where  $\circ$  represents the Hadamard product, which is also known as the element-wise product. To absorb Eqs. 4.10 and 4.11 into the LASSO framework, they must be reduced to rank-1 tensors. The same procedure of rank reduction transformation illustrated Figure 4.1 can be performed to obtain the transformed marginal magnitude and distance hazard vectors  $\lambda_M$  and  $\lambda_R$ .

Similar to the event matrix  $\Lambda$  defined in Eq. 4.8 that is consist of elements  ${}^4\Lambda_{l,j,k,i}$  in Eq. (4.4), and the hazard distribution matrix for each event is also needed. A certain event  $i$  has a specified magnitude; thus, the hazard produced by the event only contributes to the magnitude bin that included the event magnitude and the hazard contribution for other magnitude bins is zero. Likewise, for event  $i$  and site  $j$ , the source-to-site distance is determined, and the hazard contribution from the event occurs only in the distance bin that covers that distance. In consequence, the marginal magnitude and distance distributions for event  $i$  and site  $j$  can be expressed by,

$${}^5\Lambda_{b,l,j,k,i} = \begin{cases} \Lambda_{l,j,k,i}, & m_i \in (m_b - \frac{\Delta m}{2}, m_b + \frac{\Delta m}{2}) \\ 0, & \text{otherwise} \end{cases} \quad (4.12)$$

$${}^5\Lambda_{d,l,j,k,i} = \begin{cases} \Lambda_{l,j,k,i}, & r_{i,j} \in (r_d - \frac{\Delta r}{2}, r_d + \frac{\Delta r}{2}) \\ 0, & \text{otherwise} \end{cases} \quad (4.13)$$

where  $m_i$  is the magnitude of event  $i$ , and  $r_{i,j}$  is the source-to-site distance for event  $i$  and site  $j$ ,  $\Delta m$  and  $\Delta r$  are the bin widths for magnitude and distance. These hazard distributions then need to be transformed into rank-2 tensors using the approach illustrated in Figure 4.2, and the transformed event

hazard distribution matrix for magnitude and distance can be denoted as  $\Lambda_M$  and  $\Lambda_R$ .

In summary, to preserve magnitude and distance hazard contributions in the event selection for regional multi-IM hazard analysis, should be expanded by incorporating magnitude and distance hazard distributions according to Equation (4.8) and (4.9) as,

$$\lambda' = \begin{bmatrix} \lambda \\ \lambda_M \\ \lambda_R \end{bmatrix}, \Lambda' = \begin{bmatrix} \Lambda \\ \Lambda_M \\ \Lambda_R \end{bmatrix} \quad (4.14)$$

where  $\lambda_M$ ,  $\lambda_R$ ,  $\Lambda_M$ , and  $\Lambda_R$  are transformed marginal magnitude and distance hazard vectors as well as transformed event hazard distribution matrix for magnitude and distance. As for the complete and detailed procedures to construct these transformed vectors and matrices, please refer to Wang et al (2023).

#### 4.1.5 Comparison of LASSO and Mixed Integer Linear Optimization

Vaziri et al. (2012) and Han and Davidson (2012) are the first studies that formulated hazard-consistent event subset as a mathematical optimization problem, and they proposed a mixed-integer linear optimization (MILO) method to select the most suitable reduced event subset that recovers the hazard for multiple sites over a broad range of return periods by minimizing sum of absolute errors. However, the MILO method is computationally demanding and might fail to produce a solution for large problems with complex constraints (e.g., multiple intensity measure hazards matching for a relatively broad region). Miller and Baker (2015) improved the MILO method by means of replacing the mixed-integer constraint with a relaxed convex constraint. The relaxed convex constraint improved the computational efficiency, but it sacrificed some accuracy. Soleimani et al. (2021) modified the MILO by adding new constraints and extended the method for regional multi-hazard analysis, including ground motion intensity, liquefaction potential, and

surface fault rupture.

The essence of Vaziri et al. (2012) and Han and Davidson (2012), Miller and Baker (2015), and Wang et al. (2022) is a variable selection problem. Nonetheless, Wang et al. (2022) illustrated that the LASSO regression event selection methodology is significantly more computationally efficient than MILO by implementing both in the same case study given exactly same computational resources. Moreover, the LASSO regression approach can provide solutions for larger problems with many constraints for which MILO generally fails to converge. In addition, Wang (2022) also provided a concise and publicly accessible self-contained R package *RPSHA* to perform all necessary calculations involved in event selections using a variety of functions. Furthermore, Liu (2023c) provided Python scripts to prepare all required inputs and directly utilize R functions in *RPSHA* package to make the LASSO regression event selection algorithm also serviceable and operable in Python.

While the LASSO method is computationally efficient and capable of providing solutions for complex problems, it is less accurate than the MILO method.

## **4.2 Selecting Event Subset for the Delta Region**

Liu et al. (2022) utilized the LASSO-regression based event selection methodology to select a hazard-consistent event subset including 24 fault events and 20 point-sources (background seismicity) out of millions of events in the UCERF3 source model for risk assessment of Bacon Island in the central Sacramento-San Joaquin Delta. The perimeter of Bacon Island is approximately 23 km, and the selected event set, and map of Bacon Island is shown in Fig. 4.4.

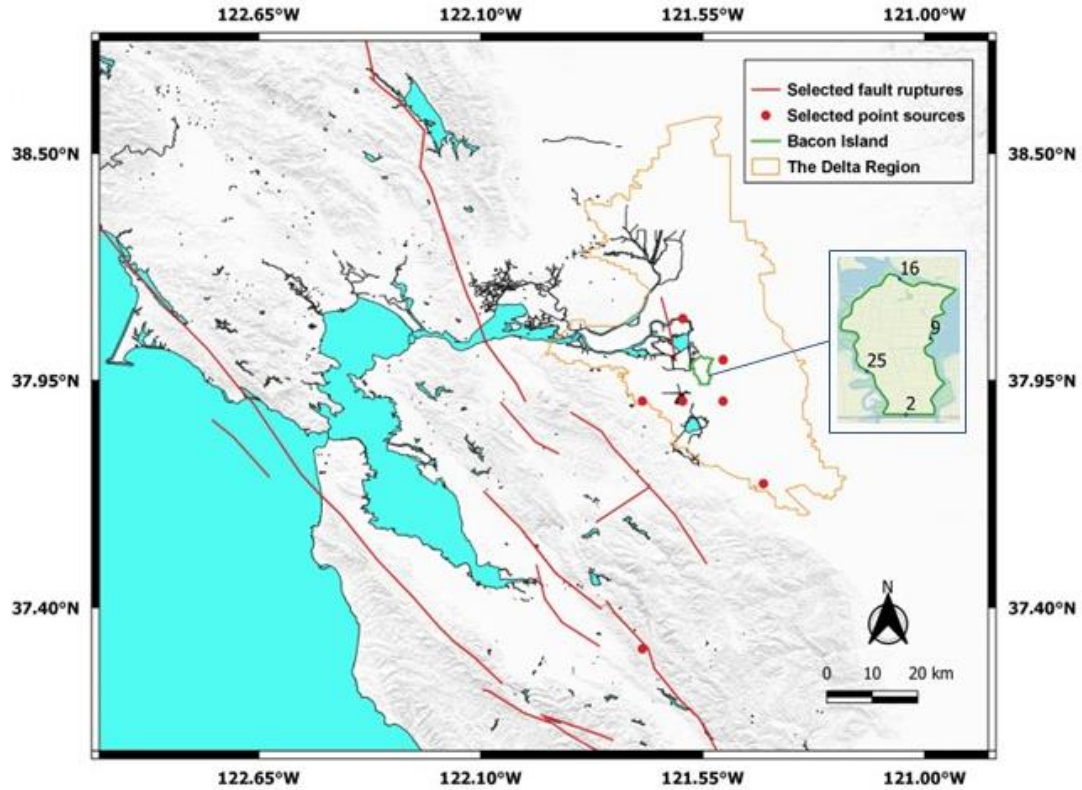


**Figure 4.4** Map showing hazard-consistent event selection results and four target example sites of the Bacon Island levee system in the central Delta region (Liu et al, 2022).

These 44 selected events closely matched *PGV* hazard curves, as illustrated in Figure 4.5 for four sites corresponding approximately to midpoints of the four sides of the island. The hazard curves from the reduced event set closely match the hazard curves for all UCERF3 events for return periods from 10-year to 10000-year.

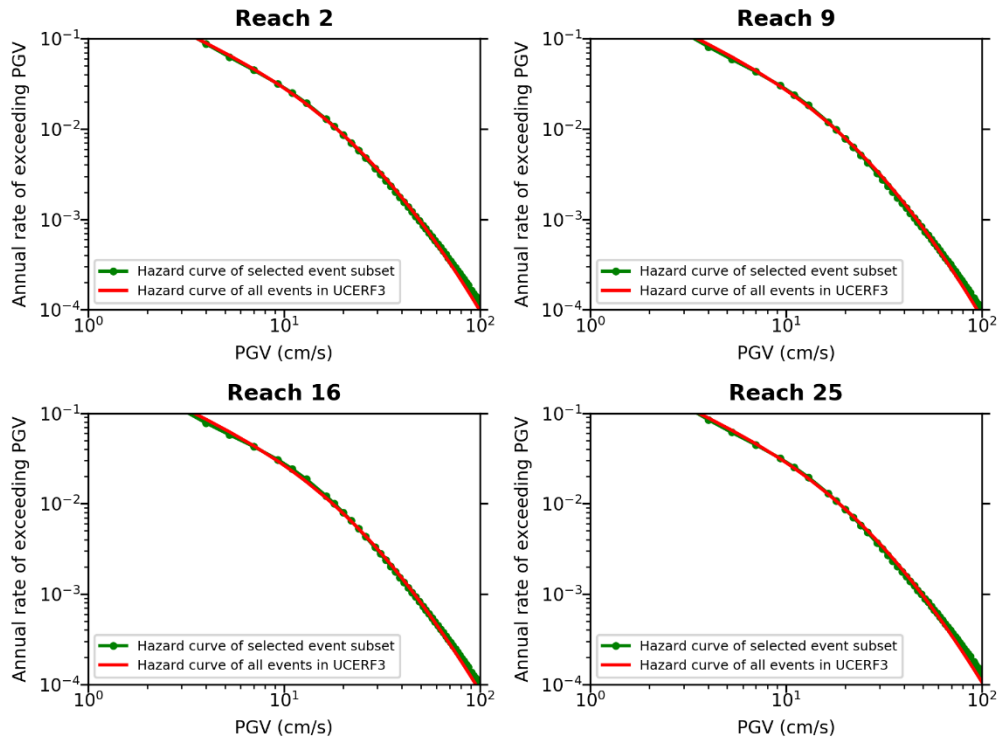


**Figure 4.5** Hazard curves for full PSHA and for event subset at four reach locations on Bacon Island (Liu et al., 2022)

This section expands the study region from Bacon Island to the entire Delta region, resulting in a set of events suitable for analyzing the Delta as a system for levees and other critical spatial distribution infrastructure such as transmission and communication lines. The ultimate goal is to facilitate other researchers and analysts who intend to conduct seismic hazard and risk analysis for infrastructures in the Delta by providing a manageable hazard-consistent event subset. The Delta is discretized into 157 target sites from a square grid with 5km separation distance. Considering the roughly triangular shape of the Delta area, sites located at the three corners are chosen as example sites to illustrate hazard matching and other results. Figure 4.6 shows the study region, labelled 157 target sites, and three example target sites.

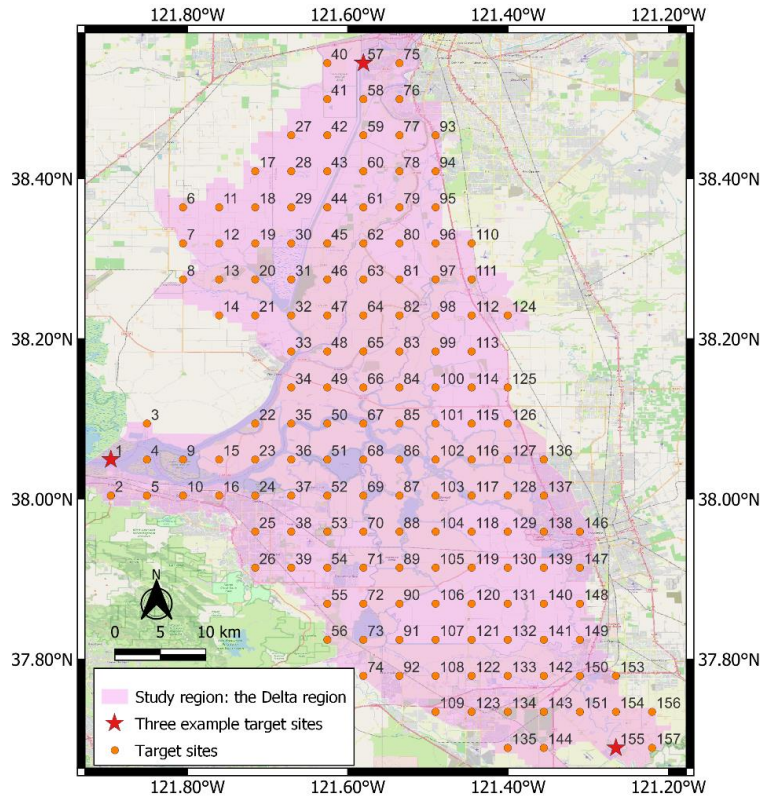


**Figure 4.6** Map showing locations of study region, 157 target sites, and three example target sites.

In this section, two event subsets are developed for the Delta region using LASSO regression event selection algorithm: (1) *PGV*, (2) *PGA*, and (3) *PGA* and **M**. The event set that matches *PGV* is well-suited to levee system analysis using the fragility functions presented herein. The event set that matches *PGA* and **M** is well-suited to liquefaction triggering analysis. (e.g., Youd et al., 2001; Cetin et al., 2004; and Zhang et al., 2004; Idriss and Boulanger, 2006). The event set that matches *PGA* is used for comparison with the accuracy of *PGV* matching, and to illustrate that accuracy decreases when **M** is included. In principle, event sets could be selected for any number of different intensity measures or combinations thereof. However, I focus on *PGV* and *PGA* + **M** in this study because I view these combinations as the most relevant for levee system analysis.

#### 4.2.1 Event Subset for *PGV* Hazard Matching

This section demonstrates event selection implementation for matching of single ground motion hazards of the entire Delta region, and regional *PGV* and *PGA* hazards are matched separately. UCERF3 is used as the source models for the Delta, the source models comprise known faults and background seismicity which are modeled as point sources. The value of time-averaged shear wave velocities in the upper 30 m of the sites of interest is assigned 350 m/s, which is the estimated reference  $V_{s30}$  of the base underneath levee models utilized in previous levee fragility functions development. The USGS National Seismic Hazard Model Program (NSHMP) hazard tool is utilized to perform PSHA at 157 sites for *PGV* and *PGA*, and an NGA-West2 GMM (Boore et al., 2014) is used to conduct ground motions prediction in PSHA. The acquired *PGV* and *PGA*-based hazard curves of 157 sites at the range of 10-year to 2475-year return period are used as the target hazard curves. Disaggregation analysis is also carried out for all sites at 6 return periods of 10, 50, 100, 225, 475, and 2475 years.

A pre-selected event subset is required rather than directly applying LASSO regression to more than 1,600,000 candidate events in UCERF3 utilizing Eq. 4.8 and 4.9, because it would be computationally demanding to invert the resulting matrix. The representative pre-selected subset is determined based on disaggregation results of all sites at 6 return periods, and one event from each source branch for each magnitude-distance bin is selected if it has a relative hazard contribution exceeding a threshold value. Moreover, this pre-selecting approach is repeated for all sites and all *IM* levels. The selection of a proper threshold of relative hazard contribution is an important consideration. Smaller threshold values will conservatively select more potential events and secure better hazard matchings, whereas larger threshold will filter out more events, which relieves the computation burden and improves computing efficiency but may result in poorer



hazard matching. An appropriate threshold balances goodness-of-fit and efficiency, and a threshold of 4% for rupture events and 1% for gridded point sources was found to work well for matching *PGV* hazards. Using this threshold results in 4303 pre-selected events. The event hazard matrix calculation and LASSO regression was implemented using *RPSHA* (Wang, 2022). More specifically,  $\Lambda$  was calculated using the functions *event\_haz\_calc* and *events\_hazmat\_calc* while event selection was conducted using *scenario\_selection* in the *RPSHA* package. Liu (2023c) provided Python scripts to prepare required input variables and call the R functions from *RPSHA* package, so this LASSO regression event selection methodology can also be performed in a Python environment. The results provided by *RPSHA* are a series of selected events and their corresponding rate adjusting multipliers  $\widehat{\beta}_R$ .

The mean of absolute arithmetic relative errors, which is similar to the MHCE (mean hazard curve error) used in Han and Davidson (2012), are utilized to quantitatively assess goodness-of-match of hazard curves from the selected events. This error metric is written as Eq. 4.15.

$$error = \frac{1}{N_S \times N_T \times N_X} \sum_{j=1}^{j=N_S} \sum_{k=1}^{k=N_T} \sum_{l=1}^{l=N_X} \left| \frac{\lambda_{j,k,l} - \sum_{i=1}^{i=N_E} \Lambda_{i,j,k,l} \widehat{\beta}_i}{\lambda_{j,k,l}} \right| \quad (4.15)$$

LASSO regression searches across a range of tuning parameters, so a series of selected event subsets with various number of events are developed. Thus, these results can be utilized to plot the error curve, as indicated in Fig.4.7 that demonstrates error metric versus the number of selected events for the *PGV* hazard matching of the study region. Figure 4.7 shows that the error decreases as the number of selected events increases and eventually saturates to a small value less than 0.1 for more than 41 events. The error decay curve depends on the size pre-selected event set, and lower relative contribution thresholds that result in more pre-selected candidate events from disaggregation cause further reduced saturated error. The error does not monotonically decrease

as the number of selected events increases. This is because after LASSO regression is performed, the rates are re-regressed using least squares regression and the error metric is computed on the re-regressed values.

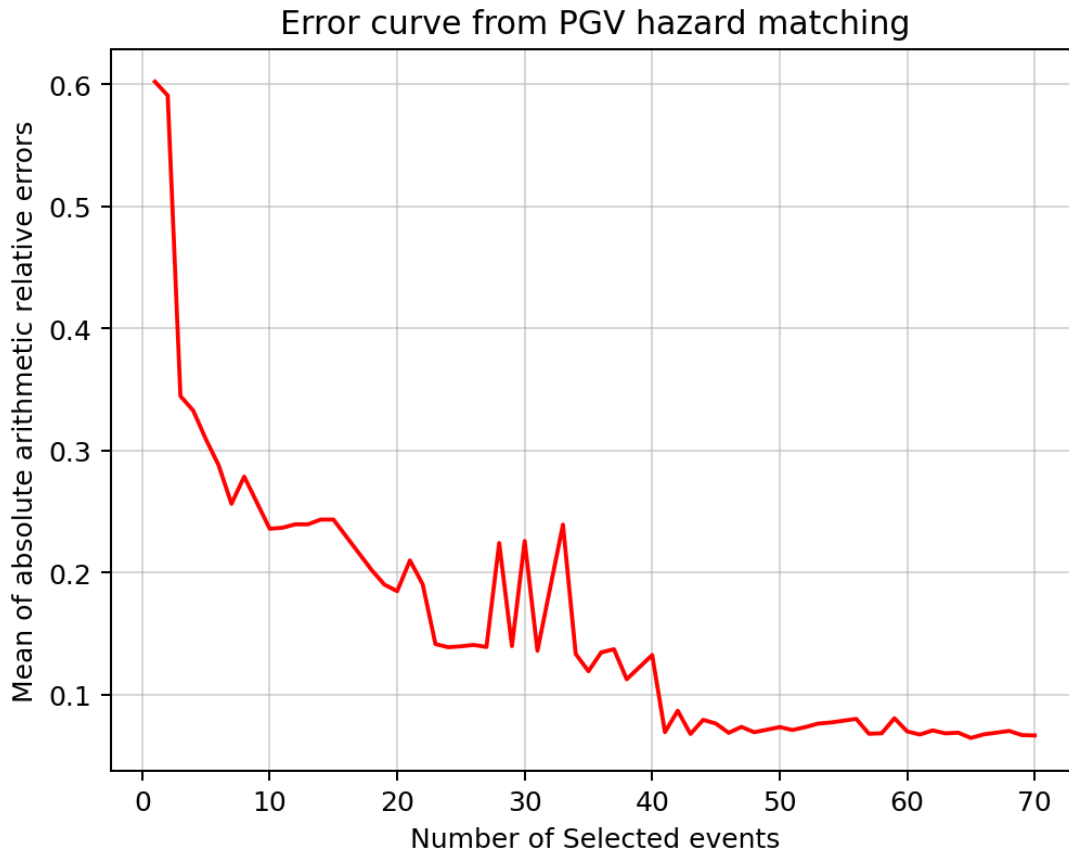


**Figure 4.7** Mean of absolute arithmetic relative errors versus number of selected events for *PGV* hazard matching of the Delta region without preservation of magnitude and distance distributions.

Selecting a preferred number of selected events according to the error decay curve is subjective, and must balance the desired accuracy with the number of events that is reasonable for a particular application. Furthermore, seismic hazard in the Delta generally has contributions from moderate

magnitude events close to the Delta, and larger magnitude events on sources to the west of the Delta (e.g., the Hayward and San Andreas faults). I therefore seek an event set that represents these contributions. Values on the relatively flat region near the end of the error curve generally do a good job of minimizing error and yielding great hazard matching. Based on Fig. 4.6, I select 42 as the recommended target number of selected events yielding the error equaling to 0.0693, and 36 events are from faults sources while 6 events are gridded points.

Liu (2023a) provided Python script to generate .kml. files for events selected from the LASSO regression approach, thereby these files can be accessible and displayed in QGIS to show spatial distributions of the selected events. Figure 4.7 shows the locations of events for *PGV* hazard matching. The nearby Midland fault in the western Delta region and the more distant Hayward and San Andreas faults are selected, which is consistent with the general understanding of the contributions of different source types to seismic hazard in the Delta. Ruptures near or within the Delta generally have moderate-magnitude, and events to the west of the Delta usually have a larger magnitude and lower frequency of occurrence, which mainly dominates hazard at long return periods. Selected points source events are not far from the Delta region, and have smaller magnitudes.

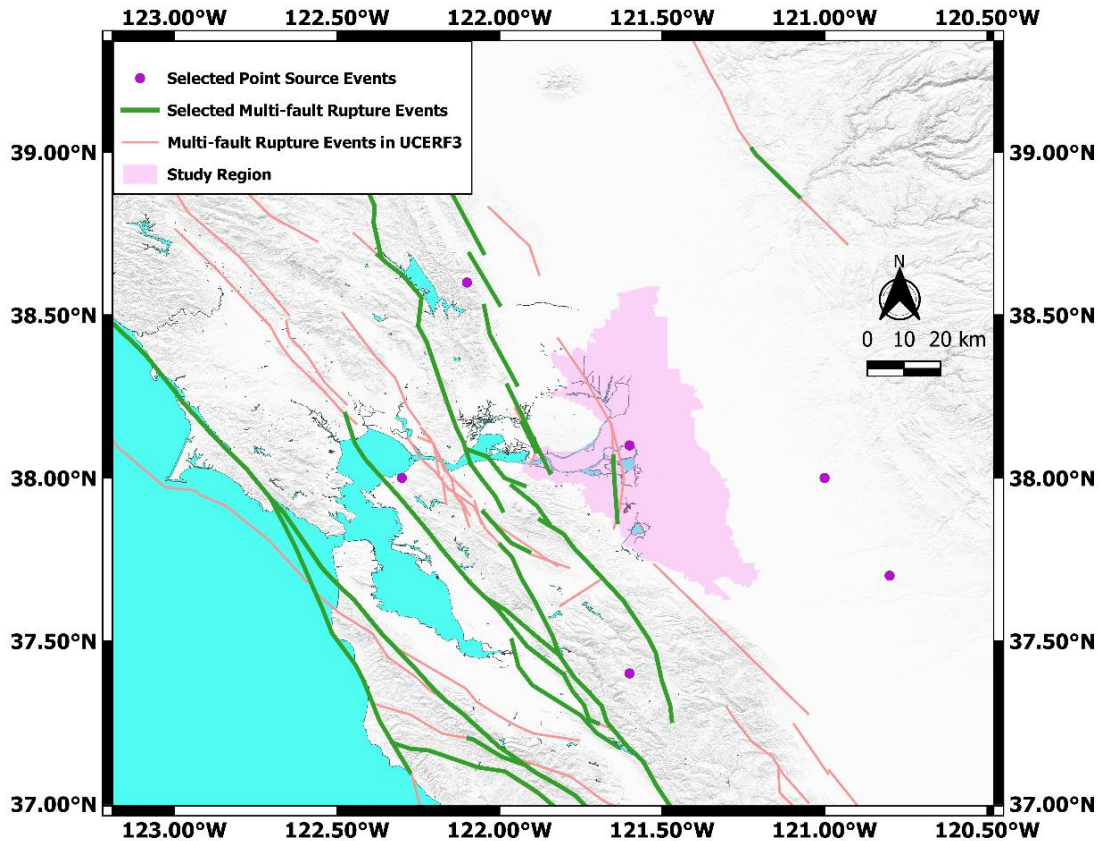


**Figure 4.8** Locations of the 42 selected events (36 selected rupture events and 6 selected point source events) of *PGV* hazard matching without magnitude and distance preservation generated by LASSO regression.

Table 4.2 summarizes type, branch, magnitude, fault section ID, as well as original and adjusted rate of occurrence (ARO) of these 42 selected events. Compared to the original rates of occurrence, the adjusted rates of occurrence in the subset significantly increase to balance the hazard from the unselected events.

**Table 4.2** Selected rupture and point events for *PGV* hazard matching.

Multi-fault Rupture Source						
Branch	Fault Section ID of Event	Magnitude	ARO (yr <sup>-1</sup> )	Type	Adjusted ARO (yr <sup>-1</sup> )	
1	FM31 68:49,951:945,958:952,775:781,346:348,136 0:1359,788:782,794:793	7.8	4.22E-07	SS	0.0007490	
2	FM31 198:200,207:202	6.8	4.42E-07	SS	0.0081612	
3	FM31 195:200,207:202	6.9	3.14E-07	SS	0.0012904	
4	FM31 711:712	6.2	1.86E-06	SS	0.0019727	
5	FM31 194:200,207:202	7.0	2.78E-07	SS	0.0003320	
6	FM31 830:835,818:827	7.2	9.70E-06	SS	0.0075399	
7	FM31 191:200,1294:1283,832:835,818:819	7.1	8.06E-08	SS	0.0012180	
8	FM31 1924:1927,1811:1822,215:208,217:222,191: 199,828:832	7.3	1.96E-08	SS	0.0008368	
9	FM31 2173:2171,2158:2153,2191:2183,2179:2177, 1945:1944,1851:1832,1778:1772,1786:1779, 1787:1797,1920:1927,1811:1831,1973:1965, 1928:1943,1864:1907	8.3	1.63E-09	SS	0.0029726	
10	FM31 221:222,191:199,828:835,818:820	7.2	6.45E-08	SS	3.08E-05	
11	FM31 221:222,191:199,828:832	7.0	5.37E-06	SS	0.0093727	
12	FM31 1872:1864,1943:1929,180:178,1966:1973,18 31:1811,1927:1920,1797:1787,1779:1786,17 72:1778,1832:1851,1944:1949,1852:1863,17 98:1803	8.2	1.76E-10	SS	0.0006477	
13	FM31 1916:1864,1943:1928,1965:1973,1831:1811, 1927:1920,1797:1787,1779:1786,1772:1778, 1832:1851,1944:1949,1852:1855	8.3	1.97E-09	SS	3.99E-07	
14	FM31 1883:1864,1943:1928,1965:1973,1831:1811, 1927:1920,1797:1787,1779:1786,1772:1778, 1832:1851,1944:1949,1852:1863,1798:1809, 157:166,972:970	8.3	4.66E-09	SS	1.32E-08	
15	FM31 1889:1864,1943:1928,1965:1973,1831:1811, 1927:1920,1797:1787,1779:1786,1772:1778, 1832:1851,1944:1945,2177:2179,2183:2191, 2153:2158,2171:2176,2159:2164,2192:2194	8.3	1.84E-08	SS	1.61E-07	
16	FM31 1959:1964,1956:1944,1851:1832,1778:1772, 1786:1779,1787:1797,1920:1927,1811:1831, 1973:1965,1928:1943,1864:1919,1247:1274	8.3	2.22E-06	SS	4.38E-08	
17	FM31 65:49,951:945,958:952,775:781,346:348,136 0:1359,788:782,794:793	7.7	1.97E-07	SS	4.03E-05	
18	FM31 193:194,2381:2389,1289:1287	6.9	2.21E-08	SS	0.0001760	
19	FM31 781:775,952:958,945:951,49:71,494:497	7.7	6.59E-07	SS	9.35E-05	
20	FM31 822:818,835:828,842:837,2383:2382	7.2	1.71E-08	SS	3.76E-05	
21	FM31 1916:1864,1943:1928,1965:1973,1831:1811, 1927:1920,1797:1787,1779:1786,1772:1778, 1832:1851,1944:1945,2180:2189	8.3	8.70E-09	SS	3.62E-06	
22	FM31 192:199,828:835,818:820	7.2	2.66E-07	SS	1.50E-05	
23	FM31 2174:2171,2158:2153,2191:2183,2179:2177, 1945:1944,1851:1832,1778:1772,1786:1779, 1787:1797,1920:1927,1811:1831,1973:1965,	8.3	2.88E-08	SS	1.51E-06	

1928:1943,1864:1907							
24	FM31	778:775,952:958,945:951,49:71,494:496	7.7	2.87E-07	SS	0.00118062	
25	FM31	1893:1864,1943:1929,180:178,1966:1973,1831:1811,1927:1920,1797:1787,1779:1786,1772:1778,1832:1851,1944:1949,1852:1863	8.3	2.34E-10	SS	2.33E-05	
26	FM31	2465:2467	6.5	1.89E-06	N	0.0297200	
27	FM31	1890:1864,1943:1928,1965:1973,1831:1811,1927:1920,1797:1787,1779:1786,1772:1778,1832:1851,1944:1949,1852:1863,1798:1809,157:166,972:963	8.3	7.37E-08	SS	2.47E-05	
28	FM31	2183:2180,1945:1944,1851:1832,1778:1772,1786:1779,1787:1797,1920:1927,1811:1831,1973:1965,1928:1943,1864:1919,1247:1277	8.3	6.70E-09	SS	1.20E-07	
29	FM31	2176:2171,2158:2153,2191:2180,1945:1944,1851:1832,1778:1772,1786:1779,1787:1797,1920:1927,1811:1831,1973:1965,1928:1943,1864:1902	8.3	2.72E-08	SS	9.31E-10	
30	FM31	1891:1865,2115:2132,2598:2605,1831:1811,1927:1920,1797:1787,1779:1786,1772:1778,1832:1851,1944:1953	8.2	1.74E-09	SS	0.0001355	
31	FM32	1987:1985	6.5	1.37E-06	SS	0.0503318	
32	FM32	219:212,221:226,195:204,1303:1300	7.1	1.53E-07	SS	0.0001563	
33	FM32	809:814,802:808,741:740,738:725,717:703	7.7	2.11E-08	R	6.14E-05	
34	FM32	797:795,971:977,964:970,53:75,519:520	7.7	6.51E-07	SS	0.0008259	
35	FM32	809:814,802:808,323:321,1163:1164,734:732	7.4	1.38E-07	SS	0.0002705	
36	FM32	813:814,802:808,741:740,738:725,717:696	7.7	6.69E-09	R	3.41E-06	
Point Sources							
	Branch	Point Longitude, Latitude, and Elevation (°, °, km)	Magnitude	ARO (yr <sup>-1</sup> )	Type	Adjusted ARO (yr <sup>-1</sup> )	
1	FM31	-122.3, 38.0, 0.0	5.9	5.18E-05	N	0.0714617	
2	FM31	-121.6, 37.4, 0.0	5.5	0.00011042	SS	0.1000437	
3	FM32	-121.6, 38.1, 0.0	6.0	1.17E-05	SS	0.0001829	
4	FM32	-122.1, 38.6, 0.0	6.1	9.88E-06	R	0.0163008	
5	FM32	-121.0, 38.0, 0.0	5.8	5.22E-06	N	0.0252002	
6	FM32	-120.8, 37.7, 0.0	5.8	5.99E-06	SS	0.0297683	

Figure 4.9 shows the comparisons of *PGV* hazard curves over the considered range of rates (approximately 0.0004 to 0.1, equivalently 10-year to 2475-year return period) between the full event set and event subset for three example sites. The hazard is quite different at these sites, being larger for site 1 and smaller for sites 57 and 155 due to their relative proximity to active faults. The

agreement is quite good between the full event set and the reduced event subset for all three locations. Moreover, though not shown here for brevity, comparisons for other sites exhibit the same trend, which illustrates that the reduced event subset can accurately quantify the regional seismic hazard in the Delta.

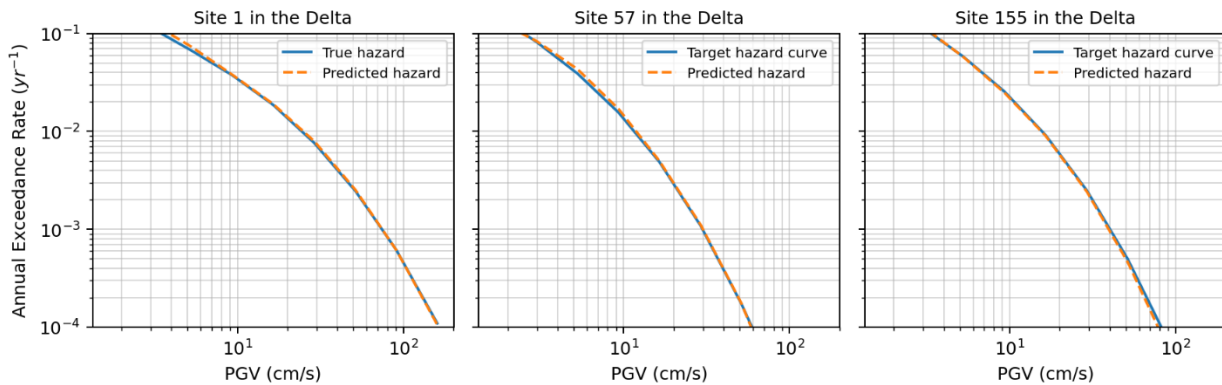


**Figure 4.9** True and recovered hazard curves for  $PGV$  by the 42 selected events from the LASSO regression method without preservation of magnitude and distance distributions hazard matching of three example sites.

#### 4.2.2 Event Subset for $PGA$ Hazard Matching

The same event selection procedure is replicated for  $PGA$  hazard, and I investigate and present the event selection results with and without point source magnitude constraints. For liquefaction evaluation,  $PGA$  and  $M$  are required, but I first focus only on  $PGA$  for the purpose of making comparisons with  $PGV$ . For the case with no point source magnitude constraints, the threshold of 5% for rupture events and 3% for gridded point sources are selected in the pre-select process, and it yields 1104 candidate events based on disaggregation results. Figure 4.10 shows the error decay curve, and 44 events are selected as the recommended target number of selected events associated

with the error equaling 0.0844. The error for the *PGA* event subset is similar to that for *PGV* from the previous section, but more events were required to achieve this error level for *PGA*. This illustrates that a different number of events may be needed for different intensity measures, which is likely the result of the rate of decay of the intensity measure with source-to-site distance. I believe more events are required for high-frequency intensity measures, like *PGA*, that decay more quickly with distance, and fewer events are needed for lower frequency *IM*'s, like *PGV*, that decay more slowly.

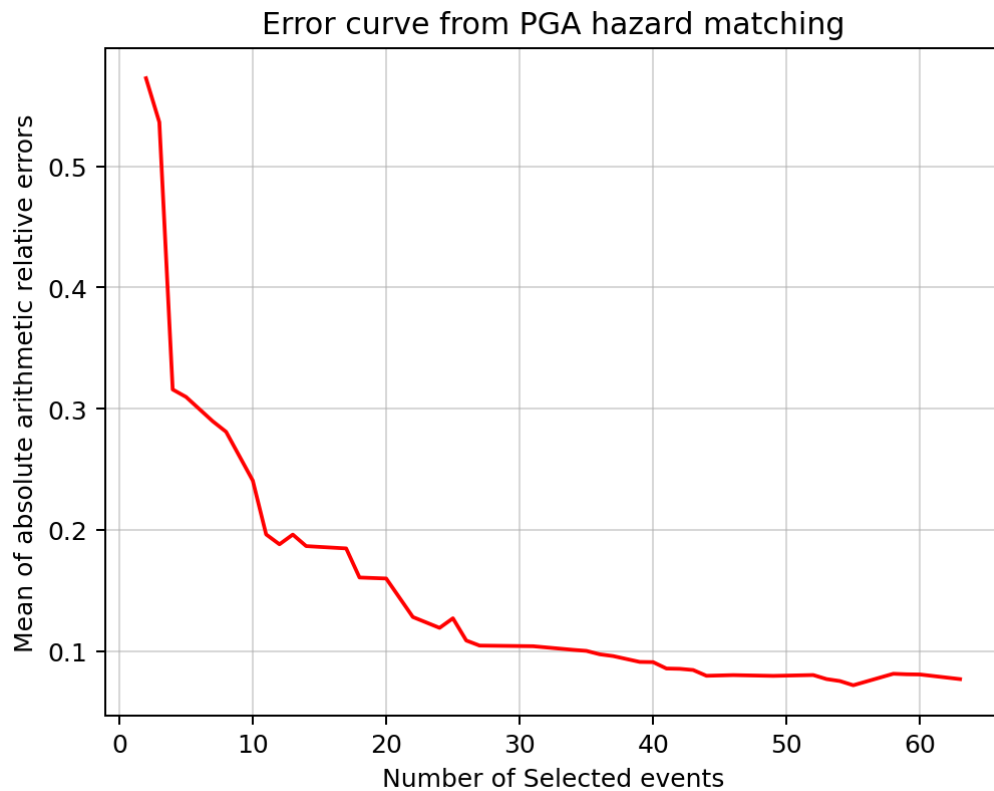


**Figure 4.10** Mean of absolute arithmetic relative errors versus number of selected events for *PGA* hazard matching of the Delta region without preservation of magnitude and distance distributions.

Figure 4.11 shows the locations of 44 selected events incorporating 10 fault events and 34 point source events, and Table 4.3 demonstrates these selected events in detail and their corresponding



computed adjusted ARO. Selected faults events are mainly on the western side of the Delta, but one fault, the Great Valley Midland fault, is within the Delta. Compared to single *PGV* hazard matching, more point sources are selected and some of them are located far from the Delta region with larger magnitudes. Rupture events involve many replicated sub-sections of faults with a variety of magnitudes, therefore, there are fewer plotted fault segments in Figure 4.10 than the number of fault events. Likewise, a single point source can generate multiple events with various magnitudes, so the number of point sources on the map in Figure 4.11 is smaller than 34.

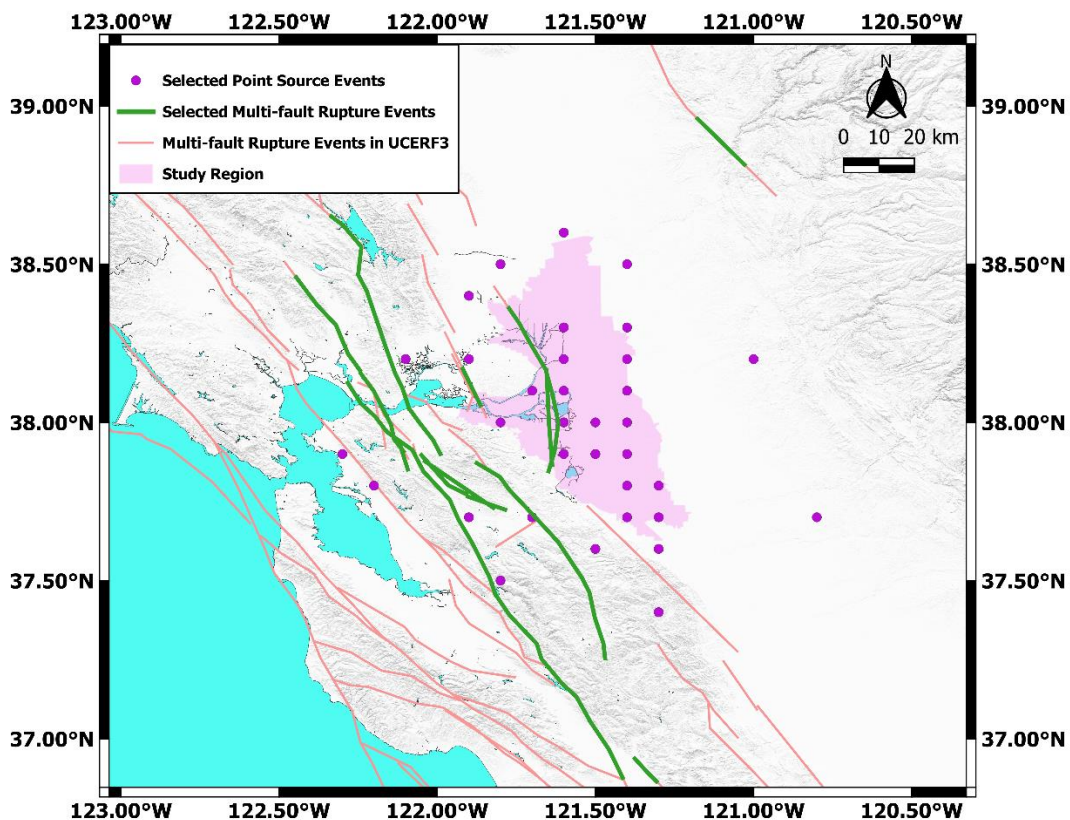


**Figure 4.11** Locations of the 44 selected events (10 selected rupture events and 34 selected point source events) of *PGA* hazard matching generated without magnitude and distance preservation by LASSO regression.

**Table 4.3** Selected rupture and point events for *PGA* hazard matching.

<b>Multi-fault Rupture Source</b>						
<b>Branch</b>	<b>Fault Section ID of Event</b>	<b>Magnitude</b>	<b>ARO (yr-1)</b>	<b>Type</b>	<b>Adjusted ARO (yr-1)</b>	
1	FM31 2537:2542,351:355,350:349,1360:1359	7.3	1.84E-08	SS	0.000754	
2	FM31 2541:2542,585:580,201:207,200:191,222:218,1639,1640	7.4	1.81E-08	SS	0.008208	
3	FM31 953:952,775:781,346:348,1360:1359,1362:1361,787:782,794:789	7.4	7.26E-07	SS	0.001102635	
4	FM31 715:721	7.2	7.57E-06	R	0.000162985	
5	FM31 2464:2466	6.5	2.34E-06	N	0.028181	
6	FM32 735:737	6.2	8.70E-06	R	0.00237882	
7	FM32 803,802	6.2	0.00016488	SS	0.00039102	
8	FM32 803:802,814:809	6.7	8.05E-05	SS	0.007595389	
9	FM32 812:814,802:807,1368:1371,351:349,801:795,971:976	7.3	1.73E-07	SS	1.98E-06	
10	FM32 807:808,741:739	7.1	7.48E-06	R	2.30E-05	
<b>Point Source</b>						
<b>Branch</b>	<b>Point Longitude, Latitude, and Elevation (°, °, km)</b>	<b>Magnitude</b>	<b>ARO (yr-1)</b>	<b>Type</b>	<b>Adjusted ARO (yr-1)</b>	
1	FM31 -121.9, 38.2, 0.0	6.9	5.78E-07	R	0.003538396	
2	FM31 -121.5, 37.9, 0.0	7.1	8.93E-07	SS	0.000184903	
3	FM31 -121.8, 38.0, 0.0	6.0	2.04E-05	R	0.001718436	
4	FM31 -121.6, 38.0, 0.0	6.6	3.27E-06	N	0.000273122	
5	FM31 -122.1, 38.2, 0.0	5.4	4.51E-05	N	0.039778721	
6	FM31 -121.9, 37.7, 0.0	5.6	7.09E-05	R	0.037138838	
7	FM31 -121.5, 38.0, 0.0	5.7	2.25E-05	R	0.000151285	
8	FM31 -121.6, 38.1, 0.0	5.4	4.10E-05	SS	0.000344455	
9	FM31 -121.4, 38.1, 0.0	6.2	5.05E-06	R	0.000202887	
10	FM31 -121.3, 37.8, 0.0	6.1	8.50E-06	SS	0.000278408	
11	FM31 -121.4, 38.0, 0.0	6.0	9.16E-06	N	0.000324019	
12	FM31 -121.4, 38.3, 0.0	6.5	1.90E-06	SS	0.000211864	
13	FM31 -121.4, 37.7, 0.0	7.0	1.63E-06	SS	8.19E-05	
14	FM31 -121.6, 37.9, 0.0	5.1	1.00E-04	R	0.001444	

							552
15	FM31	-121.7, 37.7, 0.0	6.3	2.74E-06	N	2.89E-06	
16	FM31	-121.4, 38.5, 0.0	7.1	1.87E-07	R	0.000341 159	
17	FM31	-121.0, 38.2, 0.0	5.7	4.13E-06	N	0.010191 693	
18	FM31	-121.3, 37.4, 0.0	5.3	8.62E-05	SS	0.069017 545	
19	FM31	-122.3, 37.9, 0.0	5.4	0.0001278 03	SS	0.027550 571	
20	FM31	-121.8, 37.5, 0.0	5.1	0.0002731 33	SS	0.109274 806	
21	FM32	-121.7, 38.1, 0.0	5.4	4.01E-05	SS	0.001182 697	
22	FM32	-122.2, 37.8, 0.0	7.0	1.60E-07	N	0.013738 384	
23	FM32	-121.6, 38.2, 0.0	5.3	3.88E-05	R	0.000820 176	
24	FM32	-121.6, 38.3, 0.0	6.4	3.92E-06	N	0.000298 547	
25	FM32	-121.4, 38.2, 0.0	6.5	2.40E-06	R	6.66E-05	
26	FM32	-121.4, 37.8, 0.0	6.4	7.40E-06	N	0.000380 635	
27	FM32	-121.4, 37.9, 0.0	6.5	4.75E-06	N	0.000386 638	
28	FM32	-121.3, 37.7, 0.0	6.3	8.62E-06	R	0.000449 718	
29	FM32	-121.3, 37.6, 0.0	7.0	1.51E-06	SS	0.000600 951	
30	FM32	-121.5, 37.6, 0.0	7.0	2.10E-08	R	0.000175 54	
31	FM32	-121.8, 38.5, 0.0	5.1	4.64E-05	R	0.012431 764	
32	FM32	-121.9, 38.4, 0.0	5.1	6.62E-05	SS	0.003781 147	
33	FM32	-121.6, 38.6, 0.0	7.4	5.54E-08	R	0.000300 03	
34	FM32	-120.8, 37.7, 0.0	6.1	2.79E-06	N	0.023842 876	

Figure 4.12 compares *PGA* hazard curves of three example sites from full hazard calculation to those recovered from 44 selected events with adjusted rates. The hazard curves match very well.

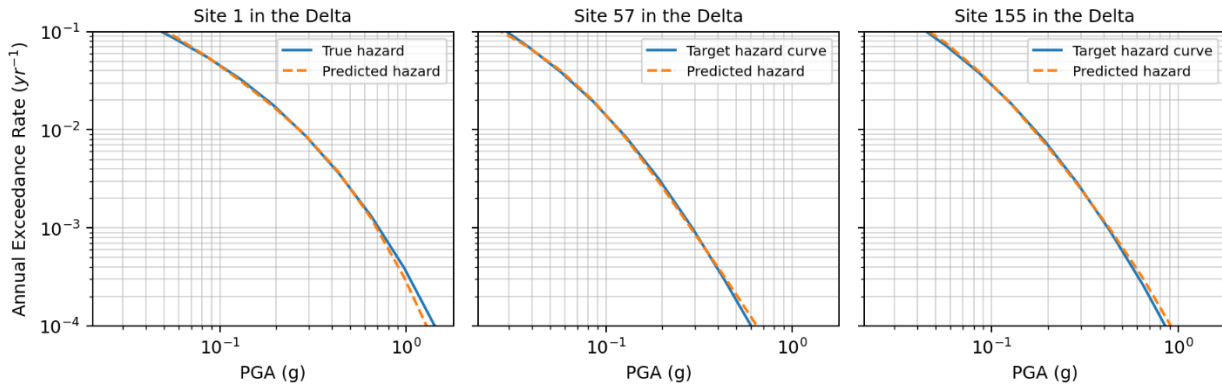
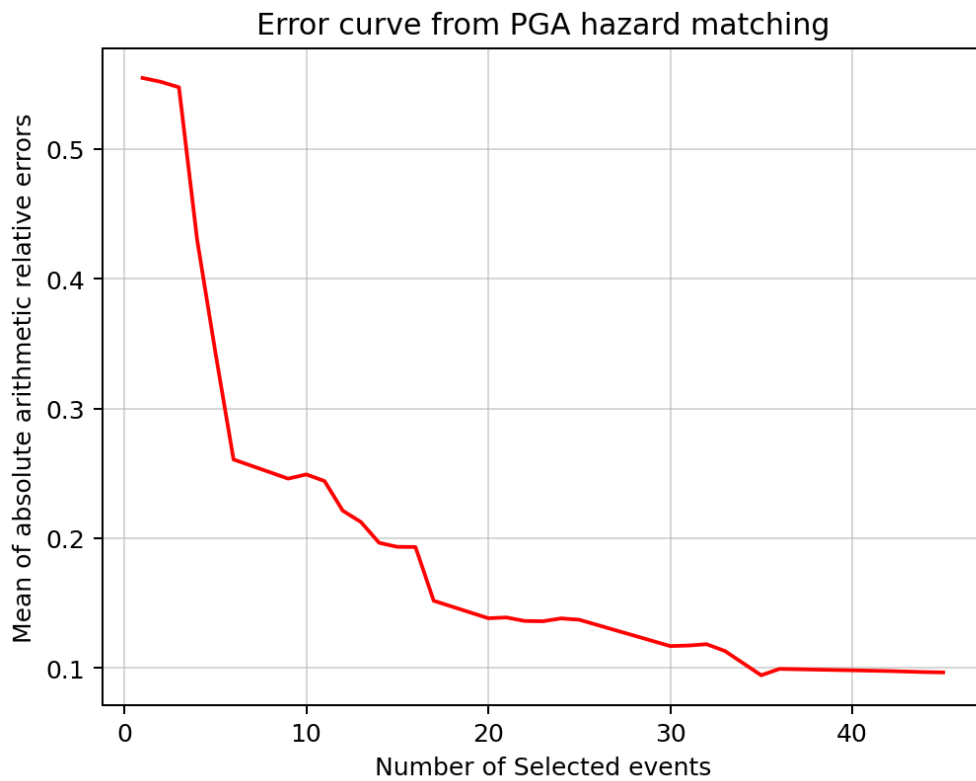


**Figure 4.12** True and recovered hazard curves for  $PGA$  by the 44 selected events from the LASSO regression method without preservation of magnitude and distance distributions hazard matching of three example sites.

Although the  $PGA$ -based hazard curve matching presented in Fig. 4.12 is excellent, a careful review of the selected points sources shows that some point source events have large magnitudes, such as 7 and 7.4. Background events in the UCERF3 model are treated as point sources, which is reasonable for small magnitude events, but unreasonable for large magnitude events for which the fault rupture zone would be very large relative to the Delta. Source-to-site distance calculations would therefore be significantly different if the point sources were modeled with realistic rupture sizes. These unreasonable events indeed exist in UCERF3 source model, and the fact they were selected in the event subset is considered a deficiency of UCERF3 rather than a deficiency of the event selection methodology. These point source events associated with large magnitudes may have little influence on PSHA results in light of their extremely low rates, but including these events in a subset is not desirable. I therefore decided to rerun the event selection after removing point source events with magnitude larger than 6.5 during the pre-selecting procedure. I had to decrease the point source hazard contribution threshold to 0.1% to ensure an adequate number of gridded point events are picked up prior implementing LASSO regression to choose final reduced

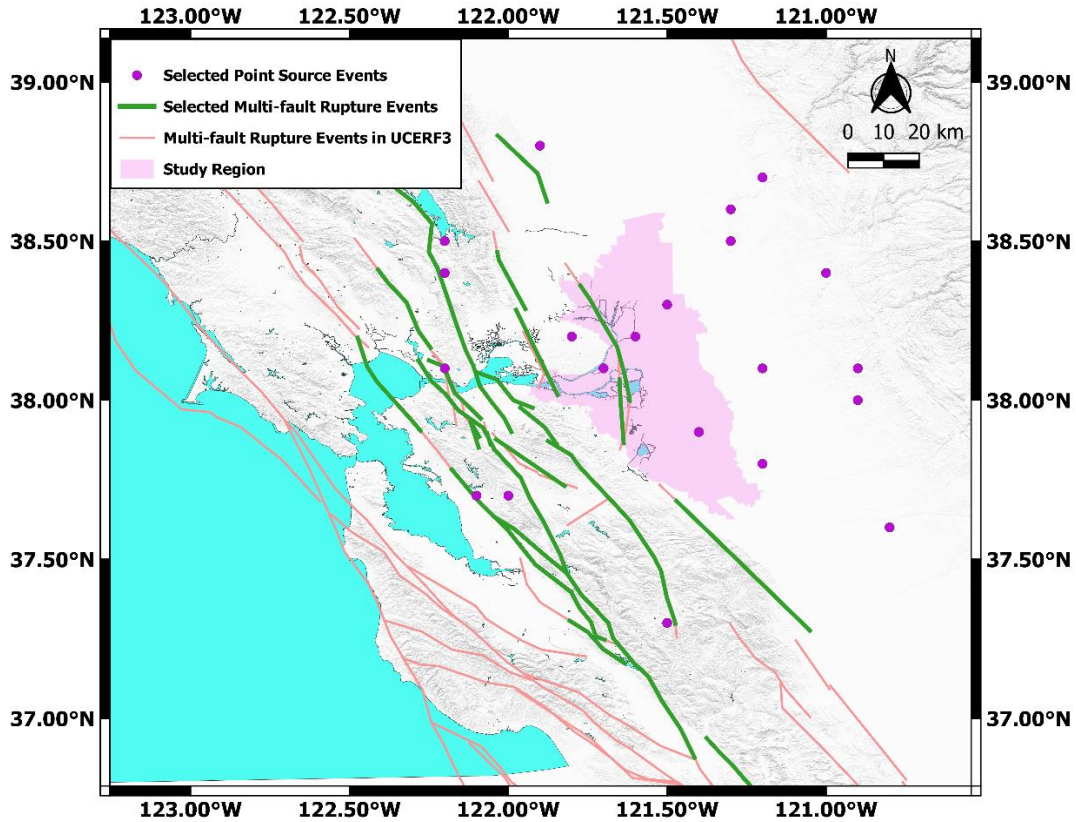
event set. Therefore, 809 fault rupture events and 182 point events are pre-selected, and then I perform LASSO regression to choose final events. Fig. 4.12 presents the specified calculated errors versus the number of the reselected events.

Fig. 4.13 shows the updated error decay curve as increasing the number of events, a greater number of events are required to remain same level of errors compared to the no magnitude constraint case. Therefore, 42 events are selected as the target number of events and the calculated error is about 0.1.



**Figure 4.13** Mean of absolute arithmetic relative errors versus number of selected events for *PGA* hazard matching of the Delta region after excluding points sources with magnitude larger than 6.5.

Based on Figure 4.14, more fault rupture and less points sources are selected, and the Hayward fault which has large magnitude and is far from the Delta is selected in the updated reduced event subset. Table 4.4 presents the fundamental information about the re-selected events.



**Figure 4.14** Locations of the 42 reselected events (19 selected rupture events and 23 selected point source events) of *PGA* hazard matching generated by LASSO regression after excluding points sources with magnitude larger than 6.5.

**Table 4.4** Re-selected rupture and point events for *PGA* hazard matching.

<b>Multi-fault Rupture Source</b>						
<b>Branch</b>	<b>Fault Section ID of Event</b>	<b>Magnitude</b>	<b>ARO (yr<sup>-1</sup>)</b>	<b>Type</b>	<b>Adjusted ARO (yr<sup>-1</sup>)</b>	
1	FM31	821:827	6.7	1.67E-05	SS	0.006805256
2	FM31	778:775,952:956	6.5	0.000199457	SS	0.000939885
3	FM31	1287:1294,200:191,222:218,1639:1643	6.9	4.81E-07	SS	0.003937211
4	FM31	724:738	6.8	1.54E-06	R	0.000557707
5	FM31	197:200,1294:1283,832:835	7.0	1.07E-07	SS	0.001547416
6	FM31	193:199,828:832	7.0	9.74E-06	SS	0.000884887
7	FM31	729:739	6.6	1.04E-05	R	0.00077342
8	FM31	204:201,580:585,2542:2539	7.2	2.65E-08	SS	0.009870812
9	FM31	778:775,952:959	6.7	7.64E-05	SS	0.003053995
10	FM31	715:719	7.0	4.27E-06	R	0.000204949
11	FM31	696:702	6.5	6.23E-05	R	0.001057472
12	FM32	225:226,195:198,2446:2449	6.6	1.32E-07	SS	0.03880714
13	FM32	196:198,2446:2448,857:862,848:850	6.9	4.34E-08	SS	9.16E-05
14	FM32	202:203,848:854	6.9	7.58E-07	SS	0.001282768
15	FM32	207:205,360,365:364,603:607,2599:2595	7.2	1.97E-09	SS	0.003347909
16	FM32	368:369,363:362,366:367,357:356,205:211,204:203,862:861	7.2	5.29E-09	SS	2.95E-06
17	FM32	810:814,802:807,1368:1371,351:349,801:795,971:977	7.4	2.06E-07	SS	0.002888224
18	FM32	805:808,323:321,1163:1164,734:729	7.3	3.89E-08	R	0.001422477
19	FM32	735:738,740:741	7.0	4.81E-08	R	0.000187041
<b>Point Source</b>						
<b>Branch</b>	<b>Point Longitude, Latitude, and Elevation (°, °, km)</b>	<b>Magnitude</b>	<b>ARO (yr<sup>-1</sup>)</b>	<b>Type</b>	<b>Adjusted ARO (yr<sup>-1</sup>)</b>	
1	FM31	-122.0, 37.7, 0.0	5.7	7.91E-05	N	0.038722077
2	FM31	-121.8, 38.2, 0.0	5.7	2.47E-05	R	0.000681317
3	FM31	-121.6, 38.2, 0.0	6.4	4.93E-06	N	0.000301839
4	FM31	-122.2, 38.1, 0.0	6.1	8.40E-06	R	0.007081357
5	FM31	-121.4, 37.9, 0.0	5.7	2.23E-05	SS	0.000401691
6	FM31	-121.5, 38.3, 0.0	6.4	3.07E-06	N	0.000410025
7	FM31	-122.2, 38.4, 0.0	5.7	2.83E-05	N	0.02166097
8	FM31	-121.3, 38.5, 0.0	6.5	9.87E-07	N	0.001065403
9	FM31	-121.3, 38.6, 0.0	6.4	1.08E-06	SS	1.30E-06
10	FM31	-121.0, 38.4, 0.0	5.8	2.64E-06	R	0.003033464
11	FM31	-121.5, 37.3, 0.0	5.3	0.000210845	N	0.169442876
12	FM31	-120.9, 38.0, 0.0	5.6	5.94E-06	N	0.00896342
13	FM31	-120.8, 37.6, 0.0	6.4	2.31E-06	N	0.001433774
14	FM31	-122.1, 37.7, 0.0	5.1	0.000248666	SS	0.072965522
15	FM31	-121.2, 38.7, 0.0	5.4	5.94E-06	R	0.010594853
16	FM31	-122.2, 38.5, 0.0	5.3	6.93E-05	SS	0.03387262

17	FM32	-121.7, 38.1, 0.0	5.5	3.33E-05	N	0.002391866
18	FM32	-121.2, 38.1, 0.0	6.4	2.23E-06	R	0.001141843
19	FM32	-121.2, 37.8, 0.0	6.0	8.65E-06	R	0.000652062
20	FM32	-121.5, 37.3, 0.0	5.6	0.000121328	R	0.00199108
21	FM32	-120.9, 38.1, 0.0	5.1	1.23E-05	SS	0.043515012
22	FM32	-120.8, 37.6, 0.0	5.1	2.62E-05	R	0.032437734
23	FM32	-121.9, 38.8, 0.0	5.1	3.28E-05	N	0.027968848

Fig. 4.15 shows the *PGA*-based hazard curves for the three example sites. Compared to the previous matching results, there are some slight differences between hazard curves over the large return periods, which is also consistent with the higher error in Fig. 4.13 compared with Fig. 4.10. Figure 4.15 demonstrates the *PGA*-based hazard curve matchings of example sites are relatively favorable and other sites also have similar exceptional hazard curve matchings, so the hazard only produced by these re-selected 42 events associated with adjusted annual rates of occurrence is a reasonable representation of the overall regional hazard of the Delta.

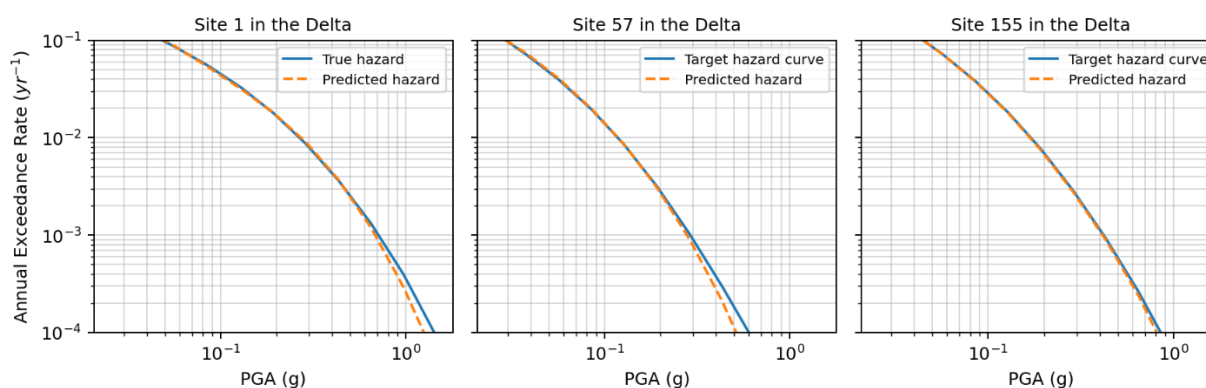


**Figure 4.15** True and recovered hazard curves for *PGA* by the 42 reselected events from the LASSO regression method of three example sites.

Overall, the hazard curves in Fig. 4.14 for the event subset reasonably match the overall hazard,



and I consider the representation of events in the subset to be more reasonable than the previous event set that included unreasonably large point source events. For this reason, I suggest that this second event subset is more reasonable and should be used in system reliability analyses, even though the hazard matching is not as good as the first event subset.

### 4.2.3 Event Subset for *PGA* and *M* Hazard Matching

Single ground motion hazard matching without preserving relative contributions to hazard across magnitude and distance bins has been demonstrated, but sometimes magnitude is also a critical parameter in seismic analysis, such as lateral displacement, landslide, and liquefaction analysis. Consequently, the event selection of *PGA* hazard matching with preserving marginal magnitude distribution for the Delta area is also discussed in this study, which can be very useful in earthquake induced liquefaction triggering analysis.

Magnitude hazard distributions for the target vector  $\lambda_M$  and event hazard matrix  $\Lambda_M$  were developed based on the procedures described in the Section 4.1. The *Deagg\_to\_MR\_Hazd* and *Event\_to\_MR\_Hazd* functions in *RPSHA* package were used to conduct these calculations. Furthermore, as indicated in Eq. 4.14, target ground motion hazard vector  $\lambda$  and target magnitude hazard distribution  $\lambda_M$  are stacked together to form a new target vector  $\lambda'$ , while event hazard matrices  $\Lambda$  and  $\Lambda_M$  are combined to develop the updated event hazard matrix  $\Lambda'$ . Then, LASSO regression was applied to  $\lambda'$  and  $\Lambda'$  to initiate event selection.

Similarly, the events selections results with and without point event magnitude constraints are both presented here. When point source magnitude is unconstrained, the LASSO regression is applied based on the 1104 pre-selected events. Figure 4.16 shows the errors versus the number of selected events, and 82 events are selected, and the associated error is approximately 0.317. In general,

more events are required when more constraints are added to the hazard matching algorithm. The error is higher than when *PGA* is matched on its own because magnitude misfit is now included in the error calculation.

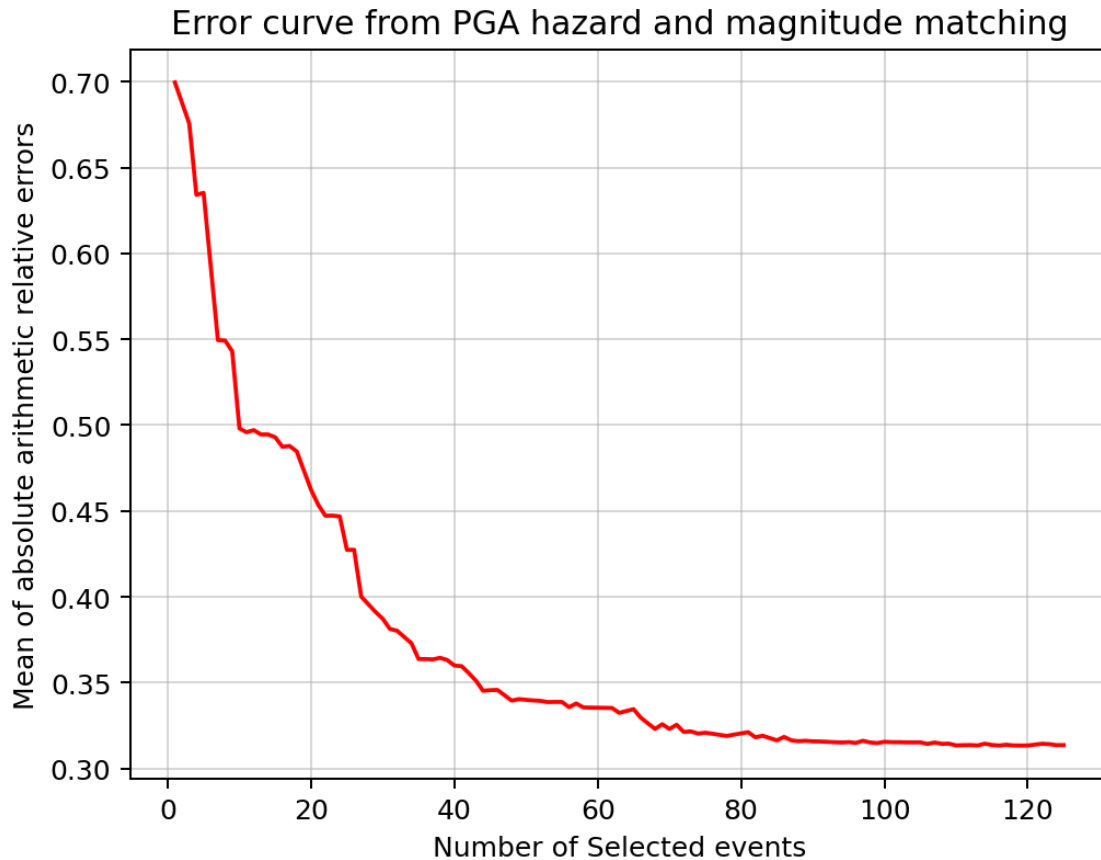


**Figure 4.16** Mean of absolute arithmetic relative errors versus number of selected events for *PGA* hazard matching of the Delta region with preservation of magnitude distributions.

Fig. 4.17 shows the locations of 82 selected events and Table 4.5 presents the fundamental information of these events, and most selected events are on the southwest side of the Delta. Large magnitude events to the west of the Delta were not selected in this subset.

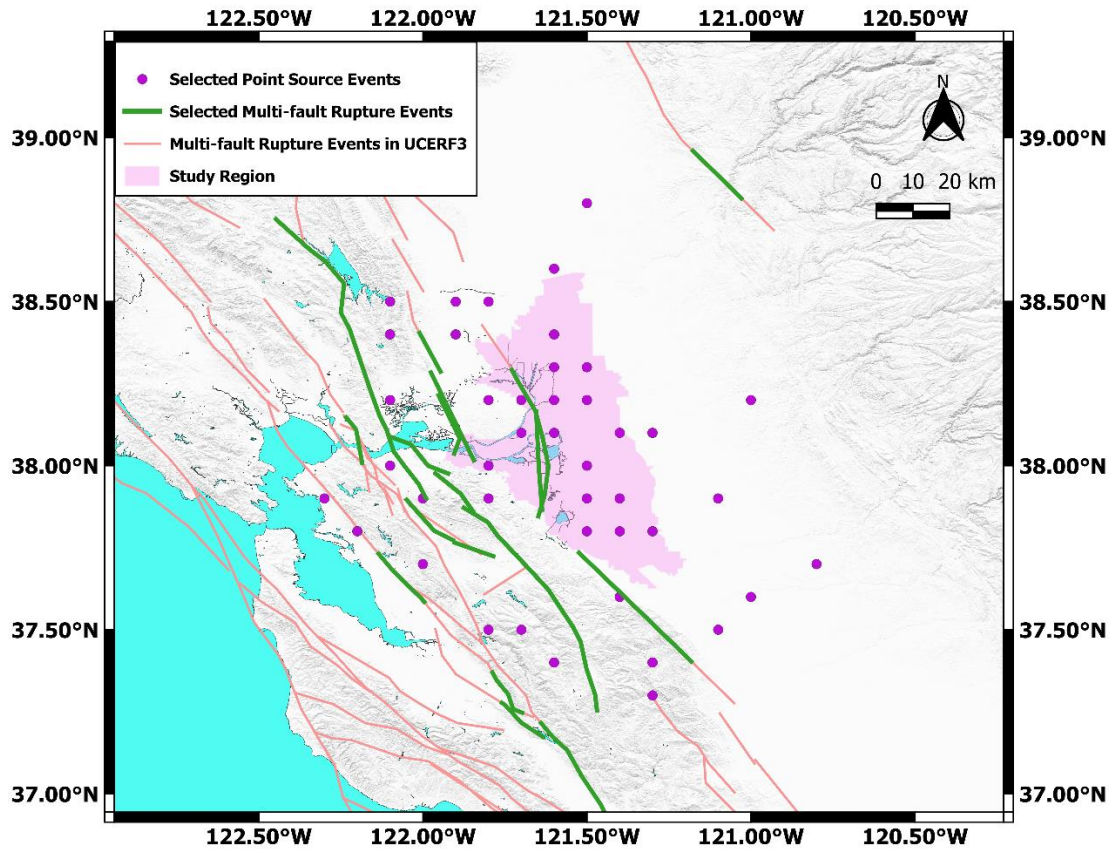


**Figure 4.17** Locations of the 82 selected events (35 selected rupture events and 47 selected point source events) of *PGA* hazard matching with magnitude preservation generated by LASSO regression.

**Table 4.5** Selected rupture and point events for *PGA* hazard matching with magnitude preservation.

Multi-fault Rupture Events						
	Branch	Fault Section ID of Event	Magnitude	ARO (yr <sup>-1</sup> )	Type	Adjusted ARO (yr <sup>-1</sup> )
1	FM31	711:712	6.2	1.86E-06	SS	0.001112596
2	FM31	716:717	6.5	3.18E-05	R	0.000206249
3	FM31	720:721	6.5	0.000143885	R	0.000308198
4	FM31	710:713	6.5	0.000671163	SS	0.000816463
5	FM31	718:719	6.5	3.38E-05	R	1.37E-06
6	FM31	724:725	5.8	8.69E-08	R	0.000674789
7	FM31	783,782	6.0	7.90E-05	SS	0.001094632
8	FM31	727:734	6.4	4.94E-06	R	0.000186683
9	FM31	783:788	6.5	1.87E-05	SS	0.000996704
10	FM31	1821:1822,215:208,217:222,191:192	6.9	1.66E-06	SS	0.008080921
11	FM31	716:719	6.9	1.07E-05	R	9.11E-06
12	FM31	776:775,952:960	6.7	3.50E-06	SS	0.002969423
13	FM31	953:952,775:781,346:348,1360:1359,1362:1361,787:782,794:789	7.4	7.26E-07	SS	0.00040696
14	FM31	775:781,1145:1144,318:320,788:782	7.3	1.12E-07	SS	2.56E-06
15	FM31	832:834	6.4	4.42E-05	SS	0.004977112
16	FM31	319:320,788:784	6.7	1.01E-06	SS	0.000657492
17	FM31	786:783	6.3	4.70E-07	SS	0.000521254
18	FM31	2464:2466	6.5	2.34E-06	N	0.014434395
19	FM31	319:320,788:782,794:793	6.9	1.60E-06	SS	0.000893429
20	FM31	786,785	6.0	1.35E-06	SS	0.000439398
21	FM31	778:781,346:348,1360:1359,788:783	7.1	1.05E-06	SS	0.00074522
22	FM31	722:729	6.4	2.64E-05	R	0.000197693
23	FM31	319:320,1362:1361,787:784	6.9	6.11E-07	SS	0.000125868
24	FM32	730:735	6.7	1.33E-05	R	9.90E-05
25	FM32	196:198,2446:2448,857:861	6.6	3.82E-08	SS	0.007546731
26	FM32	730:738	6.8	4.71E-05	R	0.000182

						093
27	FM32	745:752	6.4	2.93E-06	R	3.72E-05
28	FM32	746:753	6.4	5.37E-06	R	3.51E-05
29	FM32	354:355,358:359	6.3	7.62E-05	SS	0.002977 511
30	FM32	809:814,802:808,323:321,1163:1164,734,733	7.4	9.26E-08	SS	0.000127 964
31	FM32	973:979	6.5	5.17E-05	SS	0.005604 696
32	FM32	805:808,741:740,738:733	7.2	6.60E-08	R	5.92E-09
33	FM32	737:738,740:741	6.9	9.66E-08	R	4.20E-05
34	FM32	798:801,1164:1163,739:741	7.3	5.49E-08	R	5.43E-05
35	FM32	733:738,740:741	7.0	3.49E-08	R	9.94E-05

**Point Sources**

	<b>Branch</b>	<b>Point Longitude, Latitude, and Elevation (°, °, km)</b>	<b>Magnitude</b>	<b>ARO (yr<sup>-1</sup>)</b>	<b>Type</b>	<b>Adjusted ARO (yr<sup>-1</sup>)</b>
1	FM31	-121.7, 38.1, 0.0	6.7	4.56E-09	R	1.98E-06
2	FM31	-122.1, 38.0, 0.0	5.3	0.000263 234	SS	0.006888 076
3	FM31	-121.8, 37.9, 0.0	5.8	4.36E-05	R	0.001686 365
4	FM31	-121.8, 38.0, 0.0	6.0	2.04E-05	R	0.000542 003
5	FM31	-122.1, 38.2, 0.0	5.4	4.51E-05	N	0.014014 349
6	FM31	-121.5, 38.0, 0.0	5.7	2.25E-05	R	0.000658 676
7	FM31	-121.5, 38.2, 0.0	6.3	4.71E-06	N	9.73E-05
8	FM31	-121.4, 37.8, 0.0	6.5	5.94E-06	R	0.000160 52
9	FM31	-121.7, 38.2, 0.0	5.8	2.02E-05	SS	0.000477 709
10	FM31	-121.6, 38.1, 0.0	5.4	4.10E-05	SS	0.000450 876
11	FM31	-121.5, 38.3, 0.0	5.7	1.16E-05	R	0.000307 627
12	FM31	-121.4, 38.1, 0.0	6.2	5.05E-06	R	0.000298 373
13	FM31	-121.3, 37.8, 0.0	6.1	8.50E-06	SS	0.000314 693
14	FM31	-121.5, 37.8, 0.0	5.5	5.00E-05	SS	0.000727 289
15	FM31	-121.6, 38.3, 0.0	6.5	3.14E-06	R	2.32E-05
16	FM31	-121.4, 37.9, 0.0	5.8	1.86E-05	SS	0.000445 469
17	FM31	-121.8, 38.5, 0.0	5.3	3.21E-05	SS	0.001503 328
18	FM31	-122.1, 38.5, 0.0	6.1	1.18E-05	N	0.009766 381
19	FM31	-121.0, 38.2, 0.0	5.7	4.13E-06	N	0.003422 408

20	FM31	-121.3, 37.4, 0.0	5.3	8.62E-05	SS	0.023392
21	FM31	-121.1, 37.5, 0.0	5.6	2.72E-05	N	0.007770 866
22	FM31	-121.7, 37.5, 0.0	7.2	9.35E-07	N	0.003725 722
23	FM31	-121.0, 37.6, 0.0	7.2	3.06E-07	N	0.001734 218
24	FM31	-122.2, 37.8, 0.0	7.4	2.32E-08	SS	0.011842 513
25	FM31	-122.3, 37.9, 0.0	5.4	0.000127 803	SS	0.019910 737
26	FM31	-121.8, 37.5, 0.0	5.1	0.000273 133	SS	0.097755 325
27	FM32	-121.7, 38.1, 0.0	5.4	4.01E-05	SS	0.000134 498
28	FM32	-122.0, 37.9, 0.0	5.9	0.000102 581	SS	0.004865 915
29	FM32	-121.8, 38.2, 0.0	5.6	2.94E-05	R	0.000382 775
30	FM32	-122.2, 37.8, 0.0	7.0	1.60E-07	N	0.009519 187
31	FM32	-122.0, 37.7, 0.0	5.6	9.60E-05	N	0.019174 098
32	FM32	-121.5, 37.8, 0.0	5.7	3.46E-05	SS	0.000492 909
33	FM32	-121.5, 38.2, 0.0	5.5	2.11E-05	SS	0.000175 856
34	FM32	-121.6, 38.2, 0.0	5.3	3.88E-05	R	0.000357 438
35	FM32	-121.3, 38.1, 0.0	5.5	1.59E-05	SS	0.000175 101
36	FM32	-121.5, 37.9, 0.0	6.0	1.42E-05	R	0.000276 797
37	FM32	-121.1, 37.9, 0.0	7.1	3.31E-07	SS	8.14E-05
38	FM32	-121.4, 37.6, 0.0	6.8	1.45E-06	R	0.000261 832
39	FM32	-121.6, 38.4, 0.0	5.6	1.41E-05	R	0.000378 083
40	FM32	-121.9, 38.4, 0.0	5.1	6.62E-05	SS	0.004354 736
41	FM32	-121.6, 38.6, 0.0	7.4	5.54E-08	R	0.000181 221
42	FM32	-121.9, 38.5, 0.0	7.3	2.46E-07	N	0.001656 341
43	FM32	-121.6, 37.4, 0.0	5.5	0.000110 423	R	0.011591 734
44	FM32	-121.3, 37.3, 0.0	6.3	8.32E-06	N	0.021679 426
45	FM32	-120.8, 37.7, 0.0	6.1	2.79E-06	N	0.009274 378
46	FM32	-122.1, 38.4, 0.0	6.3	2.90E-06	N	8.47E-05
47	FM32	-121.5, 38.8, 0.0	5.9	3.34E-06	N	0.006619

Fig. 4.18 shows the *PGA* hazard curve matching of example sites, which are generally reasonable with some minor discrepancies at large return periods. Furthermore, Figure 4.19 presents the marginal magnitude distributions of example sites for 10, 50, 100, 225, 475, and 2475-year return periods, the overall magnitude preservations are good, but some outliers are present. Noticeably, large magnitude events on sources west of the Delta are absent from the selected subset, as evidenced by the lack of orange bars at magnitudes higher than 7.5.

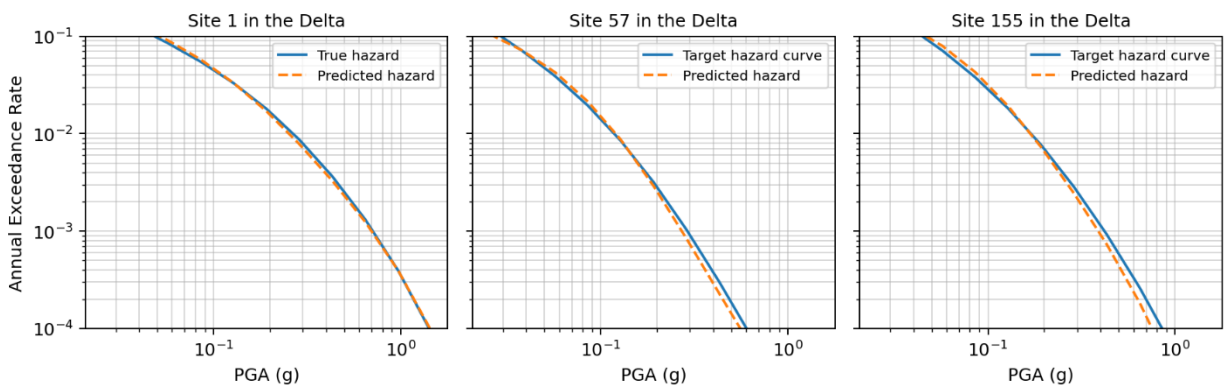


**Figure 4.18** True and recovered hazard curves for *PGA* by the 82 selected events from the LASSO regression method without preservation of magnitude and distance distributions hazard matching of three example sites.

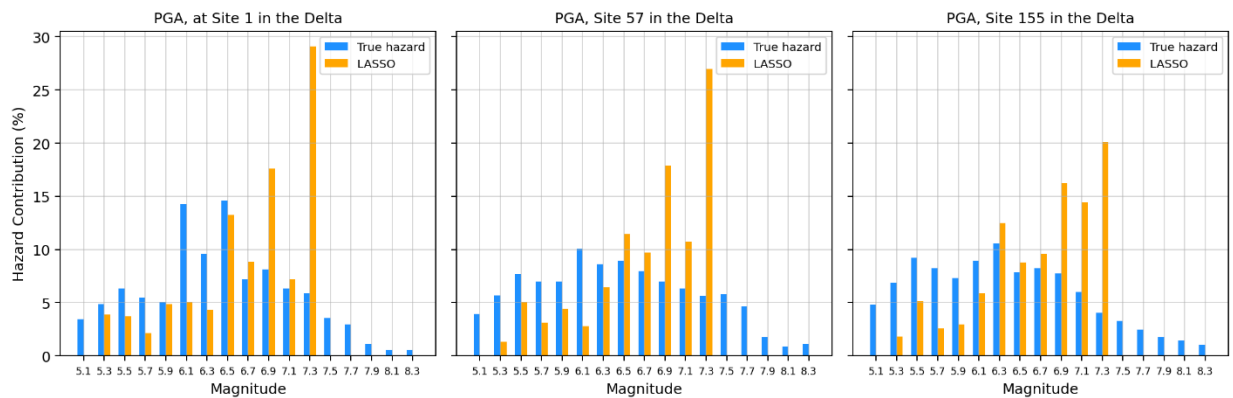


**Figure 4.19** Marginal distribution plots for *PGA* hazard at three sites with respect to magnitude. The results apply for 10, 50, 100, 225, 475, and 2475-year return periods. Results shown in the figure apply for 82 selected events by the LASSO regression method configured to match true hazard curves for both intensity measures and true magnitude distributions.

When point sources with magnitude greater than 6.5 are removed in the pre-selection stage, LASSO regression is applied based on 991 pre-selected candidate events and Fig. 4.20 shows the decaying error curve. The error in this case increased from 0.317 up to 0.381. I selected 65 events in this case.

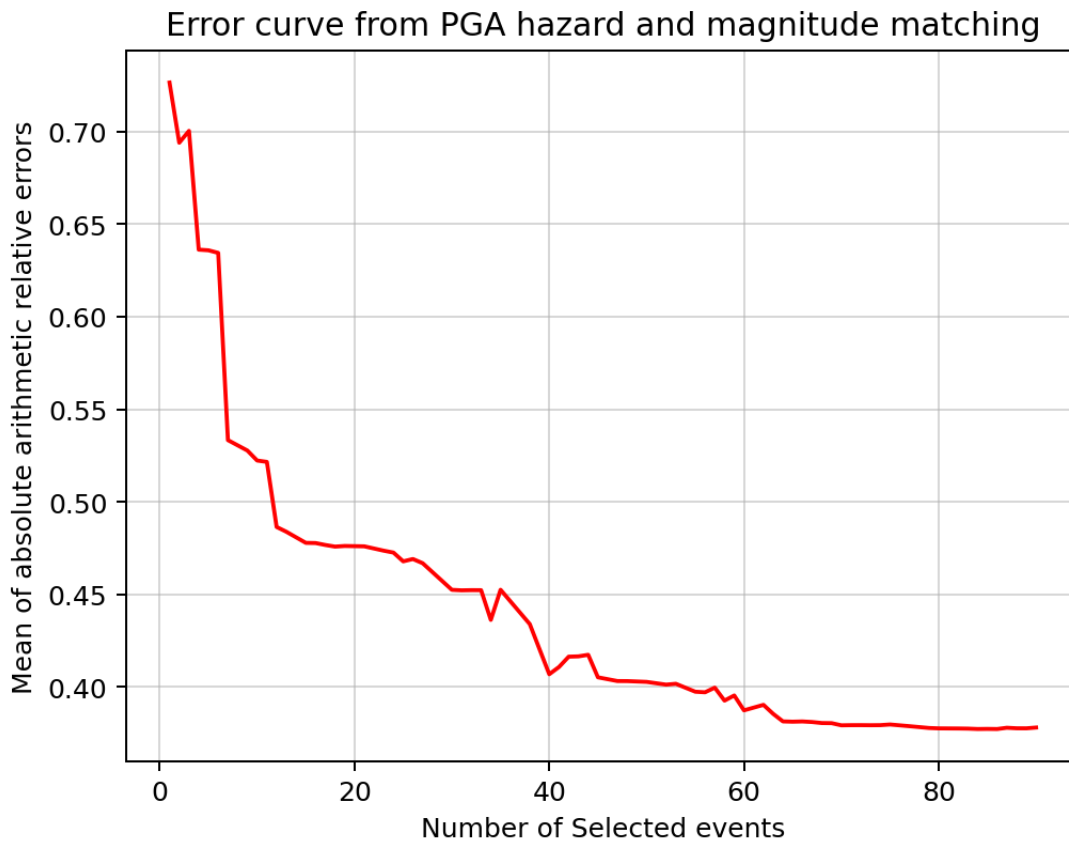


**Figure 4.20** Mean of absolute arithmetic relative errors versus number of selected events for *PGA* hazard matching of the Delta region with preservation of magnitude distributions after excluding points sources with magnitude larger than 6.5.

According to Fig. 4.21, the selected subset contains many point sources in and around the Delta. Table 4.7 shows the fundamental information of these reselected 65 events.



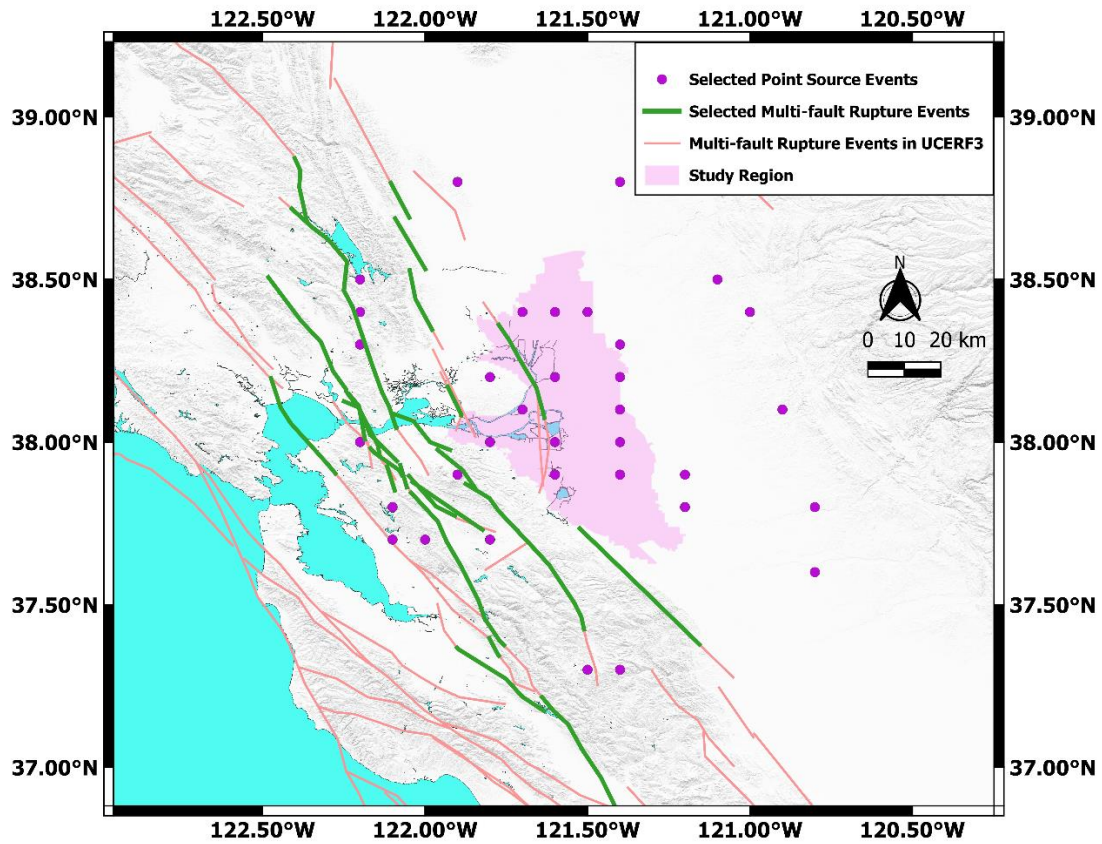


**Figure 4.21** Locations of the 65 selected events (29 selected rupture events and 36 selected point source events) of *PGA* hazard matching with magnitude preservation generated by LASSO regression after excluding points sources with magnitude larger than 6.5.

**Table 4.6** Re-selected rupture and point events for *PGA* hazard matching with magnitude preservation.

Multi-fault Rupture Events						
Branch	Fault Section ID of Event	Magnitude	AOR (yr <sup>-1</sup> )	Type	Adjusted AOR (yr <sup>-1</sup> )	
1	FM31	711:712	6.2	1.86E-06	SS	0.001049
2	FM31	821:827	6.7	1.67E-05	SS	0.009116
3	FM31	716,715	6.5	2.09E-06	R	0.000125 984
4	FM31	717:718	6.5	1.15E-05	R	0.000153 02
5	FM31	722:723	5.8	2.44E-06	R	0.000308 19
6	FM31	722:726	6.2	0.000104 666	R	0.000265 17
7	FM31	722:729	6.4	2.64E-05	R	0.000319 165
8	FM31	784:782,794:793	6.5	9.82E-06	SS	1.17E-05
9	FM31	716:717	6.5	3.18E-05	R	3.49E-06
10	FM31	785,784	6.0	1.32E-06	SS	0.001112 406
11	FM31	728:735	6.4	4.60E-06	R	0.000342 301
12	FM31	787:782	6.5	1.13E-06	SS	2.38E-07
13	FM31	1818:1822,215:208,217:222,191:194	6.9	1.09E-06	SS	0.019747 997
14	FM31	320:318,1144:1145,781:775,952:958,945:948	7.3	3.78E-08	SS	0.001201 608
15	FM31	778:775,952:959	6.7	7.64E-05	SS	0.001827 555
16	FM31	2540:2542,351:354,582:581,350:349,1360:1359,788:786	7.3	1.79E-09	SS	0.000819 102
17	FM31	206:204	6.3	1.30E-06	SS	0.004250 099
18	FM32	742:746	6.2	0.000104 537	R	9.15E-06
19	FM32	742:749	6.4	2.77E-05	R	3.29E-05
20	FM32	716:717,725:730	7.0	1.55E-06	R	0.000461 375
21	FM32	744:745	5.8	1.14E-07	R	0.000574 375
22	FM32	225:226,195:198,2446:2451	6.8	5.25E-08	SS	0.006705 064
23	FM32	354:355,358:359	6.3	7.62E-05	SS	0.002312 928
24	FM32	801:799	5.7	9.53E-07	SS	0.000585 939
25	FM32	368:369,363:362,366:367,357:356,205:211,204:203,862:861	7.2	5.29E-09	SS	0.006995 223
26	FM32	798:795,971:978	6.7	7.84E-05	SS	0.003730 767

27	FM32	207:205	6.2	3.62E-05	SS	0.003136
28	FM32	972:978	6.5	6.11E-07	SS	0.004478
29	FM32	2593:2599,359:358,355:354,366:367,361:360,1371:1368,807:805	7.4	9.65E-10	SS	0.00174896

**Point Source**

	<b>Branch</b>	<b>Point Longitude, Latitude, and Elevation (°, °, km)</b>	<b>Magnitude</b>	<b>ARO (yr<sup>-1</sup>)</b>	<b>Type</b>	<b>Adjusted ARO (yr<sup>-1</sup>)</b>
1	FM31	-122.2, 38.3, 0.0	6.0	6.21E-06	R	0.001757035
2	FM31	-122.0, 37.7, 0.0	5.7	7.91E-05	N	0.006931447
3	FM31	-122.2, 38.0, 0.0	5.4	0.00017383	N	0.017055814
4	FM31	-121.9, 37.9, 0.0	5.3	0.000157507	SS	0.001666653
5	FM31	-121.8, 38.2, 0.0	5.7	2.47E-05	R	0.001003137
6	FM31	-121.6, 38.2, 0.0	6.4	4.93E-06	N	0.000291643
7	FM31	-121.6, 37.9, 0.0	5.9	2.24E-05	N	0.000783888
8	FM31	-121.6, 38.0, 0.0	5.7	2.89E-05	R	0.000768731
9	FM31	-121.4, 37.9, 0.0	5.7	2.23E-05	SS	0.000662615
10	FM31	-121.4, 38.1, 0.0	6.1	5.52E-06	R	0.000330507
11	FM31	-121.5, 38.4, 0.0	5.9	6.16E-06	N	0.000239773
12	FM31	-121.4, 38.3, 0.0	5.8	7.42E-06	R	0.000262669
13	FM31	-121.7, 38.4, 0.0	6.3	4.76E-06	N	0.000156318
14	FM31	-122.2, 38.4, 0.0	5.7	2.83E-05	N	0.014185202
15	FM31	-121.0, 38.4, 0.0	5.8	2.64E-06	R	0.005450134
16	FM31	-121.5, 37.3, 0.0	5.3	0.000210845	N	0.132625816
17	FM31	-121.4, 37.3, 0.0	6.3	3.08E-06	N	0.011029126
18	FM31	-120.8, 37.8, 0.0	5.6	7.11E-06	R	0.001880502
19	FM31	-120.8, 37.6, 0.0	6.4	2.31E-06	N	0.007444074
20	FM31	-122.1, 37.7, 0.0	5.1	0.000248666	SS	0.056604262
21	FM31	-121.9, 38.8, 0.0	6.4	1.04E-06	N	0.0125297
22	FM31	-122.2, 38.5, 0.0	5.3	6.93E-05	SS	0.024510606
23	FM32	-121.8, 37.7, 0.0	5.4	0.000132917	SS	0.007604356

24	FM32	-121.7, 38.1, 0.0	5.5	3.33E-05	N	0.001225 365
25	FM32	-121.8, 38.0, 0.0	5.9	3.08E-05	SS	0.001214 001
26	FM32	-122.1, 37.8, 0.0	6.0	5.12E-05	SS	0.008437 184
27	FM32	-121.4, 38.0, 0.0	6.3	5.72E-06	N	0.000336 759
28	FM32	-121.4, 38.2, 0.0	6.3	3.61E-06	SS	0.000135 273
29	FM32	-121.6, 38.4, 0.0	5.5	1.70E-05	N	0.000612 645
30	FM32	-121.2, 37.9, 0.0	5.5	1.95E-05	SS	0.001019 805
31	FM32	-121.2, 37.8, 0.0	6.0	8.65E-06	R	0.000643 342
32	FM32	-121.1, 38.5, 0.0	6.2	1.16E-06	N	0.000612 047
33	FM32	-121.4, 37.3, 0.0	5.8	7.85E-05	R	0.012731 241
34	FM32	-121.5, 37.3, 0.0	5.6	0.000121 328	R	0.013877 366
35	FM32	-120.9, 38.1, 0.0	5.1	1.23E-05	SS	0.026070 771
36	FM32	-121.4, 38.8, 0.0	6.1	1.62E-06	N	0.003706 744

Figures 4.22 and 4.23 show the *PGA* hazard curve and magnitude matchings of example sites. The hazard matching in this case is poor relative to the other event subsets studied in this chapter. Including more events may be necessary to achieve higher accuracy, but that would place more demands on the analyst. I believe 65 is a reasonable subset for most applications, and therefore did not explore a larger number of events.

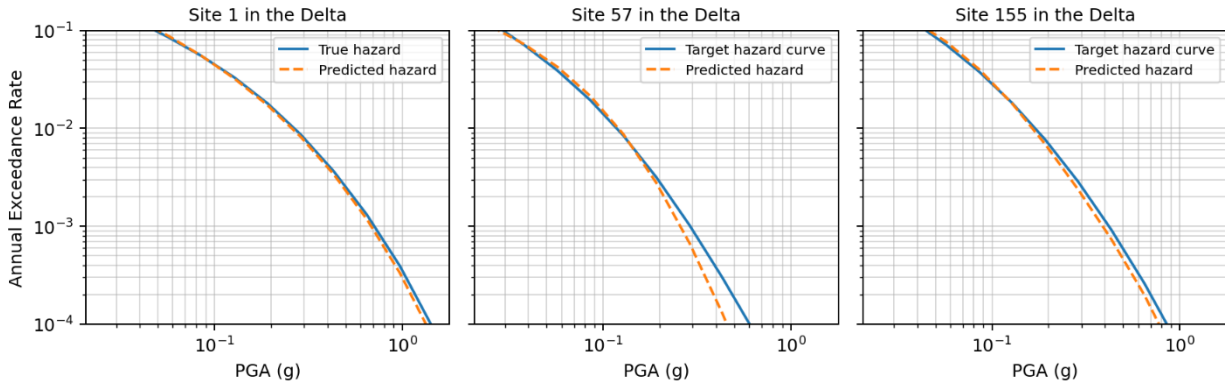


**Figure 4.22** True and recovered hazard curves for *PGA* by the 65 reselected events from the LASSO regression method of three example sites.

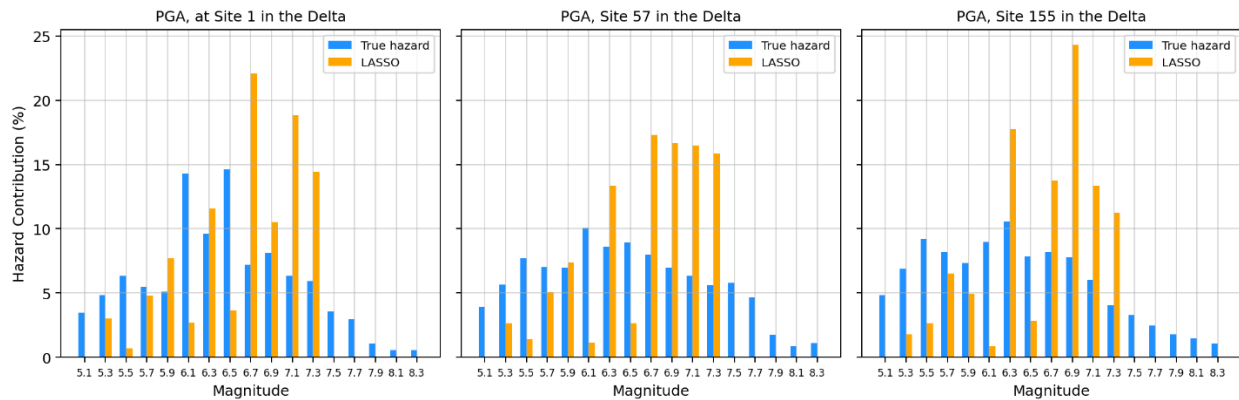


**Figure 4.23** Marginal distribution plots for *PGA* hazard at three sites with respect to magnitude. The results apply for 10, 50, 100, 225, 475, and 2475-year return period. Results shown in the figure apply for 65 reselected events by the LASSO regression method configured to match true hazard curves for both intensity measures and true magnitude distributions.

#### 4.2.4 Summary

To summarize, the LASSO regression-based event selection approach works well to obtain a manageable reduced event subset that matches hazard curves throughout the Delta. The hazard matching is quite good when few constraints are placed on the algorithm. The matching becomes

worse (or more events are required to achieve the same accuracy) when the magnitude of point source events is constrained to be smaller than 6.5, and worse yet when  $M$  is included alongside  $PGA$ . It is worthwhile pointing out the trade-off consideration between the number of selected events and the goodness of matching. The final selection of the number of events is very subjective, which completely relies on users' needs. If the system reliability analysis is computationally straightforward (i.e., using fragility analysis and level-crossing statistics, as presented in the next chapter), it might be relatively easy to simply include all of the events in the PSHA. However, in many applications a smaller event set is required.

It is interesting that the LASSO regression algorithm selected many point source events and relatively fewer events on known faults. I believe this outcome occurs because point source events can occur anywhere, and are therefore more flexible than the known faults. I did not attempt to control the relative number of point source events and known fault events herein, though that could potentially be incorporated for users who wish to have a specific mix of these event types. The UCERF3 model includes point source events with large magnitudes that are unreasonable to represent as a point source because large magnitude events have large ruptures. Errors may be averaged when all such events are considered because of compensating errors in the distance calculation. However, including these point source events with large magnitude in an event subset is undesirable. This problem would be best addressed by modeling background seismicity in UCERF3 using finite fault solutions rather than point sources.

## **CHAPTER 5: System Reliability Analysis**

Levee systems are series systems in that a breach at one location results in failure of the flood protection system. The “weakest-link-in-the-chain” concept governs series systems like levees. This chapter is concerned with the risk assessment (system reliability analysis) of spatially distributed levees in the Delta by computing the annual probability of failure. To begin with, the level crossing statistics (LCS) methodology, which is formulated for analysis of levee systems by Zimmaro et al. (2018), is defined as the core risk assessment framework in this chapter. Case studies of levee performance following two earthquakes is then performed to evaluate the reasonableness of the predictions. Seismic system reliability analysis is implemented for the Bacon Island levee system based on the seismic hazard, selected events, and levee fragility results in Chapter 2, 3 and 4. Furthermore, LCS can also be applied to other hazards threatening the levee systems, so the results of risk assessments of Bacon Island levees under other hazards such as overtopping and seepage performed by other project members are presented.

### **5.1 System Reliability Analysis Framework**

This section elaborates the mathematical framework of LCS for computing the probability of exceedance of a specified crest settlement for a particular earthquake scenario. Annual exceedance rate is then computed by multiplying the computed probability by the rate of occurrence of the event, and summing over all events. Stated mathematically, if I define demand,  $D$ , and capacity,  $C$ , I may also define a limit state function,  $Z$ , using Eq. 5.1.  $C$  may correspond to damage levels that are less than a failure condition, in which case  $Z < 0$  would not correspond to failure, but rather to exceedance of a limit corresponding to the capacity. For levees,  $C$  is defined as the shaking intensity required to cause a specified level of crest settlement. However, for simplicity in the derivation of the LCS method, I refer to  $Z < 0$  as a failure condition. I therefore seek to define the

annual probability that  $Z < 0$  for the hazards of interest.

$$Z = C - D \quad (5.1)$$

Demands are conceptualized as being random fields quantified by a mean,  $\mu_D$ , standard deviation,  $\sigma_D$ , and spatial correlation function,  $\rho_D(x)$ , where  $x$  is separation distance. Some demands may have perfect correlation throughout the levee system, while others may spatially fluctuate. For instance, sea level rise is a random variable because we cannot perfectly predict elevations into the future. Nonetheless, the increase in water level will occur uniformly throughout the system, so  $\rho_D(x) = 1.0$  for sea level rise. By contrast, earthquake shaking demands contain components of uncertainty that are perfectly spatially correlated (i.e., the event term, which is constant for a given event), and components that are spatially variable (i.e., the within-event residual term). Therefore, ground motion must be modeled as a random field for which  $\rho_D(x) \leq 1.0$ , where  $\rho_D(x)$  is a linear combination of different components, as demonstrated later. Spatial correlation of capacity and demand is modeled using a Gaussian correlation function (Eq. 5.2) because Gaussian functions are mean-square differentiable and can therefore be utilized in LCS analyses, as described later. Note that the  $\pi$  term in Eq. 5.2 is selected such that the model coefficient  $d_D$  is equal to the correlation length, defined as the integral of Eq. 5.2 over  $x$  from  $x = -\infty$  to  $+\infty$ . This convention prevents confusion between correlation length and model coefficients that may otherwise exist for model constants other than  $\pi$ .

$$\rho_D = \exp \left[ -\pi \left( \frac{x}{d_D} \right)^2 \right] \quad (5.2)$$

Similarly, capacity is quantified by a mean,  $\mu_C$ , standard deviation,  $\sigma_C$ , and spatial correlation function,  $\rho_C(x)$  defined by Eq. 5.3. Capacity is often represented by a fragility function and is



quantified in the same units as demand. For example, the capacity of a levee to resist high water is defined in terms of elevation, while capacity of a levee to resist earthquake shaking is defined in terms of earthquake ground motion intensity measure. Spatial correlation of capacity is a function of the composition of the levees, including soil strength, hydraulic conductivity, and erodibility, and how these properties change along a levee system.

$$\rho_C = \exp \left[ -\pi \left( \frac{x}{d_C} \right)^2 \right] \quad (5.3)$$

I performed simulations of levee performance using two-dimensional cross-section analysis in Chapter 3. Incorporating the output from those analysis into the system reliability framework requires definition of some terminology, illustrated in Fig. 5.1.

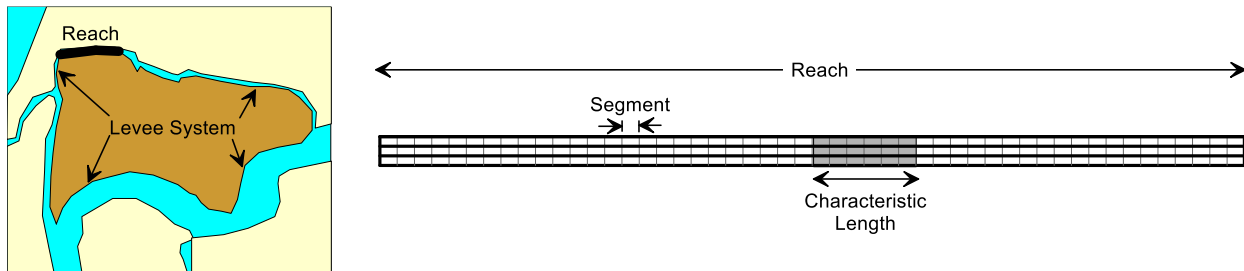


**Figure 5.1** Terminology in system reliability analysis framework. (Zimmaro et al., 2013)

Each of the terms in Figure 5.1 is defined below. Note that the definition of a reach within the system reliability framework has a specific meaning that is different from the traditional definition of a reach based on jurisdictional boundaries or other non-reliability based considerations.

**System:** A length of levee that protects a region from flooding.

**Reach (reliability definition):** A length of levee with constant values for  $\mu_D$ ,  $\sigma_D$ ,  $\rho_D(x)$ ,  $\mu_C$ ,  $\sigma_C$ , and  $\rho_C(x)$ . Capacity and demand may vary within a reach, but the random fields are stationary.

**Reach (jurisdictional definition):** A length of levee based on a jurisdictional boundary, or other non-reliability based concept.

**Characteristic length:** A length for which the probability of system failure may be computed based on the assumption of statistical independence of capacity and demand.

**Segment:** An elemental length within which capacity and demand are constant. This corresponds to the length of levee that is accurately represented by a two-dimensional cross-section analysis.

The limit state function,  $Z$ , is the difference between two random fields, and is therefore itself a random field with statistics defined by Eqs. 5.4 – 5.8 based on the assumption that capacity and demand are uncorrelated. The  $\alpha_C$  and  $\alpha_D$  terms are influence factors controlling the contribution of capacity and demand, respectively, to spatial correlation of the limit state function.

$$\mu_Z = \mu_C - \mu_D \quad (5.4)$$

$$\sigma_Z^2 = \sigma_C^2 + \sigma_D^2 \quad (5.5)$$

$$\rho_Z(x) = \alpha_C^2 \rho_C(x) + \alpha_D^2 \rho_D(x) \quad (5.6)$$

$$\alpha_C^2 = \frac{\sigma_C^2}{\sigma_C^2 + \sigma_D^2} \quad (5.7)$$

$$\alpha_D^2 = \frac{\sigma_D^2}{\sigma_C^2 + \sigma_D^2} \quad (5.8)$$

Based on Rice's (1944) formula, the probability of failure at any point within a reach is defined by Eq. 5.9, where  $\beta_Z = \mu_Z/\sigma_Z$  is the reliability index. The probability of failure is a function of the

reach length,  $L_R$ , and the longer a reach, the higher the probability of failure. By analogy, the more links there are in a chain, the higher the probability that one of them will break.

$$p_{f,reach} = 1 - (1 - p_{f,seg}) \exp \left[ -\frac{L_R}{2\pi} \sqrt{-\frac{\partial^2 \rho_Z(0)}{\partial x^2}} \exp \left( -\frac{\beta_Z^2}{2} \right) \right] \quad (5.9)$$

The probability of failure of the reach may also be formulated in terms of the characteristic length,  $L_{char}$ , by noting that characteristic lengths are statistically independent, and therefore the probability of failure may be computed as a simple product sum. Formulating that equation, setting it equal to Eq. 5.9, and solving for  $L_{char}$  results in Eq. 5.10.

$$L_{char} = p_{f,seg} \frac{2\pi}{\sqrt{-\frac{\partial^2 \rho_Z(0)}{\partial x^2}}} \exp \left( \frac{\beta_Z^2}{2} \right) \quad (5.10)$$

The probability of system failure is computed using the product sum given by Eq. 5.11.

$$p_{f,sys} = 1 - \prod_{i=1}^N (1 - p_{f,seg_i})^{L_{R_i}/L_{char_i}} \quad (5.11)$$

The annual rate of system failure is computed by summing the product of the rate occurrence of each event and the probability of system failure for that event, as given by Eq. 5.12.

$$\lambda_{f,sys} = \sum_{i=1}^{N_E} \lambda_i \cdot p_{f,sys_i} \quad (5.12)$$

For a given annual rate of occurrence, the probability of at least one failure occurring in a unit of time,  $t$ , can be computed using Eq. 5.13, assuming the hazard follows a Poisson process.

$$p_{f,sys}(t) = 1 - (1 - \lambda_{f,sys})^t \quad (5.13)$$

## 5.2 Reach Length and Spatial Correlation of Demand

Procedures for defining a random variable quantifying shaking intensity at a point for a particular

event were defined in Chapter 4. This section focuses on discretization of the levee system into reaches such that demand is approximately stationary within each reach, and spatial correlation of demands.

### **5.2.1 Reach Length**

The level crossing statistics method requires that demand and capacity be stationary within each reach. Shaking intensity varies in space because different points have different distances to the earthquake source. For this reason, the mean value of shaking intensity varies and demand is never, strictly speaking, spatially stationary. However, reach lengths can be selected such that the demand is approximately stationary with only minor errors introduced into the analysis. The amount of spatial variability within the levee system depends strongly on how different the source-to-site distances are between the earthquake fault rupture and points in the levee system. For example, the mean shaking intensity for Bacon Island levees for a **M8** earthquake on the San Andreas Fault (presented in Fig. 5.2) would be essentially constant because the San Andreas fault is far from Bacon Island, and all points are essentially equidistant. By contrast, a **M5** earthquake on the Midland fault shown in Figure 5.2 would give rise to slightly different mean shaking levels among different points within Bacon Island. Furthermore, a **M5** event (e.g., background seismicity) terminating at the southern end of Bacon Island, as shown in Fig. 5.2, would induce mean shaking levels that are significantly higher for the southern segments than for those along the northern part of the island. For the San Andreas rupture scenario, demand is stationary within the entire system, whereas for the **M5** scenario, demand is highly variable within the system and discretization into reaches must be performed to render reach lengths in which the demand is approximately stationary.

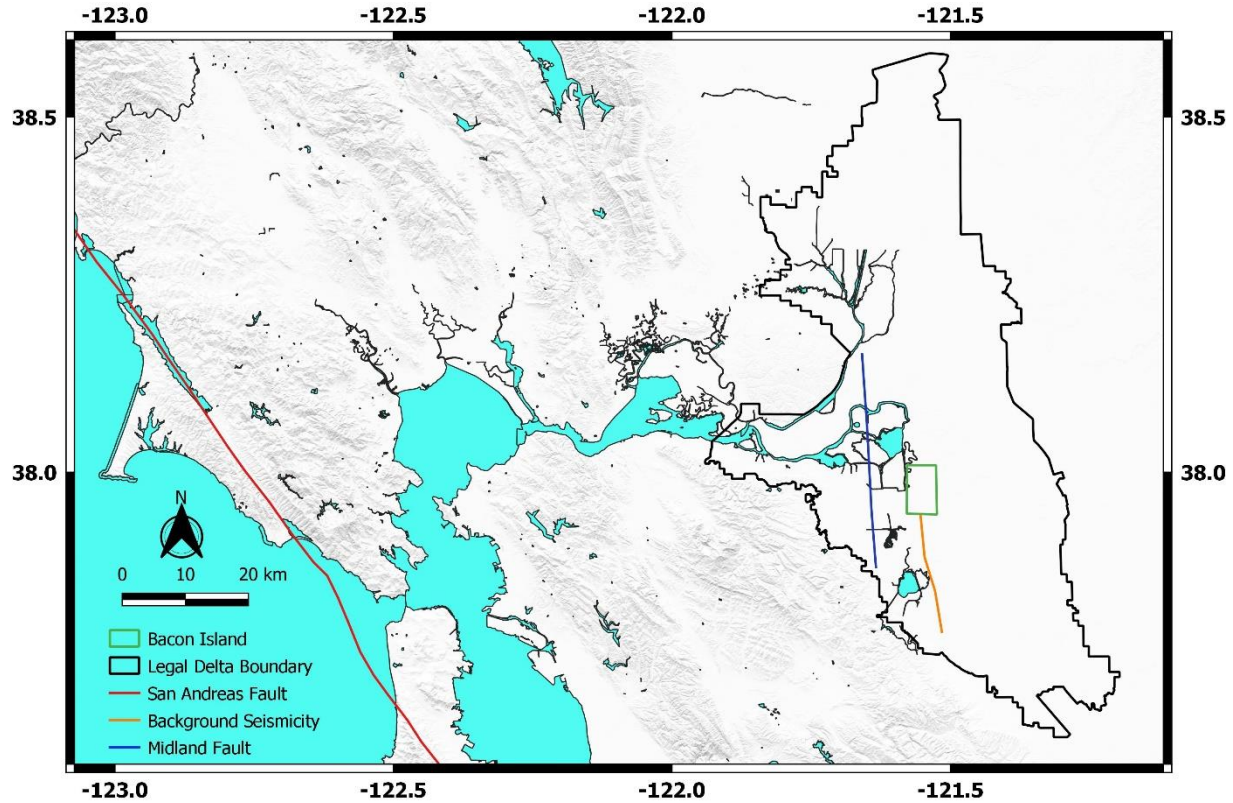


**Figure 5.2.** Overview of the Delta area, location of the three selected faults and Bacon Island.

I found that reach lengths of 1 km rendered demands for the **M5** scenario event that varied by no less than 5% within each reach. Based on this observation, I selected reaches of approximately 1km length, as shown in Fig. 3.2.

### 5.2.2 Spatial Correlation of Demand

Errors in GMM predictions are partitioned into random variables representing event-to-event variability, and within-event variability. Event-to-event variability is represented by the event term  $\eta_E$ , which has zero mean and standard deviation  $\tau$ . Within-event residuals are represented by  $\delta W$ , which has zero mean and a standard deviation  $\phi$ . GMMs provide formulations for  $\tau$  and  $\phi$ , enabling users to model these different contributions. The distinction is important for spatial correlation because the event term is constant for a particular event, such that  $\rho_{\eta_E}(x) = 1.0$ , whereas  $\delta W$  is

spatially correlated.

Jayaram and Baker (2009) formulated spatial correlation models for  $\delta W$ , and utilized an exponential function to model spatial correlation given by  $\rho(x) = \exp(-3x/b)$ , where the model coefficient  $b$  was formulated as a function of natural period  $T$ . Furthermore, they found that for short periods ( $T < 1s$ ),  $b$  further depended on whether  $V_{S30}$  values exhibited clustering. For sites with similar geology and clustered  $V_{S30}$  values, they found  $b = 8.5 + 17.2T$ . The clustered model is reasonable for the Delta because geology does not vary significantly within the Delta. They did not formulate the model for  $PGV$ , but only for spectral accelerations. In this study, I assume that  $PGV$  and spectral acceleration at 0.5s are reasonably correlated. I therefore use  $b = 17.1$  km herein. They utilized an exponential function, which cannot be implemented in level crossing statistics because the 2<sup>nd</sup> derivative of the correlation function at 0 separation distance is not defined (e.g., see Eq. 5.9). For this reason, I computed the correlation length of their variogram model by integrating it from  $-\infty$  to  $+\infty$  and found that the correlation length is 11.4 km. I then implemented that correlation length into Eq. 5.14 to define the spatial correlation of  $\delta W$ .

$$\rho_{\delta W} = \exp \left[ -\pi \left( \frac{x}{d_{\delta W}} \right)^2 \right] \quad (5.14)$$

Having formulated expressions for the spatial correlation of the event term and within event residuals, I now focus on defining the overall spatial correlation of demand. Eq. 5.15 presents the resulting expression, where the influence factors are  $\alpha_{\eta_E}^2 = \frac{\tau^2}{\tau^2 + \phi^2}$  and  $\alpha_{\delta W}^2 = \frac{\phi^2}{\tau^2 + \phi^2}$ .

$$\rho_D(x) = \alpha_{\eta_E}^2 \rho_{\eta_E}(x) + \alpha_{\delta W}^2 \rho_{\delta W}(x) \quad (5.15)$$

### 5.3 Spatial Correlation of Capacity

Capacity of a levee segment can be defined using the fragility functions derived from non-linear finite element analyses. The fragility function represents a cumulative distribution function corresponding to the capacity random variable, parameterized by its mean, standard deviation, and distribution function. Fragility functions were defined from nonlinear finite element simulations in Chapter 3. Spatial correlation of capacity is also crucial for system reliability analysis, and is the topic of this section.

Kwak et al. (2016b) utilized autocorrelation of observed levee damage, and an assumed correlation function for demand to infer the correlation of capacity for Shinano River levees damaged by the 2004 and 2007 Niigata earthquakes. They utilized an exponential correlation function expressed by,

$$\rho_{ac} = \begin{cases} 1 & \text{if } x = 0 \\ c_{DS} \cdot \exp\left(\frac{-3x}{\alpha_{DS}}\right) + \varepsilon_x & \text{if } x > 0 \end{cases} \quad (5.16)$$

and they found that model parameter  $\alpha_{DS}$  is 3.7 km for damage state 0 and 1, and 1 km for damage state 2. The correlation length  $d_c$  obtained by integrating these correlation functions from  $-\infty$  to  $+\infty$ , are 2.5 km and 0.67 km.

The observations by Kwak et al. (2016b) are specific to the Shinano levee system, and may not translate well to Delta levees. Furthermore, Kwak et al. (2016b) did not have access to site investigation data, such as the land streamer measurements of  $V_{SS}$  presented in Fig. 3.21. Rather than directly utilizing Kwak's correlation lengths, I opt to infer spatial correlation of capacity from the land streamer measurements, and subsequently compare them with the values from Kwak et al. as a reasonableness check.

The shear wave velocity profiles obtained from the land streamer data are obtained by inversion

of the measured surface wave data. This work was performed by collaborators at Lawrence Berkeley National Laboratory. Figure 5.2 (a) shows in blue the values of  $V_{S5}$ , defined as the time-averaged shear wave velocity in the upper 5 m. These values are highly variable over relatively short distances. Based on the observation that a failure mechanism will average out soil properties within the zone of influence, I opted to smooth the  $V_{S5}$  data using a Gaussian window function with weights defined by Eq. 5.17,

$$w(i) = \frac{\sum_{j=1}^N e^{-\left(\frac{x_i-x_j}{\sigma}\right)^2} \cdot y_j}{\sum_{j=1}^N e^{-\left(\frac{x_i-x_j}{\sigma}\right)^2}} \quad (5.17)$$

where  $N$  is the total number of points,  $x_i$  and  $x_j$  are the distance at indices  $i$  and  $j$  respectively,  $\sigma$  is a parameter that controls the width of the window, is the original  $V_{S5}$  at the index  $j$ . In this case, I selected  $\sigma = 80$  m, which is approximately equal to the levee base width. Figure 5.3 (a) also shows the smoothed  $V_{S5}$  versus distance in orange. The smoothed line also exhibits fluctuations with distance, but is significantly smoother than the inverted  $V_{S5}$  values.

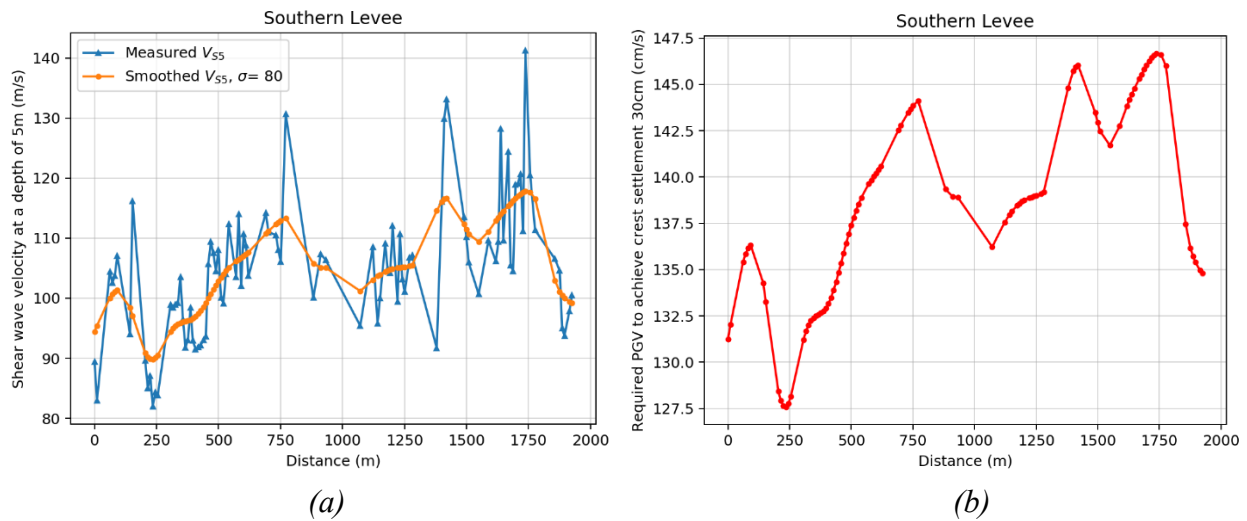


**Figure 5.3** (a) Measured  $V_{S5}$  and smoothed  $V_{S5}$  using gaussian window function along the southern levee; (b) Required  $PGV$  values to achieve 30cm crest settlement along the southern levee.



A transformation is required to relate  $V_{S5}$  to levee capacity so that the spatial correlation of capacity can be computed. This transformation is determined in Chapter 3 by running a suite of finite element simulations in which the  $V_{S5}$  values of the model was varied and quating the influence of the variation on observed settlement given a single earhtuqake ground motion. Fig. 3.70 (a) illustrates that how levee capacity is related to shear wave velocity of levee fill. Fig. 3.70 (b) shows the fitted function that is utilized to ahjust the levee capacity for cases where the measured  $V_{S5}$  value us different from the basline model, and he settlement and  $PGV$  values in the figure are normalized. Equation 5.18 is used to calculate the  $PGV$  causing  $S$  cm crest settlement for various  $V_{S5}$  along levees,

$$\ln(PGV) = \frac{\ln(S) - \left\{ m_0 + \Delta m_0 + m_2 \cdot \left[ \ln\left(\frac{V_{S5}}{V_{S5,ref}}\right) \right]^2 + m_3 \cdot \ln\left(\frac{V_{S5}}{V_{S5,ref}}\right) + m_4 \right\}}{m_1} \quad (5.18)$$

where  $\Delta m_0, m_0, m_1, m_2, m_3,$  and  $m_4$  are coefficients determined in Chapter 3, and  $V_{S5,ref}$  is the referenced  $V_{S5}$  for the baseline model. Fig. 5.3 (b) shows the  $PGV$  resulting in 30 cm crest settlement along the distance for southern levee, and the trend is very similar to the trend of the smoothed  $V_{S5}$  data in Fig. 5.3 (a).

I then calculate the matheron semi-variogram (Matheron, 1965) of levee capacity versuse separation distance. The semi-variogram function is written as,

$$\gamma(h) = \frac{1}{2N(h)} \cdot \sum_{i=1}^{N(h)} [Z(x_i + h) - Z(x_i)]^2 \quad (5.19)$$

where  $N(h)$  is the number of paris of sample locations separted by the lag distance  $h$ , and  $Z(x_i)$  is the value of the variable at location  $x_i$ .

Figure 5.4 shows the computed semi-variogram versus lag distance. I utilize a gaussian model to fit these calculated semi-variograms using maximum likelihood method, and the gaussian model is expressed by,

$$\gamma = b + c_0 \cdot \left(1 - e^{-\pi \frac{x^2}{d_c^2}}\right) \quad (5.20)$$

where  $b$  is the nugget and is set to 0,  $c_0$  and is the sill,  $x$  is separation distance, and  $d_c$  is the correlation length for capacity, which is regressed to be 0.335 km. The computed correlation length is about half of the value inferred by Kwak et al. (2016b), implying that Delta levees are more spatially variable than the Shinano River levees. Land streamer measurements are currently not available for the Shinano River levees, so it is not possible at this time to understand whether the capacity correlation inferred from the measurements would be consistent with those inferred by Kwak et al. (2016b). I opt to utilize the land-streamer based capacity correlation in this case because it is based on measurements that are specific to Delta levees. More work is needed in the future to validate this approach.

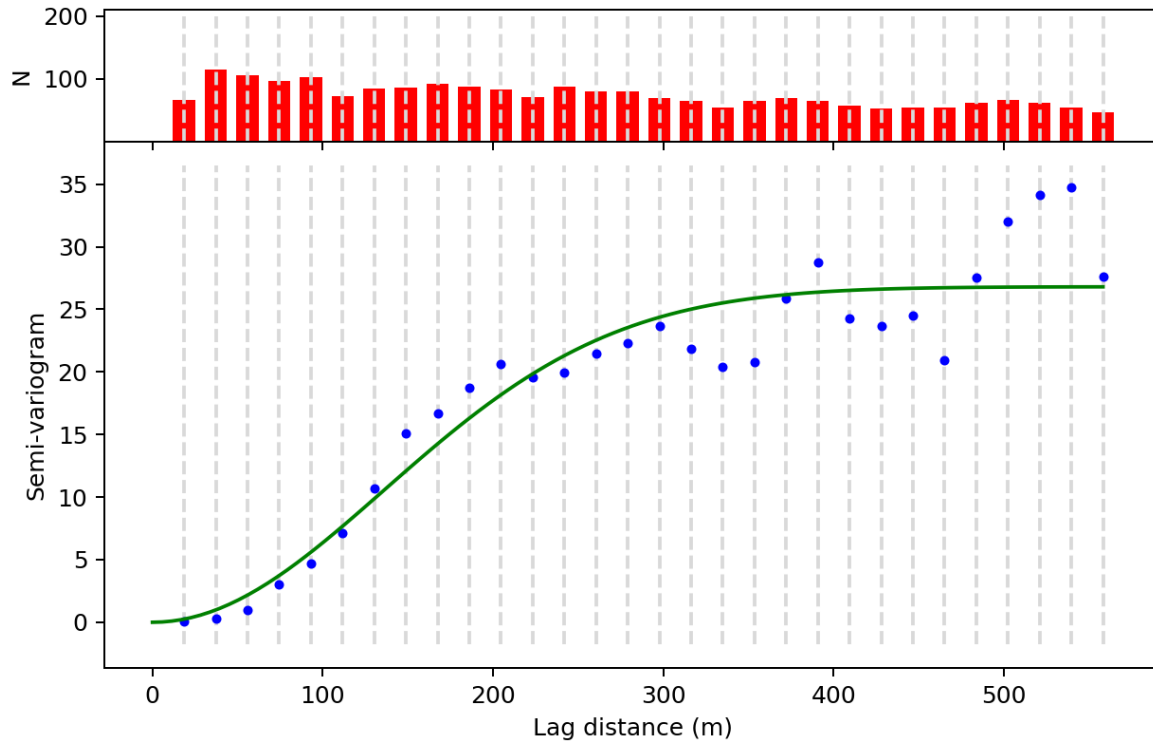


**Figure 5.4** Semi-variogram versus lag distance (m) and fitted gaussian model based required  $PGV$  values to achieve 30 cm crest settlement along the southern levee.

Likewise, I repeat the same process to derive the correlation length using land streamer measurements along the western levees. The  $\sigma$  used in in the Gaussian smoothing window in this case was 107 m, which is the levee base width of western levees. Figure 5.5 shows the  $V_{S5}$  values along the distance and computed required  $PGV$  along the distance, and the  $V_{S5}$  measurements are not as continuous as the ones for the southern levee due to several gaps where land streamer measurements could not be made.

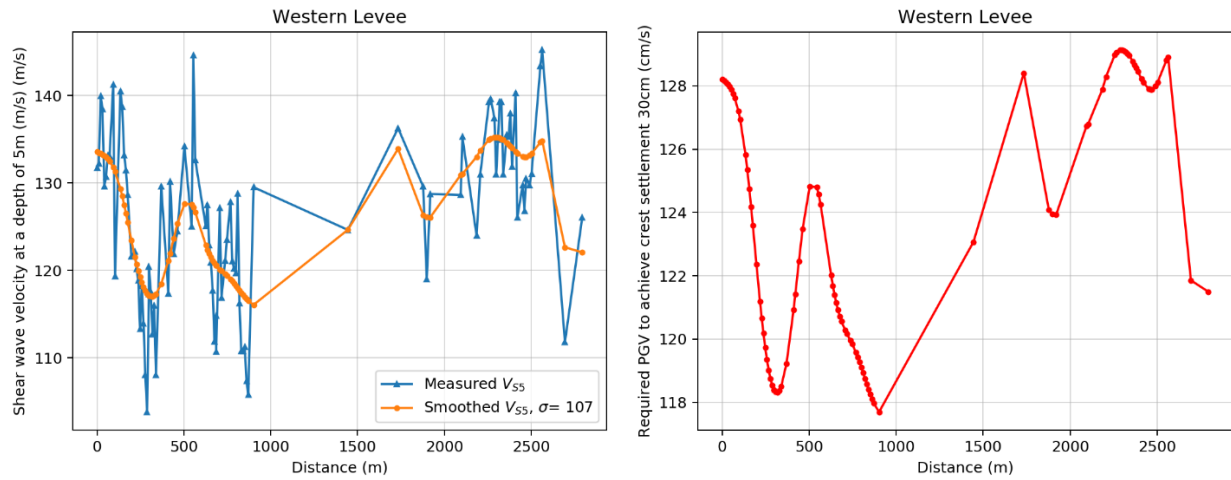


**Figure 5.5** (a) Measured  $V_{S5}$  and smoothed  $V_{S5}$  using gaussian window function along western levee; (b) Required  $PGV$  values to achieve 30cm crest settlement along western levee.

Figure 5.6 illustrates the computed semi-variograms and the fitted gaussian model, and the correlation length is 0.294 km. This is similar to, but slightly less than, the correlation length for the southern levees.

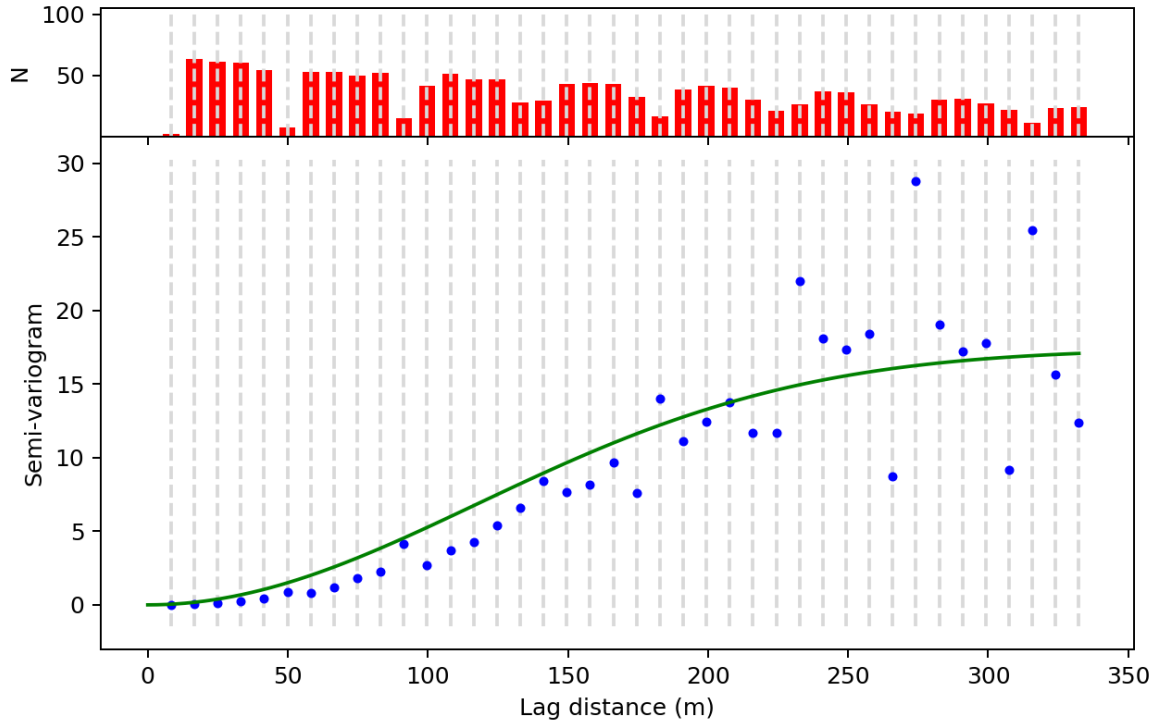


**Figure 5.6** Semi-variogram versus lag distance (m) and fitted gaussian model based required *PGV* values to achieve 30 cm crest settlement along the western levee.

#### 5.4 Spatial Correlation of Limit State Function

The mean and standard deviation of the limit state function is computed using Eqs. 5.4 and 5.5, respectively, where  $\mu_C$  is the natural log of the median capacity from the fragility function, and  $\mu_D$  is the natural log of the median value of demand. Spatial correlation of the limit state function is obtained by inserting Eq. 5.13 and the capacity correlation function into Eq. 5.6. Double differentiating the resulting expression and evaluating at zero separation distance results in Eq. 5.21.

$$\frac{\partial^2 \rho_Z(0)}{\partial x^2} = -2\pi \left( \frac{\alpha_D^2 \cdot \alpha_{\delta W}^2}{d_{\delta W}^2} + \frac{\alpha_C^2}{d_C^2} \right) \quad (5.21)$$

## 5.5 Levee System Reliability Analysis Case Studies

This section presents two case studies of earthquakes that shook Bacon Island levees for which observations of damage (or lack thereof) were made following the earthquakes. The probabilities of levee system exceeding various settlements are computed for the 1980 Livermore earthquake, for which some damage was observed to Bacon Island levees, and for the 2014 South Napa earthquake, for which no damage was observed. I compute the probability of exceedance of different settlement levels for each earthquake, and compare it with the documented observations of levee performance. It is not possible to validate a probabilistic prediction using only two events, but these two case histories nevertheless provide an important benchmark for evaluating the reasonableness of the predictions.

### 5.5.1 1980 Livermore Earthquake

The 1980 Livermore earthquake occurred on January 24 at 11:00 PST in California, and the epicenter of the 5.8  $M_w$  earthquake was a hilly area 12 km southeast of Mount Diablo and north of Livermore Valley. The mainshock was preceded by a 2.7  $M_L$  foreshock 1.5 minutes prior, and six hundred aftershocks were recorded in the 33 days after the main shock and 59 aftershocks were recorded measuring greater than 2.5  $M_L$ . Forty-four people were injured and damage across the San Francisco Bay Area totaled \$11.5 million, with the majority inflicted at the Lawrence Livermore National Laboratory. Fig. 5.7 shows the locations of the ruptured fault, epicenter, and ground motion records. At least 4.2 km of rupture occurred on the Greenville Fault which is a strike-slip fault, and only 7 earthquakes recorded ground motions caused by this event. Bacon Island is about 24 km from the epicenter.

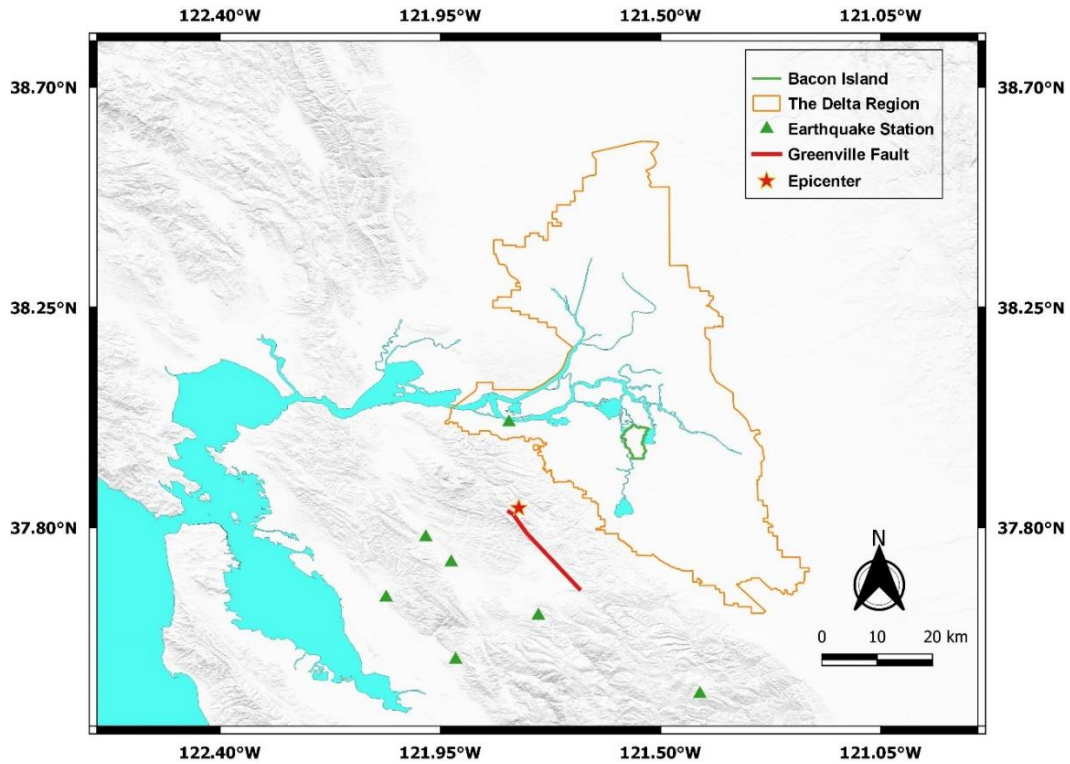


**Figure 5.7** Map showing locations of the Delta, Bacon Island levees, available earthquake stations, and the ruptured faults and epicenter of 1980 Livermore earthquake with ( $M_w = 5.8$ ).

To estimate shaking intensity at each reach location, I first calculate *PGV* residuals at each ground motion station. The mean *PGV* is predicted using BSSA14, and I used  $V_{S30}$  values reported for the NGAWest2 project. The event term  $\eta$  is calculated as the average total residual. Due to only 7 available records for this event, the standard deviation of the event term is equal to the standard error, which is defined as the standard deviation of the total residuals divided by the square root of the number of records. Therefore, the intra-event residual of each station can be computed subtracting the predicted *PGV* and the event term  $\eta$  from recorded *PGV*. Secondly, I apply the kriging approach to estimate the within-event residuals of each levee reach. Kriging is a geostatistical interpolation technique used to estimate the value of a spatially distributed variable at unobserved locations on the values observed at other locations. Specifically, the ordinary kriging,

which assumes that the spatial variation in the data is stationary, is implemented here to predict within-event residuals for levees. Kriging provides not only point estimates but also measures of uncertainty associated with those estimates, so these kriging variances can be used as the inputs in levee system reliability analyses. None of the recording stations are close to Bacon Island, so the full within-event residuals are essentially utilized.

After defining demands, I then defined the capacities for each reach, and utilized the level crossing statistics equations to compute the probabilities of exceeding various settlement levels, as summarized in Table 5.1. These probabilities reflect the probability of exceeding the specified settlement for at least one location on Bacon Island. In this case, the prediction is 64.3% that settlement would exceed 10 cm during the 1980 Livermore earthquake, and 6.7% that crest settlement would exceed 30 cm. There is only a 1% probability that settlement would exceed 1m, which I interpret as a threshold beyond which system failure might occur due to loss of freeboard.

**Table 5.1** Probability of exceeding various settlement levels of Bacon Island levee system during 1980 Livermore earthquake.

<b>Settlement (cm)</b>	<b>Probability of exceeding the settlement level (%)</b>
1	100
10	64.3
30	6.7
100	0.4

Finch (1980) presented some damage observations to Delta levees from several earthquakes in 1980's, and he mentioned that a 250-foot land-side rotational slip-out dropped several feet on the eastern side of Bacon Island. A photo of this damage is presented in Fig. 5.8. The damage occurred around the mid-slope location of the downstream face of the levee. It is difficult to get an accurate



sense for the amount of settlement associated with the slip. It is also not possible to infer from the figure whether any crest settlement occurred as a result of the earthquake. Overall, I believe that the predicted probabilities are reasonably consistent with the damage observations.



Levee damage on Bacon Island (Site 2). A 250-foot land-side rotational slip-out dropped several feet during the January 24, 1980 Livermore earthquake.

**Figure 5.8** Observed damage on levee slope on the island side of eastern Bacon Island during the January 24, 1980, Livermore earthquake. (Finch, 1980)

### 5.5.2 2014 South Napa Earthquake

The 2014 South Napa earthquake occurred in the North San Francisco Bay Area on August on August 24, and the moment magnitude is 6.0 with a maximum Mercalli intensity of VII (Serve).

The epicenter of the earthquake was located to the south of Napa and to the northwest of American

Canyon on the West Napa Fault that is a strike-slip fault. Fig. 5.9 shows the locations of the ruptured fault, epicenter, Bacon Island, and available earthquake stations. There is a total of 412 stations that recorded the ground motions during this event, and Bacon Island is about 69 km from the epicenter. I followed the same process for the South Napa earthquake as for the Livermore earthquake, and computed probabilities of exceedance of the same settlement levels.

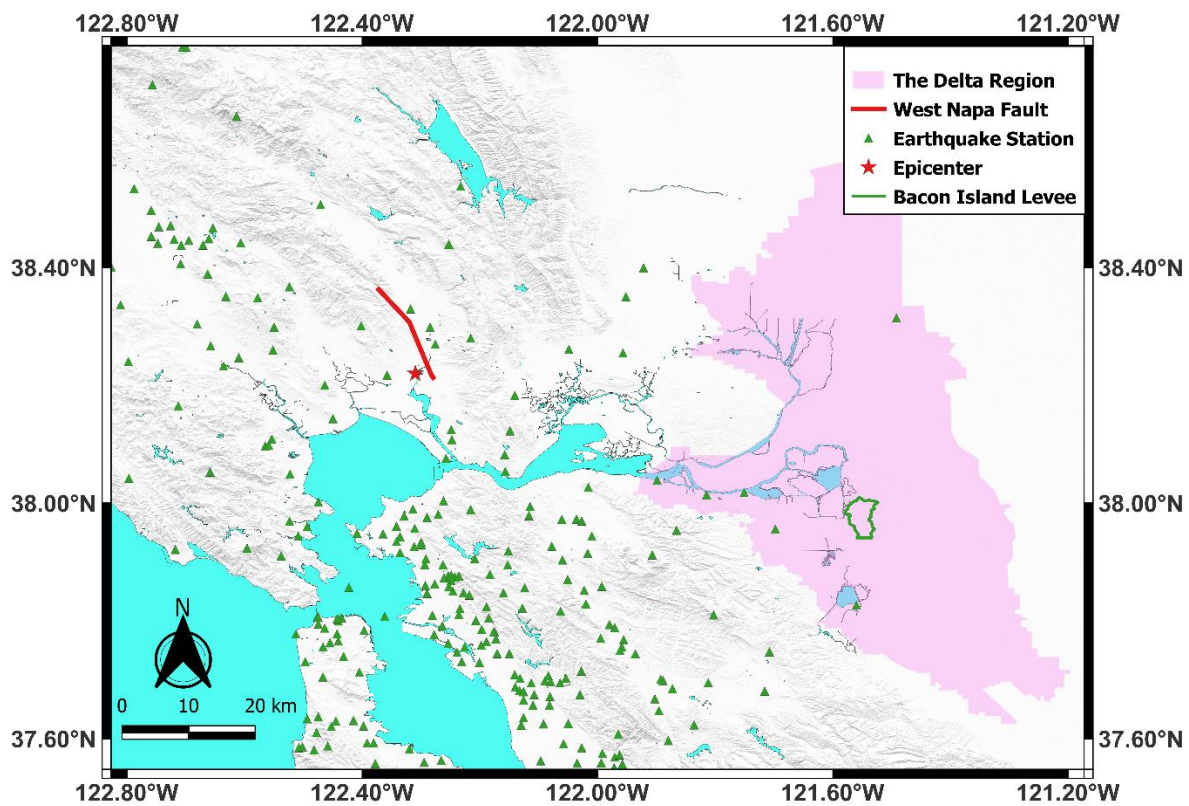


**Figure 5.9** Map showing locations of the Delta, Bacon Island levees, available earthquake stations, and the ruptured faults and epicenter of 2014 South Napa earthquake ( $M_w = 6.0$ ).

Table 5.2 demonstrates that crest settlements higher than 1cm are highly likely for the South Napa event, but settlements over 10 cm are highly unlikely. Settlements as small as 1cm would be

difficult to observe during the reconnaissance mission, and would likely go unreported. This result aligns with the fact that no significant damage observation was reported for Bacon Island levees after 2014 South Napa earthquake. As a corollary, the system reliability provided reasonable predictions in this case as well.

**Table 5.2** Probability of exceeding various settlement levels of Bacon Island levee system during 2014 South Napa earthquake.

Settlement (cm)	Probability of exceeding the settlement level (%)
1	50.7
10	$6.4e^{-3}$
30	$9.7e^{-6}$
100	$1.4e^{-8}$

## 5.6 Seismic Risk Assessment of Bacon Island Levees

This section presents the implementation of seismic risk assessment for Bacon Island levee system by convolving levee fragility functions and the seismic hazard from the selected reduced event subset. Annual rates of exceeding various settlements for levee systems due to earthquake shaking are computed. The BSSA14 GMM with Delta-specific site and path models (Buckreis. 2022) are utilized in these risk assessments because I consider them to be more reasonable than the ergodic components. The process utilized in this section is similar as that utilized to evaluate levee response for the 1980 Livermore and 2014 South Napa events, with the only differences being (1) this section utilizes many more events that are representative of seismic hazard for the Bacon Island levee system, and (2) the computed probabilities are multiplied by the annual rate of occurrence of each event, and the rates are summed to obtain an overall annual exceedance rate. The event subset defined by Liu et al. (2022) is utilized herein, as defined by Figs. 4.4 and 4.5. A value of  $V_{S30} = 350$  m/s was selected because it is consistent with the condition at the base of the finite

element models defined in Chapter 3.

Figure 5.10 shows the annual rate of exceeding various settlement levels at any point within the Bacon Island levee system. The annual rate of exceeding 1cm of earthquake-induced settlement is  $0.0394 \text{ yr}^{-1}$ . Alternatively, the return period is 2.5 years ( $1/0.394 \text{ yr}^{-1}$ ) for exceedance of 1cm of earthquake-induced settlement. Similarly, the rates of exceedance of 10, 30, and 100 cm of settlement are 0.056, 0.016, and  $0.003 \text{ yr}^{-1}$  (17.7, 60.1, and 326.8-year return periods), respectively.

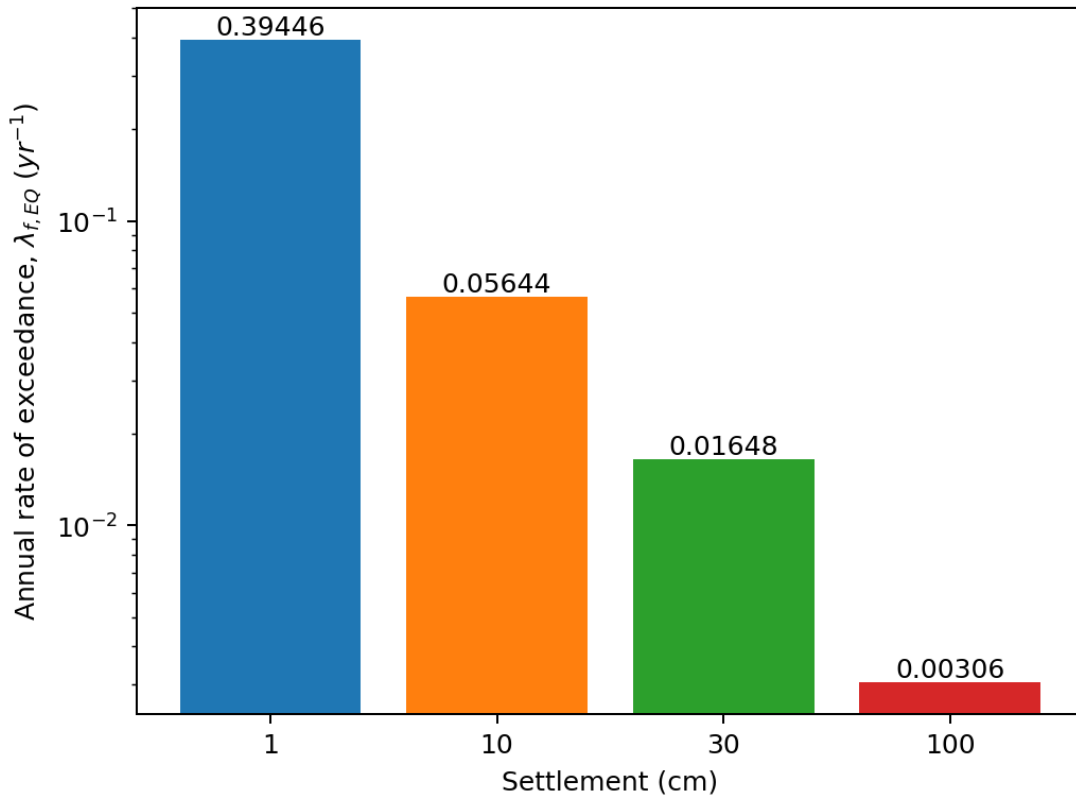


**Figure 5.10** Annual rates of exceedance of various settlements using the selected event subset.

The settlement values reported in Fig. 5.10 must be further interpreted to quantify the probability

of failure of the levee system. Earthquake-induced settlement can cause levee failure in two different ways. First, the crest settlement may result in overtopping and erosion of the land-side levee slope. Second, crest settlement may result in cracks that shorten the drainage path length, thereby resulting in higher hydraulic gradients and through-seepage erosion. Herein I evaluate only the probability of failure due to overtopping.

To define freeboard, I gathered tidal elevation data for the Port Chicago, CA tide gauge through the NOAA data service at <https://tidesandcurrents.noaa.gov/map/index.html?id=9415144>. The station is located west of the Delta at the location shown in Fig. 5.11. The tide gauge is the closest one to Bacon Island that is served through the NOAA website.



**Figure 5.11** Map of Port Chicago tide gauge where data is served by NOAA (<https://tidesandcurrents.noaa.gov/map/index.html>).

The NOAA website contains an API that allows users to query tidal elevation time series data in

31 day increments. An example 31-day increment from December 16, 2023 through January 15, 2024 is shown in Fig. 5.11. Also plotted in Fig. 5.11 are lines denoting the elevation of the crest for the southern levee, and where the crest would be under various settlement scenarios. In this case, settlement of 1m would place the levee crest very close to the highest tidal elevation during the period between December 16<sup>th</sup>, 2023, and January 15<sup>th</sup>, 2024. During 2023, the highest water elevation was 2.36 m. The levee crest elevations range from 3.23 to 3.84 m based on the 2017 LiDAR data. For this reason, 1m of settlement at the levee crest would very likely result in an overtopping failure if the levee were not repaired quickly.

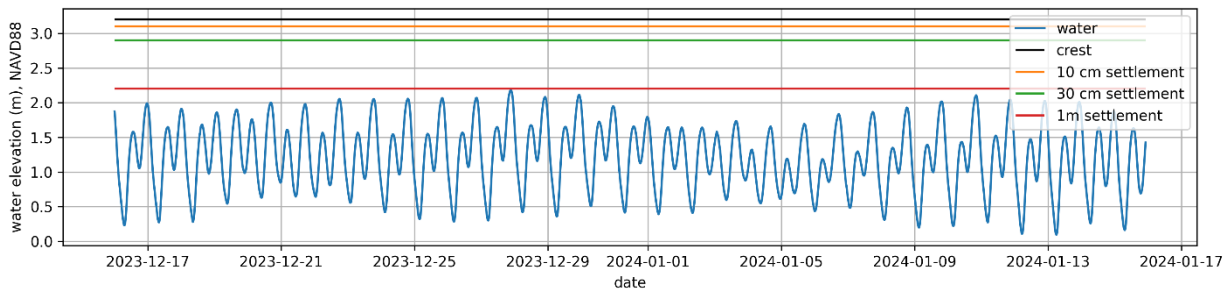


**Figure 5.12** Water elevation at Port Chicago tide gauge from December 16, 2023 through January 15, 2024 (<https://tidesandcurrents.noaa.gov/map/index.html>).

Rather than reporting results as the annual rate of exceedance, DRMS reported the probability of levee failure over time spans of 25, 50, and 100 years. Probabilities of exceedance of settlement levels 1, 10, 30, and 100 cm during those time spans are calculated using Eq. 5.13 and are presented in Table 5.3. Considering failure to correspond to 100 cm of settlement, my predictions indicate rates of failure that are about 40% lower than predicted by DRMS.

Potential reasons for the discrepancies between the failure probabilities from DRMS and the

present study are likely due to differences in (1) formulation of fragility functions, (2) handling of length effects and spatial correlation, and (3) seismic hazard analyses. Probabilistic predictions cannot be empirically validated absent observations from many earthquakes, which would require thousands of years observations. Nevertheless, some insights can be gained by noting that an earthquake has not caused inundation Bacon Island in the past 100 years. My study predicts this observation has a 74% probability, while the DRMS study considers this to be unlikely, with only an 11% probability. Of course, the levees have evolved over time, but this simplified analysis assumes the levees existed in their configuration for the past 100 years.

**Table 5.3** Probabilities of levee failure over various spans of time for this study, and DRMS (2009).

<b>Time span (years)</b>	<b>This Study</b>				<b>DRMS</b>
	<b>P (S &gt;1cm)</b>	<b>P (S &gt;10cm)</b>	<b>P (S &gt;30cm)</b>	<b>P (S &gt;100 cm)</b>	<b>P (failure)</b>
25	100%	77%	34%	7.4%	42%
50	100%	95%	56%	14%	67%
100	100%	100%	81%	26%	89%

### **5.7 Risk Assessments of Bacon Island Under other Hazards**

My collaborators in the research project ‘The Next Generation of Multi-hazard Risk Assessment of the Delta Levee’ focused on other hazards, including high water events causing overtopping and through seepage, and also subsidence of the soft peaty soils in the Delta. Stephen Andrews from Resource Management Associates performs hydraulic modeling, including selection of high-water events, hydrodynamic model description, hydrodynamic model results, and wind wave analysis. Steve Deverel and José Tomas Diaz Casanueva from Hydrofocus conducted the ground subsidence analysis of the Bacon Island levees, and they focus on drivers of subsidence and present development, update, and calibration of SUBCALC, a computer code for modeling subsidence.

Sebastian Uhlemann, Peter Nico, and Craig Ulrich from Lawrence Berkeley National Laboratory implement geophysical investigations at Bacon Island, including background information about geophysical measurements of levee properties, seismic velocity measurements, and electrical resistivity measurements. All these results are a direct input in levee modeling in overtopping, seepage, and seismic hazard analysis. Sandra Bachand from Bachand & Associates performs seepage and overtopping analysis, including a description of the methodology, development of levee response functions, development of fragility functions, and risk mitigation.

I applied the system reliability analysis framework to Sandra’s overtopping analysis, which are indicated in Table 5.4 for various sea level rise conditions and levee upgrade responses. The baseline sea level rise condition corresponds to current sea level, while medium and high amounts of sea level rise were 1.1 ft and 3.4 ft also considered. Furthermore, the calculations were performed for levees in their current condition, and also assuming that the levee crest elevation is raised 0.3–0.5 m in response to sea level rise.

**Table 5.4** Annual rates of overtopping failure.

<b>Sea Level</b>	<b><math>\lambda_{f,OT}</math> (yr<sup>-1</sup>) Current Levee Conditions</b>	<b><math>\lambda_{f,OT}</math> (yr<sup>-1</sup>) Upgraded Levee Conditions</b>
Baseline	0.0097	0.0
Med	0.077	1.6e-4
High	0.100	0.016

The annual rate of failure of the levees in their current condition for baseline sea levels is 0.0097 yr<sup>-1</sup>, which is three times larger than the annual rate of exceedance of 1m of earthquake-induced settlement. I did not study the influence of sea level rise on probability of failure due to earthquake loading, or for levees under upgraded conditions, and therefore cannot compare the other annual rates with flood hazard rates.



## **CHAPTER 6: Conclusions and Recommendations**

### **6.1 Conclusions**

This dissertation presents a comprehensive framework of seismic risk assessment of a spatially distributed levee system in the Delta, and this framework can be also easily applied to other infrastructure systems including pipelines and roadways. This risk assessment framework incorporates two essential components: (1) earthquake analysis including system seismic capacity and demand quantification, and (2) system reliability analysis.

Seismic capacity is represented by fragility functions representing levee crest settlement as a function of ground motion intensity. Levee fragility depends on many factors, including soil strength and stiffness, layering/stratigraphy, levee geometry, soil type, and groundwater conditions. Geometry was defined using LiDAR and bathymetry data. Soil strength, and type were defined based on available geotechnical site investigations including cone penetration tests, boring logs, and laboratory tests performed on samples gathered from the boring logs. Soil stiffness was defined based on geophysical land streamer surveys that utilized multi-channel analysis of surface waves and inversions of surface measurements to define shear wave velocity as a function of depth. Geotechnical investigations were available only at select locations around the perimeter of Bacon Island. As a result, I developed two cross-sections that are broadly representative of levees that are composed of peat along the southern end of Bacon Island, and levees that contain a significant fraction of sand along the western, eastern, and northern portions of Bacon Island. These cross-sections are assumed to be broadly representative of these levees, though extrapolations are admittedly present in my interpretations. I used finite element simulations of the levee cross-sections to formulate fragility functions by shaking the cross-sections with a suite of earthquake ground motions. Fragility was formulated based on levee crest settlement vs. input peak ground

velocity. Land streamer measurements provided detailed information about the shear wave velocity of the levee fill at many locations around Bacon Island, more locations than the geotechnical data required to formulate cross-sections. So, I further conditioned the fragility functions on  $V_{S5}$ , or the time-averaged shear wave velocity in the upper 5 m of the profile. Furthermore, I utilized the land streamer data to quantify the spatial correlation of capacity (i.e., correlation of levee fragility), which is important for system reliability analysis.

Seismic demand is represented by ground motion intensity measures arising from an earthquake defined by a finite fault solution (and corresponding magnitude) and distance from the sites of interest to the fault rupture based on GMMs. Probabilistic seismic hazard analysis was performed by considering the ground motion intensity measures for all plausible earthquake scenarios, and the corresponding rate of occurrence of each earthquake event. Uncertainties in the GMMs were incorporated into the seismic hazard analysis to represent the annual rate of exceedance of various intensity measures. Moderate magnitude earthquakes within or near the Delta contributed most significantly to seismic hazard, with some contribution from more distance larger magnitude events. The intensity measure adopted for analysis was the peak ground velocity,  $PGV$ , input at the base of the finite element models, which corresponds to  $V_{S30} = 350$  m/s. Several other intensity measures were considered, including  $PGV$  at the elevation of the levee crest in the absence of liquefaction effects, input  $PGA$ , and  $PGA$  at the levee crest. The input  $PGV$  was selected because it produced the smallest dispersion in the fragility functions. Spatial correlation of seismic demands was represented based on Jayaram and Baker (2009), who studied spatial correlation of within-event residuals for 7 earthquakes in California. The event term (i.e., the average misfit between a GMM prediction and the observed ground motion levels) was treated as a random

variable that is spatially constant for a particular earthquake.

Levees are commonly analyzed using cross-sections, as was done in the finite element simulations performed in this study. However, levees are spatially variable along their length, and the capacity of the cross-sections and the demand imposed on the cross-sections are therefore spatially correlated random fields. The question of whether the levee system will fail is treated herein using a system reliability analysis procedure that uses level-crossing statistics to assess the probability that the demand will exceed the capacity at some point within the system. The system reliability analysis solves the “weakest-link-in-the-chain” problem by modeling capacity and demand as spatially correlated random fields, and using a level crossing statistics technique.

The fundamental scientific contributions provided by this thesis are summarized as follows,

(1) I developed a framework for utilizing geophysical testing measurements to quantify spatial correlation of levee capacity. This is important because land streamer measurements are relatively inexpensive, non-invasive, and quick, but procedures for engineers to utilize the detailed information provided by the land streamers previously did not exist.

(2) Fragility functions for Bacon Island levees were developed utilizing state-of-the-art numerical simulations utilizing dynamic non-linear finite element analyses capable of capturing the effects of liquefaction. Previous studies were based on combinations of elastic dynamic simulations, slope stability analyses, and experts’ opinion.

(3) I found that the input ground motion intensity measurement is a more efficient predictor of levee settlement than the surface ground motion in the absence of liquefaction effects. This finding is contrary to the current standard of practice, in which  $V_{S30}$  utilized in the seismic hazard analysis corresponds to surface conditions rather than to the stiffer conditions for the soils that underlie the

levee soils. I postulate that the reason for this finding is that nonlinear total stress site response analyses result in saturation of ground motion intensity due to mobilization of the strength of the soils. Therefore, the shaking intensity at the surface does not continue to increase beyond a certain threshold input intensity. However, increasing the input shaking intensity causes more damage to the soil as the waves propagate through the levee, resulting in more settlement. For this reason, settlement correlates more closely with input shaking intensity than with surface shaking intensity.

(4) This study adopted an efficient LASSO regression-based methodology for selecting an event subset for analysis of Bacon Island, as demonstrated in Chapter 4, which demonstrates application of the methodology for analysis of spatially distributed infrastructure systems. Furthermore, I developed an event subset for seismic analysis of the entire Sacramento-San Joaquin Delta. This work product will be useful for future system reliability analyses. Python scripts developed in this study will benefit users in preparing the input files, and conducting post-processing analysis based on the selected event subset.

(5) The system reliability analysis method was compared with response of levee systems during two past earthquakes. Computed probabilities of failure are reasonably consistent with observed damage for both events. Though it is impossible to validate a probabilistic prediction using such a small number of events, it is encouraging that the method produced predictions that are reasonably consistent with observations.

(6) The calculated annual rates of exceedance of 100 cm of settlement due to earthquake shaking for Bacon Island are lower than the annual rate of failure in the DRMS study from 2009 (URS 2009). Furthermore, 100 cm of settlement would place the levee crest near the high tide level, and more settlement might be required to cause levee failure. Though I stopped short of computing the

annual failure probability, I consider the probability of exceedance of 100 cm of settlement to be a reasonable indicator of failure. While lower, the risks remain appreciable, appropriate mitigation solutions should be considered to alleviate seismic risks.

(7) The analysis presented herein is well-suited to evaluating the impact of future sea level rise, and potential alternative mitigation strategies. This would require development of fragility functions specific to a particular mitigation solution for assessment of the overall benefit afforded to the Delta in terms of annual failure probability.

## **6.2 Recommendations for Future Research**

The research presented in this thesis illustrates that seismic capacity, demand, correlation length, and system reliability analysis approach are crucial elements in seismic risk evaluation of a series system. Aspects of the analysis that were not addressed in this thesis may provide fruitful opportunities for future researchers, and include the following items.

### 1. Seismic capacity:

(a) As described in Chapter 3, I did not correctly conduct post-shaking reconsolidation analysis for peaty soils because of insufficient assigned analysis time. Furthermore, soil constitutive models in OpenSees underestimate post-cyclic reconsolidation strains, and do not capture secondary compression settlements of soft clay and peat. This means that the computed settlements may under-predict actual settlements during real earthquakes, so additional research should be considered to quantify the additional settlement induced by reconsolidation.

(b) Kwak et al. (2016a), Yang (2021), and this study all utilize *PGV* as the intensity measure for defining the levee fragility functions, whereas Tsai (2018) derived fragility functions for levees using *PGA* because of the lack of a suitable *PGV* model for subduction earthquakes in Japan at the

time of her dissertation. Alternative intensity measures such as aria intensity and cumulative absolute velocity that inherently account for duration might also be good variables in levee fragility functions. More research is required to investigate optimal intensity measures.

(c) Epistemic uncertainty in modeling is another issue that would require additional work to assess. For example, the PIMY and PDMY03 material models used in finite element modeling are one of many suitable constitutive models. PM4Sand and PM4Silt were not evaluated in this work because they were not reliably implemented in OpenSees at the time my simulations were run. Moreover, the vertical component of ground motion that also has impact on levee response during earthquake is ignored in this study.

## 2. Seismic demand:

NSHMP package developed by USGS has not yet adopted updated linear site and path models developed by Buckreis (2022) and Buckreis et al. (2023) that are more specific to the Delta yet, so the PSHA I ran for multiple sites on the levees does not incorporate these newly available models. Additional work is needed to rerun all PSHA with these updated site and path models, and then reselect event subset for risk assessment.

## 3. Correlation length:

I develop correlation length of levee capacity for Bacon Island levee system by collecting and analyzing geophysical measurements obtained from land streamers. On the contrary, Kwak et al. (2016) performed back calculations to derive correlations according to observations of levee damage in past earthquakes, but there was no land streamer data available. Kwak et al. (2016) found that the correlation lengths were about twice as large for the Japanese levee system as those I computed for the Delta levee system. It is currently unclear whether land streamer measurements

collected along the Japanese levee system would confirm the back-calculated value by Kwak et al. (2016), or whether additional corrections are required to utilize geophysical measurements to obtain correlation lengths.

#### 4. System reliability analysis:

(a) To achieve the goal of implement risk assessment of the levee systems in the Delta, extra work is needed to examine the seismic risks for other Delta islands levees besides Bacon and McDonald Islands so that risk can be properly assessed for the overall region. Specifically, Yang (2021) formulated his fragility functions based on surface  $PGV$ , whereas we now know that the input  $PGV$  is a more efficient intensity measure.

(b) The system reliability analysis by means of level crossing statistics is well suited to risk assessment of other spatially distributed systems such as pipelines and roadways, but to my knowledge, this has not yet been performed. Future research is required to develop suitable fragility functions for other infrastructure systems, and implement them into the system reliability analysis framework.

# APPENDIX A: CPT Profiles for Northern and Southern Levees

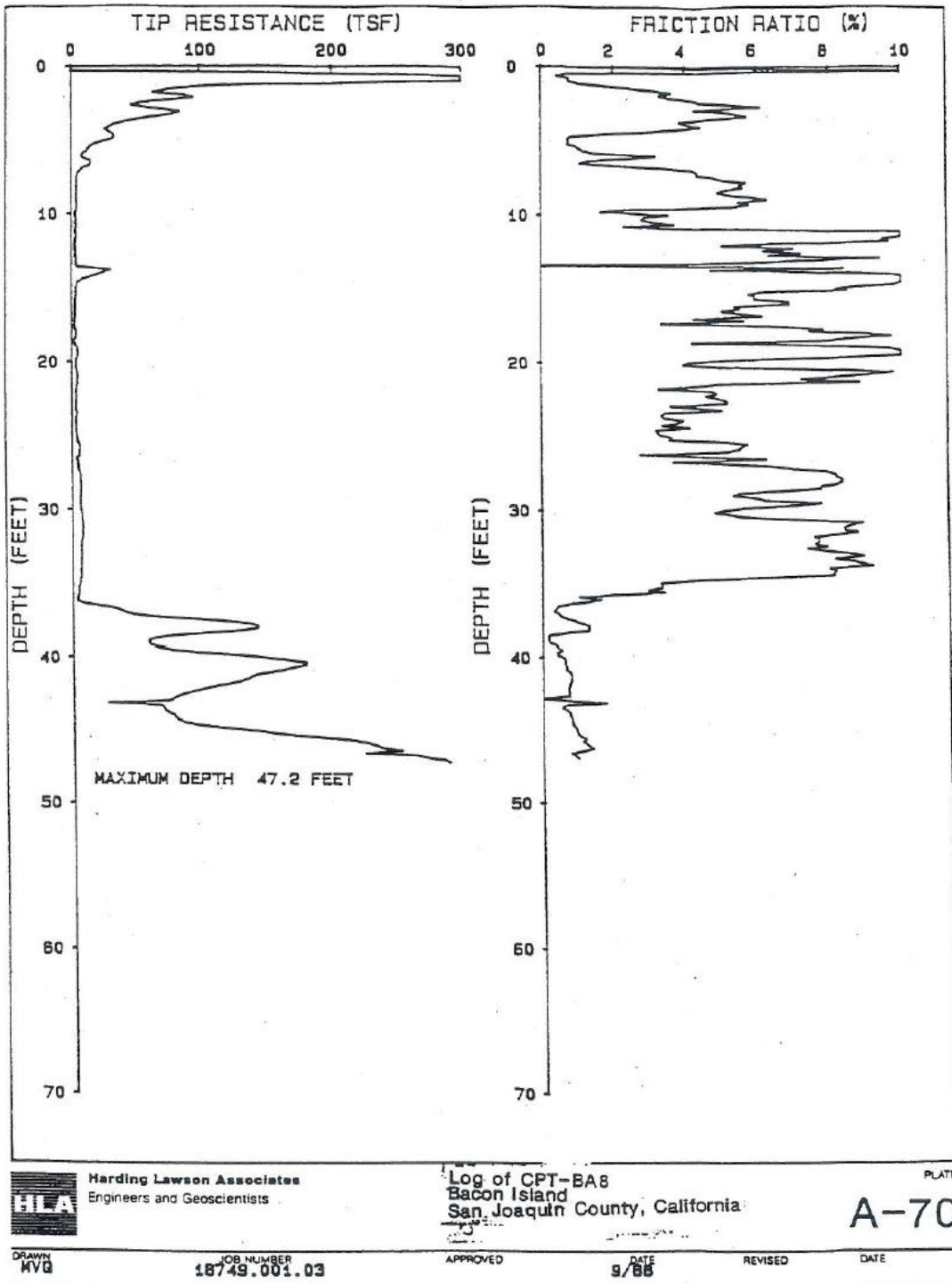


Figure A.1 CPT (dwp-bi-ba8) profile through northern levee crest.



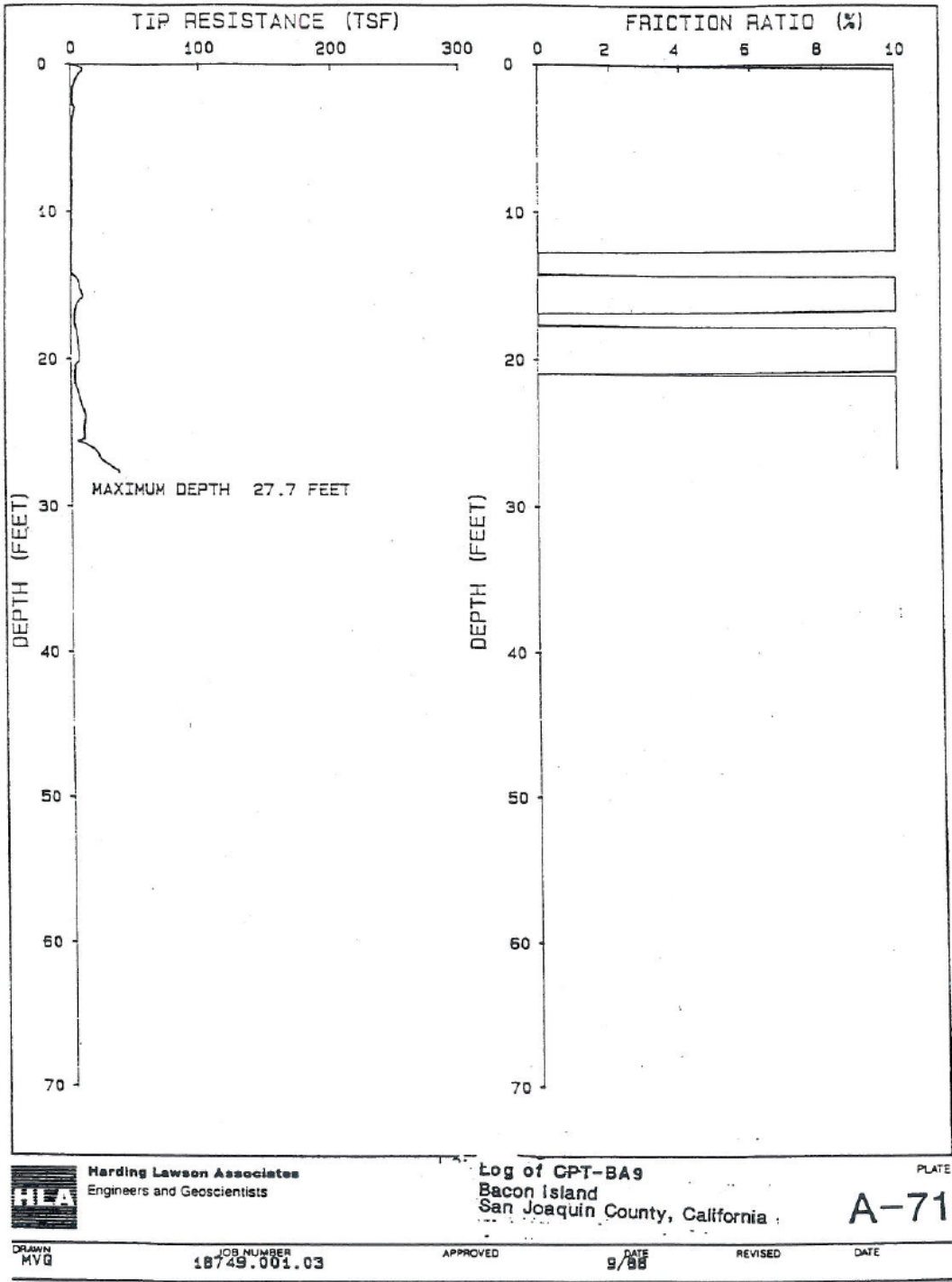


Figure A.2 CPT (dwp-bi-ba9) profile through northern levee crest.

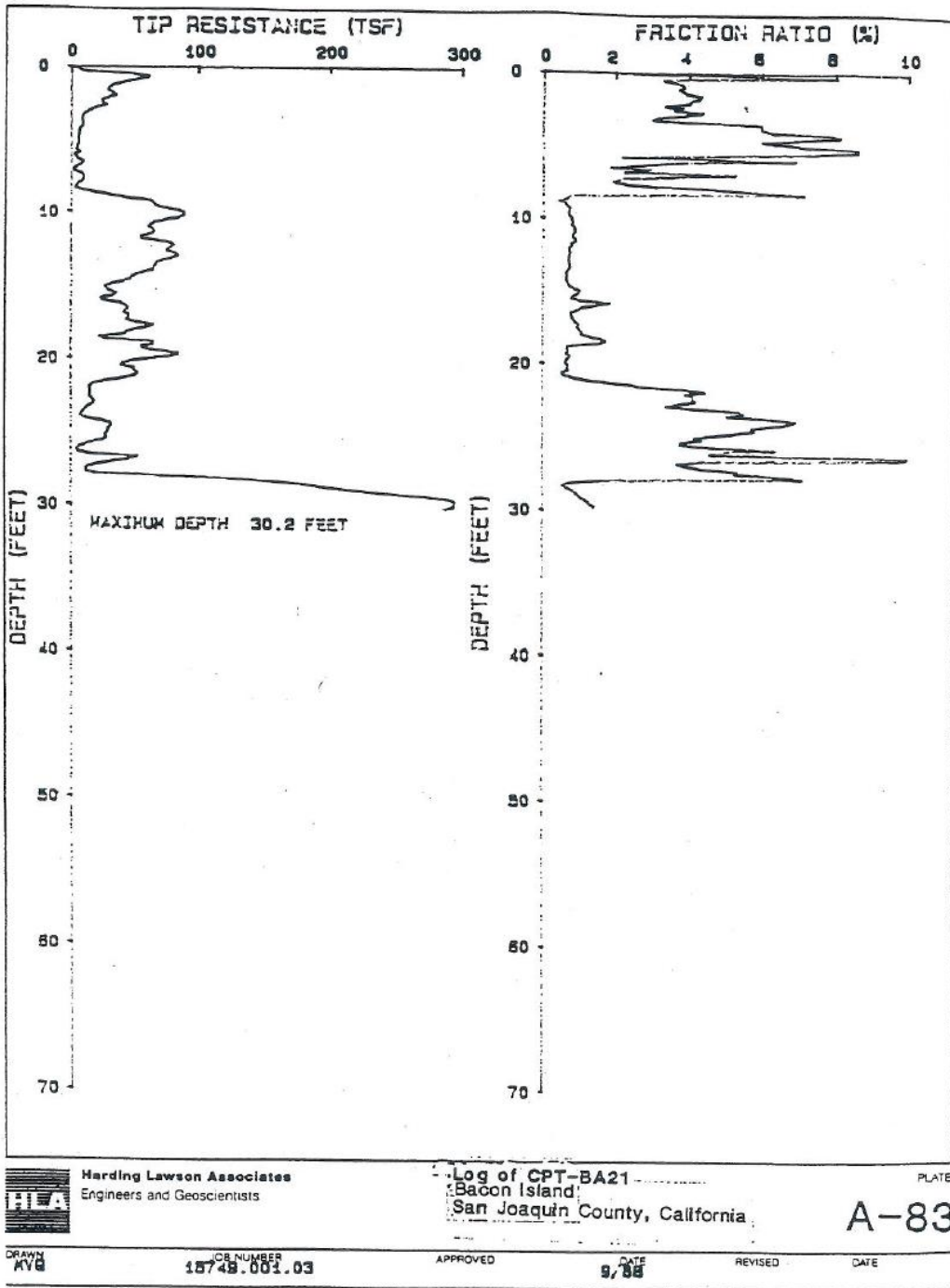


Figure A.3 CPT (dwp-bi-ba21-cpt) profile through southern levee crest.

## APPENDIX B: Selected Unscaled Ground Motions for Simulating Levee Fragility Functions

RSN	Name	YEAR	MO DY	HRM N	Station Name	Magnitude	Strike (°)	Dip (°)	Rake (°)	Hypocenter Latitude (°)	Hypocenter Longitude (°)	Hypocenter Depth (km)	R <sub>jb</sub> (km)	V <sub>s30</sub> (m/s)	Geologic al Unit	Station Latitude (°)	Station Longitude (°)	PGA (g)	PGV (cm/s)
15	Kern County	1952	721	1153	Taft Lincoln School	7.36	51	75	61	34.9906	-119.024	15.63	38.42	385. 43	Qal, thin	35.15	-119.46	0.16	16.97
20	Northern Calif-03	1954	122 1	1956	Ferndale City Hall	6.5	65.6	90	0	40.8167	-124.083	10	26.72	219. 31	Qal, thin	40.576	-124.263	0.19	31.33
26	Hollister- 01	1961	409	723	Hollister City Hall	5.6	269	90	0	36.683	-121.3	7.4	19.55	198. 77	Qoa	36.85	-121.4	0.08	10.16
27	Hollister- 02	1961	409	725	Hollister City Hall	5.5	19.8	90	0	36.7	-121.3	7.4	17.2	198. 77	Qoa	36.85	-121.4	0.06	7.48
36	Borrego Mtn	1968	409	230	El Centro Array #9	6.63	317	78	-178	33.189	-116.143	8	45.12	213. 44	Qal, deep, Imperial V.	32.794	-115.549	0.09	19.01
45	Lytle Creek	1970	912	1430	Devil's Canyon	5.33	325	48	59	34.2698	-117.54	8	18.39	667. 13	Kgr	34.21	-117.33	0.17	5.08
56	San Fernando	1971	209	1400	Carbon Canyon Dam	6.61	288	50	83	34.44	-118.41	13	61.79	235	Tss	33.9121	-117.838	0.07	4.78
71	San Fernando	1971	209	1400	Lake Hughes #12	6.61	288	50	83	34.44	-118.41	13	13.99	602. 1	Tss	34.571	-118.56	0.32	14.67
72	San Fernando	1971	209	1400	Lake Hughes #4	6.61	288	50	83	34.44	-118.41	13	19.45	600. 06	pCg	34.65	-118.478	0.18	7.55
73	San Fernando	1971	209	1400	Lake Hughes #9	6.61	288	50	83	34.44	-118.41	13	17.22	670. 84	pCg	34.608	-118.558	0.15	5.00
75	San Fernando	1971	209	1400	Maricopa Array #2	6.61	288	50	83	34.44	-118.41	13	108.56	443. 85	QT	35.04	-119.429	0.01	6.82
80	San Fernando	1971	209	1400	Pasadena - Old Seismo Lab	6.61	288	50	83	34.44	-118.41	13	21.5	969. 07	Kgr	34.1486	-118.171	0.14	9.86
97	Point Mugu	1973	221	1445	Port Hueneme	5.65	249	49	75	34.065	-119.035	8	15.48	248. 98	Qs	34.145	-119.206	0.10	10.32
104	Northern Calif-07	1975	607	846	Shelter Cove, Sta A	5.2	75	72	0	40.57	-124.14	21	58.78	594. 83	Tss	40.039	-124.064	0.03	1.35
132	Friuli, Italy-02	1976	915	315	Forgaria Cornino	5.91	215.1	18. 9	70	46.375	13.067	3.69	14.65	412. 37	-999	46.221	12.997	0.22	9.50
137	Tabas, Iran	1978	916	-999	Bajestan	7.35	330	25	110	33.215	57.323	5.75	119.77	377. 56	-999	34.51	58.18	0.07	5.45
139	Tabas, Iran	1978	916	-999	Dayhook	7.35	330	25	110	33.215	57.323	5.75	0	471. 53	-999	33.3	57.52	0.33	25.87
140	Tabas, Iran	1978	916	-999	Ferdows	7.35	330	25	110	33.215	57.323	5.75	89.76	302. 64	-999	34.01	58.16	0.10	6.08
143	Tabas, Iran	1978	916	-999	Tabas	7.35	330	25	110	33.215	57.323	5.75	1.79	766. 77	-999	33.58	56.92	0.81	113.5 3
146	Coyote Lake	1979	806	1705	Gilroy Array #1	5.74	336	80	176	37.065	-121.49	8	10.21	142 8.14	KJf	36.973	-121.572	0.11	7.65
147	Coyote Lake	1979	806	1705	Gilroy Array #2	5.74	336	80	176	37.065	-121.49	8	8.47	270. 84	Qal, deep (incl LA)	36.982	-121.556	0.25	24.34
154	Coyote Lake	1979	806	1705	San Juan Bautista, 24 Polk St	5.74	336	80	176	37.065	-121.49	8	19.46	335. 5	Qoa	36.86	-121.54	0.10	6.86
167	Imperial Valley-06	1979	101 5	2316	Compuertas	6.53	323	80	180	32.644	-115.307	9.96	13.52	259. 86	-999	32.573	-115.083	0.15	10.56
172	Imperial Valley-06	1979	101 5	2316	El Centro Array #1	6.53	323	80	180	32.644	-115.307	9.96	19.76	237. 33	Qal, deep, Imperial V.	32.96	-115.319	0.14	13.33

RSN	Name	YEAR	MO DY	HRM N	Station Name	Magnitude	Strike (°)	Dip (°)	Rake (°)	Hypocenter Latitude (°)	Hypocenter Longitude (°)	Hypocenter Depth (km)	R <sub>jb</sub> (km)	V <sub>s30</sub> (m/s)	Geologic Unit	Station Latitude (°)	Station Longitude (°)	PGA (g)	PGV (cm/s)
173	Imperial Valley-06	1979	101 5	2316	El Centro Array #10	6.53	323	80	180	32.644	-115.307	9.96	8.6	202. 85	Qal, deep, Imperial V.	32.7806	-115.568	0.20	50.43
174	Imperial Valley-06	1979	101 5	2316	El Centro Array #11	6.53	323	80	180	32.644	-115.307	9.96	12.56	196. 25	Qal, deep, Imperial V.	32.7517	-115.595	0.37	40.77
178	Imperial Valley-06	1979	101 5	2316	El Centro Array #3	6.53	323	80	180	32.644	-115.307	9.96	10.79	162. 94	Qal, deep, Imperial V.	32.894	-115.38	0.26	45.33
180	Imperial Valley-06	1979	101 5	2316	El Centro Array #5	6.53	323	80	180	32.644	-115.307	9.96	1.76	205. 63	Qal, deep, Imperial V.	32.855	-115.466	0.41	78.29
184	Imperial Valley-06	1979	101 5	2316	El Centro Differential Array	6.53	323	80	180	32.644	-115.307	9.96	5.09	202. 26	Qal, deep, Imperial V.	32.796	-115.535	0.44	57.84
187	Imperial Valley-06	1979	101 5	2316	Parachute Test Site	6.53	323	80	180	32.644	-115.307	9.96	12.69	348. 69	Qal, coarse	32.929	-115.701	0.17	19.80
193	Imperial Valley-07	1979	101 5	2319	Bonds Corner	5.01	319.9	90	180	32.7667	-115.441	9.5	10.83	223. 03	Qal, deep, Imperial V.	32.6931	-115.338	0.10	6.23
209	Imperial Valley-08	1979	101 6	658	Westmorlan d Fire Sta	5.62	157	90	180	33.022	-115.506	3.3	9.39	193. 67	Qal, deep, Imperial V.	33.037	-115.623	0.12	11.14
231	Mammoth Lakes-01	1980	525	1634	Long Valley Dam (Upr L Abut)	6.06	12	50	-35	37.609	-118.846	9	12.56	537. 16	Qal, coarse	37.588	-118.705	0.37	17.63
243	Mammoth Lakes-04	1980	525	2035	Long Valley Dam (Upr L Abut)	5.7	22	50	28	37.625	-118.859	5	12.75	537. 16	Qal, coarse	37.588	-118.705	0.25	10.14
249	Mammoth Lakes-06	1980	527	1451	Fish & Game (FIS)	5.94	22	50	-28	37.506	-118.826	14	6.45	373. 18	Qal, thin	37.614	-118.83	0.39	17.86
250	Mammoth Lakes-06	1980	527	1451	Long Valley Dam (Upr L Abut)	5.94	22	50	-28	37.506	-118.826	14	9.65	537. 16	Qal, coarse	37.588	-118.705	0.72	33.85
268	Victoria, Mexico	1980	609	328	SAHOP Casa Flores	6.33	318	90	0	32.185	-115.076	11	39.1	259. 59	-999	32.618	-115.436	0.08	8.35
285	Irpinia, Italy-01	1980	112 3	1934	Bagnoli Irpino	6.9	312.8	60	-90	40.8059	15.3372	9.5	8.14	649. 67	-999	40.821	15.069	0.15	29.99
290	Irpinia, Italy-01	1980	112 3	1934	Mercato San Severino	6.9	312.8	60	-90	40.8059	15.3372	9.5	29.79	428. 57	-999	40.791	14.764	0.14	9.13
295	Irpinia, Italy-02	1980	112 3	1935	Auletta	6.2	124	70	-90	40.8464	15.3316	7	28.69	476. 62	-999	40.56	15.558	0.02	3.10
302	Irpinia, Italy-02	1980	112 3	1935	Rionero In Vulture	6.2	124	70	-90	40.8464	15.3316	7	22.68	574. 88	-999	40.929	15.669	0.10	11.38
311	Taiwan SMART1( 5)	1981	129	451	SMART1 O01	5.9	109	64	64	24.4292	121.8963	11.1	27.3	267. 67	-999	24.6922	121.7686	0.11	10.81
312	Taiwan SMART1( 5)	1981	129	451	SMART1 O07	5.9	109	64	64	24.4292	121.8963	11.1	23.77	314. 33	-999	24.6561	121.7621	0.08	8.71
329	Coalinga- 01	1983	502	2342	Parkfield - Cholame 4AW	6.36	137	30	90	36.233	-120.31	4.6	46.73	283. 38	Qal, thin	35.707	-120.316	0.06	5.97
334	Coalinga- 01	1983	502	2342	Parkfield - Fault Zone 1	6.36	137	30	90	36.233	-120.31	4.6	41.04	178. 27	Qal, thin	35.758	-120.307	0.12	19.05
337	Coalinga- 01	1983	502	2342	Parkfield - Fault Zone 12	6.36	137	30	90	36.233	-120.31	4.6	27.96	265. 21	Qal, thin	35.899	-120.433	0.11	14.33

RSN	Name	YEAR	MO DY	HRM N	Station Name	Magnitude	Strike (°)	Dip (°)	Rake (°)	Hypocenter Latitude (°)	Hypocenter Longitude (°)	Hypocenter Depth (km)	R <sub>jb</sub> (km)	V <sub>s30</sub> (m/s)	Geologic al Unit	Station Latitude (°)	Station Longitude (°)	PGA (g)	PGV (cm/s)
367	Coalinga-01	1983	502	2342	Pleasant Valley P.P. - bldg	6.36	137	30	90	36.233	-120.31	4.6	7.69	257.38	Qal, thin	36.308	-120.249	0.29	29.92
368	Coalinga-01	1983	502	2342	Pleasant Valley P.P. - yard	6.36	137	30	90	36.233	-120.31	4.6	7.69	257.38	Qal, thin	36.308	-120.249	0.52	46.58
369	Coalinga-01	1983	502	2342	Slack Canyon	6.36	137	30	90	36.233	-120.31	4.6	25.98	648.09	Kgr	36.034	-120.59	0.16	15.93
412	Coalinga-05	1983	722	239	Pleasant Valley P.P. - yard	5.77	355	38	102	36.241	-120.409	7.4	13.16	257.38	Qal, thin	36.308	-120.249	0.43	26.57
415	Coalinga-05	1983	722	239	Transmitter Hill	5.77	355	38	102	36.241	-120.409	7.4	3.7	477.25	Tsh	36.249	-120.343	0.84	47.59
426	Taiwan SMART1(25)	1983	921	1920	SMART1 E01	6.5	73	80	80	23.9382	122.3167	18	93.17	308.39	-999	24.6487	121.7644	0.03	3.39
447	Morgan Hill	1984	424	2115	Agnews State Hospital	6.19	148	90	180	37.306	-121.695	8.5	24.48	239.69	Qal, deep (incl LA)	37.397	-121.952	0.03	5.25
454	Morgan Hill	1984	424	2115	Gilroy - Gavilan Coll.	6.19	148	90	180	37.306	-121.695	8.5	14.83	729.65	KJf	36.973	-121.568	0.11	3.07
464	Morgan Hill	1984	424	2115	Hollister Differential Array #3	6.19	148	90	180	37.306	-121.695	8.5	26.42	215.54	Tss	36.888	-121.413	0.08	9.03
492	Taiwan SMART1(33)	1985	612	1722	SMART1 O07	5.8	248.9	61.5	-90	24.573	122.1947	3.3	41.24	314.33	-999	24.6561	121.7621	0.06	3.12
495	Nahanni, Canada	1985	1223	-999	Site 1	6.76	160	25	90	62.187	-124.243	8	2.48	605.04	-999	62.202	-124.37	1.16	40.41
496	Nahanni, Canada	1985	1223	-999	Site 2	6.76	160	25	90	62.187	-124.243	8	0	605.04	-999	62.234	-124.168	0.40	29.42
506	Taiwan SMART1(40)	1986	520	525	SMART1 I07	6.32	43	57	100	24.0817	121.5915	15.8	58.48	309.41	-999	24.672	121.7642	0.16	25.29
538	N. Palm Springs	1986	708	920	Sunnymead	6.06	287	46	150	34	-116.612	11	37.66	340.32	Qal, deep (incl LA)	33.946	-117.151	0.12	4.73
544	Chalfant Valley-01	1986	720	1429	Bishop - LADWP South St	5.77	48	90	20	37.576	-118.448	6.7	23.38	303.47	Qal, deep (incl LA)	37.36	-118.396	0.10	9.42
549	Chalfant Valley-02	1986	721	1442	Bishop - LADWP South St	6.19	148	55	-163	37.5383	-118.443	10	14.38	303.47	Qal, deep (incl LA)	37.36	-118.396	0.20	20.95
568	San Salvador	1986	1010	1749	Geotech Investig Center	5.8	32	85	0	13.633	-89.2	10.9	2.14	489.34	-999	13.7	-89.175	0.58	65.96
570	Taiwan SMART1(45)	1986	1114	2120	SMART1 C00	7.3	43	57	100	23.9918	121.8332	15	56.01	309.41	-999	24.6738	121.7646	0.14	27.61
572	Taiwan SMART1(45)	1986	1114	2120	SMART1 E02	7.3	43	57	100	23.9918	121.8332	15	51.35	671.52	-999	24.6296	121.761	0.14	13.68
573	Taiwan SMART1(45)	1986	1114	2120	SMART1 I01	7.3	43	57	100	23.9918	121.8332	15	56.18	275.82	-999	24.6755	121.765	0.14	28.87
577	Taiwan SMART1(45)	1986	1114	2120	SMART1 O01	7.3	43	57	100	23.9918	121.8332	15	57.9	267.67	-999	24.6922	121.7686	0.16	22.36
579	Taiwan SMART1(45)	1986	1114	2120	SMART1 O04	7.3	43	57	100	23.9918	121.8332	15	55.18	288.24	-999	24.6703	121.784	0.15	27.64

RSN	Name	YEAR	MO DY	HRM N	Station Name	Magnitude	Strike (°)	Dip (°)	Rake (°)	Hypocenter Latitude (°)	Hypocenter Longitude (°)	Hypocenter Depth (km)	R <sub>jb</sub> (km)	V <sub>s30</sub> (m/s)	Geologic al Unit	Station Latitude (°)	Station Longitude (°)	PGA (g)	PGV (cm/s)
584	Taiwan SMART1(45)	1986	1114	2120	SMART1 O12	7.3	43	57	100	23.9918	121.8332	15	58	303.36	-999	24.691	121.7589	0.14	23.42
595	Whittier Narrows-01	1987	1001	1442	Bell Gardens - Jaboneria	5.99	280	30	150	34.0493	-118.081	14.6	10.31	267.13	Qal, deep, LA basin	33.965	-118.158	0.23	23.62
600	Whittier Narrows-01	1987	1001	1442	Brea Dam (Downstream)	5.99	280	30	150	34.0493	-118.081	14.6	19.11	437.5	Qoa	33.89	-117.927	0.26	10.65
611	Whittier Narrows-01	1987	1001	1442	Compton - Castlegate St	5.99	280	30	150	34.0493	-118.081	14.6	18.32	266.9	Qal, deep, LA basin	33.899	-118.196	0.32	24.26
613	Whittier Narrows-01	1987	1001	1442	Covina - W Badillo	5.99	280	30	150	34.0493	-118.081	14.6	9.49	324.79	Qal, deep (incl LA)	34.087	-117.915	0.10	7.89
621	Whittier Narrows-01	1987	1001	1442	Glendora - N Oakbank	5.99	280	30	150	34.0493	-118.081	14.6	13.67	362.31	Qal, coarse	34.137	-117.883	0.10	4.31
637	Whittier Narrows-01	1987	1001	1442	LA - N Figueroa St	5.99	280	30	150	34.0493	-118.081	14.6	6	364.91	Tsh	34.111	-118.189	0.16	11.78
638	Whittier Narrows-01	1987	1001	1442	LA - N Westmoreland	5.99	280	30	150	34.0493	-118.081	14.6	15.34	315.06	Qoa	34.082	-118.298	0.21	9.44
642	Whittier Narrows-01	1987	1001	1442	LA - W 70th St	5.99	280	30	150	34.0493	-118.081	14.6	16.77	241.41	Qal, thin, west LA	33.976	-118.289	0.16	14.14
644	Whittier Narrows-01	1987	1001	1442	LB - Harbor Admin FF	5.99	280	30	150	34.0493	-118.081	14.6	34.1	230	Qal, fine	33.754	-118.2	0.06	6.74
653	Whittier Narrows-01	1987	1001	1442	Lancaster - Med Off FF	5.99	280	30	150	34.0493	-118.081	14.6	65.32	339.14	Qal, deep (incl LA)	34.688	-118.156	0.06	2.77
692	Whittier Narrows-01	1987	1001	1442	Santa Fe Springs - E.Joslin	5.99	280	30	150	34.0493	-118.081	14.6	11.47	339.06	Qal, deep, LA basin	33.944	-118.087	0.46	33.07
701	Whittier Narrows-01	1987	1001	1442	Terminal Island - S Seaside	5.99	280	30	150	34.0493	-118.081	14.6	37.67	260.6	Qal, fine	33.736	-118.269	0.04	3.77
716	Whittier Narrows-02	1987	1004	1059	San Marino - SW Academy	5.27	170	70	140	34.06	-118.104	13.3	4.42	379.43	Qoa	34.115	-118.13	0.18	11.73
725	Superstition Hills-02	1987	1124	1316	Poe Road (temp)	6.54	127	90	180	33.0222	-115.831	9	11.16	316.64	Qal, deep, Imperial V.	33.097	-115.751	0.34	33.89
735	Loma Prieta	1989	1018	5	APEEL 7 - Pulgas	6.93	128	70	140	37.0407	-121.883	17.48	41.68	415.27	Tss	37.484	-122.313	0.12	15.64
743	Loma Prieta	1989	1018	5	Bear Valley #10, Webb Residence	6.93	128	70	140	37.0407	-121.883	17.48	66.89	304.08	Qal, thin	36.532	-121.143	0.09	8.39
744	Loma Prieta	1989	1018	5	Bear Valley #12, Williams Ranch	6.93	128	70	140	37.0407	-121.883	17.48	50.71	331.21	Qal, thin	36.658	-121.249	0.16	21.76
753	Loma Prieta	1989	1018	5	Corralitos	6.93	128	70	140	37.0407	-121.883	17.48	0.16	462.24	Tss	37.05	-121.803	0.50	48.34
759	Loma Prieta	1989	1018	5	Foster City - APEEL 1	6.93	128	70	140	37.0407	-121.883	17.48	43.77	116.35	Qi	37.545	-122.231	0.28	36.95
782	Loma Prieta	1989	1018	5	Monterey City Hall	6.93	128	70	140	37.0407	-121.883	17.48	39.69	638.63	Kgr	36.597	-121.897	0.07	4.80

RSN	Name	YEAR	MO DY	HRM N	Station Name	Magnitude	Strike (°)	Dip (°)	Rake (°)	Hypocenter Latitude (°)	Hypocenter Longitude (°)	Hypocenter Depth (km)	R <sub>jb</sub> (km)	V <sub>s30</sub> (m/s)	Geologic Unit	Station Latitude (°)	Station Longitude (°)	PGA (g)	PGV (cm/s)
801	Loma Prieta	1989	101 8	5	San Jose - Santa Teresa Hills	6.93	128	70	140	37.0407	-121.883	17.48	14.18	671. 77	serpentine	37.21	-121.803	0.28	25.65
802	Loma Prieta	1989	101 8	5	Saratoga - Aloha Ave	6.93	128	70	140	37.0407	-121.883	17.48	7.58	380. 89	Qoa	37.255	-122.031	0.37	47.33
803	Loma Prieta	1989	101 8	5	Saratoga - W Valley Coll.	6.93	128	70	140	37.0407	-121.883	17.48	8.48	347. 9	Qoa	37.262	-122.009	0.30	63.86
807	Loma Prieta	1989	101 8	5	Sunol - Forest Fire Station	6.93	128	70	140	37.0407	-121.883	17.48	47.41	400. 62	Qal, thin	37.597	-121.88	0.08	8.71
808	Loma Prieta	1989	101 8	5	Treasure Island	6.93	128	70	140	37.0407	-121.883	17.48	77.32	155. 11	af/qi	37.825	-122.373	0.14	25.63
810	Loma Prieta	1989	101 8	5	UCSC Lick Observatory	6.93	128	70	140	37.0407	-121.883	17.48	12.04	713. 59	Kgr	37.001	-122.06	0.46	21.81
811	Loma Prieta	1989	101 8	5	WAHO	6.93	128	70	140	37.0407	-121.883	17.48	11.03	388. 33	Tsh	36.972	-121.995	0.54	29.52
821	Erzican, Turkey	1992	313	1718	Erzincan	6.69	122	63	-164	39.705	39.587	9	0	352. 05	-999	39.75	39.5	0.44	93.84
825	Cape Mendocino	1992	425	1806	Cape Mendocino	7.01	350	14	105	40.327	-124.233	9.5	0	567. 78	Kss	40.348	-124.352	1.40	91.16
836	Landers	1992	628	1158	Baker Fire Station	7.28	336	90	180	34.2	-116.436	7	87.94	324. 62	Qal, deep (incl LA)	35.271	-116.066	0.10	10.22
838	Landers	1992	628	1158	Barstow	7.28	336	90	180	34.2	-116.436	7	34.86	370. 08	Qoa	34.887	-117.047	0.13	22.68
848	Landers	1992	628	1158	Coolwater	7.28	336	90	180	34.2	-116.436	7	19.74	352. 98	Qal, deep (incl LA)	34.851	-116.858	0.35	33.22
854	Landers	1992	628	1158	Featherly Park - Maint	7.28	336	90	180	34.2	-116.436	7	121.8	367. 54	Qal, coarse	33.869	-117.709	0.05	6.01
855	Landers	1992	628	1158	Fort Irwin	7.28	336	90	180	34.2	-116.436	7	62.98	367. 43	Qal, coarse	35.268	-116.684	0.12	12.66
885	Landers	1992	628	1158	Pomona - 4th & Locust FF	7.28	336	90	180	34.2	-116.436	7	117.5	384. 44	Qal, fine	34.056	-117.748	0.06	10.83
907	Big Bear- 01	1992	628	1506	Hesperia - 4th & Palm	6.46	55	85	-10	34.21	-116.83	13	44.48	358. 36	Qal, coarse	34.405	-117.313	0.07	7.44
947	Northridg e-01	1994	117	1231	Arcadia - Arcadia Av	6.69	122	40	103	34.2057	-118.554	17.5	39.41	330. 5	Qal, deep (incl LA)	34.127	-118.059	0.09	9.29
949	Northridg e-01	1994	117	1231	Arleta - Nordhoff Fire Sta	6.69	122	40	103	34.2057	-118.554	17.5	3.3	297. 71	Qal, deep (incl LA)	34.236	-118.439	0.33	29.29
950	Northridg e-01	1994	117	1231	Baldwin Park - N Holly	6.69	122	40	103	34.2057	-118.554	17.5	47.72	544. 68	Qoa	34.1	-117.974	0.12	5.13
951	Northridg e-01	1994	117	1231	Bell Gardens - Jaboneria	6.69	122	40	103	34.2057	-118.554	17.5	41.27	267. 13	Qal, deep, LA basin	33.965	-118.158	0.08	8.62
971	Northridg e-01	1994	117	1231	Elizabeth Lake	6.69	122	40	103	34.2057	-118.554	17.5	36.2	326. 19	Qal, coarse	34.662	-118.387	0.14	8.45
975	Northridg e-01	1994	117	1231	Glendora - N Oakbank	6.69	122	40	103	34.2057	-118.554	17.5	53.71	362. 31	Qal, coarse	34.137	-117.883	0.07	4.20
979	Northridg e-01	1994	117	1231	Huntington Beh - Waikiki	6.69	122	40	103	34.2057	-118.554	17.5	66.43	270. 54	Qal, deep, LA basin	33.727	-118.044	0.08	6.52
980	Northridg e-01	1994	117	1231	Huntington Beach - Lake St	6.69	122	40	103	34.2057	-118.554	17.5	74.7	315. 52	Qoa	33.662	-117.997	0.08	5.51

RSN	Name	YEAR	MO DY	HRM N	Station Name	Magnitude	Strike (°)	Dip (°)	Rake (°)	Hypocenter Latitude (°)	Hypocenter Longitude (°)	Hypocenter Depth (km)	R <sub>jb</sub> (km)	V <sub>s30</sub> (m/s)	Geologic Unit	Station Latitude (°)	Station Longitude (°)	PGA (g)	PGV (cm/s)
999	Northridge e-01	1994	117	1231	LA - Obregon Park	6.69	122	40	103	34.2057	-118.554	17.5	35.43	349. 43	Qoa	34.037	-118.178	0.49	20.51
1005	Northridge e-01	1994	117	1231	LA - Temple & Hope	6.69	122	40	103	34.2057	-118.554	17.5	28.82	452. 15	Tsh	34.059	-118.246	0.17	16.04
1019	Northridge e-01	1994	117	1231	Lake Hughes #1	6.69	122	40	103	34.2057	-118.554	17.5	35.46	425. 34	Qal, coarse	34.674	-118.43	0.08	9.32
1042	Northridge e-01	1994	117	1231	Hollywood - Coldwater Can	6.69	122	40	103	34.2057	-118.554	17.5	7.89	326. 47	Qal, deep (incl LA)	34.194	-118.412	0.27	24.17
1054	Northridge e-01	1994	117	1231	Pardee - SCE	6.69	122	40	103	34.2057	-118.554	17.5	5.54	325. 67	Qal, coarse	34.435	-118.582	0.42	65.20
1062	Northridge e-01	1994	117	1231	Rancho Palos Verdes - Luconia	6.69	122	40	103	34.2057	-118.554	17.5	50.47	508. 83	Tsh	33.74	-118.335	0.14	9.08
1063	Northridge e-01	1994	117	1231	Rinaldi Receiving Sta	6.69	122	40	103	34.2057	-118.554	17.5	0	282. 25	Qal, deep (incl LA)	34.281	-118.478	0.71	114.4 0
1078	Northridge e-01	1994	117	1231	Santa Susana Ground	6.69	122	40	103	34.2057	-118.554	17.5	1.69	715. 12	Kss	34.232	-118.71	0.26	16.41
1082	Northridge e-01	1994	117	1231	Sun Valley - Roscoe Blvd	6.69	122	40	103	34.2057	-118.554	17.5	5.59	320. 93	Qal, deep (incl LA)	34.221	-118.421	0.35	32.42
1084	Northridge e-01	1994	117	1231	Sylmar - Converter Sta	6.69	122	40	103	34.2057	-118.554	17.5	0	251. 24	Qal, thin	34.311	-118.49	0.70	102.5 6
1086	Northridge e-01	1994	117	1231	Sylmar - Olive View Med FF	6.69	122	40	103	34.2057	-118.554	17.5	1.74	440. 54	Qal, thin	34.326	-118.444	0.64	94.53
1087	Northridge e-01	1994	117	1231	Tarzana - Cedar Hill A	6.69	122	40	103	34.2057	-118.554	17.5	0.37	257. 21	Tsh	34.16	-118.534	1.64	93.60
1093	Northridge e-01	1994	117	1231	Villa Park - Serrano Ave	6.69	122	40	103	34.2057	-118.554	17.5	76.38	416. 93	Qoa	33.821	-117.818	0.04	3.51
1094	Northridge e-01	1994	117	1231	West Covina - S Orange Ave	6.69	122	40	103	34.2057	-118.554	17.5	51.46	334. 69	Qal, deep (incl LA)	34.064	-117.952	0.06	6.76
1109	Kobe, Japan	1995	116	2046	MZH	6.9	230	85	180	34.596	135.011	17.9	69.04	609	-999	35.448	135.32	0.06	5.31
1111	Kobe, Japan	1995	116	2046	Nishi- Akashi	6.9	230	85	180	34.596	135.011	17.9	7.08	609	-999	34.664	134.964	0.47	39.49
1123	Kozani, Greece-01	1995	513	847	Florina	6.4	253	43	-95	40.1569	21.6746	12.64	72.82	649. 67	-999	40.787	21.404	0.02	1.27
1144	Gulf of Agaba	1995	112 2	415	Eilat	7.2	201	78	0	28.76	34.66	12.5	43.29	354. 88	-999	29.563	34.938	0.09	13.27
1147	Kocaeli, Turkey	1999	817	-999	Ambarli	7.51	271	80	180	40.748	29.99	16	68.09	175	-999	40.9805	28.692	0.21	37.11
1148	Kocaeli, Turkey	1999	817	-999	Arcecik	7.51	271	80	180	40.748	29.99	16	10.56	523	-999	40.8236	29.3607	0.17	31.14
1149	Kocaeli, Turkey	1999	817	-999	Atakoy	7.51	271	80	180	40.748	29.99	16	56.49	310. 01	-999	40.989	28.849	0.12	17.79
1157	Kocaeli, Turkey	1999	817	-999	Cekmece	7.51	271	80	180	40.748	29.99	16	64.95	346	-999	41.0238	28.7594	0.16	12.93
1160	Kocaeli, Turkey	1999	817	-999	Fatih	7.51	271	80	180	40.748	29.99	16	53.34	386. 75	-999	41.0537	28.95	0.17	18.22
1166	Kocaeli, Turkey	1999	817	-999	Iznik	7.51	271	80	180	40.748	29.99	16	30.73	476. 62	-999	40.44	29.75	0.11	20.56



RSN	Name	YEAR	MO DY	HRM N	Station Name	Magnitude	Strike (°)	Dip (°)	Rake (°)	Hypocenter Latitude (°)	Hypocenter Longitude (°)	Hypocenter Depth (km)	R <sub>b</sub> (km)	V <sub>s30</sub> (m/s)	Geologic al Unit	Station Latitude (°)	Station Longitude (°)	PGA (g)	PGV (cm/s)
1169	Kocaeli, Turkey	1999	817	-999	Maslak	7.51	271	80	180	40.748	29.99	16	52.96	445. 66	-999	41.104	29.019	0.04	6.32
1170	Kocaeli, Turkey	1999	817	-999	Mecidiyekoy	7.51	271	80	180	40.748	29.99	16	51.17	384. 86	-999	41.065	28.997	0.05	8.10
1176	Kocaeli, Turkey	1999	817	-999	Yarimca	7.51	271	80	180	40.748	29.99	16	1.38	297	-999	40.7644	29.762	0.29	70.87
1177	Kocaeli, Turkey	1999	817	-999	Zeytinburnu	7.51	271	80	180	40.748	29.99	16	51.98	341. 56	-999	40.986	28.908	0.11	15.55
1180	Chi-Chi, Taiwan	1999	920	-999	CHY002	7.62	20	33	55	23.85	120.82	8	24.96	235. 13	-999	23.7192	120.4125	0.12	46.13
1183	Chi-Chi, Taiwan	1999	920	-999	CHY008	7.62	20	33	55	23.85	120.82	8	40.43	210. 73	-999	23.4853	120.2692	0.12	27.75
1184	Chi-Chi, Taiwan	1999	920	-999	CHY010	7.62	20	33	55	23.85	120.82	8	19.93	538. 69	-999	23.4653	120.544	0.20	18.50
1188	Chi-Chi, Taiwan	1999	920	-999	CHY016	7.62	20	33	55	23.85	120.82	8	66.64	200. 86	-999	23.2212	120.1532	0.10	14.98
1192	Chi-Chi, Taiwan	1999	920	-999	CHY023	7.62	20	33	55	23.85	120.82	8	81.07	279. 78	-999	22.9655	120.28	0.05	8.16
1193	Chi-Chi, Taiwan	1999	920	-999	CHY024	7.62	20	33	55	23.85	120.82	8	9.62	427. 73	-999	23.757	120.6062	0.23	46.42
1195	Chi-Chi, Taiwan	1999	920	-999	CHY026	7.62	20	33	55	23.85	120.82	8	29.52	226. 01	-999	23.7987	120.4113	0.07	33.20
1204	Chi-Chi, Taiwan	1999	920	-999	CHY039	7.62	20	33	55	23.85	120.82	8	31.87	201. 21	-999	23.5207	120.344	0.10	23.89
1205	Chi-Chi, Taiwan	1999	920	-999	CHY041	7.62	20	33	55	23.85	120.82	8	19.37	492. 26	-999	23.4388	120.5957	0.50	30.51
1206	Chi-Chi, Taiwan	1999	920	-999	CHY042	7.62	20	33	55	23.85	120.82	8	27.47	665. 2	-999	23.3583	120.5833	0.08	14.86
1210	Chi-Chi, Taiwan	1999	920	-999	CHY050	7.62	20	33	55	23.85	120.82	8	44.74	538. 93	-999	23.2803	120.4083	0.08	8.04
1215	Chi-Chi, Taiwan	1999	920	-999	CHY058	7.62	20	33	55	23.85	120.82	8	59.79	269. 28	-999	23.1725	120.3192	0.05	11.65
1217	Chi-Chi, Taiwan	1999	920	-999	CHY060	7.62	20	33	55	23.85	120.82	8	68.86	228. 92	-999	23.1243	120.2392	0.05	16.50
1218	Chi-Chi, Taiwan	1999	920	-999	CHY061	7.62	20	33	55	23.85	120.82	8	57.5	538. 69	-999	23.0768	120.5107	0.04	4.28
1220	Chi-Chi, Taiwan	1999	920	-999	CHY063	7.62	20	33	55	23.85	120.82	8	71.94	246. 88	-999	23.027	120.3402	0.06	8.16
1222	Chi-Chi, Taiwan	1999	920	-999	CHY066	7.62	20	33	55	23.85	120.82	8	89.38	211. 97	-999	22.9205	120.2078	0.05	11.09
1230	Chi-Chi, Taiwan	1999	920	-999	CHY079	7.62	20	33	55	23.85	120.82	8	46.59	573. 04	-999	23.1848	120.528	0.04	5.68
1232	Chi-Chi, Taiwan	1999	920	-999	CHY081	7.62	20	33	55	23.85	120.82	8	41.36	573. 04	-999	23.267	120.488	0.05	9.17
1235	Chi-Chi, Taiwan	1999	920	-999	CHY087	7.62	20	33	55	23.85	120.82	8	28.79	505. 2	-999	23.3845	120.519	0.14	12.40
1243	Chi-Chi, Taiwan	1999	920	-999	CHY100	7.62	20	33	55	23.85	120.82	8	53.46	230. 11	-999	23.2272	120.3418	0.07	16.37
1244	Chi-Chi, Taiwan	1999	920	-999	CHY101	7.62	20	33	55	23.85	120.82	8	9.94	258. 89	-999	23.6862	120.5622	0.38	91.28
1249	Chi-Chi, Taiwan	1999	920	-999	CHY110	7.62	20	33	55	23.85	120.82	8	40.37	573. 04	-999	23.2517	120.5295	0.03	3.80
1256	Chi-Chi, Taiwan	1999	920	-999	HWA002	7.62	20	33	55	23.85	120.82	8	53.3	789. 18	-999	23.6012	121.5122	0.07	8.25
1259	Chi-Chi, Taiwan	1999	920	-999	HWA006	7.62	20	33	55	23.85	120.82	8	43.49	559. 11	-999	23.6732	121.4173	0.09	8.32
1265	Chi-Chi, Taiwan	1999	920	-999	HWA014	7.62	20	33	55	23.85	120.82	8	51.49	277. 28	-999	23.9732	121.5993	0.10	23.33

RSN	Name	YEAR	MO DY	HRM N	Station Name	Magnitude	Strike (°)	Dip (°)	Rake (°)	Hypocenter Latitude (°)	Hypocenter Longitude (°)	Hypocenter Depth (km)	R <sub>jb</sub> (km)	V <sub>s30</sub> (m/s)	Geologic al Unit	Station Latitude (°)	Station Longitude (°)	PGA (g)	PGV (cm/s)
1272	Chi-Chi, Taiwan	1999	920	-999	HWA023	7.62	20	33	55	23.85	120.82	8	47.08	671. 52	-999	24.08	121.5955	0.04	7.27
1275	Chi-Chi, Taiwan	1999	920	-999	HWA026	7.62	20	33	55	23.85	120.82	8	47.96	457. 49	-999	24.1185	121.6165	0.06	9.72
1276	Chi-Chi, Taiwan	1999	920	-999	HWA027	7.62	20	33	55	23.85	120.82	8	47.58	437. 8	-999	24.055	121.591	0.11	15.15
1277	Chi-Chi, Taiwan	1999	920	-999	HWA028	7.62	20	33	55	23.85	120.82	8	49.99	406. 7	-999	24.0172	121.6013	0.09	15.13
1283	Chi-Chi, Taiwan	1999	920	-999	HWA034	7.62	20	33	55	23.85	120.82	8	39.55	379. 18	-999	23.5905	121.3772	0.14	11.00
1290	Chi-Chi, Taiwan	1999	920	-999	HWA043	7.62	20	33	55	23.85	120.82	8	54.5	543. 06	-999	23.7092	121.54	0.07	8.92
1294	Chi-Chi, Taiwan	1999	920	-999	HWA048	7.62	20	33	55	23.85	120.82	8	47.35	345. 89	-999	24.0113	121.5715	0.14	19.49
1297	Chi-Chi, Taiwan	1999	920	-999	HWA051	7.62	20	33	55	23.85	120.82	8	49.69	440. 5	-999	23.8703	121.548	0.15	20.36
1302	Chi-Chi, Taiwan	1999	920	-999	HWA057	7.62	20	33	55	23.85	120.82	8	46.48	671. 52	-999	24.16	121.61	0.10	8.42
1304	Chi-Chi, Taiwan	1999	920	-999	HWA059	7.62	20	33	55	23.85	120.82	8	44.89	208. 56	-999	23.8713	121.5005	0.13	14.81
1305	Chi-Chi, Taiwan	1999	920	-999	HWA060	7.62	20	33	55	23.85	120.82	8	53.92	573. 04	-999	23.8703	121.59	0.04	9.04
1307	Chi-Chi, Taiwan	1999	920	-999	ILA001	7.62	20	33	55	23.85	120.82	8	101.24	909. 09	-999	24.8827	121.836	0.03	6.14
1310	Chi-Chi, Taiwan	1999	920	-999	ILA004	7.62	20	33	55	23.85	120.82	8	86.61	124. 27	-999	24.745	121.7828	0.07	30.41
1314	Chi-Chi, Taiwan	1999	920	-999	ILA008	7.62	20	33	55	23.85	120.82	8	82.4	299. 28	-999	24.7088	121.7628	0.07	16.94
1315	Chi-Chi, Taiwan	1999	920	-999	ILA010	7.62	20	33	55	23.85	120.82	8	77.64	573. 04	-999	24.619	121.7812	0.05	7.94
1317	Chi-Chi, Taiwan	1999	920	-999	ILA013	7.62	20	33	55	23.85	120.82	8	81.7	199. 48	-999	24.732	121.7294	0.14	22.40
1319	Chi-Chi, Taiwan	1999	920	-999	ILA015	7.62	20	33	55	23.85	120.82	8	83.02	782. 59	-999	24.7807	121.6912	0.04	8.49
1320	Chi-Chi, Taiwan	1999	920	-999	ILA016	7.62	20	33	55	23.85	120.82	8	79.9	271. 1	-999	24.749	121.684	0.08	16.30
1324	Chi-Chi, Taiwan	1999	920	-999	ILA030	7.62	20	33	55	23.85	120.82	8	83.25	200. 98	-999	24.7278	121.755	0.11	25.09
1325	Chi-Chi, Taiwan	1999	920	-999	ILA031	7.62	20	33	55	23.85	120.82	8	80.88	649. 25	-999	24.5995	121.8337	0.07	8.76
1336	Chi-Chi, Taiwan	1999	920	-999	ILA048	7.62	20	33	55	23.85	120.82	8	86.67	199. 59	-999	24.7663	121.7612	0.08	24.44
1340	Chi-Chi, Taiwan	1999	920	-999	ILA052	7.62	20	33	55	23.85	120.82	8	82.74	612. 47	-999	24.6092	121.8488	0.03	6.84
1343	Chi-Chi, Taiwan	1999	920	-999	ILA056	7.62	20	33	55	23.85	120.82	8	89.84	223. 71	-999	24.7622	121.8088	0.06	33.30
1344	Chi-Chi, Taiwan	1999	920	-999	ILA059	7.62	20	33	55	23.85	120.82	8	83.97	236. 84	-999	24.6667	121.8205	0.06	14.26
1346	Chi-Chi, Taiwan	1999	920	-999	ILA062	7.62	20	33	55	23.85	120.82	8	70.43	447. 51	-999	24.4677	121.7933	0.08	11.21
1347	Chi-Chi, Taiwan	1999	920	-999	ILA063	7.62	20	33	55	23.85	120.82	8	57.69	996. 51	-999	24.6157	121.518	0.09	9.56
1349	Chi-Chi, Taiwan	1999	920	-999	ILA066	7.62	20	33	55	23.85	120.82	8	67.44	481. 17	-999	24.4473	121.7707	0.09	11.29
1350	Chi-Chi, Taiwan	1999	920	-999	ILA067	7.62	20	33	55	23.85	120.82	8	33.27	665. 2	-999	24.44	121.3728	0.21	15.70
1353	Chi-Chi, Taiwan	1999	920	-999	KAU006	7.62	20	33	55	23.85	120.82	8	113.37	218. 49	-999	22.591	120.3173	0.02	8.60

RSN	Name	YEAR	MO DY	HRM N	Station Name	Magnitude	Strike (°)	Dip (°)	Rake (°)	Hypocenter Latitude (°)	Hypocenter Longitude (°)	Hypocenter Depth (km)	R <sub>b</sub> (km)	V <sub>s30</sub> (m/s)	Geologic al Unit	Station Latitude (°)	Station Longitude (°)	PGA (g)	PGV (cm/s)
1354	Chi-Chi, Taiwan	1999	920	-999	KAU007	7.62	20	33	55	23.85	120.82	8	105.92	290. 86	-999	22.6462	120.3585	0.02	8.25
1355	Chi-Chi, Taiwan	1999	920	-999	KAU008	7.62	20	33	55	23.85	120.82	8	107.02	285. 94	-999	22.6295	120.3672	0.03	8.34
1361	Chi-Chi, Taiwan	1999	920	-999	KAU020	7.62	20	33	55	23.85	120.82	8	72.17	373. 33	-999	22.902	120.5352	0.06	12.77
1373	Chi-Chi, Taiwan	1999	920	-999	KAU044	7.62	20	33	55	23.85	120.82	8	119.96	221. 24	-999	22.4397	120.5028	0.04	11.75
1375	Chi-Chi, Taiwan	1999	920	-999	KAU047	7.62	20	33	55	23.85	120.82	8	52.89	573. 04	-999	23.0817	120.5827	0.04	5.67
1381	Chi-Chi, Taiwan	1999	920	-999	KAU057	7.62	20	33	55	23.85	120.82	8	112.48	535. 13	-999	22.6342	120.2633	0.02	5.85
1387	Chi-Chi, Taiwan	1999	920	-999	KAU069	7.62	20	33	55	23.85	120.82	8	67.82	500. 15	-999	22.8873	120.6567	0.04	3.25
1392	Chi-Chi, Taiwan	1999	920	-999	KAU078	7.62	20	33	55	23.85	120.82	8	86.72	531. 85	-999	22.7112	120.6412	0.04	2.55
1402	Chi-Chi, Taiwan	1999	920	-999	NST	7.62	20	33	55	23.85	120.82	8	38.36	491. 08	-999	24.6312	121.0005	0.37	24.86
1409	Chi-Chi, Taiwan	1999	920	-999	TAP	7.62	20	33	55	23.85	120.82	8	98.3	235. 82	-999	25.0392	121.507	0.05	11.81
1415	Chi-Chi, Taiwan	1999	920	-999	TAP010	7.62	20	33	55	23.85	120.82	8	99.89	226. 38	-999	25.063	121.4813	0.10	25.57
1416	Chi-Chi, Taiwan	1999	920	-999	TAP012	7.62	20	33	55	23.85	120.82	8	100.11	207. 99	-999	25.0563	121.5078	0.08	15.70
1417	Chi-Chi, Taiwan	1999	920	-999	TAP013	7.62	20	33	55	23.85	120.82	8	100.84	205. 11	-999	25.0572	121.5253	0.08	16.66
1424	Chi-Chi, Taiwan	1999	920	-999	TAP028	7.62	20	33	55	23.85	120.82	8	94.73	287. 94	-999	25.0045	121.5073	0.05	12.63
1428	Chi-Chi, Taiwan	1999	920	-999	TAP036	7.62	20	33	55	23.85	120.82	8	86.16	671. 52	-999	24.9043	121.5447	0.03	6.37
1430	Chi-Chi, Taiwan	1999	920	-999	TAP042	7.62	20	33	55	23.85	120.82	8	105.49	375. 85	-999	25.1255	121.4532	0.09	18.45
1432	Chi-Chi, Taiwan	1999	920	-999	TAP046	7.62	20	33	55	23.85	120.82	8	116.64	816. 9	-999	25.1037	121.7683	0.06	8.85
1433	Chi-Chi, Taiwan	1999	920	-999	TAP047	7.62	20	33	55	23.85	120.82	8	83.57	403. 2	-999	24.9538	121.3375	0.06	16.33
1435	Chi-Chi, Taiwan	1999	920	-999	TAP051	7.62	20	33	55	23.85	120.82	8	102.46	403. 17	-999	25.1008	121.4403	0.09	17.36
1436	Chi-Chi, Taiwan	1999	920	-999	TAP052	7.62	20	33	55	23.85	120.82	8	98.51	433. 88	-999	25.0817	121.3828	0.11	18.09
1437	Chi-Chi, Taiwan	1999	920	-999	TAP053	7.62	20	33	55	23.85	120.82	8	90.34	538. 69	-999	24.959	121.5143	0.08	10.46
1453	Chi-Chi, Taiwan	1999	920	-999	TAP087	7.62	20	33	55	23.85	120.82	8	101.7	573. 04	-999	25.1008	121.4177	0.06	17.25
1460	Chi-Chi, Taiwan	1999	920	-999	TAP103	7.62	20	33	55	23.85	120.82	8	114.28	429. 49	-999	25.071	121.781	0.13	19.36
1463	Chi-Chi, Taiwan	1999	920	-999	TCU003	7.62	20	33	55	23.85	120.82	8	86.57	517. 33	-999	25.0473	121.1357	0.06	28.15
1464	Chi-Chi, Taiwan	1999	920	-999	TCU006	7.62	20	33	55	23.85	120.82	8	72.52	607. 4	-999	24.9118	121.1405	0.07	26.43
1467	Chi-Chi, Taiwan	1999	920	-999	TCU009	7.62	20	33	55	23.85	120.82	8	80.83	460. 1	-999	24.9655	121.22	0.07	27.15
1469	Chi-Chi, Taiwan	1999	920	-999	TCU011	7.62	20	33	55	23.85	120.82	8	74.41	471. 07	-999	24.8855	121.2783	0.07	22.66
1470	Chi-Chi, Taiwan	1999	920	-999	TCU014	7.62	20	33	55	23.85	120.82	8	92.26	496. 47	-999	25.0463	121.3075	0.07	19.45
1471	Chi-Chi, Taiwan	1999	920	-999	TCU015	7.62	20	33	55	23.85	120.82	8	49.81	426	-999	24.7572	120.9345	0.12	33.56

RSN	Name	YEAR	MO DY	HRM N	Station Name	Magnitude	Strike (°)	Dip (°)	Rake (°)	Hypocenter Latitude (°)	Hypocenter Longitude (°)	Hypocenter Depth (km)	R <sub>b</sub> (km)	V <sub>s30</sub> (m/s)	Geologic al Unit	Station Latitude (°)	Station Longitude (°)	PGA (g)	PGV (cm/s)
1473	Chi-Chi, Taiwan	1999	920	-999	TCU018	7.62	20	33	55	23.85	120.82	8	66.25	573.04	-999	24.88	121.0535	0.06	31.45
1476	Chi-Chi, Taiwan	1999	920	-999	TCU029	7.62	20	33	55	23.85	120.82	8	28.04	406.53	-999	24.5588	120.7492	0.17	47.04
1477	Chi-Chi, Taiwan	1999	920	-999	TCU031	7.62	20	33	55	23.85	120.82	8	30.17	489.22	-999	24.5615	120.701	0.12	48.85
1479	Chi-Chi, Taiwan	1999	920	-999	TCU034	7.62	20	33	55	23.85	120.82	8	35.68	393.77	-999	24.639	120.8568	0.23	35.97
1484	Chi-Chi, Taiwan	1999	920	-999	TCU042	7.62	20	33	55	23.85	120.82	8	26.31	578.98	-999	24.5542	120.8077	0.21	37.70
1485	Chi-Chi, Taiwan	1999	920	-999	TCU045	7.62	20	33	55	23.85	120.82	8	26	704.64	-999	24.5412	120.9137	0.49	45.96
1486	Chi-Chi, Taiwan	1999	920	-999	TCU046	7.62	20	33	55	23.85	120.82	8	16.74	465.55	-999	24.4683	120.8543	0.13	28.41
1489	Chi-Chi, Taiwan	1999	920	-999	TCU049	7.62	20	33	55	23.85	120.82	8	3.76	487.27	-999	24.179	120.6902	0.25	56.23
1491	Chi-Chi, Taiwan	1999	920	-999	TCU051	7.62	20	33	55	23.85	120.82	8	7.64	350.06	-999	24.1603	120.6518	0.19	42.38
1496	Chi-Chi, Taiwan	1999	920	-999	TCU056	7.62	20	33	55	23.85	120.82	8	10.48	403.2	-999	24.1588	120.6238	0.16	38.96
1497	Chi-Chi, Taiwan	1999	920	-999	TCU057	7.62	20	33	55	23.85	120.82	8	11.83	555.23	-999	24.1732	120.6107	0.11	39.21
1499	Chi-Chi, Taiwan	1999	920	-999	TCU060	7.62	20	33	55	23.85	120.82	8	8.51	375.42	-999	24.2247	120.644	0.15	41.86
1500	Chi-Chi, Taiwan	1999	920	-999	TCU061	7.62	20	33	55	23.85	120.82	8	17.17	379.64	-999	24.1355	120.549	0.14	38.61
1502	Chi-Chi, Taiwan	1999	920	-999	TCU064	7.62	20	33	55	23.85	120.82	8	16.59	645.72	-999	24.3457	120.61	0.11	49.60
1506	Chi-Chi, Taiwan	1999	920	-999	TCU070	7.62	20	33	55	23.85	120.82	8	19	401.26	-999	24.196	120.5403	0.19	52.32
1508	Chi-Chi, Taiwan	1999	920	-999	TCU072	7.62	20	33	55	23.85	120.82	8	0	468.14	-999	24.0407	120.8488	0.43	57.81
1512	Chi-Chi, Taiwan	1999	920	-999	TCU078	7.62	20	33	55	23.85	120.82	8	0	443.04	-999	23.812	120.8455	0.38	36.04
1513	Chi-Chi, Taiwan	1999	920	-999	TCU079	7.62	20	33	55	23.85	120.82	8	0	363.99	-999	23.8395	120.8942	0.47	50.60
1514	Chi-Chi, Taiwan	1999	920	-999	TCU081	7.62	20	33	55	23.85	120.82	8	55.48	430.47	-999	24.8022	120.9695	0.08	36.81
1516	Chi-Chi, Taiwan	1999	920	-999	TCU083	7.62	20	33	55	23.85	120.82	8	80.18	354.63	-999	24.97	121.1867	0.09	28.35
1517	Chi-Chi, Taiwan	1999	920	-999	TCU084	7.62	20	33	55	23.85	120.82	8	0	665.2	-999	23.883	120.8998	0.74	109.14
1518	Chi-Chi, Taiwan	1999	920	-999	TCU085	7.62	20	33	55	23.85	120.82	8	55.14	999.66	-999	24.6755	121.3583	0.06	7.13
1519	Chi-Chi, Taiwan	1999	920	-999	TCU087	7.62	20	33	55	23.85	120.82	8	6.98	538.69	-999	24.3482	120.7733	0.12	42.41
1520	Chi-Chi, Taiwan	1999	920	-999	TCU088	7.62	20	33	55	23.85	120.82	8	4.67	665.2	-999	24.2533	121.1758	0.52	26.03
1521	Chi-Chi, Taiwan	1999	920	-999	TCU089	7.62	20	33	55	23.85	120.82	8	0	671.52	-999	23.9037	120.8565	0.27	33.48
1522	Chi-Chi, Taiwan	1999	920	-999	TCU092	7.62	20	33	55	23.85	120.82	8	87.67	422.28	-999	25.0117	121.2792	0.07	20.76
1525	Chi-Chi, Taiwan	1999	920	-999	TCU096	7.62	20	33	55	23.85	120.82	8	54.45	454.58	-999	24.7957	120.9558	0.08	32.12
1532	Chi-Chi, Taiwan	1999	920	-999	TCU105	7.62	20	33	55	23.85	120.82	8	17.16	575.54	-999	24.239	120.559	0.12	39.28
1533	Chi-Chi, Taiwan	1999	920	-999	TCU106	7.62	20	33	55	23.85	120.82	8	14.97	451.37	-999	24.0833	120.5518	0.15	38.18

RSN	Name	YEAR	MO DY	HRM N	Station Name	Magnitude	Strike (°)	Dip (°)	Rake (°)	Hypocenter Latitude (°)	Hypocenter Longitude (°)	Hypocenter Depth (km)	R <sub>b</sub> (km)	V <sub>s30</sub> (m/s)	Geologic al Unit	Station Latitude (°)	Station Longitude (°)	PGA (g)	PGV (cm/s)
1537	Chi-Chi, Taiwan	1999	920	-999	TCU111	7.62	20	33	55	23.85	120.82	8	22.12	237. 53	-999	24.1137	120.4872	0.11	41.83
1538	Chi-Chi, Taiwan	1999	920	-999	TCU112	7.62	20	33	55	23.85	120.82	8	27.48	190. 54	-999	24.0557	120.424	0.07	38.09
1542	Chi-Chi, Taiwan	1999	920	-999	TCU117	7.62	20	33	55	23.85	120.82	8	25.42	198. 58	-999	24.1335	120.4598	0.13	56.86
1544	Chi-Chi, Taiwan	1999	920	-999	TCU119	7.62	20	33	55	23.85	120.82	8	37.93	221. 7	-999	23.9242	120.3122	0.06	20.85
1546	Chi-Chi, Taiwan	1999	920	-999	TCU122	7.62	20	33	55	23.85	120.82	8	9.34	475. 46	-999	23.8128	120.6097	0.23	42.61
1547	Chi-Chi, Taiwan	1999	920	-999	TCU123	7.62	20	33	55	23.85	120.82	8	14.91	270. 22	-999	24.0187	120.5437	0.15	37.50
1548	Chi-Chi, Taiwan	1999	920	-999	TCU128	7.62	20	33	55	23.85	120.82	8	13.13	599. 64	-999	24.4162	120.7607	0.16	63.28
1554	Chi-Chi, Taiwan	1999	920	-999	TCU145	7.62	20	33	55	23.85	120.82	8	35.32	240. 43	-999	23.98	120.3368	0.07	21.55
1572	Chi-Chi, Taiwan	1999	920	-999	TTN018	7.62	20	33	55	23.85	120.82	8	71.72	573. 04	-999	22.8207	121.0717	0.03	4.17
1576	Chi-Chi, Taiwan	1999	920	-999	TTN024	7.62	20	33	55	23.85	120.82	8	56.58	671. 52	-999	22.9725	121.1083	0.03	3.77
1577	Chi-Chi, Taiwan	1999	920	-999	TTN025	7.62	20	33	55	23.85	120.82	8	62.67	704. 96	-999	22.9045	121.072	0.05	4.42
1584	Chi-Chi, Taiwan	1999	920	-999	TTN036	7.62	20	33	55	23.85	120.82	8	77.46	538. 69	-999	22.7988	121.1855	0.03	7.57
1591	Chi-Chi, Taiwan	1999	920	-999	TTN047	7.62	20	33	55	23.85	120.82	8	71.25	573. 04	-999	22.8402	121.131	0.03	5.84
1593	Chi-Chi, Taiwan	1999	920	-999	TTN050	7.62	20	33	55	23.85	120.82	8	87.01	573. 04	-999	22.674	121.0293	0.02	3.48
1594	Chi-Chi, Taiwan	1999	920	-999	TTN051	7.62	20	33	55	23.85	120.82	8	30.77	665. 2	-999	23.1887	121.0168	0.03	5.32
1602	Duzce, Turkey	1999	1112	-999	Bolu	7.14	270	65	-178	40.8345	31.1346	14	12.02	293. 57	-999	40.745	31.61	0.78	62.90
1613	Duzce, Turkey	1999	1112	-999	Lamont 1060	7.14	270	65	-178	40.8345	31.1346	14	25.78	782	-999	40.777	30.613	0.04	8.23
1614	Duzce, Turkey	1999	1112	-999	Lamont 1061	7.14	270	65	-178	40.8345	31.1346	14	11.46	481	-999	40.72	30.792	0.12	11.52
1617	Duzce, Turkey	1999	1112	-999	Lamont 375	7.14	270	65	-178	40.8345	31.1346	14	3.93	454. 2	-999	40.743	30.876	0.68	27.89
1618	Duzce, Turkey	1999	1112	-999	Lamont 531	7.14	270	65	-178	40.8345	31.1346	14	8.03	638. 39	-999	40.703	30.855	0.15	11.83
1619	Duzce, Turkey	1999	1112	-999	Mudurnu	7.14	270	65	-178	40.8345	31.1346	14	34.3	535. 24	-999	40.463	31.182	0.09	13.28
1626	Sitka, Alaska	1972	730	-999	Sitka Observatory	7.68	347	90	180	56.77	-135.784	15	34.61	649. 67	-999	57.06	-135.32	0.09	11.10
1629	St Elias, Alaska	1979	228	-999	Yakutat	7.54	250	10	90	60.64	-141.59	12.23	80	336. 98	-999	59.543	-139.726	0.07	36.00
1740	Little Skull Mtn,NV	1992	629	-999	Station #1- Lathrop Wells	5.65	60	70	-70	36.728	-116.286	12	14.12	302. 64	-999	36.64	-116.4	0.18	8.57
1741	Little Skull Mtn,NV	1992	629	-999	Station #2- NTS Control Pt. 1	5.65	60	70	-70	36.728	-116.286	12	23.83	593. 35	-999	36.93	-116.06	0.09	4.51
1762	Hector Mine	1999	101 6	-999	Amboy	7.13	332	82	179	34.5981	-116.265	14.8	41.81	382. 93	Qal, deep (incl LA)	34.56	-115.743	0.19	23.78
1771	Hector Mine	1999	101 6	-999	Bombay Beach Fire Station	7.13	332	82	179	34.5981	-116.265	14.8	120.69	257. 03	Qal, fine	33.3527	-115.733	0.04	13.59
1784	Hector Mine	1999	101 6	-999	Frink	7.13	332	82	179	34.5981	-116.265	14.8	118.5	384. 66	Qal, coarse	33.398	-115.657	0.07	12.57

RSN	Name	YEAR	MO DY	HRM N	Station Name	Magnitude	Strike (°)	Dip (°)	Rake (°)	Hypocenter Latitude (°)	Hypocenter Longitude (°)	Hypocenter Depth (km)	R <sub>jb</sub> (km)	V <sub>s30</sub> (m/s)	Geologic al Unit	Station Latitude (°)	Station Longitude (°)	PGA (g)	PGV (cm/s)
1787	Hector Mine	1999	101 6	-999	Hector	7.13	332	82	179	34.5981	-116.265	14.8	10.35	726	Kgr	34.8294	-116.335	0.31	34.78
1794	Hector Mine	1999	101 6	-999	Joshua Tree	7.13	332	82	179	34.5981	-116.265	14.8	31.06	379. 32	Qal, coarse	34.13	-116.314	0.15	19.15
1795	Hector Mine	1999	101 6	-999	Joshua Tree N.M. - Keys View	7.13	332	82	179	34.5981	-116.265	14.8	50.42	686. 12	Kgr	33.925	-116.172	0.08	7.84
1810	Hector Mine	1999	101 6	-999	Mecca - CVWD Yard	7.13	332	82	179	34.5981	-116.265	14.8	91.96	318	Qal, coarse	33.564	-115.987	0.09	17.71
1823	Hector Mine	1999	101 6	-999	Salton City	7.13	332	82	179	34.5981	-116.265	14.8	123.25	324. 5	Qal, coarse	33.28	-115.984	0.05	7.46
1825	Hector Mine	1999	101 6	-999	San Bernardino - E & Hospitality	7.13	332	82	179	34.5981	-116.265	14.8	105.2	296. 97	Qal, deep (incl LA)	34.065	-117.292	0.07	15.17
1831	Hector Mine	1999	101 6	-999	San Jacinto - Soboba	7.13	332	82	179	34.5981	-116.265	14.8	92.71	447. 22	Qoa	33.797	-116.88	0.06	7.33
1832	Hector Mine	1999	101 6	-999	Seven Oaks Dam Project Office	7.13	332	82	179	34.5981	-116.265	14.8	87.2	564. 93	-999	34.1105	-117.099	0.05	9.44
1838	Hector Mine	1999	101 6	-999	Whitewater Trout Farm	7.13	332	82	179	34.5981	-116.265	14.8	62.91	425. 02	Qal, coarse	33.99	-116.656	0.05	7.79
2161	Chi-Chi, Taiwan- 02	1999	920	1757	CHY026	5.9	35	50	100	23.94	121.01	8	56.17	226. 01	-999	23.7987	120.4113	0.02	2.07
2229	Chi-Chi, Taiwan- 02	1999	920	1757	HWA022	5.9	35	50	100	23.94	121.01	8	68.91	567. 64	-999	24.2675	121.7325	0.04	3.08
2233	Chi-Chi, Taiwan- 02	1999	920	1757	HWA026	5.9	35	50	100	23.94	121.01	8	51.73	457. 49	-999	24.1185	121.6165	0.02	1.97
2299	Chi-Chi, Taiwan- 02	1999	920	1757	ILA067	5.9	35	50	100	23.94	121.01	8	55.69	665. 2	-999	24.44	121.3728	0.05	2.48
2386	Chi-Chi, Taiwan- 02	1999	920	1757	TCU073	5.9	35	50	100	23.94	121.01	8	8.49	473. 65	-999	24.014	120.9492	0.13	5.64
2410	Chi-Chi, Taiwan- 02	1999	920	1757	TCU110	5.9	35	50	100	23.94	121.01	8	40.03	212. 72	-999	23.9622	120.5695	0.06	6.33
2435	Chi-Chi, Taiwan- 02	1999	920	1757	TTN020	5.9	35	50	100	23.94	121.01	8	82.06	453. 71	-999	23.1268	121.2057	0.01	0.59
2448	Chi-Chi, Taiwan- 02	1999	920	1757	TTN044	5.9	35	50	100	23.94	121.01	8	94.39	419. 63	-999	23.0068	121.1655	0.01	1.19
2456	Chi-Chi, Taiwan- 03	1999	920	1803	CHY022	6.2	360	10	80	23.81	120.85	7.8	86.23	564. 07	-999	23.0457	120.4615	0.02	2.29
2457	Chi-Chi, Taiwan- 03	1999	920	1803	CHY024	6.2	360	10	80	23.81	120.85	7.8	18.47	427. 73	-999	23.757	120.6062	0.13	24.62
2459	Chi-Chi, Taiwan- 03	1999	920	1803	CHY026	6.2	360	10	80	23.81	120.85	7.8	38.3	226. 01	-999	23.7987	120.4113	0.04	19.85
2466	Chi-Chi, Taiwan- 03	1999	920	1803	CHY035	6.2	360	10	80	23.81	120.85	7.8	33.86	573. 04	-999	23.52	120.584	0.14	21.96

RSN	Name	YEAR	MO DY	HRM N	Station Name	Magnitude	Strike (°)	Dip (°)	Rake (°)	Hypocenter Latitude (°)	Hypocenter Longitude (°)	Hypocenter Depth (km)	R <sub>jb</sub> (km)	V <sub>s30</sub> (m/s)	Geologic al Unit	Station Latitude (°)	Station Longitude (°)	PGA (g)	PGV (cm/s)
2467	Chi-Chi, Taiwan-03	1999	920	1803	CHY036	6.2	360	10	80	23.81	120.85	7.8	35.78	233.14	-999	23.6073	120.4788	0.10	18.10
2469	Chi-Chi, Taiwan-03	1999	920	1803	CHY041	6.2	360	10	80	23.81	120.85	7.8	40.79	492.26	-999	23.4388	120.5957	0.11	7.88
2471	Chi-Chi, Taiwan-03	1999	920	1803	CHY044	6.2	360	10	80	23.81	120.85	7.8	76.24	194.47	-999	23.3832	120.1635	0.02	9.01
2475	Chi-Chi, Taiwan-03	1999	920	1803	CHY052	6.2	360	10	80	23.81	120.85	7.8	60.18	573.04	-999	23.2878	120.501	0.04	4.90
2490	Chi-Chi, Taiwan-03	1999	920	1803	CHY074	6.2	360	10	80	23.81	120.85	7.8	27.84	553.43	-999	23.5103	120.8052	0.08	8.70
2492	Chi-Chi, Taiwan-03	1999	920	1803	CHY076	6.2	360	10	80	23.81	120.85	7.8	59.24	169.84	-999	23.638	120.2217	0.04	10.64
2503	Chi-Chi, Taiwan-03	1999	920	1803	CHY094	6.2	360	10	80	23.81	120.85	7.8	47.55	221.92	-999	23.7935	120.3205	0.03	12.74
2517	Chi-Chi, Taiwan-03	1999	920	1803	HWA009	6.2	360	10	80	23.81	120.85	7.8	75.19	373.23	-999	23.9925	121.6165	0.01	2.00
2519	Chi-Chi, Taiwan-03	1999	920	1803	HWA012	6.2	360	10	80	23.81	120.85	7.8	75.87	414.42	-999	23.993	121.6233	0.01	2.06
2523	Chi-Chi, Taiwan-03	1999	920	1803	HWA016	6.2	360	10	80	23.81	120.85	7.8	68.95	576.55	-999	23.9648	121.56	0.01	1.40
2540	Chi-Chi, Taiwan-03	1999	920	1803	HWA037	6.2	360	10	80	23.81	120.85	7.8	60.49	469.64	-999	23.4542	121.384	0.02	2.63
2542	Chi-Chi, Taiwan-03	1999	920	1803	HWA039	6.2	360	10	80	23.81	120.85	7.8	62.75	459.67	-999	23.3845	121.3523	0.02	1.95
2543	Chi-Chi, Taiwan-03	1999	920	1803	HWA041	6.2	360	10	80	23.81	120.85	7.8	68.4	484.97	-999	23.2675	121.2942	0.03	2.07
2548	Chi-Chi, Taiwan-03	1999	920	1803	HWA048	6.2	360	10	80	23.81	120.85	7.8	71.21	345.89	-999	24.0113	121.5715	0.01	2.13
2563	Chi-Chi, Taiwan-03	1999	920	1803	ILA062	6.2	360	10	80	23.81	120.85	7.8	114.27	447.51	-999	24.4677	121.7933	0.01	0.74
2612	Chi-Chi, Taiwan-03	1999	920	1803	TCU057	6.2	360	10	80	23.81	120.85	7.8	40.17	555.23	-999	24.1732	120.6107	0.03	6.36
2618	Chi-Chi, Taiwan-03	1999	920	1803	TCU065	6.2	360	10	80	23.81	120.85	7.8	25.17	305.85	-999	24.0588	120.6912	0.32	27.28
2645	Chi-Chi, Taiwan-03	1999	920	1803	TCU107	6.2	360	10	80	23.81	120.85	7.8	35.27	409	-999	24.0727	120.5402	0.08	12.45
2646	Chi-Chi, Taiwan-03	1999	920	1803	TCU109	6.2	360	10	80	23.81	120.85	7.8	34.11	535.13	-999	24.0848	120.5713	0.09	12.09
2647	Chi-Chi, Taiwan-03	1999	920	1803	TCU112	6.2	360	10	80	23.81	120.85	7.8	43.45	190.54	-999	24.0557	120.424	0.03	10.26
2658	Chi-Chi, Taiwan-03	1999	920	1803	TCU129	6.2	360	10	80	23.81	120.85	7.8	10.95	511.18	-999	23.8783	120.6843	0.69	26.41

RSN	Name	YEAR	MO DY	HRM N	Station Name	Magnitude	Strike (°)	Dip (°)	Rake (°)	Hypocenter Latitude (°)	Hypocenter Longitude (°)	Hypocenter Depth (km)	R <sub>jb</sub> (km)	V <sub>s30</sub> (m/s)	Geologic al Unit	Station Latitude (°)	Station Longitude (°)	PGA (g)	PGV (cm/s)
2662	Chi-Chi, Taiwan-03	1999	920	1803	TCU140	6.2	360	10	80	23.81	120.85	7.8	45.17	223.6	-999	23.9578	120.3593	0.03	12.02
2663	Chi-Chi, Taiwan-03	1999	920	1803	TCU141	6.2	360	10	80	23.81	120.85	7.8	32.92	223.04	-999	23.8338	120.464	0.06	20.41
2668	Chi-Chi, Taiwan-03	1999	920	1803	TTN004	6.2	360	10	80	23.81	120.85	7.8	97.61	463.59	-999	22.9102	121.1287	0.01	1.80
2671	Chi-Chi, Taiwan-03	1999	920	1803	TTN012	6.2	360	10	80	23.81	120.85	7.8	113.31	288.3	-999	22.7662	121.133	0.00	2.02
2697	Chi-Chi, Taiwan-04	1999	920	2146	CHY019	6.2	330	89	15	23.6	120.82	18	54.43	497.53	-999	23.1795	120.4778	0.03	2.70
2698	Chi-Chi, Taiwan-04	1999	920	2146	CHY022	6.2	330	89	15	23.6	120.82	18	66.27	564.07	-999	23.0457	120.4615	0.02	2.04
2703	Chi-Chi, Taiwan-04	1999	920	2146	CHY028	6.2	330	89	15	23.6	120.82	18	17.63	542.61	-999	23.632	120.6052	0.15	13.52
2710	Chi-Chi, Taiwan-04	1999	920	2146	CHY036	6.2	330	89	15	23.6	120.82	18	30.81	233.14	-999	23.6073	120.4788	0.10	16.18
2716	Chi-Chi, Taiwan-04	1999	920	2146	CHY050	6.2	330	89	15	23.6	120.82	18	53.92	538.93	-999	23.2803	120.4083	0.03	3.93
2722	Chi-Chi, Taiwan-04	1999	920	2146	CHY058	6.2	330	89	15	23.6	120.82	18	67.9	269.28	-999	23.1725	120.3192	0.04	4.81
2727	Chi-Chi, Taiwan-04	1999	920	2146	CHY063	6.2	330	89	15	23.6	120.82	18	76.29	246.88	-999	23.027	120.3402	0.02	2.94
2728	Chi-Chi, Taiwan-04	1999	920	2146	CHY065	6.2	330	89	15	23.6	120.82	18	85.86	250	-999	22.906	120.345	0.03	4.67
2739	Chi-Chi, Taiwan-04	1999	920	2146	CHY080	6.2	330	89	15	23.6	120.82	18	12.44	496.21	-999	23.5972	120.6777	0.12	16.87
2746	Chi-Chi, Taiwan-04	1999	920	2146	CHY092	6.2	330	89	15	23.6	120.82	18	33.02	253.72	-999	23.7913	120.4783	0.05	11.37
2748	Chi-Chi, Taiwan-04	1999	920	2146	CHY094	6.2	330	89	15	23.6	120.82	18	48.19	221.92	-999	23.7935	120.3205	0.03	6.94
2751	Chi-Chi, Taiwan-04	1999	920	2146	CHY100	6.2	330	89	15	23.6	120.82	18	62.77	230.11	-999	23.2272	120.3418	0.04	6.14
2757	Chi-Chi, Taiwan-04	1999	920	2146	CHY115	6.2	330	89	15	23.6	120.82	18	90.38	259.43	-999	23.149	120.079	0.03	4.49
2770	Chi-Chi, Taiwan-04	1999	920	2146	HWA019	6.2	330	89	15	23.6	120.82	18	90.18	494.82	-999	23.977	121.605	0.01	2.00
2785	Chi-Chi, Taiwan-04	1999	920	2146	HWA037	6.2	330	89	15	23.6	120.82	18	51.57	469.64	-999	23.4542	121.384	0.03	3.07
2791	Chi-Chi, Taiwan-04	1999	920	2146	HWA045	6.2	330	89	15	23.6	120.82	18	121.15	484.45	-999	24.3095	121.7405	0.01	0.68
2807	Chi-Chi, Taiwan-04	1999	920	2146	KAU007	6.2	330	89	15	23.6	120.82	18	109.06	290.86	-999	22.6462	120.3585	0.01	2.42



RSN	Name	YEAR	MO DY	HRM N	Station Name	Magnitude	Strike (°)	Dip (°)	Rake (°)	Hypocenter Latitude (°)	Hypocenter Longitude (°)	Hypocenter Depth (km)	R <sub>jb</sub> (km)	V <sub>s30</sub> (m/s)	Geologic al Unit	Station Latitude (°)	Station Longitude (°)	PGA (g)	PGV (cm/s)
2812	Chi-Chi, Taiwan-04	1999	920	2146	KAU018	6.2	330	89	15	23.6	120.82	18	79.56	538.69	-999	22.891	120.4738	0.01	2.04
2829	Chi-Chi, Taiwan-04	1999	920	2146	KAU073	6.2	330	89	15	23.6	120.82	18	113.14	216.33	-999	22.5348	120.5362	0.01	2.89
2832	Chi-Chi, Taiwan-04	1999	920	2146	KAU077	6.2	330	89	15	23.6	120.82	18	85.44	665.2	-999	22.747	120.7233	0.01	0.96
2837	Chi-Chi, Taiwan-04	1999	920	2146	KAU087	6.2	330	89	15	23.6	120.82	18	114.69	276.11	-999	22.6128	120.3113	0.01	3.23
2838	Chi-Chi, Taiwan-04	1999	920	2146	KAU088	6.2	330	89	15	23.6	120.82	18	111.8	227.46	-999	22.6461	120.306	0.01	2.47
2848	Chi-Chi, Taiwan-04	1999	920	2146	TCU036	6.2	330	89	15	23.6	120.82	18	87.03	478.07	-999	24.4488	120.6963	0.02	2.26
2852	Chi-Chi, Taiwan-04	1999	920	2146	TCU042	6.2	330	89	15	23.6	120.82	18	98.43	578.98	-999	24.5542	120.8077	0.02	2.31
2885	Chi-Chi, Taiwan-04	1999	920	2146	TCU112	6.2	330	89	15	23.6	120.82	18	55.85	190.54	-999	24.0557	120.424	0.04	8.72
2890	Chi-Chi, Taiwan-04	1999	920	2146	TCU118	6.2	330	89	15	23.6	120.82	18	51.48	236.19	-999	24.0027	120.4235	0.04	7.25
2903	Chi-Chi, Taiwan-04	1999	920	2146	TTN003	6.2	330	89	15	23.6	120.82	18	99.07	506.64	-999	22.6178	120.9975	0.01	1.19
2919	Chi-Chi, Taiwan-04	1999	920	2146	TTN025	6.2	330	89	15	23.6	120.82	18	69.29	704.96	-999	22.9045	121.072	0.02	1.84
2921	Chi-Chi, Taiwan-04	1999	920	2146	TTN027	6.2	330	89	15	23.6	120.82	18	80.04	428.95	-999	22.8078	121.086	0.01	2.18
2932	Chi-Chi, Taiwan-04	1999	920	2146	TTN046	6.2	330	89	15	23.6	120.82	18	69.68	528.12	-999	22.9658	121.232	0.03	3.18
2943	Chi-Chi, Taiwan-05	1999	922	14	CHY025	6.2	165	70	100	23.81	121.08	10	50.92	277.5	-999	23.7795	120.5137	0.17	8.60
2947	Chi-Chi, Taiwan-05	1999	922	14	CHY030	6.2	165	70	100	23.81	121.08	10	58.57	204.71	-999	23.6443	120.4758	0.16	10.04
2959	Chi-Chi, Taiwan-05	1999	922	14	CHY055	6.2	165	70	100	23.81	121.08	10	94.31	225.77	-999	23.2698	120.2705	0.09	8.18
2963	Chi-Chi, Taiwan-05	1999	922	14	CHY059	6.2	165	70	100	23.81	121.08	10	113.93	191.09	-999	23.184	120.1025	0.03	4.96
2972	Chi-Chi, Taiwan-05	1999	922	14	CHY070	6.2	165	70	100	23.81	121.08	10	118.86	265.45	-999	22.971	120.2286	0.03	3.86
2973	Chi-Chi, Taiwan-05	1999	922	14	CHY071	6.2	165	70	100	23.81	121.08	10	116.62	202.95	-999	23.0648	120.1645	0.04	4.72
2997	Chi-Chi, Taiwan-05	1999	922	14	HWA005	6.2	165	70	100	23.81	121.08	10	32.71	459.32	-999	23.6608	121.414	0.08	6.12
3013	Chi-Chi, Taiwan-05	1999	922	14	HWA026	6.2	165	70	100	23.81	121.08	10	61.4	457.49	-999	24.1185	121.6165	0.04	2.14

RSN	Name	YEAR	MO DY	HRM N	Station Name	Magnitude	Strike (°)	Dip (°)	Rake (°)	Hypocenter Latitude (°)	Hypocenter Longitude (°)	Hypocenter Depth (km)	R <sub>jb</sub> (km)	V <sub>s30</sub> (m/s)	Geologic al Unit	Station Latitude (°)	Station Longitude (°)	PGA (g)	PGV (cm/s)
3014	Chi-Chi, Taiwan-05	1999	922	14	HWA027	6.2	165	70	100	23.81	121.08	10	56.48	437.8	-999	24.055	121.591	0.04	2.71
3025	Chi-Chi, Taiwan-05	1999	922	14	HWA038	6.2	165	70	100	23.81	121.08	10	39.93	642.73	-999	23.4615	121.3445	0.04	4.89
3033	Chi-Chi, Taiwan-05	1999	922	14	HWA049	6.2	165	70	100	23.81	121.08	10	51.43	508.61	-999	23.9952	121.5577	0.06	4.61
3048	Chi-Chi, Taiwan-05	1999	922	14	ILA008	6.2	165	70	100	23.81	121.08	10	114.76	299.28	-999	24.7088	121.7628	0.02	2.29
3070	Chi-Chi, Taiwan-05	1999	922	14	ILA059	6.2	165	70	100	23.81	121.08	10	114.96	236.84	-999	24.6667	121.8205	0.02	2.56
3073	Chi-Chi, Taiwan-05	1999	922	14	ILA064	6.2	165	70	100	23.81	121.08	10	97.09	488.61	-999	24.477	121.7787	0.02	1.41
3107	Chi-Chi, Taiwan-05	1999	922	14	KAU077	6.2	165	70	100	23.81	121.08	10	114.41	665.2	-999	22.747	120.7233	0.02	2.77
3165	Chi-Chi, Taiwan-05	1999	922	14	TCU033	6.2	165	70	100	23.81	121.08	10	89.88	423.4	-999	24.6855	120.8623	0.05	4.14
3168	Chi-Chi, Taiwan-05	1999	922	14	TCU039	6.2	165	70	100	23.81	121.08	10	71.17	540.66	-999	24.4917	120.7837	0.06	4.39
3178	Chi-Chi, Taiwan-05	1999	922	14	TCU052	6.2	165	70	100	23.81	121.08	10	43.94	579.1	-999	24.198	120.7393	0.06	5.43
3182	Chi-Chi, Taiwan-05	1999	922	14	TCU056	6.2	165	70	100	23.81	121.08	10	49.06	403.2	-999	24.1588	120.6238	0.11	4.74
3188	Chi-Chi, Taiwan-05	1999	922	14	TCU067	6.2	165	70	100	23.81	121.08	10	36.73	433.63	-999	24.0912	120.72	0.10	6.28
3195	Chi-Chi, Taiwan-05	1999	922	14	TCU087	6.2	165	70	100	23.81	121.08	10	56.63	538.69	-999	24.3482	120.7733	0.03	2.62
3217	Chi-Chi, Taiwan-05	1999	922	14	TCU129	6.2	165	70	100	23.81	121.08	10	32.21	511.18	-999	23.8783	120.6843	0.41	10.74
3223	Chi-Chi, Taiwan-05	1999	922	14	TCU145	6.2	165	70	100	23.81	121.08	10	68.39	240.43	-999	23.98	120.3368	0.14	5.59
3224	Chi-Chi, Taiwan-05	1999	922	14	TTN001	6.2	165	70	100	23.81	121.08	10	58.74	484.6	-999	23.3178	121.4425	0.03	4.35
3236	Chi-Chi, Taiwan-05	1999	922	14	TTN015	6.2	165	70	100	23.81	121.08	10	109.28	487.91	-999	22.754	121.1465	0.02	3.24
3239	Chi-Chi, Taiwan-05	1999	922	14	TTN022	6.2	165	70	100	23.81	121.08	10	72.58	398.81	-999	23.0973	121.2105	0.06	5.34
3260	Chi-Chi, Taiwan-06	1999	925	2352	CHY016	6.3	5	30	100	23.87	121.01	16	95.51	200.86	-999	23.2212	120.1532	0.05	9.28
3265	Chi-Chi, Taiwan-06	1999	925	2352	CHY025	6.3	5	30	100	23.87	121.01	16	39.07	277.5	-999	23.7795	120.5137	0.10	19.64
3266	Chi-Chi, Taiwan-06	1999	925	2352	CHY026	6.3	5	30	100	23.87	121.01	16	49.64	226.01	-999	23.7987	120.4113	0.09	11.74

RSN	Name	YEAR	MO DY	HRM N	Station Name	Magnitude	Strike (°)	Dip (°)	Rake (°)	Hypocenter Latitude (°)	Hypocenter Longitude (°)	Hypocenter Depth (km)	R <sub>jb</sub> (km)	V <sub>s30</sub> (m/s)	Geologic al Unit	Station Latitude (°)	Station Longitude (°)	PGA (g)	PGV (cm/s)
3270	Chi-Chi, Taiwan-06	1999	925	2352	CHY030	6.3	5	30	100	23.87	121.01	16	44.17	204.71	-999	23.6443	120.4758	0.10	19.67
3274	Chi-Chi, Taiwan-06	1999	925	2352	CHY035	6.3	5	30	100	23.87	121.01	16	40.36	573.04	-999	23.52	120.584	0.17	17.96
3281	Chi-Chi, Taiwan-06	1999	925	2352	CHY046	6.3	5	30	100	23.87	121.01	16	53.17	442.15	-999	23.4765	120.4632	0.12	13.56
3284	Chi-Chi, Taiwan-06	1999	925	2352	CHY052	6.3	5	30	100	23.87	121.01	16	64.77	573.04	-999	23.2878	120.501	0.09	7.71
3286	Chi-Chi, Taiwan-06	1999	925	2352	CHY055	6.3	5	30	100	23.87	121.01	16	82.76	225.77	-999	23.2698	120.2705	0.08	10.05
3290	Chi-Chi, Taiwan-06	1999	925	2352	CHY060	6.3	5	30	100	23.87	121.01	16	96.14	228.92	-999	23.1243	120.2392	0.03	6.66
3292	Chi-Chi, Taiwan-06	1999	925	2352	CHY062	6.3	5	30	100	23.87	121.01	16	82.87	602.63	-999	23.1213	120.45	0.04	3.65
3297	Chi-Chi, Taiwan-06	1999	925	2352	CHY069	6.3	5	30	100	23.87	121.01	16	112.54	224.42	-999	22.9737	120.1815	0.02	4.99
3304	Chi-Chi, Taiwan-06	1999	925	2352	CHY079	6.3	5	30	100	23.87	121.01	16	72.64	573.04	-999	23.1848	120.528	0.05	3.61
3311	Chi-Chi, Taiwan-06	1999	925	2352	CHY092	6.3	5	30	100	23.87	121.01	16	42.77	253.72	-999	23.7913	120.4783	0.08	17.81
3327	Chi-Chi, Taiwan-06	1999	925	2352	HWA009	6.3	5	30	100	23.87	121.01	16	53.55	373.23	-999	23.9925	121.6165	0.03	3.63
3331	Chi-Chi, Taiwan-06	1999	925	2352	HWA015	6.3	5	30	100	23.87	121.01	16	47.12	453.05	-999	23.9757	121.553	0.03	3.33
3349	Chi-Chi, Taiwan-06	1999	925	2352	HWA037	6.3	5	30	100	23.87	121.01	16	44.77	469.64	-999	23.4542	121.384	0.04	8.10
3356	Chi-Chi, Taiwan-06	1999	925	2352	HWA050	6.3	5	30	100	23.87	121.01	16	50.25	313.9	-999	23.9897	121.584	0.03	3.13
3358	Chi-Chi, Taiwan-06	1999	925	2352	HWA055	6.3	5	30	100	23.87	121.01	16	52.89	369.75	-999	23.3232	121.3323	0.04	7.25
3360	Chi-Chi, Taiwan-06	1999	925	2352	HWA057	6.3	5	30	100	23.87	121.01	16	56.14	671.52	-999	24.16	121.61	0.03	1.53
3362	Chi-Chi, Taiwan-06	1999	925	2352	HWA059	6.3	5	30	100	23.87	121.01	16	42.79	208.56	-999	23.8713	121.5005	0.05	3.89
3376	Chi-Chi, Taiwan-06	1999	925	2352	ILA019	6.3	5	30	100	23.87	121.01	16	94.93	671.52	-999	24.6437	121.6912	0.01	1.23
3380	Chi-Chi, Taiwan-06	1999	925	2352	ILA030	6.3	5	30	100	23.87	121.01	16	106.25	200.98	-999	24.7278	121.755	0.02	3.00
3381	Chi-Chi, Taiwan-06	1999	925	2352	ILA041	6.3	5	30	100	23.87	121.01	16	108.27	196.88	-999	24.7233	121.7917	0.02	2.96
3389	Chi-Chi, Taiwan-06	1999	925	2352	ILA062	6.3	5	30	100	23.87	121.01	16	89.01	447.51	-999	24.4677	121.7933	0.02	1.84

RSN	Name	YEAR	MO DY	HRM N	Station Name	Magnitude	Strike (°)	Dip (°)	Rake (°)	Hypocenter Latitude (°)	Hypocenter Longitude (°)	Hypocenter Depth (km)	R <sub>jb</sub> (km)	V <sub>s30</sub> (m/s)	Geologic al Unit	Station Latitude (°)	Station Longitude (°)	PGA (g)	PGV (cm/s)
3415	Chi-Chi, Taiwan-06	1999	925	2352	KAU078	6.3	5	30	100	23.87	121.01	16	117.82	531.85	-999	22.7112	120.6412	0.01	1.16
3458	Chi-Chi, Taiwan-06	1999	925	2352	TCU051	6.3	5	30	100	23.87	121.01	16	32.36	350.06	-999	24.1603	120.6518	0.05	5.82
3463	Chi-Chi, Taiwan-06	1999	925	2352	TCU059	6.3	5	30	100	23.87	121.01	16	46.69	272.67	-999	24.2687	120.5637	0.08	8.91
3465	Chi-Chi, Taiwan-06	1999	925	2352	TCU061	6.3	5	30	100	23.87	121.01	16	40.46	379.64	-999	24.1355	120.549	0.07	8.40
3470	Chi-Chi, Taiwan-06	1999	925	2352	TCU072	6.3	5	30	100	23.87	121.01	16	8.34	468.14	-999	24.0407	120.8488	0.08	8.62
3472	Chi-Chi, Taiwan-06	1999	925	2352	TCU076	6.3	5	30	100	23.87	121.01	16	23.84	614.98	-999	23.9077	120.6757	0.13	8.81
3494	Chi-Chi, Taiwan-06	1999	925	2352	TCU108	6.3	5	30	100	23.87	121.01	16	41.34	260.62	-999	24.0865	120.5235	0.07	7.51
3499	Chi-Chi, Taiwan-06	1999	925	2352	TCU115	6.3	5	30	100	23.87	121.01	16	45.25	215.34	-999	23.9595	120.4693	0.05	8.69
3528	Chi-Chi, Taiwan-06	1999	925	2352	TTN020	6.3	5	30	100	23.87	121.01	16	68.69	453.71	-999	23.1268	121.2057	0.02	3.31
3532	Chi-Chi, Taiwan-06	1999	925	2352	TTN025	6.3	5	30	100	23.87	121.01	16	91.9	704.96	-999	22.9045	121.072	0.02	1.31
3585	Taiwan SMART1( 25)	1983	921	1920	SMART1 I11	6.5	73	80	80	23.9382	122.3167	18	95.73	309.41	-999	24.6749	121.7634	0.03	3.40
3657	Taiwan SMART1( 40)	1986	520	525	SMART1 O06	6.32	43	57	100	24.0817	121.5915	15.8	56.96	293.46	-999	24.6565	121.7708	0.18	29.91
3670	Taiwan SMART1( 45)	1986	1114	2120	SMART1 I11	7.3	43	57	100	23.9918	121.8332	15	56.15	309.41	-999	24.6749	121.7634	0.11	27.31
3677	Taiwan SMART1( 45)	1986	1114	2120	SMART1 M09	7.3	43	57	100	23.9918	121.8332	15	55.87	321.63	-999	24.6703	121.7553	0.11	26.78
3683	Taiwan SMART1( 45)	1986	1114	2120	SMART1 O11	7.3	43	57	100	23.9918	121.8332	15	57.64	295.17	-999	24.6856	121.7506	0.13	24.07
3737	Whittier Narrows- 02	1987	1004	1059	Sun Valley - Roscoe Blvd	5.27	170	70	140	34.06	-118.104	13.3	32.61	320.93	Qal, deep (incl LA)	34.221	-118.421	0.08	3.32
3745	Cape Mendocin o	1992	425	1806	Butler Valley Station 2	7.01	350	14	105	40.327	-124.233	9.5	43.82	525.26	-999	40.78	-123.88	0.15	17.38
3746	Cape Mendocin o	1992	425	1806	Centerville Beach, Naval Fac	7.01	350	14	105	40.327	-124.233	9.5	16.44	459.04	-999	40.563	-124.348	0.45	50.40
3747	Cape Mendocin o	1992	425	1806	College of the Redwoods	7.01	350	14	105	40.327	-124.233	9.5	29.22	492.74	-999	40.6994	-124.201	0.16	28.08
3749	Cape Mendocin o	1992	425	1806	Fortuna Fire Station	7.01	350	14	105	40.327	-124.233	9.5	16.54	355.18	-999	40.5891	-124.148	0.31	34.31
3750	Cape Mendocin o	1992	425	1806	Loleta Fire Station	7.01	350	14	105	40.327	-124.233	9.5	23.46	515.65	-999	40.6442	-124.221	0.25	34.21

RSN	Name	YEAR	MO DY	HRM N	Station Name	Magnitude	Strike (°)	Dip (°)	Rake (°)	Hypocenter Latitude (°)	Hypocenter Longitude (°)	Hypocenter Depth (km)	R <sub>jb</sub> (km)	V <sub>s30</sub> (m/s)	Geologic al Unit	Station Latitude (°)	Station Longitude (°)	PGA (g)	PGV (cm/s)
3752	Landers	1992	628	1158	Forest Falls Post Office	7.28	336	90	180	34.2	-116.436	7	45.34	436.14	Qal, coarse	34.088	-116.919	0.11	9.24
3760	Landers	1992	628	1158	Big Bear Lake - Civic Center	7.28	336	90	180	34.2	-116.436	7	45.48	430.36	Qal, thin	34.238	-116.935	0.18	12.84
3772	Northridge-06	1994	320	2120	LA - Wadsworth VA Hospital South	5.28	308	40	106	34.2313	-118.475	13.09	16.89	413.81	Qoa	34.052	-118.451	0.08	3.09
3815	Hector Mine	1999	101 6	-999	Riverside - Hole & La Sierra	7.13	332	82	179	34.5981	-116.265	14.8	128.94	334.99	Qoa	33.919	-117.488	0.04	5.67
3816	Hector Mine	1999	101 6	-999	Riverside - I215 & 3rd	7.13	332	82	179	34.5981	-116.265	14.8	114.1	340.65	Qoa	33.979	-117.344	0.05	7.15
3817	Hector Mine	1999	101 6	-999	Riverside - Van Buren&Tra utwein	7.13	332	82	179	34.5981	-116.265	14.8	117.4	581.8	Kgr	33.895	-117.32	0.03	5.52
3818	Hector Mine	1999	101 6	-999	Riverside - Limonite & Downey	7.13	332	82	179	34.5981	-116.265	14.8	125.7	329.84	Qoa	33.975	-117.486	0.03	5.79
3848	Chi-Chi (aftershock k 2), Taiwan	1999	920	1803	CHY012	6.2	360	10	80	23.81	120.85	7.8	80.4	198.4	-999	23.3328	120.1523	0.03	6.63
3856	Chi-Chi (aftershock k 3), Taiwan	1999	920	2146	CHY014	6.2	330	89	15	23.6	120.82	18	37.89	347.63	-999	23.2963	120.5828	0.13	7.98
3863	Chi-Chi (aftershock k 5), Taiwan	1999	925	2352	CHY002	6.3	5	30	100	23.87	121.01	16	49.27	235.13	-999	23.7192	120.4125	0.17	16.54
3865	Chi-Chi (aftershock k 5), Taiwan	1999	925	2352	CHY006	6.3	5	30	100	23.87	121.01	16	39.39	438.19	-999	23.5815	120.552	0.15	20.57
3868	Chi-Chi (aftershock k 5), Taiwan	1999	925	2352	CHY012	6.3	5	30	100	23.87	121.01	16	88.54	198.4	-999	23.3328	120.1523	0.05	7.60
3873	Tottori, Japan	2000	100 6	430	HRS004	6.61	330	90	0	35.275	133.35	12.5	115.23	670.13	-999	34.723	132.2797	0.09	3.38
3881	Tottori, Japan	2000	100 6	430	HRS015	6.61	330	90	0	35.275	133.35	12.5	72.3	250.27	-999	34.4816	133.3641	0.13	6.45
3887	Tottori, Japan	2000	100 6	430	HRSH03	6.61	330	90	0	35.275	133.35	12.5	73.91	486.78	-999	34.515	133.1401	0.29	7.14
3899	Tottori, Japan	2000	100 6	430	HYGH02	6.61	330	90	0	35.275	133.35	12.5	88.75	617.44	-999	35.0639	134.4261	0.03	1.79
3908	Tottori, Japan	2000	100 6	430	OKY005	6.61	330	90	0	35.275	133.35	12.5	28.81	293.37	-999	35.0066	133.7344	0.31	16.27
3911	Tottori, Japan	2000	100 6	430	OKY008	6.61	330	90	0	35.275	133.35	12.5	50.35	450.61	-999	34.8669	133.9063	0.17	7.88
3921	Tottori, Japan	2000	100 6	430	OKYH03	6.61	330	90	0	35.275	133.35	12.5	49.81	316.76	-999	34.775	133.7917	0.11	7.94
3926	Tottori, Japan	2000	100 6	430	OKYH08	6.61	330	90	0	35.275	133.35	12.5	24.84	694.21	-999	34.9071	133.4081	0.24	9.67
3932	Tottori, Japan	2000	100 6	430	OKYH14	6.61	330	90	0	35.275	133.35	12.5	26.51	709.86	-999	34.9331	133.6232	0.37	18.28
3946	Tottori, Japan	2000	100 6	430	SMN018	6.61	330	90	0	35.275	133.35	12.5	85.31	271.29	-999	36.1894	133.2358	0.07	4.30

RSN	Name	YEAR	MO DY	HRM N	Station Name	Magnitude	Strike (°)	Dip (°)	Rake (°)	Hypocenter Latitude (°)	Hypocenter Longitude (°)	Hypocenter Depth (km)	R <sub>jb</sub> (km)	V <sub>s30</sub> (m/s)	Geologic al Unit	Station Latitude (°)	Station Longitude (°)	PGA (g)	PGV (cm/s)
3948	Tottori, Japan	2000	100 6	430	SMNH02	6.61	330	90	0	35.275	133.35	12.5	23.64	502. 66	-999	35.2203	133.0882	0.44	16.10
3949	Tottori, Japan	2000	100 6	430	SMNH03	6.61	330	90	0	35.275	133.35	12.5	52.3	439. 68	-999	35.2212	132.7249	0.16	8.26
3952	Tottori, Japan	2000	100 6	430	SMNH06	6.61	330	90	0	35.275	133.35	12.5	112.15	287. 61	-999	34.8807	132.2051	0.08	4.54
3962	Tottori, Japan	2000	100 6	430	TTR005	6.61	330	90	0	35.275	133.35	12.5	45.98	169. 16	-999	35.4258	133.828	0.17	8.88
3964	Tottori, Japan	2000	100 6	430	TTR007	6.61	330	90	0	35.275	133.35	12.5	11.28	469. 79	-999	35.2794	133.4902	0.74	37.09
4013	San Simeon, CA	2003	122 2	1915	San Antonio Dam - Toe	6.52	292	52	97	35.697	-121.085	8.5	16.17	509. 04	-999	35.799	-120.884	0.11	13.64
4066	Parkfield- 02, CA	2004	928	1715	PARKFIEL D - FROELICH	6	141	89	-175	35.817	-120.365	8.1	1.85	226. 63	-999	35.911	-120.486	0.41	13.55
4069	Parkfield- 02, CA	2004	928	1715	PARKFIEL D - JACK CANYON	6	141	89	-175	35.817	-120.365	8.1	9.12	576. 21	-999	35.713	-120.203	0.16	9.14
4081	Parkfield- 02, CA	2004	928	1715	Parkfield - Cholame 5W	6	141	89	-175	35.817	-120.365	8.1	6.27	236. 59	Qal, thin	35.697	-120.328	0.23	14.97
4085	Parkfield- 02, CA	2004	928	1715	Shandon-1- story High School Bldg	6	141	89	-175	35.817	-120.365	8.1	12.59	357. 35	-999	35.655	-120.377	0.19	6.88
4096	Parkfield- 02, CA	2004	928	1715	Bear Valley Ranch, Parkfield, CA, USA	6	141	89	-175	35.817	-120.365	8.1	3.38	527. 95	-999	35.945	-120.542	0.16	9.22
4098	Parkfield- 02, CA	2004	928	1715	Parkfield - Cholame 1E	6	141	89	-175	35.817	-120.365	8.1	1.66	326. 64	Qal, thin	35.743	-120.277	0.39	39.72
4099	Parkfield- 02, CA	2004	928	1715	Parkfield - Cholame 2E	6	141	89	-175	35.817	-120.365	8.1	3.22	522. 74	Tsh	35.751	-120.259	0.48	22.77
4102	Parkfield- 02, CA	2004	928	1715	Parkfield - Cholame 3W	6	141	89	-175	35.817	-120.365	8.1	2.55	230. 57	Qal, thin	35.724	-120.294	0.41	34.26
4112	Parkfield- 02, CA	2004	928	1715	Parkfield - Fault Zone 8	6	141	89	-175	35.817	-120.365	8.1	3.05	308. 84	Tsh	35.878	-120.381	0.48	20.46
4121	Parkfield- 02, CA	2004	928	1715	Parkfield - Gold Hill 3E	6	141	89	-175	35.817	-120.365	8.1	5.79	450. 61	Qoa	35.87	-120.334	0.16	9.59
4131	Parkfield- 02, CA	2004	928	1715	Parkfield - Vineyard Cany 1W	6	141	89	-175	35.817	-120.365	8.1	1	284. 21	Tsh	35.934	-120.497	0.16	15.55
4133	Parkfield- 02, CA	2004	928	1715	Parkfield - Vineyard Cany 2W	6	141	89	-175	35.817	-120.365	8.1	2.33	438. 74	Qal, thin	35.927	-120.509	0.46	23.99
4159	Niigata, Japan	2004	102 3	856	FKS028	6.63	212	47	93	37.307	138.839	10.6	30.11	305. 54	-999	37.3491	139.3144	0.16	12.09
4161	Niigata, Japan	2004	102 3	856	FKS030	6.63	212	47	93	37.307	138.839	10.6	48.26	499. 18	-999	37.453	139.5133	0.12	4.46
4163	Niigata, Japan	2004	102 3	856	FKSH03	6.63	212	47	93	37.307	138.839	10.6	73.46	349. 74	-999	37.6048	139.7566	0.09	5.08
4171	Niigata, Japan	2004	102 3	856	GNM003	6.63	212	47	93	37.307	138.839	10.6	63.56	373. 23	-999	36.6578	139.0784	0.32	8.87
4176	Niigata, Japan	2004	102 3	856	GNM008	6.63	212	47	93	37.307	138.839	10.6	98	369. 84	-999	36.3478	139.1368	0.03	3.72

RSN	Name	YEAR	MO DY	HRM N	Station Name	Magnitude	Strike (°)	Dip (°)	Rake (°)	Hypocenter Latitude (°)	Hypocenter Longitude (°)	Hypocenter Depth (km)	R <sub>jb</sub> (km)	V <sub>s30</sub> (m/s)	Geologic al Unit	Station Latitude (°)	Station Longitude (°)	PGA (g)	PGV (cm/s)
4185	Niigata, Japan	2004	102 3	856	NGN003	6.63	212	47	93	37.307	138.839	10.6	62.54	525. 27	-999	36.7403	138.4129	0.08	3.14
4200	Niigata, Japan	2004	102 3	856	NIG010	6.63	212	47	93	37.307	138.839	10.6	55.9	173. 09	-999	37.9146	139.0108	0.09	7.61
4203	Niigata, Japan	2004	102 3	856	NIG013	6.63	212	47	93	37.307	138.839	10.6	38	174. 55	-999	37.7638	138.8834	0.12	12.89
4205	Niigata, Japan	2004	102 3	856	NIG015	6.63	212	47	93	37.307	138.839	10.6	39.83	488. 65	-999	37.6935	139.1886	0.07	4.46
4208	Niigata, Japan	2004	102 3	856	NIG018	6.63	212	47	93	37.307	138.839	10.6	21.55	198. 26	-999	37.3724	138.5579	0.13	22.33
4211	Niigata, Japan	2004	102 3	856	NIG021	6.63	212	47	93	37.307	138.839	10.6	10.21	418. 5	-999	37.1281	138.7468	1.48	51.76
4212	Niigata, Japan	2004	102 3	856	NIG022	6.63	212	47	93	37.307	138.839	10.6	17.57	193. 2	-999	37.0364	138.8462	0.34	20.41
4227	Niigata, Japan	2004	102 3	856	NIGH10	6.63	212	47	93	37.307	138.839	10.6	39.17	653. 28	-999	37.5408	139.3681	0.17	8.65
4234	Niigata, Japan	2004	102 3	856	NIGH18	6.63	212	47	93	37.307	138.839	10.6	53.99	311. 1	-999	36.9394	138.2625	0.10	7.20
4320	Lazio Abruzzo (aftershoc k 1), Italy	1984	511	1041	Cassino- Sant' Elia	5.5	273	55	-90	41.7318	13.9208	8	21.59	436. 79	-999	41.523	13.864	0.04	2.81
4345	Umbria Marche, Italy	1997	926	940	Assisi- Stallone	6	326	55	-90	43.031	12.862	6	16.55	376. 6	-999	43.075	12.607	0.17	9.16
4393	Umbria Marche (aftershoc k 2), Italy	1997	101 4	1523	Rieti	5.6	5.4	55	-90	42.919	12.926	7	51.72	313. 07	-999	42.4303	12.8211	0.03	4.15
4456	Monteneg ro, Yugo.	1979	415	619	Petrovac - Hotel Olivia	7.1	300	14	88	42.04	19.21	7	0	543. 26	-999	42.204	18.948	0.37	32.09
4460	L'Aquila, Italy	2009	406	133	Antrodoco	6.3	139	48	-98	42.3476	13.38	9.27	18.76	525. 95	-999	42.418	13.079	0.02	2.02
4481	L'Aquila, Italy	2009	406	133	L'Aquila - V. Aterno - Colle Grilli	6.3	139	48	-98	42.3476	13.38	9.27	0	685	-999	42.373	13.337	0.46	33.14
4549	L'Aquila (aftershoc k 2), Italy	2009	409	52	L'Aquila - V. Aterno - Il Moro	5.4	136	46	-99	42.484	13.343	15.4	9.98	563. 74	-999	42.3786	13.3493	0.08	2.53
4846	Chuetsu- oki	2007	716	1013	Joetsu Yanagishim a paddocks	6.8	34	36	90	37.5382	138.6174	9	28.07	605. 71	-999	37.0764	138.3861	0.31	25.89
4855	Chuetsu- oki	2007	716	1013	Sanjo	6.8	34	36	90	37.5382	138.6174	9	21.4	245. 45	-999	37.6381	138.9589	0.11	16.17
4859	Chuetsu- oki	2007	716	1013	Mitsuke Kazuiti Arita Town	6.8	34	36	90	37.5382	138.6174	9	11.35	274. 23	-999	37.5431	138.8886	0.13	20.10
4866	Chuetsu- oki	2007	716	1013	Kawanishi Izumozaki	6.8	34	36	90	37.5382	138.6174	9	0	338. 32	-999	37.5278	138.7125	0.36	36.13
4875	Chuetsu- oki	2007	716	1013	Kariwa	6.8	34	36	90	37.5382	138.6174	9	0	282. 57	-999	37.4189	138.6258	0.40	128.3 9
4876	Chuetsu- oki	2007	716	1013	Kashiwazak i Nishiyamac ho Ikeura	6.8	34	36	90	37.5382	138.6174	9	0	655. 45	-999	37.4539	138.67	0.86	70.67
4886	Chuetsu- oki	2007	716	1013	Tamati Yone Izumozaki	6.8	34	36	90	37.5382	138.6174	9	0	338. 32	-999	37.5317	138.7095	0.52	44.94
4893	Chuetsu- oki	2007	716	1013	Toyotsu Nakano	6.8	34	36	90	37.5382	138.6174	9	61.16	561. 59	-999	36.77	138.3276	0.23	22.22

RSN	Name	YEAR	MO DY	HRM N	Station Name	Magnitude	Strike (°)	Dip (°)	Rake (°)	Hypocenter Latitude (°)	Hypocenter Longitude (°)	Hypocenter Depth (km)	R <sub>jb</sub> (km)	V <sub>s30</sub> (m/s)	Geologic al Unit	Station Latitude (°)	Station Longitude (°)	PGA (g)	PGV (cm/s)
4991	Chuetsu- oki	2007	716	1013	FKS022	6.8	34	36	90	37.5382	138.6174	9	78.49	211. 76	-999	37.6002	139.6467	0.05	2.99
4997	Chuetsu- oki	2007	716	1013	FKS028	6.8	34	36	90	37.5382	138.6174	9	52.63	305. 54	-999	37.3491	139.3144	0.06	5.42
5083	Chuetsu- oki	2007	716	1013	GNMH13	6.8	34	36	90	37.5382	138.6174	9	65.56	323. 08	-999	36.8589	139.0659	0.08	3.45
5118	Chuetsu- oki	2007	716	1013	ISK003	6.8	34	36	90	37.5382	138.6174	9	129.88	538. 9	-999	37.3919	136.9083	0.03	3.56
5130	Chuetsu- oki	2007	716	1013	ISKH01	6.8	34	36	90	37.5382	138.6174	9	97.49	344. 86	-999	37.5236	137.2875	0.05	4.92
5132	Chuetsu- oki	2007	716	1013	ISKH03	6.8	34	36	90	37.5382	138.6174	9	100.09	310. 94	-999	37.3428	137.2467	0.11	7.00
5193	Chuetsu- oki	2007	716	1013	NGN001	6.8	34	36	90	37.5382	138.6174	9	51.48	303. 73	-999	36.8514	138.366	0.16	19.14
5236	Chuetsu- oki	2007	716	1013	NGNH26	6.8	34	36	90	37.5382	138.6174	9	98.68	300. 47	-999	36.4632	138.1505	0.06	3.79
5239	Chuetsu- oki	2007	716	1013	NGNH29	6.8	34	36	90	37.5382	138.6174	9	43.54	464. 92	-999	36.9072	138.4439	0.10	5.71
5242	Chuetsu- oki	2007	716	1013	NGNH32	6.8	34	36	90	37.5382	138.6174	9	125.54	309. 6	-999	36.2546	137.9929	0.03	1.96
5247	Chuetsu- oki	2007	716	1013	NIG001	6.8	34	36	90	37.5382	138.6174	9	71.79	648. 63	-999	38.2584	138.4337	0.06	3.60
5250	Chuetsu- oki	2007	716	1013	NIG004	6.8	34	36	90	37.5382	138.6174	9	34.31	318. 62	-999	37.8205	138.2795	0.10	3.99
5251	Chuetsu- oki	2007	716	1013	NIG005	6.8	34	36	90	37.5382	138.6174	9	33.8	288. 72	-999	37.9204	138.4981	0.14	5.91
5255	Chuetsu- oki	2007	716	1013	NIG009	6.8	34	36	90	37.5382	138.6174	9	69.29	179. 6	-999	37.9507	139.3375	0.03	2.29
5270	Chuetsu- oki	2007	716	1013	NIG024	6.8	34	36	90	37.5382	138.6174	9	20.6	375. 22	-999	37.1268	138.444	0.18	16.82
5279	Chuetsu- oki	2007	716	1013	NIGH05	6.8	34	36	90	37.5382	138.6174	9	67.6	244. 84	-999	37.9731	139.2819	0.08	5.65
5283	Chuetsu- oki	2007	716	1013	NIGH10	6.8	34	36	90	37.5382	138.6174	9	53.52	653. 28	-999	37.5408	139.3681	0.07	3.77
5284	Chuetsu- oki	2007	716	1013	NIGH11	6.8	34	36	90	37.5382	138.6174	9	21.19	375	-999	37.1697	138.7472	0.14	18.96
5285	Chuetsu- oki	2007	716	1013	NIGH12	6.8	34	36	90	37.5382	138.6174	9	35.41	564. 25	-999	37.2208	138.9853	0.15	5.83
5286	Chuetsu- oki	2007	716	1013	NIGH13	6.8	34	36	90	37.5382	138.6174	9	29.84	461. 1	-999	37.0514	138.3997	0.25	23.52
5292	Chuetsu- oki	2007	716	1013	NIGH19	6.8	34	36	90	37.5382	138.6174	9	57.07	625	-999	36.8083	138.7881	0.11	5.03
5348	Chuetsu- oki	2007	716	1013	TCG009	6.8	34	36	90	37.5382	138.6174	9	120.1	225. 04	-999	36.7258	139.7155	0.10	3.97
5465	Iwate	2008	613	2343	AKT010	6.9	209	40	104	39.027	140.878	6.5	90.53	425. 15	-999	39.7225	140.1002	0.06	6.34
5474	Iwate	2008	613	2343	AKT019	6.9	209	40	104	39.027	140.878	6.5	26.03	640. 14	-999	39.0384	140.451	0.18	12.08
5475	Iwate	2008	613	2343	AKT020	6.9	209	40	104	39.027	140.878	6.5	75.91	213. 11	-999	39.2022	139.9085	0.04	6.97
5480	Iwate	2008	613	2343	AKTH02	6.9	209	40	104	39.027	140.878	6.5	58.34	620. 4	-999	39.6606	140.5756	0.07	4.01
5493	Iwate	2008	613	2343	AKTH17	6.9	209	40	104	39.027	140.878	6.5	46.55	288. 82	-999	39.5547	140.615	0.08	6.81
5541	Iwate	2008	613	2343	AOMH18	6.9	209	40	104	39.027	140.878	6.5	121.28	369. 11	-999	40.2934	141.018	0.08	1.63
5542	Iwate	2008	613	2343	FKS001	6.9	209	40	104	39.027	140.878	6.5	115.66	276. 35	-999	37.7949	140.9196	0.08	6.11



RSN	Name	YEAR	MO DY	HRM N	Station Name	Magnitude	Strike (°)	Dip (°)	Rake (°)	Hypocenter Latitude (°)	Hypocenter Longitude (°)	Hypocenter Depth (km)	R <sub>jb</sub> (km)	V <sub>s30</sub> (m/s)	Geologic al Unit	Station Latitude (°)	Station Longitude (°)	PGA (g)	PGV (cm/s)
5545	Iwate	2008	613	2343	FKS004	6.9	209	40	104	39.027	140.878	6.5	128.46	388.58	-999	37.6799	140.7346	0.06	2.49
5623	Iwate	2008	613	2343	IWT015	6.9	209	40	104	39.027	140.878	6.5	17.05	567.45	-999	39.318	140.7792	0.21	11.29
5630	Iwate	2008	613	2343	IWT022	6.9	209	40	104	39.027	140.878	6.5	100.25	392.5	-999	40.1011	141.0523	0.04	1.78
5633	Iwate	2008	613	2343	IWTH01	6.9	209	40	104	39.027	140.878	6.5	120.32	438.04	-999	40.2356	141.3458	0.08	3.18
5636	Iwate	2008	613	2343	IWTH04	6.9	209	40	104	39.027	140.878	6.5	29.53	455.93	-999	39.1781	141.3944	0.16	6.50
5652	Iwate	2008	613	2343	IWTH20	6.9	209	40	104	39.027	140.878	6.5	18.74	288.75	-999	39.3406	141.0508	0.25	12.99
5657	Iwate	2008	613	2343	IWTH25	6.9	209	40	104	39.027	140.878	6.5	0	506.44	-999	39.0061	140.8667	1.35	64.88
5658	Iwate	2008	613	2343	IWTH26	6.9	209	40	104	39.027	140.878	6.5	5.97	371.06	-999	38.9661	141.0047	1.03	50.68
5665	Iwate	2008	613	2343	MYG006	6.9	209	40	104	39.027	140.878	6.5	30.38	146.72	-999	38.5801	140.9654	0.24	37.31
5666	Iwate	2008	613	2343	MYG007	6.9	209	40	104	39.027	140.878	6.5	45.55	166.75	-999	38.5876	141.251	0.13	7.88
5672	Iwate	2008	613	2343	MYG013	6.9	209	40	104	39.027	140.878	6.5	63.53	252.68	-999	38.2663	140.9293	0.27	18.76
5674	Iwate	2008	613	2343	MYG015	6.9	209	40	104	39.027	140.878	6.5	80.97	211.2	-999	38.1049	140.8699	0.14	11.57
5684	Iwate	2008	613	2343	MYGH10	6.9	209	40	104	39.027	140.878	6.5	99.62	347.54	-999	37.9381	140.8958	0.16	6.36
5685	Iwate	2008	613	2343	MYGH11	6.9	209	40	104	39.027	140.878	6.5	57.15	859.19	-999	38.5129	141.3456	0.14	4.17
5744	Iwate	2008	613	2343	YMT001	6.9	209	40	104	39.027	140.878	6.5	76.08	177.81	-999	38.914	139.8127	0.03	11.69
5746	Iwate	2008	613	2343	YMT003	6.9	209	40	104	39.027	140.878	6.5	79.22	368.93	-999	38.7292	139.8013	0.03	3.51
5748	Iwate	2008	613	2343	YMT005	6.9	209	40	104	39.027	140.878	6.5	55.76	192.29	-999	38.607	140.1621	0.06	4.14
5752	Iwate	2008	613	2343	YMT009	6.9	209	40	104	39.027	140.878	6.5	66.57	443.63	-999	38.3898	140.2743	0.03	12.15
5768	Iwate	2008	613	2343	YMTH09	6.9	209	40	104	39.027	140.878	6.5	47.01	291.48	-999	38.7469	140.1814	0.05	5.03
5773	Iwate	2008	613	2343	Miyagi Great Village	6.9	209	40	104	39.027	140.878	6.5	41.12	531.25	-999	38.4647	140.8833	0.20	13.04
5774	Iwate	2008	613	2343	Nakashinde n Town	6.9	209	40	104	39.027	140.878	6.5	29.37	276.3	-999	38.5689	140.8589	0.18	26.73
5780	Iwate	2008	613	2343	Iwadeyama	6.9	209	40	104	39.027	140.878	6.5	20.77	345.55	-999	38.6494	140.8803	0.34	39.31
5783	Iwate	2008	613	2343	Semine Kurihara City	6.9	209	40	104	39.027	140.878	6.5	28.9	362.57	-999	38.6533	141.0718	0.16	17.39
5788	Iwate	2008	613	2343	Masuda Natori	6.9	209	40	104	39.027	140.878	6.5	74.08	319.66	-999	38.1681	140.8953	0.35	24.98
5794	Iwate	2008	613	2343	Wakabayas hi-ku Sendai Tomizuka	6.9	209	40	104	39.027	140.878	6.5	66.18	295.35	-999	38.2411	140.9175	0.20	15.92
5797	Iwate	2008	613	2343	Oomagari Hanazono- cho, Daisen	6.9	209	40	104	39.027	140.878	6.5	46.32	262.25	-999	39.4506	140.4789	0.12	10.51
5812	Iwate	2008	613	2343	Kitakami Yanagiharac h	6.9	209	40	104	39.027	140.878	6.5	16.44	348.99	-999	39.29	141.1133	0.20	8.90

RSN	Name	YEAR	MO DY	HRM N	Station Name	Magnitude	Strike (°)	Dip (°)	Rake (°)	Hypocenter Latitude (°)	Hypocenter Longitude (°)	Hypocenter Depth (km)	R <sub>jb</sub> (km)	V <sub>s30</sub> (m/s)	Geologic al Unit	Station Latitude (°)	Station Longitude (°)	PGA (g)	PGV (cm/s)
5818	Iwate	2008	613	2343	Kurihara City	6.9	209	40	104	39.027	140.878	6.5	12.83	512. 26	-999	38.8233	140.9933	0.59	48.58
5821	Iwate	2008	613	2343	Sendai Airport	6.9	209	40	104	39.027	140.878	6.5	78.05	311. 6	-999	38.135	140.9311	0.14	12.88
5824	El Mayor- Cucapah	2010	404	2240	CICESE	7.2	236	63	-164	32.3	-115.267	5.45	118.4	505. 23	-999	31.8683	-116.664	0.02	3.40
5826	El Mayor- Cucapah	2010	404	2240	HEROES OF THE REVOLUT ION	7.2	236	63	-164	32.3	-115.267	5.45	80.59	415. 23	-999	31.615	-115.882	0.06	3.01
5833	El Mayor- Cucapah	2010	404	2240	TRES HERMAN OS	7.2	236	63	-164	32.3	-115.267	5.45	95.2	521. 76	-999	31.69	-116.19	0.05	3.66
5836	El Mayor- Cucapah	2010	404	2240	El Centro - Meloland Geot. Array	7.2	236	63	-164	32.3	-115.267	5.45	28.53	264. 57	Qal, deep, Imperial V.	32.773	-115.447	0.38	27.13
5841	El Mayor- Cucapah	2010	404	2240	Alpine Fire Station	7.2	236	63	-164	32.3	-115.267	5.45	97.09	567. 81	-999	32.838	-116.775	0.03	3.56
5846	El Mayor- Cucapah	2010	404	2240	San Diego - Hwy 15 & Ocean	7.2	236	63	-164	32.3	-115.267	5.45	127.37	371. 81	-999	32.702	-117.12	0.04	8.04
5851	El Mayor- Cucapah	2010	404	2240	San Diego - 45th & Orange	7.2	236	63	-164	32.3	-115.267	5.45	125.58	374. 5	-999	32.754	-117.097	0.03	5.41
5862	El Mayor- Cucapah	2010	404	2240	Bombay Beach - Bertram	7.2	236	63	-164	32.3	-115.267	5.45	81.42	491. 44	-999	33.397	-115.776	0.05	7.11
5878	El Mayor- Cucapah	2010	404	2240	Indio - Riverside Co Fair Grnds	7.2	236	63	-164	32.3	-115.267	5.45	125.51	282. 14	Qal, deep, Imperial V.	33.715	-116.221	0.04	6.36
5968	El Mayor- Cucapah	2010	404	2240	Bombay Beach	7.2	236	63	-164	32.3	-115.267	5.45	77.72	348. 77	-999	33.365	-115.73	0.05	9.30
5971	El Mayor- Cucapah	2010	404	2240	Borrego Springs - Scripps Clinic	7.2	236	63	-164	32.3	-115.267	5.45	80.27	357. 64	Qal, deep (incl LA)	33.1937	-116.329	0.04	8.95
5976	El Mayor- Cucapah	2010	404	2240	Calipatria Fire Station	7.2	236	63	-164	32.3	-115.267	5.45	54.77	205. 78	Qal, deep, Imperial V.	33.1266	-115.516	0.07	21.53
5977	El Mayor- Cucapah	2010	404	2240	Chihuahua Valley - Private Res	7.2	236	63	-164	32.3	-115.267	5.45	118.77	487. 2	-999	33.3822	-116.69	0.02	5.34
5990	El Mayor- Cucapah	2010	404	2240	El Centro Array #7	7.2	236	63	-164	32.3	-115.267	5.45	27.42	210. 51	Qal, deep, Imperial V.	32.829	-115.504	0.25	23.77
5991	El Mayor- Cucapah	2010	404	2240	El Centro Array #10	7.2	236	63	-164	32.3	-115.267	5.45	19.36	202. 85	Qal, deep, Imperial V.	32.7806	-115.568	0.37	49.96
6014	El Mayor- Cucapah	2010	404	2240	Mecca Fire Station	7.2	236	63	-164	32.3	-115.267	5.45	105.96	298. 71	Qal, deep, Imperial V.	33.572	-116.076	0.06	10.40
6027	El Mayor- Cucapah	2010	404	2240	Ocotillo Wells - Veh. Rec. Area	7.2	236	63	-164	32.3	-115.267	5.45	67.71	361. 22	Qoa	33.1557	-116.168	0.07	10.08
6031	El Mayor- Cucapah	2010	404	2240	Anza - Pinyon Flat	7.2	236	63	-164	32.3	-115.267	5.45	124.4	724. 89	Kgr	33.607	-116.453	0.01	3.21
6036	El Mayor- Cucapah	2010	404	2240	Rock Hill	7.2	236	63	-164	32.3	-115.267	5.45	58.24	309	-999	33.183	-115.623	0.05	7.86
6044	El Mayor- Cucapah	2010	404	2240	Salton Beach	7.2	236	63	-164	32.3	-115.267	5.45	92.03	367. 18	-999	33.485	-115.866	0.01	6.36

RSN	Name	YEAR	MO DY	HRM N	Station Name	Magnitude	Strike (°)	Dip (°)	Rake (°)	Hypocenter Latitude (°)	Hypocenter Longitude (°)	Hypocenter Depth (km)	R <sub>jb</sub> (km)	V <sub>s30</sub> (m/s)	Geologic al Unit	Station Latitude (°)	Station Longitude (°)	PGA (g)	PGV (cm/s)
6209	Tottori, Japan	2000	100 6	430	HRS019	6.61	330	90	0	35.275	133.35	12.5	127.22	182. 75	-999	34.2485	132.5647	0.07	6.57
6235	Tottori, Japan	2000	100 6	430	HYGH10	6.61	330	90	0	35.275	133.35	12.5	128.51	223. 87	-999	34.8132	134.8106	0.04	4.28
6515	Niigata, Japan	2004	102 3	856	FKS016	6.63	212	47	93	37.307	138.839	10.6	111.33	279. 58	-999	37.1228	140.1914	0.02	1.44
6720	Niigata, Japan	2004	102 3	856	NGNH32	6.63	212	47	93	37.307	138.839	10.6	128.26	309. 6	-999	36.2546	137.9929	0.02	0.92
6725	Niigata, Japan	2004	102 3	856	NIG001	6.63	212	47	93	37.307	138.839	10.6	101.11	648. 63	-999	38.2584	138.4337	0.04	2.01
6728	Niigata, Japan	2004	102 3	856	NIGH02	6.63	212	47	93	37.307	138.839	10.6	111.74	360	-999	38.2769	139.5519	0.04	3.01
6878	Joshua Tree, CA	1992	423	450	North Palm Springs Fire Sta #36	6.1	340	90	180	33.96	-116.317	12.4	21.4	367. 84	Qal, coarse	33.9247	-116.548	0.16	8.50
6886	Darfield, New Zealand	2010	903	1635	Canterbury Aero Club	7	85.1	82. 2	180	-43.615	172.049	10.9	14.48	280. 26	-999	- 43.4848	172.5299	0.19	41.66
6888	Darfield, New Zealand	2010	903	1635	Christchur h Cathedral College	7	85.1	82. 2	180	-43.615	172.049	10.9	19.89	198	-999	- 43.5395	172.6464	0.20	49.97
6889	Darfield, New Zealand	2010	903	1635	Christchur h Hospital	7	85.1	82. 2	180	-43.615	172.049	10.9	18.4	194	-999	- 43.5355	172.6261	0.18	48.88
6890	Darfield, New Zealand	2010	903	1635	Christchur h Cashmere High School	7	85.1	82. 2	180	-43.615	172.049	10.9	17.64	204	-999	- 43.5673	172.6241	0.24	35.94
6901	Darfield, New Zealand	2010	903	1635	FDSCS	7	85.1	82. 2	180	-43.615	172.049	10.9	90.17	389. 54	-999	- 44.1019	170.8285	0.11	9.58
6923	Darfield, New Zealand	2010	903	1635	Kaiapoi North School	7	85.1	82. 2	180	-43.615	172.049	10.9	30.53	255	-999	- 43.3781	172.6636	0.33	36.98
6928	Darfield, New Zealand	2010	903	1635	LPCC	7	85.1	82. 2	180	-43.615	172.049	10.9	25.21	649. 67	-999	- 43.6056	172.7223	0.30	24.96
6931	Darfield, New Zealand	2010	903	1635	LTZ	7	85.1	82. 2	180	-43.615	172.049	10.9	89.18	638. 39	-999	- 42.7834	172.2709	0.03	6.71
6933	Darfield, New Zealand	2010	903	1635	MAYC	7	85.1	82. 2	180	-43.615	172.049	10.9	33.54	342. 7	-999	- 43.8247	171.4216	0.07	6.92
6948	Darfield, New Zealand	2010	903	1635	OXZ	7	85.1	82. 2	180	-43.615	172.049	10.9	30.63	481. 62	-999	- 43.3259	172.0383	0.14	12.50
6960	Darfield, New Zealand	2010	903	1635	Riccarton High School	7	85.1	82. 2	180	-43.615	172.049	10.9	13.64	293	-999	- 43.5362	172.5644	0.21	48.47
6962	Darfield, New Zealand	2010	903	1635	ROLC	7	85.1	82. 2	180	-43.615	172.049	10.9	0	295. 74	-999	- 43.5945	172.381	0.39	83.83
6963	Darfield, New Zealand	2010	903	1635	RPZ	7	85.1	82. 2	180	-43.615	172.049	10.9	57.37	638. 39	-999	- 43.7192	171.0539	0.05	4.90
6966	Darfield, New Zealand	2010	903	1635	Shirley Library	7	85.1	82. 2	180	-43.615	172.049	10.9	22.33	207	-999	- 43.5053	172.6634	0.18	49.03
6971	Darfield, New Zealand	2010	903	1635	SPFS	7	85.1	82. 2	180	-43.615	172.049	10.9	29.86	389. 54	-999	- 43.3396	171.9288	0.16	20.86

RSN	Name	YEAR	MO DY	HRM N	Station Name	Magnitude	Strike (°)	Dip (°)	Rake (°)	Hypocenter Latitude (°)	Hypocenter Longitude (°)	Hypocenter Depth (km)	R <sub>jb</sub> (km)	V <sub>s30</sub> (m/s)	Geologic al Unit	Station Latitude (°)	Station Longitude (°)	PGA (g)	PGV (cm/s)
6975	Darfield, New Zealand	2010	903	1635	TPLC	7	85.1	82. 2	180	-43.615	172.049	10.9	6.11	249. 28	-999	- 43.5517	172.4718	0.24	64.40
6989	Darfield, New Zealand	2010	903	1635	WVAS	7	85.1	82. 2	180	-43.615	172.049	10.9	102.49	469. 44	-999	- 43.0731	170.737	0.03	5.83
8058	Christchur ch, New Zealand	2011	221	2351	APPS	6.2	59	67	135	-43.571	172.703	6	112.49	494. 96	-999	- 42.9506	171.5676	0.02	1.75
8071	Christchur ch, New Zealand	2011	221	2351	DFHS	6.2	59	67	135	-43.571	172.703	6	47.02	344. 02	-999	- 43.4913	172.102	0.06	4.03
8090	Christchur ch, New Zealand	2011	221	2351	Hulverstone Drive Pumping Station	6.2	59	67	135	-43.571	172.703	6	4.32	206	-999	- 43.5016	172.7022	0.25	38.54
8133	Christchur ch, New Zealand	2011	221	2351	SLRC	6.2	59	67	135	-43.571	172.703	6	31.81	249. 28	-999	- 43.6751	172.3175	0.09	8.70
8151	Christchur ch, New Zealand	2011	221	2351	WIGC	6.2	59	67	135	-43.571	172.703	6	91.59	490. 25	-999	- 42.7029	172.8002	0.01	1.46
8160	El Mayor- Cucapah	2010	404	2240	El Centro Array #4	7.2	236	63	-164	32.3	-115.267	5.45	35.08	208. 91	Qal, deep, Imperial V.	32.864	-115.432	0.25	24.10
8166	Duzce, Turkey	1999	1112	-999	IRIGM 498	7.14	270	65	-178	40.8345	31.1346	14	3.58	425	-999	40.7458 2	30.879	0.37	25.27
8167	San Simeon, CA	2003	122 2	1915	Diablo Canyon Power Plant	6.52	292	52	97	35.697	-121.085	8.5	37.92	110 0	-999	35.2126 3	-120.855	0.04	8.45
8501	El Mayor- Cucapah	2010	404	2240	Barrett	7.2	236	63	-164	32.3	-115.267	5.45	85.37	511	-999	32.6800 5	-116.672	0.06	3.65
8597	El Mayor- Cucapah	2010	404	2240	Sam W. Stewart	7.2	236	63	-164	32.3	-115.267	5.45	31.79	503	-999	32.9450 8	-115.8	0.08	9.95
8732	40204628	2007	103 1	304	Pacheco Peak, CA, USA	5.45	323	87	-180	37.4317	-121.777	7.486	61.27	686. 73	-999	37.008	-121.287	0.09	2.27
8834	14383980	2008	729	1842	Quigley Station	5.39	296	66	146	33.9465	-117.767	14.89	81.46	394. 66	-999	34.3956	-118.498	0.01	0.86
8898	14383980	2008	729	1842	Phelan - Centola & Phelan Rds	5.39	296	66	146	33.9465	-117.767	14.89	56.13	402. 6	-999	34.425	-117.544	0.03	1.90
8921	14383980	2008	729	1842	San Bernardino - Sycamore FS	5.39	296	66	146	33.9465	-117.767	14.89	39.82	630. 66	J metamorp hic	34.193	-117.427	0.02	1.03
8971	14383980	2008	729	1842	Los Angeles; Sepulveda Canyon	5.39	296	66	146	33.9465	-117.767	14.89	65.34	681. 24	-999	34.0967	-118.48	0.02	0.72
9076	14151344	2005	612	1541	Red Mountain, Riverside Co., Ca, Usa	5.2	304	58	172	33.5328	-116.57	15.48	25.97	704. 1	-999	33.63	-116.848	0.16	4.24
9152	14095628	2004	929	2254	Calstate Bakersfield	5.03	105	82	173	35.3852	-118.629	7.3	41.75	275	-999	35.3444	-119.105	0.01	0.71

## REFERENCES

- Ancheta, T. D., Darragh, R. B., Stewart, J. P., Seyhan, E., Silva, W. J., Chiou, B. S. J., ... & Donahue, J. L. (2014). NGA-West2 database. *Earthquake Spectra*, *30*(3), 989-1005.
- Applied Technology Council, & National Earthquake Hazards Reduction Program (US). (2012). *Seismic performance assessment of buildings*. Federal Emergency Management Agency.
- Applied Technology Council. (2009). *Quantification of building seismic performance factors*. US Department of Homeland Security, FEMA.
- Atwater, B. F. (1982). *Geologic maps of the Sacramento-San Joaquin Delta, California* (No. 1401). US Government Printing Office.
- Baker, J. W. (2008). An introduction to probabilistic seismic hazard analysis (PSHA). *White paper, version, 1*, 72.
- Baker, J. W. (2015). Efficient analytical fragility function fitting using dynamic structural analysis. *Earthquake Spectra*, *31*(1), 579-599.
- Baker, J. W., & Lee, C. (2018). An improved algorithm for selecting ground motions to match a conditional spectrum. *Journal of Earthquake Engineering*, *22*(4), 708-723.
- Bazzurro, P., & Allin Cornell, C. (1999). Disaggregation of seismic hazard. *Bulletin of the Seismological Society of America*, *89*(2), 501-520.
- Boore, D. M., Stewart, J. P., Seyhan, E., & Atkinson, G. M. (2014). NGA-West2 equations for predicting PGA, PGV, and 5% damped PSA for shallow crustal earthquakes. *Earthquake Spectra*, *30*(3), 1057-1085.

Brandenberg, S. J., Stewart, J. P., Liu, Z., Wang, P., Zimmaro, P., Bachand S., ... & Ulrich, C. Next Generation Multi-Hazard Levee Risk Assessment. (February 1, 2022).

Buckreis, T. E. (2022). *Customization of Path and Site Response Components of Global Ground Motion Models for Application in Sacramento-San Joaquin Delta Region of California*. University of California, Los Angeles.

Buckreis, T. E., Stewart, J. P., Brandenberg, S. J., & Wang, P. (2023). Subregional anelastic attenuation model for California. *Bulletin of the Seismological Society of America*, 113(6), 2292-2310.

Bullock, Z., Dashti, S., Liel, A. B., Porter, K. A., & Karimi, Z. (2019). Assessment supporting the use of outcropping rock evolutionary intensity measures for prediction of liquefaction consequences. *Earthquake Spectra*, 35(4), 1899-1926.

Burton, H. V., & Baker, J. W. (2023). Evaluating the effectiveness of ground motion intensity measures through the lens of causal inference. *Earthquake Engineering & Structural Dynamics*.

Calvi, G. M., Pinho, R., Magenes, G., Bommer, J. J., Restrepo-Vélez, L. F., & Crowley, H. (2006). Development of seismic vulnerability assessment methodologies over the past 30 years. *ISET journal of Earthquake Technology*, 43(3), 75-104.

Campbell, K. W., & Seligson, H. A. (2003). Quantitative method for developing hazard-consistent earthquake scenarios. In *Advancing Mitigation Technologies and Disaster Response for Lifeline Systems* (pp. 829-838).

Cetin, K. O., Seed, R. B., Der Kiureghian, A., Tokimatsu, K., Harder, L. F., Kayen, R. E., and Moss, R.E. S. 2004. Standard penetration test-based probabilistic and deterministic assessment of

seismic soil liquefaction potential, *J. Geotechnical and Geoenvironmental Eng.*, ASCE 130(12): 1314–340.

Chang, S. E., Shinozuka, M., & Moore, J. E. (2000). Probabilistic earthquake scenarios: extending risk analysis methodologies to spatially distributed systems. *Earthquake Spectra*, 16(3), 557-572.

Chernozhukov, V., Chetverikov, D., Demirer, M., Duflo, E., Hansen, C., & Newey, W. (2017). Double/debiased/neyman machine learning of treatment effects. *American Economic Review*, 107(5), 261-265.

Cuthill, E., & McKee, J. (1969, August). Reducing the bandwidth of sparse symmetric matrices. In *Proceedings of the 1969 24th national conference* (pp. 157-172).

Darendeli, M. B. (2001). *Development of a new family of normalized modulus reduction and material damping curves*. The University of Texas at Austin.

Deverel, S. J., Ingrum, T., & Leighton, D. (2016). Present-day oxidative subsidence of organic soils and mitigation in the Sacramento-San Joaquin Delta, California, USA. *Hydrogeology Journal*, 24, 569.

Edward H. Field, Kevin R. Milner, Alexandra E. Hatem, Peter M. Powers, Fred F. Pollitz, Andrea L. Llenos, Yuehua Zeng, Kaj M. Johnson, Bruce E. Shaw, Devin McPhillips, Jessica Thompson Jobe, Allison M. Shumway, Andrew J. Michael, Zheng-Kang Shen, Eileen L. Evans, Elizabeth H. Hearn, Charles S. Mueller, Arthur D. Frankel, Mark D. Petersen, Christopher DuRoss, Richard W. Briggs, Morgan T. Page, Justin L. Rubinstein, Julie A. Herrick; The USGS 2023 Conterminous U.S. Time-Independent Earthquake Rupture Forecast. *Bulletin of the Seismological Society of America* 2023; doi: <https://doi.org/10.1785/0120230120>

Elgamal, A., Yang, Z., Parra, E., & Ragheb, A. (2003). Modeling of cyclic mobility in saturated cohesionless soils. *International Journal of Plasticity*, 19(6), 883-905.

Erdem, J.E., Boatwright, J., and Fletcher, J.B. (2019). “Ground-Motion Attenuation in the Sacramento–San Joaquin Delta, California, from 14 Bay Area Earthquakes, including the 2014 M 6.0 South Napa Earthquake” *Bulletin of the Seismological Society of America*, 109(3) 1025-1033.

Field, E.H., and 2014 Working Group on California Earthquake Probabilities, 2015, UCERF3: A new earthquake forecast for California’s complex fault system: U.S. Geological Survey 2015–3009, 6 p., <https://dx.doi.org/10.3133/fs20153009>. Cornell, C. A. (1968). Engineering seismic risk analysis. *Bulletin of the seismological society of America*, 58(5), 1583-1606.

Finch, M. (1985). Earthquake Damage in the Sacramento-San Joaquin Delta. *California Geology*, 38(2), 39-44.

Foxgrover, A., Smith, R.E., and Jaffe, B.E., 2007, Suisun Bay and Delta bathymetry: U.S. Geological Survey [<http://sfbay.wr.usgs.gov/sediment/delta/>, last accessed February 15, 2008]

Goyal, C. R. (2017). *Uncertainty Quantification in non-linear seismic wave propagation* (Doctoral dissertation, Carleton University).

Han Y. and Davidson R.A. 2012. Probabilistic seismic hazard analysis for spatially distributed infrastructure. *Earthq. Eng. Struct. Dyn.*, 41 (15): 2141–2158.

Harder Jr, L. F., & Boulanger, R. (1997). Application of K and K correction factors. In *Proceeding of the NCEER workshop on evaluation of liquefaction resistance of soils* (pp. 167-90).

Hastie, T., Tibshirani, R., & Wainwright, M. 2015. Statistical learning with sparsity: the Lasso and



generalizations (1st ed.). *Chapman and Hall/CRC*. <https://doi.org/10.1201/b18401>

Idriss, I. M., and Boulanger, R. W. 2006. Semi-empirical procedures for evaluating liquefaction potential during earthquakes, *J. Soil Dynamics and Earthquake Eng.* 26: 115–30.

Jayaram N. and Baker J. 2010. Efficient sampling and data reduction techniques for probabilistic seismic lifeline risk assessment. *Earthq. Eng. Struct. Dyn.*, 39 (10):1109–1131.

Jayaram, N., & Baker, J. W. (2009). Correlation model for spatially distributed ground-motion intensities. *Earthquake Engineering & Structural Dynamics*, 38(15), 1687-1708.

Jibson, R. W. 2007. Regression models for estimating coseismic land-slide displacement. *Eng. Geol.*, 91: 209–218.

Joyner, W. B., & Chen, A. T. (1975). Calculation of nonlinear ground response in earthquakes. *Bulletin of the Seismological Society of America*, 65(5), 1315-1336.

Kennedy, R. P., & Ravindra, M. K. (1984). Seismic fragilities for nuclear power plant risk studies. *Nuclear engineering and design*, 79(1), 47-68.

Khosravifar, A., Elgamal, A., Lu, J., & Li, J. (2018). A 3D model for earthquake-induced liquefaction triggering and post-liquefaction response. *Soil Dynamics and Earthquake Engineering*, 110, 43-52.

Kim, S. H., & Shinozuka, M. (2004). Development of fragility curves of bridges retrofitted by column jacketing. *Probabilistic Engineering Mechanics*, 19(1-2), 105-112.

Kiremidjian, A., Stergiou, E., and Lee, R. 2007. Issues in seismic risk assessment of transportation networks, in *Earthquake Geotechnical Engineering*, ed. K. Pitilakis (Springer, Dordrecht), pp. 461–480.

Kwak, D. Y., Stewart, J. P., Brandenburg, S. J., & Mikami, A. (2016a). Characterization of seismic levee fragility using field performance data. *Earthquake Spectra*, 32(1), 193-215.

Kwak, D. Y., Stewart, J. P., Brandenburg, S. J., & Mikami, A. (2016b). Seismic levee system fragility considering spatial correlation of demands and component fragilities. *Earthquake Spectra*, 32(4), 2207-2228.

Kwak, D., Ahdi, S. K., Wang, P., Zimmaro, P., Brandenburg, S. J., & Stewart, J. P. (2021). Web portal for shear wave velocity and HVSR databases in support of site response research and applications.

Liu, Z. (2023a). Create KML files for selected events. GitHub. [https://github.com/zehanliu623/Create\\_KML\\_files](https://github.com/zehanliu623/Create_KML_files).

Liu, Z. (2023b). Implement Updated Linear Site and Path Models in BSSA14 through OpenQuake. GitHub. [https://github.com/zehanliu623/Linear\\_Site\\_and\\_Path\\_Model\\_in\\_BSSA14\\_of\\_OQ-Engine](https://github.com/zehanliu623/Linear_Site_and_Path_Model_in_BSSA14_of_OQ-Engine).

Liu, Z. (2023c). LASSO Regression-based Event Selection Implementation using Python. GitHub. <https://github.com/zehanliu623/LRBES>.

Liu, Z. (2023d). Seismic Risk Assessment Using Level Crossing Statistics. GitHub. [https://github.com/zehanliu623/Seismic\\_Risk\\_Assessment](https://github.com/zehanliu623/Seismic_Risk_Assessment).

Liu, Z., Wang, P., Brandenburg, S. J., Zimmaro, P., & Stewart, J. P. (2022). Validation of Regression-Based Event Selection for Seismic Risk Assessment of Distributed Levee System in California. In *Proceedings of the 12th National Conference on Earthquake Engineering*.

Matheron, G. (1965). Les variables régionalisées et leur estimation: une application de la théorie

de fonctions aléatoires aux sciences de la nature. (*No Title*).

McGann, C. R., & Arduino, P. (2014). Numerical assessment of three-dimensional foundation pinning effects during lateral spreading at the Mataquito River Bridge. *Journal of Geotechnical and Geoenvironmental Engineering*, 140(8), 04014037.

McGann, C. R., & Arduino, P. (2015). Numerical assessment of the influence of foundation pinning, deck resistance, and 3D site geometry on the response of bridge foundations to demands of liquefaction-induced lateral soil deformation. *Soil Dynamics and Earthquake Engineering*, 79, 379-390.

McGann, C. R., Arduino, P., & Mackenzie-Helnwein, P. (2012). Stabilized single-point 4-node quadrilateral element for dynamic analysis of fluid saturated porous media. *Acta Geotechnica*, 7, 297-311.

McGuire, R. K. (1995). Probabilistic seismic hazard analysis and design earthquakes: closing the loop. *Bulletin of the Seismological Society of America*, 85(5), 1275-1284.

McGuire, R. K. (2001). Deterministic vs. probabilistic earthquake hazards and risks. *Soil Dynamics and Earthquake Engineering*, 21(5), 377-384.

Menq, F. Y. (2003). *Dynamic properties of sandy and gravelly soils*. The University of Texas at Austin.

Miller, M., & Baker, J. (2015). Ground-motion intensity and damage map selection for probabilistic infrastructure network risk assessment using optimization. *Earthquake Engineering & Structural Dynamics*, 44(7), 1139-1156.

Mount, J., & Twiss, R. (2005). Subsidence, sea level rise, and seismicity in the Sacramento–San

Joaquin Delta. *San Francisco Estuary and Watershed Science*, 3(1).

OCM Partners, 2023: 2017 CA DWR Lidar: Sacramento Delta, CA, <https://www.fisheries.noaa.gov/inport/item/65524>.

Pagani, M., Monelli, D., Weatherill, G., Danciu, L., Crowley, H., Silva, V., ... & Vigano, D. (2014). OpenQuake engine: An open hazard (and risk) software for the global earthquake model. *Seismological Research Letters*, 85(3), 692-702.

Peter, P. (2018). nshmp-haz. GitHub. <https://github.com/usgs/nshmp-haz>

Porter, K., Kennedy, R., & Bachman, R. (2007). Creating fragility functions for performance-based earthquake engineering. *Earthquake spectra*, 23(2), 471-489.

Rathje, E. M., Dawson, C., Padgett, J. E., Pinelli, J. P., Stanzione, D., Adair, A., ... & Mosqueda, G. (2017). DesignSafe: New cyberinfrastructure for natural hazards engineering. *Natural Hazards Review*, 18(3), 06017001.

Rathje, E.M., Saygili, G., 2011. Estimating fully probabilistic seismic sliding displacements of slopes from a pseudo probabilistic approach. *Journal of Geotechnical and Geoenvironmental Engineering*. 137 (3): 208–217.

Rosidi, D. (2007). Seismic risk assessment of levees. *Civil Engineering Dimension*, 9(2), 57-63.

Salah-Mars, S., Rajendram, A., Kulkarni, R., McCann, Jr, M. W., Logeswaran, S., Thangalingam, K., ... & Bagheban, S. (2008). Seismic vulnerability of the Sacramento-San Joaquin Delta levees. In *Geotechnical Earthquake Engineering and Soil Dynamics IV* (pp. 1-10).

Schwartz, D. P., & Coppersmith, K. J. (1984). Fault behavior and characteristic earthquakes: Examples from the Wasatch and San Andreas fault zones. *Journal of Geophysical Research: Solid*

Earth, 89(B7), 5681-5698.

Seed HB, Idriss IM (1982) Ground motions and soil liquefaction during earthquakes. Earthq Eng Res Institute, Berkeley 134 pp.

Seyhan, E and JP Stewart (2014). Semi-empirical nonlinear site amplification from NGA-West 2 data and simulations, *Earthquake Spectra*, 30, 1241-1256.

Shafei, B., Zareian, F., & Lignos, D. G. (2011). A simplified method for collapse capacity assessment of moment-resisting frame and shear wall structural systems. *Engineering Structures*, 33(4), 1107-1116.

Shafiee, A. (2016). Cyclic and post-cyclic behavior of Sherman Island peat. University of California, Los Angeles.

SHLEMON, R. J., & EL, B. (1975). LATE QUATERNARY EVOLUTION OF THE SACRAMENTO-SAN JOAQUIN DELTA, CALIFORNIA.

Soleimani N., Davidson R.A., Davis C., O'Rourke T.D., Nozick L.K. 2021. Multihazard scenarios for regional seismic risk assessment of spatially distributed infrastructure. *Journal of Infrastructure Systems*. 27(1): 04021001

Spearman, C. (1961). The proof and measurement of association between two things.

Tokimatsu, K., & Sekiguchi, T. (2006). Effects of nonlinear properties of surface soils on strong ground motions recorded in Ojiya during 2004 Mid Niigata Prefecture earthquake. *Soils and foundations*, 46(6), 765-775.

Tsai, Y.T. (2018). *Charactering Seismic Performance of Levees on Peaty Oragnic Soils from Case Histories and Simulations*. University of California, Los Angeles.

Uhlemann, S., C. Ulrich, A. Gniazdowska, M. Craig, P. Nico, S. Brandenburg. (2021) "Geophysical Data - Next Generation Multi-Hazard Levee Assessment." DesignSafe-CI. <https://doi.org/10.17603/ds2-fp5z-1a55 v1>

Unruh, J., Hitchcock, C., Blake, K., & Hector, S. (2016). Characterization of the Southern Midland Fault in the Sacramento–San Joaquin Delta. *Applied Geology in California. Belmont CA: Association of Environmental & Engineering Geologists Special Publication, Star Publishing Co,* 26.

URS/JBA [URS Corporation/Jack R. Benjamin & Associates, Inc.]. 2008. Delta Risk Management Strategy, Phase 1, Risk Analysis Report, Section 9. Prepared for California Department of Water Resources, Dec.

Vaziri P., Davidson R.A., Apivataganul P., and & Nozick L. 2012. Identification of optimization-based probabilistic earthquake scenarios for regional loss estimation. *Journal of Earthquake Engineering*, 16 (2): 296–315, DOI:10.1080/13632469.2011.597486

Villaverde, R. (2007). Methods to assess the seismic collapse capacity of building structures: State of the art. *Journal of Structural Engineering*, 133(1), 57-66.

Wang P. (2022). Regional Probabilistic Seismic Hazard Assessment (RPSHA) Package. Available at <https://github.com/wlrcwfp/RPSHA>. Last updated March, 2022.

Wang, P., Buckreis, T. E., Brandenburg, S. J., & Stewart, J. P. Modified Hyperbolic Model for Dynamic Properties of Peaty Organic Soils. In *Geo-Congress 2023* (pp. 273-282).

Wang, P., Liu, Z., Brandenburg, S. J., Zimmaro, P., & Stewart, J. P. (2022). Regression-based event selection for hazard-consistent seismic risk assessment. In *Proceedings of the 12th National*

*Conference on Earthquake Engineering.*

Wang, P., Liu, Z., Brandenberg, S. J., Zimmaro, P., & Stewart, J. P. (2023). Regression-based scenario earthquake selection for regional hazard-consistent risk assessments. *Earthquake Spectra*, 39(4), 2236-2262.

Yang, Y. (2021). *Calibrated Fragility Functions for Seismic Loading of Sacramento-San Joaquin River Delta Levees*. University of California, Los Angeles.

Yee, E., Stewart, J. P., & Tokimatsu, K. (2013). Elastic and large-strain nonlinear seismic site response from analysis of vertical array recordings. *Journal of Geotechnical and Geoenvironmental Engineering*, 139(10), 1789-1801.

Yoshimi, Y., Tokimatsu, K., Kaneko, O., & Makihara, Y. (1984). Undrained cyclic shear strength of a dense Niigata sand. *Soils and Foundations*, 24(4), 131-145.

Youd, T. L., Idriss, I. M., Andrus, R. D., Arango, I., Castro, G., Christian, J. T., Dobry, R., Finn, W. D. L., Harder, L. F., Hynes, M. E., Ishihara, K., Koester, J. P., Liao, S. S. C., Marcuson, W. F., Martin, G. R., Mitchell, J. K., Moriwaki, Y., Power, M. S., Robertson, P. K., Seed, R. B., and Stokoe, K. H. 2001. Liquefaction resistance of soils: summary report from the 1996 NCEER and 1998 NCEER/NSF workshops on evaluation of liquefaction resistance of soils, *J. Geotechnical and Geoenvironmental Eng.*, ASCE 127(10): 817–33.

Zhang, G., Robertson, P. K., Brachman, R. W. I. 2004. Estimating liquefaction-induced lateral displacements using the standard penetration test or cone penetration test. *J. Geotechnical and Geoenvironmental Eng.*, 130(8): 861–871.

Zienkiewicz, O. C., & Shiomi, T. (1984). Dynamic behaviour of saturated porous media; the

generalized Biot formulation and its numerical solution. *International journal for numerical and analytical methods in geomechanics*, 8(1), 71-96.

Zimmaro, P., Stewart, J. P., Brandenberg, S. J., Kwak, D. Y., & Jongejan, R. (2019). Multi-hazard system reliability of flood control levees. *Soil Dynamics and Earthquake Engineering*, 124, 345-353.